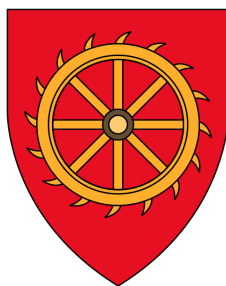




Self-Assembly in Physisorbed Monolayers via Directional Intermolecular Interactions



Jonathan Alexander Davidson

Department of Chemistry
University of Cambridge

This dissertation is submitted for the degree of
Doctor of Philosophy

I would like to dedicate this thesis to my mother. I know how much this means to her.

Declaration

This thesis is the result of my own work and includes nothing which is the outcome of work done in collaboration except as declared in the Preface and specified in the text. I further state that no substantial part of my thesis has already been submitted, or, is being concurrently submitted for any such degree, diploma or other qualification at the University of Cambridge or any other University or similar institution except as declared in the Preface and specified in the text. It does not exceed the prescribed word limit for the relevant Degree Committee

Jonathan Alexander Davidson
July 2021

Self-Assembly in Physisorbed Monolayers via Directional Intermolecular Interactions

Jonathan Alexander Davidson

In this work, the ability of two non-covalent directional interactions (halogen and hydrogen bonds) to influence the structure of self-assembled physisorbed organic monolayers is considered. These layers exhibit only weak, non-directional interactions with the substrate, and so their structure is driven by the adsorbate-adsorbate interactions.

In the initial phase of work, scanning tunnelling microscopy (STM) images of perylene tetracarboxylic diimide on a gold {111} surface are collected, exhibiting an unprecedented level of sub-molecular resolution of the structural detail of the molecular monolayer. In addition to this, a novel monolayer phase of 4,4'-bipyridine is identified, and the difficulty of utilising halogen bonds for self assembly on a metallic surface demonstrated.

The major technique used in this work is powder X-ray diffraction of monolayers deposited on a recompressed graphite surface. A novel scattering geometry and the use of a 2D area detector has allowed the collection of near-synchrotron-quality diffractograms using a lab based rotating anode X-ray source within a reasonable timeframe. Using this technique it has been possible to characterise the assembly of a range of pure adsorbed monolayers, and a number of co-crystalline monolayers. 1,3,5-triiodotrifluorobenzene was successfully characterised both alone, and upon co-deposition with 4,4'-bipyridine and s-triazine. It has also been possible to demonstrate the assembly of a homologous series of co-crystals between various α,ω -diiodinated perfluoroalkanes and 4,4'-bipyridine. All of the above systems have been structurally characterised for the first time.

Importantly, for several of these key systems the experimental structures have been used to allow collaborators to theoretically simulate the layers using DFT. This DFT work provides a more detailed, quantitative understanding of the key factors determining the structure of these novel halogen-bonded monolayers, particularly the relative importance of the halogen bonding and van-der Waals forces. This balance of forces is used to discuss the long-term aim of designing porous monolayer systems.

In addition to the above, a parallel stream of work considers the assembly of trimesic acid on graphite. This system has been explored by others using STM, however the quantitative details of the lattice constant, and the reality of the coexistence of two monolayer phases has until now been uncertain. Very significant experimental challenges have been overcome in this work, particularly depositing monolayer samples of the trimesic acid, to successfully determine diffraction patterns. These patterns allow calculation of the lattice constants of the “flower” and “chickenwire” phases, and to estimate the relative proportions of each. These

experiments provide a demonstration of the utility of XRD as a complementary technique to STM for study of systems such as these.

Acknowledgements

Well it's been a long time coming but it's finally here. After all the stress of lockdown and thesis writing it feels like a huge weight off my shoulders to only have the acknowledgements left to do. However of course this is still a hugely important section, to thank everyone whose love and support helped make everything written here possible.

First and foremost I need to thank both of my supervisors; Stuart Clarke and Stephen Jenkins. This whole project was a collaboration aimed at combining the expertise of the two surface science groups in the department and having the benefit of their different perspectives was hugely rewarding. Alongside this I must thank our external collaborators; Marco Sacchi began his involvement in DFT simulation of halogen bonding more than eight years ago, and it was fantastic that he was able to pick up from his previous work with Adam Brewer. Markus Lackinger inspired some of the TMA work presented in chapter seven, and it was hugely helpful to have him supportive of our efforts to build upon his STM work through original diffraction experiments. Finally I am indebted to Fabrice Gorrec at the Laboratory of Molecular Biology for allowing me to use a rotating anode diffractometer for data collection. Although some novel geometric correction was required, it was more accessible than synchrotron beamtime, and produced data of far greater quality than other available X-ray sources.

Beyond my academic mentors I am also hugely grateful to everyone else in the Jenkins Group and at the BPI; when times were tough and experiments don't work it's so important to have supportive and helpful co-workers. There's too many for me to list everyone here, but in particular Bianca, Sabine, Fin, and Bee, it was an honour going through the trial of academia with all of you!

Outside of the departments I was also lucky to also have the support of the wider St Catharine's College MCR community. The ability to have stimulating and fascinating discussions in academic fields far removed from my own provided a much needed pressure release and the cheese and wine didn't hurt either! Having been at Catz for far too long there really are too many names to list individually, but a special thanks goes to everyone involved in the MCR committee. Being Dining Officer and then Co-President was a huge part of my postgraduate experience and I learned almost as much in those roles as I did in the lab!

Publications

List of publications arising from this work:

- **J. A. Davidson**, S. J. Jenkins, F. Gorrec and S.M. Clarke, 2D constraint modifies packing behaviour: a halobenzene monolayer with X₃ halogen-bonding motif, *Mol. Phys.*, 2021
- **J. A. Davidson**, M. Sacchi, F. Gorrec, S. M. Clarke and S. J. Jenkins, Halogen Bonding in Bicomponent Monolayers: Self-Assembly of a Homologous Series of Iodinated Perfluoroalkanes with Bipyridine, *Langmuir*, 2021, 37, 2, 627–635
- **J. A. Davidson**, S. J. Jenkins, F. Gorrec and S. M. Clarke, C–H . . . N hydrogen bonding in an overlayer of s-triazine physisorbed on a graphite surface, *Mol. Phys.*, 2019, 8976, 1–5.
- D. Amabilino, I. Bâldea, O. Barykina, J. Batteas, P. Besenius, P. Beton, N. Bilbao, M. Buck, L. Chi, S. Clarke, G. Costantini, **J. Davidson**, P. Davies, S. De Feyter, Y. Diaz Fernandez, D. Dwivedi, K.-H. Ernst, A. Flood, J. Gautrot, A. Jabbarzadeh, V. Korolkov, A. Kühnle, M. Lackinger, C.-M. Pradier, T. Rahman, R. Raval, S. Schwaminger, J. Seibel, S. Tait, J. Teyssandier, and H. Zuilhof, “Preparing macromolecular systems on surfaces: General discussion,” *Faraday Discussions*, vol. 204, pp. 395–418, 2017.
- D. Amabilino, I. Bâldea, J. Batteas, P. Beton, N. Bilbao, G. Costantini, **J. Davidson**, S. De Feyter, Y. Diaz Fernandez, K.-H. Ernst, B. Hirsch, A. Jabbarzadeh, R. Jones, A. Kühnle, M. Lackinger, Z. Li, N. Lin, T. Linderoth, N. Martsinovich, M. Nalbach, C.-M. Pradier, T. Rahman, R. Raval, N. Robinson, F. Rosei, M. Sacchi, M. Samperi, A. Sanz Matias, A. Saywell, S. Schwaminger, and S. Tait, “Probing properties of molecule-based interface systems: General discussion and Discussion of the Concluding Remarks,” *Faraday Discussions*, vol. 204, pp. 503–530, 2017.

Table of contents

1	Introduction	1
1.1	Introduction	1
1.2	Intermolecular Interactions	3
1.2.1	Hydrogen Bonds	4
1.2.2	Halogen Bonds	5
1.2.3	Halogen-Halogen contacts	10
1.3	Supramolecular Chemistry	11
1.3.1	Terminology	11
1.3.2	Host-Guest Chemistry	12
1.3.3	Crystal Engineering	12
1.3.4	Co-existence of phases	13
1.4	Monolayers	13
1.4.1	Definition	13
1.4.2	History	14
1.4.3	Adsorption on Solid Surfaces	15
1.4.4	Techniques	18
1.4.5	Hydrogen-bonded Monolayers: Trimesic acid	20
1.4.6	Hydrogen-bonded Monolayers: PTCDI	28
1.4.7	Halogen-bonded Monolayers	30
1.5	Scope of this Work	33
2	Experimental Techniques	35
2.1	Scanning Tunnelling Microscopy(STM)	35
2.1.1	Introduction	35
2.1.2	Theory of Operation	36
2.1.3	Image Processing	38
2.1.4	Practical Considerations	39
2.1.5	Substrate	41

2.1.6	Substrate Cleaning	42
2.1.7	STM Instrumental details	44
2.1.8	Instrument Effects	47
2.2	X-Ray Diffraction (XRD)	47
2.2.1	Substrate	48
2.2.2	Sample Dosing	49
2.2.3	X-ray sources	50
2.2.4	Instruments Used	54
2.2.5	Theory	58
2.2.6	Atomic Scattering Factors	59
2.2.7	Powder Diffraction	62
2.2.8	Temperature Effects	62
2.2.9	Diffraction From 2D systems	63
2.2.10	Data fitting	67
2.2.11	Neutron diffraction	72
3	STM data	75
3.1	Introduction	75
3.2	PTCDI	76
3.2.1	Experimental	77
3.2.2	Initial images	77
3.2.3	High Resolution Images	79
3.2.4	Discussion	82
3.2.5	Summary	84
3.3	Trimesic acid on gold	85
3.3.1	Experimental	85
3.3.2	Results	85
3.3.3	Summary	87
3.4	Halogen Bonded layers	87
3.4.1	Experimental	88
3.4.2	4,4'-Bipyridine	88
3.5	Graphite	93
3.5.1	Experimental	93
3.5.2	Results	93

4	Substrate Analysis	97
4.1	Introduction	97
4.1.1	Highly Oriented Pyrolytic Graphite (HOPG)	97
4.1.2	Powdered Graphites	97
4.2	BET	99
4.2.1	Theory	99
4.2.2	Method	101
4.2.3	Results	102
4.3	Rocking curve	102
4.3.1	Geometric correction	104
4.3.2	Experimental	111
4.3.3	Analysis	112
4.3.4	Summary	116
4.4	Flat Plate Geometry	116
4.4.1	Setup	117
4.4.2	Derivation	119
5	Triiodotrifluorobenzene	127
5.1	Introduction	127
5.2	Monocomponent	128
5.2.1	Introduction	128
5.2.2	Experimental	131
5.2.3	Results	132
5.3	Co-deposition of TITFB with Bipyridine	136
5.3.1	Introduction	136
5.3.2	Experimental	137
5.3.3	Results	138
5.3.4	Conclusion	140
5.4	Co-deposition of TITFB with Triazine	140
5.4.1	Introduction	140
5.4.2	Experimental	141
5.4.3	Conclusion	142
6	Perfluoroalkane Halogen Bond Donors	143
6.1	Terminally Iodinated Perfluoroalkanes	143
6.1.1	Introduction	143
6.1.2	Experimental	146

6.1.3	Monocomponent 2D systems	146
6.1.4	Co-deposition of α,ω -terminally iodinated perfluoroalkanes with Bipyridine	149
6.1.5	Conclusion	158
6.2	Terminally Brominated Perfluoroalkanes	159
6.3	Computational	160
6.3.1	TITFB Simulation	161
6.3.2	Terminally Iodinated Perfluoroalkanes	163
6.4	Conclusion	167
7	Hydrogen Bonded systems	169
7.1	Triazine	169
7.1.1	Introduction	169
7.1.2	Experimental	170
7.1.3	Results	170
7.1.4	DFT analysis	174
7.1.5	Summary	175
7.2	Trimesic acid	176
7.2.1	Introduction	176
7.2.2	Bulk diffraction	176
7.2.3	Dosing Monolayer Samples	177
7.2.4	Monolayer Diffraction Results	189
7.2.5	Conclusion	194
8	Conclusion	197
8.1	Summary	197
8.2	Further Work	198
8.3	Concluding Remarks	199
	References	201

Chapter 1

Introduction

1.1 Introduction

Self-Assembly is the organisation of molecules into defined arrangements without any external stimulus. Such assembly can occur in a variety of formats, from the zipping of complementary strands of DNA,¹ to the formation of molecular machinery such as artificial motors at the nanoscale.²

By techniques able to manipulate single atoms and molecules, it is now possible to generate a single example of nearly any feasible nanostructure. However, to have a measurable impact on the macroscopic world, such structures must be capable of being produced in significant quantities. Self assembly is of great interest because, unlike nanoscience techniques such as molecular manipulation, it provides a method to generate systems using macroscopic synthesis and mixing techniques which can be designed to have desirable nanoscale structures.³

This is possible because the structure of the components of self-assembled systems encode the eventual pattern of the whole, a phenomenon that can be most clearly observed in biological systems such as in the folding of proteins. All proteins consist of just 21 amino acids, and yet the quantity and order of these amino acids encodes a complex nanoscale structure that self assembles once the protein is made. The end structure is encoded through the intermolecular interactions that occur between the amino acid components of the protein which, when optimised, generate the equilibrium self-assembled structure.

Intermolecular interactions are relevant to a huge number of materials encountered in everyday life.⁴ They occur in a variety of different contexts, in a variety of different phases. Nearly all interactions are electromagnetic in origin, but for convenience different subdivisions have been developed for understanding the interactions in specific contexts. Many such interactions have been identified and studied including hydrogen bonds,^{5,6}

the related hydrophobic effect^{7,8} and even the various interactions of π systems.^{9,10} An interaction that has recently gained renewed prominence is halogen bonding.

The halogen bond is the interaction observed for certain halogen atoms in which they favourably interact with a Lewis base lone pair donor (see section 1.2.2). The interaction was first encountered in the 19th century,¹¹ but for many years was denied recognition as a class of interactions, with specific examples being noted, but little unifying theory to group the phenomena together. More recently, increased focus has been placed on halogen bonding as a specific class of interaction. A demonstration of this was in 2013, when IUPAC officially defined the halogen bond.¹² Halogen bonds have been used for sensing,¹³ binding of guests in cavities,¹⁴ and for building supramolecular frameworks.¹⁵ Perhaps most surprisingly, halogen bonds have also been observed to occur in certain biological contexts,¹⁶ though biological halogen bonding systems are generally weaker than the highly fluorinated synthetic systems designed for the previously mentioned applications.

This renaissance in studies of halogen bonding has coincided with a renewed interest in self-assembly of physisorbed monolayers.¹⁷ Much work over the last 30 years on self-assembled monolayers has considered chemisorbed monolayers, best exemplified by the ubiquitous class of gold-thiol monolayers.¹⁸ Chemisorbed monolayers consist of molecules with a strong, generally chemical, bond to the surface. They generally exhibit only weak, non-directional interactions between adjacent adsorbates, and hence show minimal tunable self-assembly behaviour. As the layer formation in chemisorbed systems tends to be irreversible, these systems cannot exhibit responsive behaviour whereby a layer can form and un-form depending on conditions.

Physisorbed monolayers, by contrast, consist of molecules only weakly bound to the surface. This weak binding permits easy diffusion across the surface to achieve thermodynamic equilibrium. Hence, in these layers, molecules will be arranged in such a way so as to maximise the strength of inter-adsorbate interactions. These interactions can be divided into non-directional interactions that favour close packing, such as Van der Waals interactions, or more directional interactions, such as hydrogen bonds, that due to their variety can lead to more varied structures.

Structures of particular interest are those that exhibit porosity in the surface plane. These porous layers are of interest for multiple reasons, for example such layers can provide control over the spatial distribution of surface functionalisation,¹⁹ or be used for molecular recognition.²⁰ A long-term target application could be the generation of nano-reactors, with functionalisation of the interior of the pore providing opportunity for improved selectivity of the surface catalyst towards certain substrates.

This first chapter shall provide a more detailed background of these two concepts of intermolecular interactions, and self-assembled monolayers, followed by an overview of key work uniting the two concepts. Chapter two will discuss the experimental methods utilised in this work, with further chapters presenting the results and analysis of these experiments.

1.2 Intermolecular Interactions

The two interactions of main interest to this work are hydrogen and halogen bonds. These two differ from many other interactions in both their strength, and their directionality. Figure 1.1 is an extract from a textbook schematically comparing the total energy against bond angle for various interactions. Covalent bonds exhibit a low energy structure for a narrow and well defined distribution of angles. By contrast Van der Waals interactions exhibit favourable binding energies across a range of angles relative to the energetic minimum. This information helps to explain the directionality of these interactions. Although not plotted, halogen bonds are somewhere between covalent and hydrogen bonds in their directionality. This makes halogen bonds of great interest for rational design of supramolecular systems, as the optimum geometry is thought to be more well defined than for many other interactions.

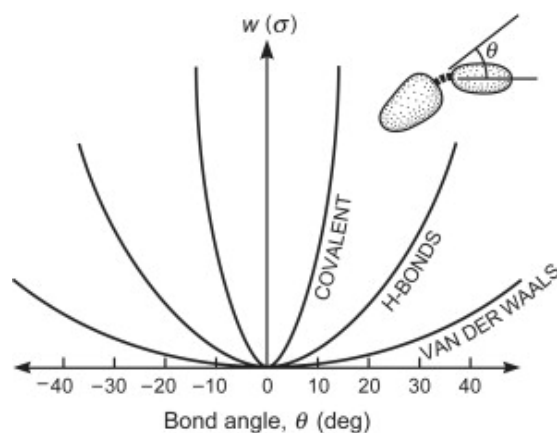


Fig. 1.1 Schematic of the change in interaction energy with bond angle. Taken from reference 4. Covalent bonds are highly directional, due to the geometric constraints of orbital overlap. By comparison Van der Waals interactions are weakly or non-directional. Hydrogen bonds fall somewhere between these two extremes, exhibit a preferred direction, but with more flexibility than covalent bonds. Although not plotted, halogen bonds are more directional still, for reasons discussed in section 1.2.2

1.2.1 Hydrogen Bonds

The hydrogen bond is a very common and well known intermolecular interactions, and so will only be discussed relatively briefly. Hydrogen bonds are intermolecular interactions of comparatively high strength (the strongest exhibit a bond energy of over 100 kJ/mol)⁶ that occur between a hydrogen atom bonded to an electronegative atom (D) and an electron lone pair containing acceptor atom (A).

Generally, hydrogen bonds have the form D-H...A, where a hydrogen bond donating molecule shares a proton with a hydrogen bond accepting molecule. The D atom is electronegative, leading to a polarised D(δ^-)-H(δ^+) bond. The interaction can then be considered to be A donating an electron pair to the δ^+ polarised proton. The interaction occurs due to both an effective orbital overlap, as well as favourable electrostatics when a δ^+ hydrogen interacts with a δ^- electronegative atom. For most systems the electrostatic contribution is dominant.⁴ However the orbital and other contributions can still be important for some systems.²¹

The most well recognised hydrogen bonds occur when both D is highly electronegative (leading to a highly polarised D-H bond) and A has a high energy electron lone pair. For example the O-H...O hydrogen bonds between molecules of water, or the N-H...N bonds in liquid ammonia. Due to the high degrees of polarisation, hydrogen bonds such as these are particularly strong, having bond strengths of the order of 25-40 kJmol⁻¹.²²

A particularly notable strong hydrogen bond occurs between carboxylic acid functional groups. These often form dimers with two hydrogen bonds locked together, such as in figure 1.2. The geometry of the two bonds means that this motif is rigid as well as strong, making it extremely useful for rational design of supramolecular systems. These bonds are of particular relevance when considering monolayers formed from 1,3,5-tribenzoic acid, which shall be further explored in section 1.4.5.

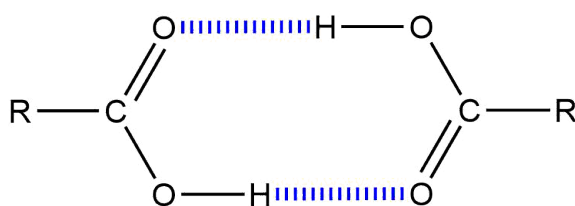


Fig. 1.2 Schematic of carboxylic acid dimerisation through hydrogen bonds

Similar cooperative hydrogen bonding also occurs in living creatures, for example the base pairs of DNA are held together by matching configurations of hydrogen bond donor and acceptor motifs. Assembly of DNA shows the power of intermolecular interactions

to generate complex assemblies through instructions encoded within the molecule, a key concept in self-assembly.

When the D-H bond is not so highly polarised, such as when H is bound to carbon, weaker hydrogen bonds occur. These historically may not have been recognised as hydrogen bonds at all,²³ as they are generally substantially weaker than polar hydrogen bonds (<15 kJmol⁻¹). However, they can be significant due to the quantity of weakly polarised hydrogen atoms in many systems. The C-H...N hydrogen bond between nitrogen atoms and C-H of adjacent aromatic systems is particularly common, due to the favourable geometry and lack of steric clash.

Hydrogen bonding motifs occur widely in organic molecules and so this interaction is particularly common in systems of interest to chemists. Due to the predominant electrostatic contribution to the strength of the interaction, it is possible to quantify "good" and "bad" hydrogen bond donors and acceptors using just two parameters based on electron density.²⁴ It is then observed that in the vast majority of cases binding occurs between the best donor and best acceptor motifs, with (if feasible) the second best donor and acceptor motifs also pairing up and so on. This property has allowed great progress in the design of artificial hydrogen bonding systems to be made.

1.2.2 Halogen Bonds

Definition

Halogen bonds are often considered to be an analogue of the hydrogen bond.¹¹ When polarised through bonding with an electronegative atom, the halogen/hydrogen bond "donor" forms a strong interaction with the electron pair of a nucleophile "acceptor". The general motif for such bonding is shown in Figure 1.3.

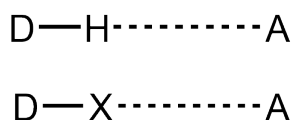


Fig. 1.3 General motif for hydrogen (top) and halogen (bottom) bonding. D represents a halogen/hydrogen bond donor, while A represents a bond acceptor containing a high energy lone pair.

Despite being known for many years, the halogen bond was only officially defined by IUPAC in 2013.¹² The definition is reproduced below.

A halogen bond occurs when there is evidence of a net attractive interaction between an electrophilic region associated with a halogen atom in a molecular entity and a nucleophilic region in another, or the same, molecular entity

At first glance, this description can appear surprising. Halogens are extremely electronegative elements. Hence, when bonded in a molecular entity, they would be expected to have an overall negative charge, and hence to act as nucleophiles. Indeed, interactions between halogen-containing molecules and electrophiles are well known in the chemical literature. For example, studies have shown halogen atoms acting as hydrogen bond acceptors.²⁵ This behaviour would seem to preclude them from showing any type of electrophilic character, as charge on atoms is traditionally considered to be well distributed across the atomic surface. The fact that such behaviour is observed is thus evidence of a deficiency in this model of charge distribution in molecules.

History

Although unexpected, interactions between halogens and nucleophiles have been observed for over 200 years. In 1814, J.J. Colin was the first to isolate a complex between iodine and ammonia,²⁶ although the 1:1 donor-acceptor structure for the complex was not suggested until 1863.²⁷ These halogen-donor complexes were generally considered to be a form of charge-transfer interaction, although progress in better understanding the nature of these interactions was slow. Hassel won the Nobel prize in 1969 and used his acceptance lecture to consider the then state of knowledge of these interactions.²⁸

A key result was his discovery of the infinite chains formed from the interaction between dihalogens and 1,4-dioxane (Figure 1.4). Previous work had considered dihalogens to only be capable of forming one interaction with nucleophiles, as the accepted theory of the time indicated that the charge-transfer component of the interaction would leave the second halogen with an excess of negative charge. The fact that it was possible for both halogens to accept electron pairs at the same time indicated the charge-transfer explanation to be lacking. Theoretical techniques at this time were incapable of satisfactorily explaining the phenomena. Despite this, Hassel's work does demonstrate much that is now accepted about halogen bonds. A key point is their directionality, with isolated structures showing the electron donor located within a narrow cone centred 180° from the halogen-halogen bond. He also noted the now-accepted fact that the strength of the interaction increases going down the periodic table. For example, the electron accepting abilities of the dihalogens is in the order $I_2 > Br_2 > Cl_2 > F_2$. This generally contrasts with hydrogen bonding where the more electronegative atoms at the top of the group have stronger interactions.

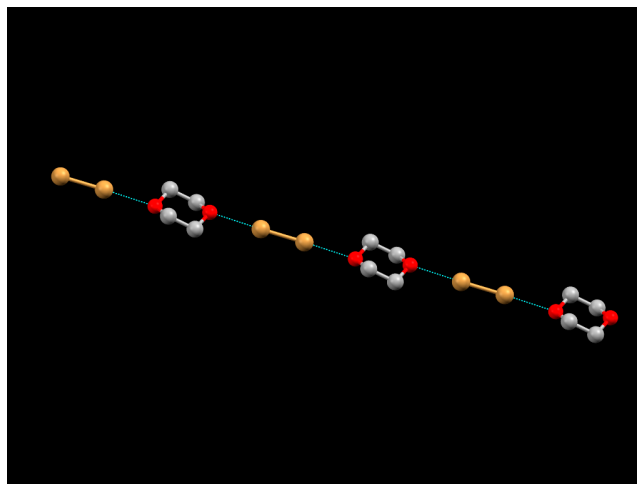


Fig. 1.4 Crystal structure of the Br₂ dioxane co-crystal considered by Hassel. Image of structure DOXABR from the Cambridge Structural Database²⁹

The sigma hole

As has been discussed, halogen bonding was initially considered to be a charge-transfer effect. This explanation was unsatisfactory as it did not explain many observed properties of the interaction. An important example is halogen bonding in halocarbons, where the halogen atom can unambiguously be assigned a partial negative charge due to being significantly more electronegative than carbon. Despite this, it is found that such halogens can interact strongly with electron donors. That this occurs despite the obvious coulombic repulsion between two negative charges was difficult to explain.

A key advance in explaining this phenomena was made when Brinck et al. calculated the surface electrostatic potential of the set of halocarbons of the form CF₃X ab initio.³⁰ These are reproduced in figure 1.5 which plots the surface electrostatic potentials around the molecules. In these plots red/yellow/green indicate progressively less positive charge, while blue indicates negative charge. The charge plotted in these figures is generated by summing the positive Coulombic charge contribution from atomic nuclei, and the negative contribution from electrons in the system. The plots demonstrate that the charge distribution is not uniform over the halogen X but is polarised, as would be expected, towards the bond. Most significantly, the face of the halogen X opposite the bond has less electron density than would be expected from a uniform distribution. For X = F this manifests as a region that is "less negative" than the surface of the halogen atom, however for the set of molecules with X = Cl, Br and I it is found that this polarisation leads to an area of net positive charge (shown as red in figure 1.5). The largest δ^+ is found for X=I and the smallest for X=Cl. This is consistent with the observation that CF₄ does not interact with nucleophiles and that, of

the other three molecules, the strength of interaction with nucleophiles is in the order $\text{CF}_3\text{I} > \text{CF}_3\text{Br} > \text{CF}_3\text{Cl}$.

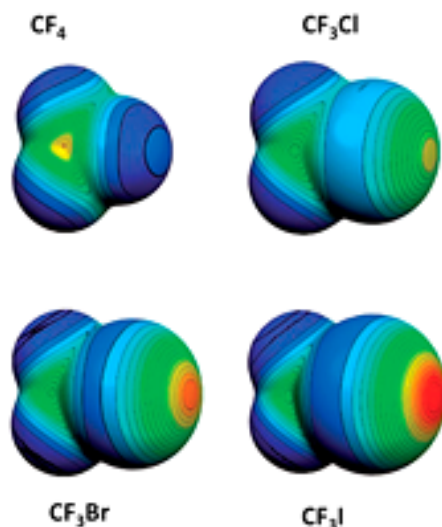


Fig. 1.5 Molecular electrostatic potential surface for the series of halocarbons CF_3X ; red/yellow/green indicate progressively less positive charge, blue indicates negative charge. Reproduced from reference 31

This area of partial positive charge was later termed the σ -hole.³² There has been much debate about interpretations of the σ -hole, with many authors assigning it to the unoccupied σ^* anti-bonding orbital.³³ This allows a simple two-centre-two-electron (2c-2e) model as in figure 1.6 to be used to understand some simple aspects of the interaction.

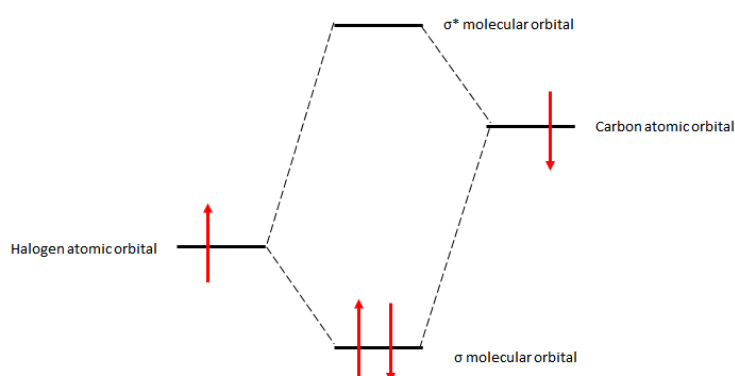


Fig. 1.6 An illustrative molecular orbital (MO) diagram for a halogen-carbon bond. The bonding MO is closest in energy to the low lying halogen atomic orbital, while the unoccupied antibonding MO is closest in energy to the relatively high energy carbon MO.

A key concept in this model is that the molecular orbital (MO) formed is most similar in character to the atomic orbital (AO) closest in energy to it. Thus, in a C-X bond the σ bonding orbital, which contains the bonding pair of electrons, is most similar to the halogen orbital, leading to a partial negative charge on the halogen. Conversely, the unoccupied antibonding σ^* orbital is most similar to the carbon atomic orbital, leading to a partial positive charge on the carbon. Hence, there is a dipole moment along the bond, due to the unequal coefficients of the electron containing orbitals. This also means that the lowest unoccupied molecular orbital (LUMO) has the highest coefficient on the carbon, explaining the susceptibility of C-X bonds to nucleophilic substitution. However, there will still be some finite contribution to the LUMO from the halogen atom, and so, if interaction with carbon is sterically or otherwise prevented, nucleophiles may instead favourably interact with the halogen. This is a halogen bond.

It is apparent from the above model that anything that increases the coefficient of the LUMO on the halogen will promote halogen bonding. This can be accomplished either by raising the energy of the halogen atomic orbital, or by lowering the energy of the carbon orbital. Hence iodine, which has higher energy valence orbitals than chlorine, will have a larger component of the σ^* than chlorine and hence be a better lone-pair acceptor. Alternately, attaching electronegative elements like fluorine to the carbon, or using an sp-hybridised atomic orbital, will lower the carbon AO energy and so also promote halogen bonding. These predictions are borne out by experiment, and demonstrate the utility of this simple model.

Politzer has pointed out that, though correct, such analysis is not necessary, and that a simple consideration of polarisability of halogens will give the same trends, without needing to consider orbitals (which are a purely mathematical construction, designed to explain the observed behaviour of electrons in molecules).³³ Nonetheless, this simple model is a conceptually easy way to understand the observed strength of halocarbons as electrophiles. For example, it could be difficult at first to understand the increased halogen-bonding ability of a triply-bonded iodoalkyne compared to a single bonded iodoalkane by simply considering the polarisability of the carbon-iodine bond. However, understanding the effect of a lowered carbon AO on the form of the σ^* orbital is a straightforward problem. The lower the energy of the carbon AO, the greater the relative contribution of the carbon AO to the σ bonding orbital, and conversely the greater the relative contribution of the halogen AO to the σ^* antibonding orbital that contributes to the σ -hole. Hence, a lowering of the carbon AO energy leads to an enlargement of the σ -hole on the bonded halogen.

σ -holes can be predicted to occur for a wide variety of atoms in the appropriate context. Chalcogen bonds³⁴ (Group VI), pnictogen bonds³⁵ (Group V), and even tetrel bonds³⁶ (Group IV) have all been observed. In some instances, these interactions can even achieve

similar binding energies to halogen bonds. However, species exhibiting such types of bonding generally have high coordination numbers. The resultant unfavourable steric interactions weaken the net strength of the σ -hole interaction. Thus, these higher order interactions are generally more difficult to use for supramolecular design than the less sterically encumbered halogen bond.

Halogen Bond Acceptors

Good halogen bond acceptors are atoms with a lone pair that can interact with the σ hole. A wide variety of atoms can act as halogen bond acceptors, including oxygen,^{37,38} sulphur,³⁹ nitrogen^{40,41,15} and even other halogen atoms.^{42,43} Although most rationally designed halogen bonding motifs utilise lone pair donating acceptors, it has recently been noted that as many as 66% of all close halogen contacts in the Cambridge Structural Database (CSD) have π systems acting as halogen bond acceptors.⁴⁴ These "halogen bonds" are comparatively weak however, and their ubiquity mainly a sign of the sheer number of halogen σ hole bearing molecules deposited in the CSD independently of designed halogen bonding motifs.

In common with hydrogen bonds, it has been observed to generally be the case that the system arranges such that the best halogen bond donor matches with the best acceptor.⁴⁵ This means that it is generally possible to predict with which acceptor a halogen bond donor will bind. The best halogen bond accepting atom can be predicted via calculation of the molecular electrostatic potential. Although this is not always the case if the difference between the best and second-best acceptor is small.⁴⁶

1.2.3 Halogen-Halogen contacts

A particular subset of halogen bonds are those of close halogen-halogen contacts. Close contacts between halogen atoms are observed repeatedly in bulk crystals, though are observed to occur in two distinct types. Figure 5.2a outlines the molecular geometry and defines two angles, θ_1 and θ_2 that can be used to categorise close halogen-halogen contacts as either Type I ($\theta_1 \approx \theta_2$) or Type II ($\theta_1 \approx 180^\circ$ and $\theta_2 \approx 90^\circ$).⁴²

Type I interactions are symmetrical ($\theta_1 \approx \theta_2$) and are simply the result of the VdW close-packing of large, polarisable, halogen atoms.

Type II contacts by contrast are asymmetric and are now recognised as halogen bonds that contain an electron-rich halogen atom as the halogen bond acceptor. They ideally have $\theta_1 = 180^\circ$ and $\theta_2 = 90^\circ$, though can vary from this geometry due to the influence of close-packing and other effects.⁴⁷ They are of interest for supramolecular assembly due to the simplicity of having the same atom be able to act as both acceptor and donor in the intermolecular

interaction. One of the earliest cases that illustrated type II interactions, is that of the crystal structures of the pure halide dimers.

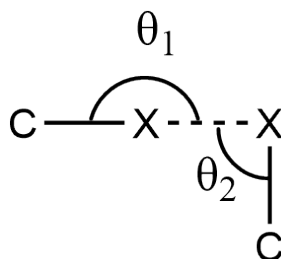


Fig. 1.7 Schematic of the key parameters θ_1 and θ_2 used to characterise halogen-halogen contacts. If $\theta_1 \approx \theta_2$ the contact is type I and not considered halogen bonded. Type II contacts typically exhibit $\theta_1 \geq 150^\circ$ and $\theta_2 \leq 120^\circ$. For an ideal halogen bond $\theta_1 = 180^\circ$ and $\theta_2 = 90^\circ$.

1.3 Supramolecular Chemistry

Supramolecular chemistry has been defined by J-M. Lehn to be concerned with "Chemistry beyond the molecule". The term was first coined almost 40 years ago, in reference to host-guest chemistry in solution.⁴⁸ Since then, it has been expanded to cover a range of phenomena whose behaviour is governed largely by intermolecular interactions. These can include behaviour of molecules in solution, but also in bulk and at interfaces. Surface supramolecular chemistry shall be considered in depth section 1.4, however this section will cover key concepts in supramolecular chemistry, as well as exploring relevant examples of supramolecular chemistry in the bulk.

1.3.1 Terminology

Supramolecular chemistry has been used to design a wide array of systems. In observing and designing supramolecular systems, it is observed that certain patterns of intermolecular interactions occur repeatedly in different structures. An example would be the formation of hydrogen-bonded dimers of carboxylic acids discussed in section 1.2.1. These patterns of interactions generally occur because the interaction is so energetically favourable that it dominates the other intermolecular interactions to play a determining role in the final structure. These patterns have been called "synthons"⁴⁹ to provide a short-hand way of referring to the library of previously observed highly favourable supramolecular configurations.

A related term is "tecton" for the subunits that make up a molecule (alkyl chain, aromatic system, functional groups...)⁵⁰ As an example, it may be said that a given tecton (carboxylic

acid) has a tendency to arrange into a certain synthon (doubly hydrogen bonded dimers). This tendency can then be used for the rational design of a supramolecular system, through predicting the final supramolecular structure based on the molecular tectons present, and predicting the intermolecular synthons that these will generate.

1.3.2 Host-Guest Chemistry

A particular subset of supramolecular chemistry occurs where a framework generates a pocket or other binding site (a host) that can interact with a small molecule/fragment (a guest). This binding is often of most interest when it is specific to certain guest molecules, analogous to the binding of enzymes and other biological "lock and key" systems.

As well as biological applications, host-guest chemistry is of interest in a range of other fields such as sensing, catalysis, or purification. The ability to selectively identify and/or separate components from a mixture with high specificity is of immense industrial interest. An example of a more long-term field of interest would be in the ability to mimic enzymes in designing selective systems for catalysis.

Although many of the concepts and early work on host-guest systems was developed in organic and aqueous solutions, more recent work has considered the transferability of these concepts to two dimensional assemblies on solid surfaces⁵¹ for example as shall be seen in section 1.4.5.

1.3.3 Crystal Engineering

The structure of organic crystals depends on the total of all non-covalent interactions between the crystal components. The total number of interactions that must be considered can be extremely large, even for a simple system. Crystal engineering is the attempt to recognise patterns and develop an understanding of key substructures that can be reliably used to design crystals of a given form.⁵² Study of molecular crystals is useful, both as a technique in its own right, and for the lessons that can be transferred to other fields. There is a vast number of solved crystal structures available through repositories such as the Cambridge Structural Database.²⁹ Through statistical analysis of this large number of structures, it is possible to obtain useful information on contacts that reliably form, and benchmark typical separations and angles between supramolecular synthons.

Many of the cited papers in this thesis have involved study of experimentally grown crystals, or statistical analysis of repository data. Where relevant the CSD code of the crystal structure will be reported.

1.3.4 Co-existence of phases

All matter can exist in multiple phases. The most familiar of these are solid, liquid, and gas; but across a wide range of temperature, pressure, and compositional conditions many more phases can be observed. In thermodynamics there is a rule for the number of phases that can coexist at given conditions, first formulated by Gibbs.⁵³ The rule defines the number of phases that can coexist (P) as being related to the number of components in the system (C) and the degrees of freedom of the system (F) by the equation $F = C - P + 2$.

Here degrees of freedom are defined in PVT (pressure, volume, temperature) space, while phases are defined by the existence of phase boundaries at which both different phases must coexist and be at equilibrium. Components are defined as chemically distinct species.

As an example application of the rule it is possible to consider pure water. This can simplistically be considered to only exist as liquid (water), solid (ice), and gas (steam), ignoring various separate phases of ice generally only relevant at high pressure or extremely low temperatures. As there is one component (H_2O) $C = 1$. Hence, the phase rules can be simplified as $F = 3 - P$. This means that there are two degrees of freedom (e.g. pressure and temperature) that can be independently chosen for one phase (P) of water to exist. By contrast if two phases are to coexist ($P = 2$) there is only one degree of freedom. This means that pressure and temperature cannot be independently specified. Thus, a mix of water and ice at a certain pressure (e.g. atmospheric) will always have a certain temperature (0°). If the pressure is changed then the temperature of the water-ice mixture will also change through shifting the equilibrium by melting/freezing until either a new equilibrium exists, or the system is reduced to a single phase by complete freezing/melting.

The phase rule provides a powerful tool to understand the equilibria of systems. For example, if observations at multiple temperatures and surface pressures find coexistence of two phases of a mono-component system, this is an indication the system may not be fully equilibrated. This concept will be further explored in chapter 7.

1.4 Monolayers

1.4.1 Definition

A monolayer is an arrangement of atoms or molecules that is one layer thick. Although some systems of this type, such as graphene or certain exfoliated clays are free-standing, most systems exist only as "supported" monolayers adsorbed onto a substrate. Generally, monolayers that are of research interest exhibit some form of order in the surface plane. This order can be influenced both by the periodicity of the substrate, and by the internal structure

of the components of the monolayer. These ordered monolayers can also be described as "self-assembled monolayers".¹ Monolayers are of interest due to the ability to use them to modify the surface of a substrate. Although only a miniscule proportion of the volume of a material, the surface is where it interacts with the rest of the universe, and so the properties of the surface have an outsized importance in the overall behaviour of a material.

1.4.2 History

Some of the first monolayers to be observed were due to the study of surfactants on liquid surfaces. One of the earliest examples was when Benjamin Franklin dropped a teaspoon of olive oil on a pond on Clapham common. He observed it to have a calming effect on the ripples, with the effect extending over almost half an acre.⁵⁴ By comparing the volume of oil used ($\sim 1 \text{ cm}^3$) to the area affected ($\sim 1000 \text{ m}^2$) one can calculate the thickness of the layer ($\sim 1 \text{ nm}$). Pleasingly, this is now known to be approximately the length of a single oleic acid molecule, the principle component of olive oil.

Much subsequent work on thin films and monolayers similarly focused on either liquid-air or liquid-liquid interfaces. This is partly due to the great commercial interest in such interfaces, but also because measurement of surface tension provides a sensitive method to access surface thermodynamics and aid understanding of surface behaviour. Using a variety of apparatus, the change in the surface tension of a liquid due to the presence of molecules at the surface, can be measured to a high degree of precision. Study of solid surfaces is not as straightforward. Solids have a fixed shape, so changes in the surface energy are not easy to measure. Also, most other analytical techniques normally used to study solids are incapable of distinguishing bulk solid from surface. Techniques that are able to distinguish between surface and bulk are said to be either surface sensitive or surface specific, depending on whether the bulk signal is merely suppressed, or eliminated entirely. Measurement of contact angles of liquid drops on solid surfaces was for many years the sole measure of interfacial energies available, and represents a result of three boundaries, liquid-solid, solid-vapour and liquid-vapour.

Langmuir was the first to identify the similarities between adsorption on a solid-air interface with surfactant action at liquid-air interfaces.⁵⁶ However, the first actual construction of such a monolayer on a solid surface was performed by Blodgett in 1935.⁵⁷ This technique, which involves depositing a monolayer on a liquid-air interface and then transferring it onto a solid support (Figure 1.8), has proven extremely versatile. However, it is limited by the need to find molecules that will form an initial layer at the liquid-air interface, before they

¹Much confusion can arise as, due to their near ubiquity, those less familiar with surface science often use "self-assembled monolayers" or "SAMs" in reference exclusively to gold-thiol monolayers.

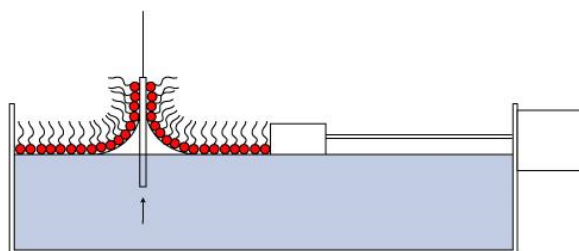


Fig. 1.8 Schematic from reference 55 showing the use of a Langmuir-Blodgett trough to deposit a monolayer on a surface

can be transferred to the solid. These early monolayers generally consist of amphiphilic molecules with a polar head and non-polar tail and hence a resultant dipole moment. Thus, the predominant ordering forces are fundamentally electrostatic and hydrophobic in nature. The first example of monolayer formation on solids from solution was found by Bigelow in 1946, considering the adsorption of polar organic molecules onto metal surfaces.⁵⁸ Despite this, adsorption from solution proved relatively unreliable and so Langmuir-Blodgett depositions remained the most prevalent way to produce monolayers through much of the early 20th century.⁵⁹ It was only later, with the advent of ultra-high vacuum surface science, that adsorption directly onto the solid surface from the vapour could be investigated fully.

1.4.3 Adsorption on Solid Surfaces

With respect to monolayer formation, there are essentially just two types of adsorption onto solid surfaces to consider: chemisorption and physisorption.

Physisorbed molecules exhibit only minimal change in structure upon adsorption. This is because the dominant interactions with the surface are physical in nature (Van der Waals, dipole-surface, hydrogen bonding etc.). These forces are relatively weak and fairly uniform across the substrate, so both surface diffusion and desorption are commonly observed. Due to the ease of diffusion, the layers are fairly well equilibrated, with reversible adsorption meaning that adsorbed molecules are capable of rearranging into the optimal conformation. Any adsorbate-adsorbate interactions thus become key to the organisation of the layer.

By way of contrast, chemisorbed monolayers exhibit some form of chemical change upon binding. In extreme cases, this can even manifest as a covalent bond to the surface atoms. Whatever form they take, these links are strong and directional, so both desorption and surface diffusion are minimised. This means that it is much easier to "trap" these layers in local minima, as the system is less able to respond to changes in conditions. Schematic diagrams of the two forms of layer are shown in Figure 1.9

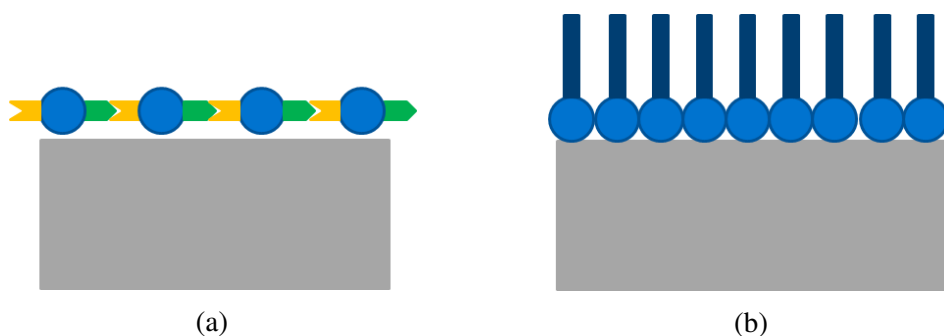


Fig. 1.9 Schematic diagram of binding in typical Physisorbed (a) and Chemisorbed (b) monolayers. In physisorbed monolayers directional adsorbate-adsorbate interactions define the structure within the surface plane, while in chemisorbed monolayers adsorbate-adsorbate interactions are generally non-directional. Hence close packing within the surface plane is generally observed.

Chemisorption

As discussed, chemisorbed monolayers exhibit some form of chemical bond between the monolayer and the surface, though what form this bond takes can vary depending on the particular monolayer being studied. Generally, these layers can be considered as a functional head that binds to the surface, attached to a long alkyl chain tail. In certain cases, a second functional group is attached to the end of the tail to allow further functionalisation of the surface; however, care must be taken to ensure this doesn't interfere with binding of the head group.

The earliest chemisorbed monolayers were based on trichlorosilane derivatives. These have a polar head group attached to a non-polar alkyl chain. When their adsorption from solution on silica was studied it was found that, unlike most previous amphiphilic monolayers, once formed they were extremely resistant to dissolution back into the solvent. This was taken as evidence that some form of chemical change had occurred on adsorption.⁶⁰ This is now known to be hydrolysis by the surface hydroxyl groups to form a covalent bond. The applications for a durable monolayer which does not diffuse across the surface were quickly realised, and attempts were made to find an analogous monolayer that would form on metal surfaces.⁶¹

Probably the most ubiquitous self-assembled monolayer is the family of gold-thiol monolayers.⁶² These rely on the extremely strong attraction between sulphur and gold. Surprisingly despite their widespread use, a comprehensive theory of the exact nature of the sulphur-gold boundary remains elusive.^{18,63} Figure 1.10 gives an overview of the structure of a "typical" gold-thiol SAM. The sulphur head group strongly interacts with the surface, anchoring the molecule. The organic interphase generally consists of alkyl chains which

closepack to form a diffusion barrier, with the "tail" of the SAM providing a functionalised interface.

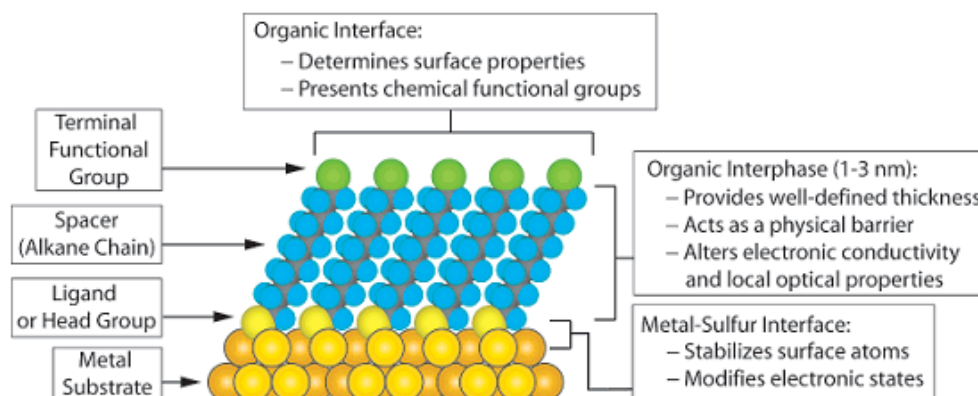


Fig. 1.10 Schematic diagram of a typical gold-thiol SAM. From reference 64

Such monolayers have seen widespread use, as their versatility and ease of formation has allowed applications in a wide range of areas of science.⁶⁴ A classic application has been the formation of gold nanoparticle clusters by anchoring with long organic molecules with thiol functional groups at both ends.⁶⁵

Although the interaction between surface and adsorbate is extremely strong for all these chemisorbed monolayers, generally they exhibit comparatively weak inter-adsorbate interactions. Typically, only non-directional Van der Waals type interactions are present, although some work has been done studying more specific non-covalent interactions in the surface plane.⁶¹ Thus, for the vast majority of chemisorbed SAMs there is little possibility to chemically design structure within the surface plane. However, the lack of surface diffusion can be exploited to overcome this disadvantage.

When forming a chemisorbed monolayer, conditions are generally used such that there is a significant time gap between initial adsorption of the species and formation of the strong surface-adsorbate bond. This allows the adsorbate to diffuse to (at least) a local energy minimum before the covalent chemisorption "locks" the adsorbate in position. Once the covalent bond is formed, the monolayer is extremely stable, with minimal diffusion of adsorbates across the surface. Thus, an area of surface can be masked from initial adsorption, the monolayer formed, and the mask removed to leave behind patterned areas of bare surface. The disadvantage in this, and similar, techniques is that it is still a "top down" approach; a long-held goal of nanoscience has been to achieve "bottom-up" patterning which would be significantly less time-consuming. Such patterning does not seem possible using only these systems.

Physisorption

The structure of physisorbed molecules does not change significantly upon adsorption. Although, in reality, the surface will always perturb the adsorbate to some extent. The forces binding the molecule to the surface are physical in nature, generally with Van der Waals and dipole-dipole interactions forming the largest component of the attractive interaction.

The in-plane structure of physisorbed monolayers was historically difficult to determine experimentally. If deposited from solution, Gibbs adsorption isotherms can be used to calculate an average "area per molecule". This provides some information on molecular orientation, however the results only provide a lower bound on the surface area in contact with the surface, and gives no detail on long range order or different phases. Thanks to the aforementioned low diffusion barriers of physisorbed monolayers the final surface structure can (ideally) be predicted by theoretical simulation of the strengths of the various intramolecular interactions. In practice, simulation of intramolecular interactions is an extremely challenging task, even when constrained to two dimensions. Also, in some practical systems kinetic barriers are still large enough to lead to the observation of non-equilibrium phases.⁶⁶ This can be minimised by annealing of the monolayer, but indicates surface diffusion is not as completely free as was once assumed.

1.4.4 Techniques

Early investigations of physisorbed monolayers generally considered simple adsorbates such as noble or simple diatomic gases. Investigation of these monolayers was performed using a variety of techniques, with diffraction techniques such as low energy electron diffraction (LEED)⁶⁷ and X-ray or neutron diffraction⁶⁸ most common for structural analysis.

LEED

LEED is a well established technique often used to check the quality of monolayers deposited in UHV systems. It involves use of an electron gun to fire low energy electrons at the surface. These electrons can interact with the surface inelastically (losing or gaining energy) or elastically. Those back-scattered elastically preserve diffraction information about the structure at the surface of the sample. A series of electron energy analysers filter out electrons with energy different to that of the incident beam, ensuring that only elastically scattered electrons can reach the detector. The detector is generally a simple phosphorescent screen, this converts detected electrons into visible light, which can be directly observed or captured by a camera.

In many cases LEED is simply used qualitatively, where the intensity and shape of the diffraction spots are used to confirm the surface is prepared as expected (exhibits the correct symmetry) and is free of significant impurities (has strong peaks). However, by measuring the change in beam intensities as a function of incident beam energy it is possible to obtain so-called I-V curves that contain significant structural information about the atomic positions within the unit cell.

LEED has been used historically to investigate relatively simple systems such as nitrogen,⁶⁹ or hydrogen⁷⁰ on graphite. Such studies were more common in the 1960s-1980s when alternative techniques were less developed, as beam damage from the strongly interacting electrons can be an issue when considering larger molecules such as methane.⁷¹ However, modern optics do allow the use of low beam energies, allowing the study of weakly adsorbed molecules such as acetylene,⁷² further developments such as Fiber-Optic LEED have allowed even less invasive investigations of structures such as methanethiolate.⁷³ Despite these advances, LEED has been largely supplanted by other techniques, due to relative difficulty of using quantitative LEED to obtain detailed structural information, and the requirement for high, or ideally ultra-high, vacuum conditions due to the high attenuation of electrons by the atmosphere.

Powder diffraction

Investigation of monolayer structures through diffraction from powdered substrates is more fully discussed in the next chapter. Similar to LEED the technique was originally used to investigate simple systems interacting through weak dispersion interactions such as noble^{74,75} and diatomic^{76,77} gases on graphite. These systems were found to exhibit a rich phase behaviour at a range of temperatures and surface coverages, with the technique allowing facile modification of gas pressure to modify surface coverage. Further work extended these results to larger molecules, for example alkanes^{78,79} and perfluoroalkanes.⁸⁰

Meanwhile, work had also been published investigating the structures of monolayers of polar physisorbed gases. For example chloromethane,⁸¹ bromomethane,⁸² and iodomethane.⁸³ Strongly interacting adsorbates such as these are found to form incommensurate structures. Strong halogen-halogen interactions with the type II geometry were identified, but not explicitly noted as hydrogen bonds. Further investigations considered other strongly interacting adsorbates such as carboxylic acids,⁸⁴ alkylamides,⁸⁵ and long chain haloalkanes such as bromoheptane.⁸⁶ Again, for strongly interacting substrates it was found that incommensurability with the surface was common, as the optimisation of interadsorbate interactions outweighs any benefits to commensurate adsorption sites.

The most commonly investigated substrate by powder diffraction is papyex graphite, but other substrates have also been investigated using this technique. For example, recent work considered adsorption of alkanes on hexagonal Boron Nitride,⁸⁷ and studies have also investigated on substrates such as MgO.⁸⁸ The key parameter for a substrate to be applicable to this technique is for it to be available in a format that is high enough surface area for detectable quantities of monolayer to be deposited, and for it to have large, flat, domains on which crystalline monolayers can grow.

Scanning Probe microscopy

Scanning tunnelling microscopy is more fully discussed in the next chapter. Unlike the previously considered diffraction techniques, it allows direct observation of the in-plane structure of molecules adsorbed on a surface. Most early studies were performed on long-chain molecules, which bind strongly (compared to many other physisorbed molecules) due to their large surface area, over which dispersion interactions can act. It was generally found that, as expected, these molecules adopted a close-packed structure on the surface, maximising the attractive interactions between the long alkyl chains.⁸⁹

Although generally leading to close packing, it has been shown that, for suitable designed systems, it is possible to form porous and other novel in-plane structures using interdigitated alkyl chains.^{90,91,92} However, by far the most common method to control in-plane monolayer structure is through the use of directional intermolecular interactions. The interactions relevant to this work are hydrogen and halogen bonds, as considered in section 1.2. The use of such interactions in monolayer systems will be discussed in the next section.

1.4.5 Hydrogen-bonded Monolayers: Trimesic acid

Hydrogen bonding is one of the best understood of the directional intermolecular interactions. It was thus inevitable that the earliest work on designed monolayers would consider hydrogen bonding systems. One of the earliest examples of such a monolayer was that of trimesic acid (TMA) on a graphite surface.⁹³ Although this work is concerned with monolayer systems, the TMA system is also considered in chapter 7. Hence the next section shall briefly discuss the bulk structure of TMA.

Bulk Trimesic acid

1,3,5-tricarboxylicbenzoic acid, or trimesic acid, is a trifunctional carboxylic acid with a structure as shown in figure 1.11. As discussed in section 1.2.1 carboxylic acids are known to form hydrogen bonded dimers, with the two hydrogen bonds acting cooperatively to enhance

both the rigidity and strength of the interaction. Carboxylic acids are thus an extremely useful tool in rational design of supramolecular systems, as the strength and predictability of their interactions allows a high degree of accuracy in prediction of the final structure, something less often seen in alternative functionalities. The rigidity of aromatic systems is also advantageous for design of supramolecular systems, as they reduce the possible alternate conformations that molecules could exist in, both simplifying design and reducing the entropic cost of self-assembly relative to more flexible backbone motifs.

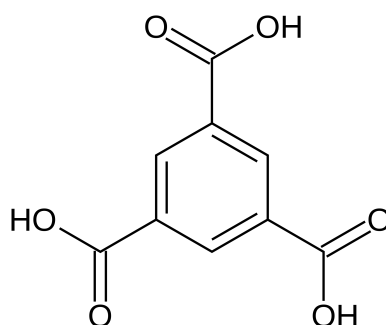


Fig. 1.11 Chemical structure of trimesic acid (TMA). TMA contains three carboxylic groups which can hydrogen bond to other molecules to form different crystalline phases.

The crystal structure of trimesic acid was first reported in 1967 by Duchamp and Marsh.⁹⁴ The structure was reported as a monoclinic crystal with lattice parameters $a = 26.52$, $b = 16.42$, $c = 26.55$ Å, and $\beta = 91.53^\circ$. The structure was found to consist of a basic motif consisting of multiple two-dimensional hydrogen bonded sheets containing pores of 14 Å diameter. The 2D structure consisting of three carboxylic acid dimers was termed “chickenwire”, a designation that has since become common for this motif. Due to the large gaps in the chickenwire structure, interpenetration of two sheets at an angle of approximately 70° occurs, allowing close-packing. This means the pores are filled in the crystal, and so inaccessible to any guest molecules.

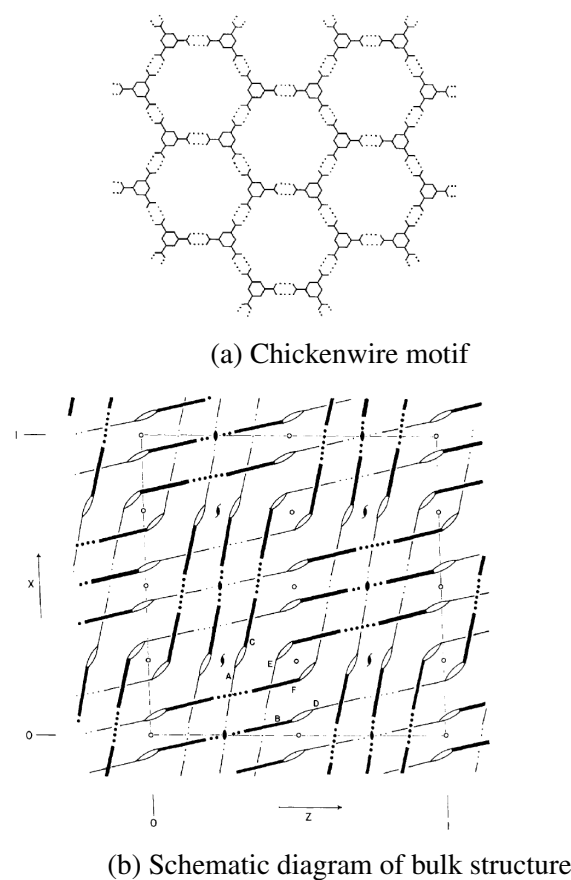


Fig. 1.12 Schematic diagram of the bulk structure of TMA (BTCOAC in the CSD). Bold lines represent TMA molecules, dotted lines represent in-plane hydrogen bonds in the “chickenwire” substructure, while ovals represent out-of-plane hydrogen bonds. Figure taken from reference 94

Further work with trimesic acid was performed by Herbstein.⁹⁵ A survey of co-crystals of trimesic acid with varying amounts of water and other guests present during crystallisation found a variety of alternate structural motifs, with inclusion of guest molecules. However, the guest occupancy was seldom high, and structures still consisted predominantly of interpenetrating layers, due to the favourability of close-packing. Several structures were discovered whereby the large size of the guests prevented catenation of the chicken-wire motifs however, disorder in the guest molecule prevented detailed structural refinement.⁹⁶ Overall, the bulk structures of TMA were not considered useful due to their inability to form a porous network without being co-crystallised with a guest species, and the inability to exchange or otherwise manipulate the contents of pore in such co-crystallised networks.

Trimesic acid Monolayer

As discussed in the previous section, in the bulk the porous "chickenwire" layers formed interpenetrate, meaning the pores are inaccessible in the crystalline state. Limiting the system to two dimensions was a logical method of ensuring the layers could not interpenetrate.

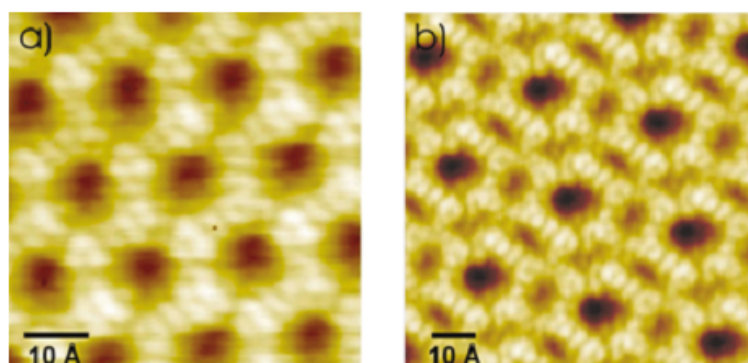


Fig. 1.13 STM images of the two phases of TMA monolayer observed "chicken-wire" (a) and "flower" (b) Reproduced from reference 93

Griessl et al. deposited TMA onto an Au {111} single crystal surface and studied it via ultra-high vacuum STM. Figure 1.13 is taken from their work, and shows the two structures they observed. The "expected" chickenwire phase was simple a 2-dimensional equivalent of the hydrogen bonding motif observed in bulk. This phase contains triply dimerised carboxylic acid groups, and 14 Å pores. In addition to this a new "flower" phase was also observed. This more dense phase is formed via the assembly of three carboxylic acid groups into a trimer (see figure 1.14c). The unexpected emergence of a new phase, even when considering a system containing a motif with a well known preference for forming hydrogen bonded dimers, shows the challenges in predicting ab-initio the ways in which even a simple system can self-assemble.

Later DFT simulation work has found that the "chickenwire" and "flower" phases are extremely close in energy, with the chickenwire found to be slightly more stable.⁹⁷ The small energy difference between the two phases provides a possible reason why they are observed to coexist, despite 2 phases of a mono-component system existing for more than a single temperature violating the phase rule as discussed in section 1.3.4.

Interestingly, at high coverages it was observed that excess TMA molecules could act as guests in the pores, forming bifurcated hydrogen bonds (Figure 1.15). This illustrates how concepts familiar to solution-phase supramolecular chemistry can also be applied in the study of monolayers, and how more advanced design could lead to a range of potential applications.

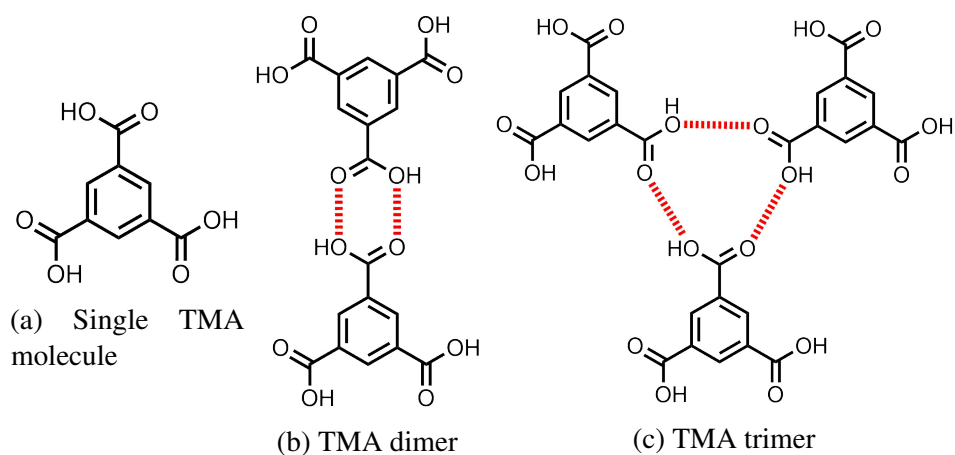


Fig. 1.14 Different hydrogen bonding schemes for the trimesic acid (TMA)

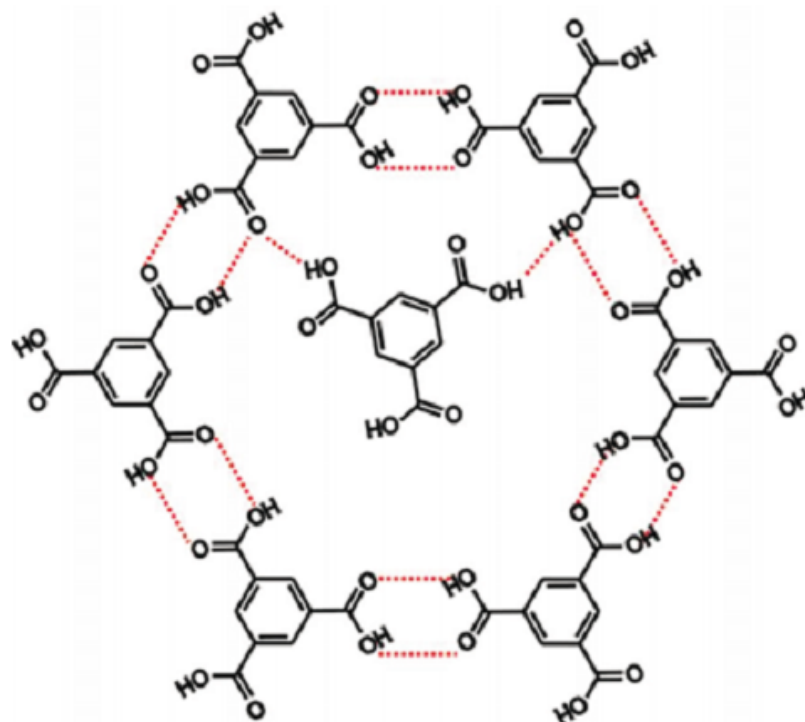


Fig. 1.15 Excess TMA molecule acting as a guest inside a cavity from the TMA monolayer. Bifurcated hydrogen bonds provide the favourable binding interaction. Reproduced from reference 93

Liquid-solid interface

Further work on TMA found that, as well as under UHV conditions, a porous network could be formed at the solid-liquid interface, adsorbed from a range of carboxylic acid solvents.⁹⁸ Here it was found that both the so-called “chickenwire” and “flower” phases could be reliably imaged in STM through varying the solvent. Short chain fatty acids showed a higher solubility for TMA, and exhibited formation of the dense “flower” phase in contact with graphite, while under long chain acids the less dense “chickenwire” phase was observed. Later work observed that sonication of the solution to enhance the dissolved amount could also affect the observed phase, with several novel phases at supersaturated concentrations being observed.⁹⁹ Assembly of TMA under a variety of solvents has led to mapping out of a rich range of phases, including even a close-packed phase that formed under phenyl-octane.¹⁰⁰

Variety of Surface Phases observed

The richness of this phase behaviour for TMA adsorbed on graphite was also observed on alternative substrates. Self-assembly of TMA on Au(111) under UHV conditions, without an annealing step and with a variety of dosing times saw a wide range of phases being observed.¹⁰¹ These were shown to be built from a closely related family of unit cells (see figure 1.16 with some dimerised and some tri-cyclic hydrogen bonds holding the structure together. Further development of this model led to simulation to attempt to better explain how the various phases could interconvert in response to changing coverage.¹⁰²

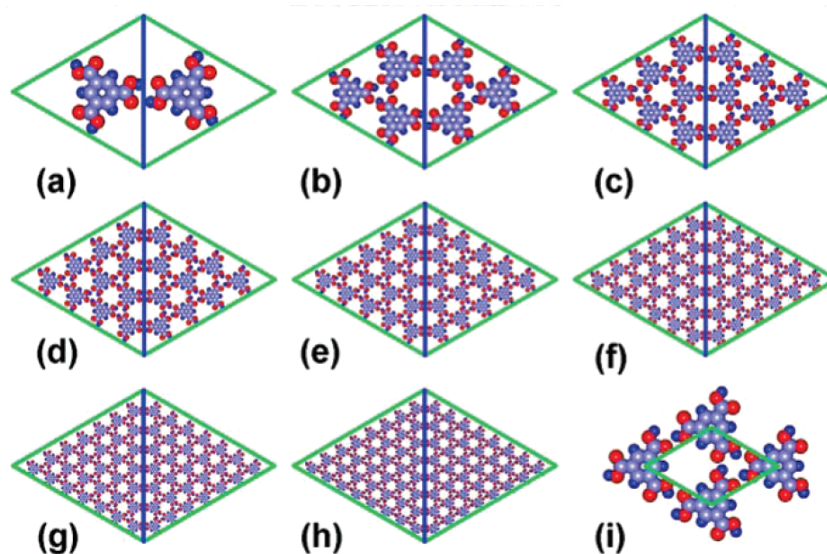


Fig. 1.16 Schematic diagram of the unit cells of the various TMA phases reported in reference¹⁰¹

Structural study

Although the phase behaviour of TMA could be easily followed using STM, detailed structural information can be difficult to extract from this technique. Uncertainty about calibration, as well as the effect of the tip on the structure being imaged means that pore sizes and lattice parameters were comparatively badly defined for the surface phases, relative to those discovered for the bulk. An ingenious attempt to work around this limitation was recently published.¹⁰³ This used the periodicity of observed Moire patterns formed from interference between two periodic structures, as well as the well defined periodicity of graphite to calculate an improved lattice constant for the “chickenwire” phase of TMA of $16.52 \pm 0.002 \text{ \AA}$. However, this technique is still reliant on using an invasive STM tip to probe the system, meaning that the effect of interaction with the tip is impossible to remove from the observations.

Host Guest Chemistry

Once it was discovered that the porous networks formed by TMA could be reliably formed under liquid, study was shifted towards host-guest chemistry. Poly-aromatic-hydrocarbons (PAHs) are an ideal initial guest species. Due to their planarity and lack of significant directional interaction, and since π interactions with the substrate are similar at all adsorption sites, their binding either outside of a system, or in a pocket is a function simply of pore size and shape. Coronene is a good fit to the 14 \AA pore size of the TMA porous networks, and

was found to bind well in the solution phase. Interestingly the choice of solvent was found to influence the dynamics of guest binding. The equilibrated structure, with a well-defined coronene position within the pore, was obtained almost instantaneously, within the time resolution of the experiment, when heptanoic acid was used as the solvent. However, for experiments using the longer chain nonanoic acid as solvent there was a measurable delay between introduction of the guest, and the equilibrium adsorption position being reached.¹⁰⁴

Monolayer to Thin film transition

The problem of “moving up” from monolayer, in the third dimension to thin films and eventually to bulk is one of great research interest. This is because the vast majority of applications of functional organic layers involve thicknesses in the transition region between thin film and bulk thicknesses. Multiple models have been developed to explain growth, though which behaviour a particular layer exhibits can be difficult to reliably predict from first principles. Structural studies in this regime have proven difficult. This is because the layers shares the “surface science problem” of not having a large amount of material of interest present, while also no longer being surface confined, nor consisting only of the outer exposed surface, meaning that surface specific techniques such as scanning probe techniques cannot be easily applied.

Recent work utilised TEM to study multilayers of two different molecules on graphene.¹⁰⁵ The two molecules considered were TMA and the related benzene-1,4-dicarboxylic acid. Using TEM, it was possible to observe the diffraction pattern of samples of multilayer TMA, which was compared to the structures observed for monolayer thick layers imaged using scanning probe techniques. From these experiments it was possible to study the transition from monolayer to bulk. For example the benzene-1,4-dicarboxylic acid was observed to exhibit Stranski-Krastanov (layer plus island) growth, with an initial monolayer structure with further adsorbate being deposited as islands on top of this layer. Within these islands the structure of the benzene-1,4-dicarboxylic acid gradually and continuously transitions to the bulk structure as the layer is built up. By contrast the TMA was shown to exhibit Frank-van der Merwe (layer-by-layer) growth, with multiple layers of identical structure to the monolayer formed up to 20 μm in thickness, followed by an abrupt transition to a polycrystalline phase with random in-plane orientations upon further deposition.

Although the electron diffraction technique utilised was not sensitive enough to characterise the monolayer thick samples, this example shows how diffraction based techniques can be utilised to bridge the gap between surface and bulk structural investigations, and examine systems that scanning probe techniques cannot.

1.4.6 Hydrogen-bonded Monolayers: PTCDI

Taking inspiration from work on TMA, it was soon realised that application of hydrogen bonding motifs familiar to solution-phase supramolecular chemistry could aid in the design of monolayers. A reliable motif for hydrogen bonding is the triply-hydrogen bonding complex between 2,6-di(acetylamino)pyridines and imide groups.¹⁰⁶ Theobald et al. thus studied the co-crystal formed when perylenetetracarboxylic diimide and melamine were sublimed onto a surface under ultra-high vacuum conditions. (Figure 1.17).¹⁰⁷

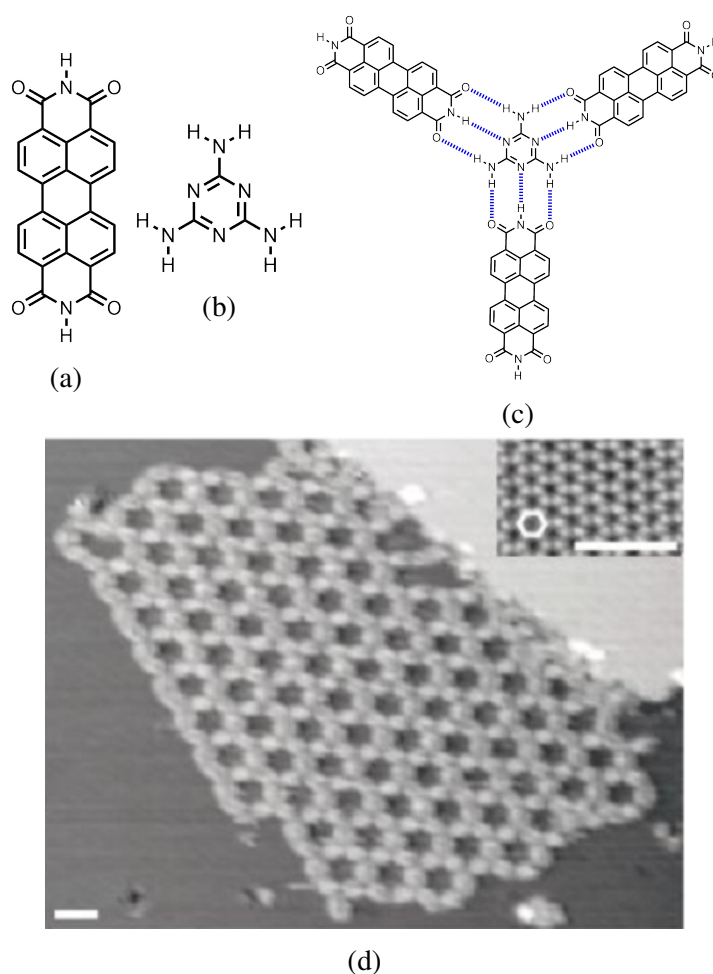


Fig. 1.17 (a) PTCDI and (b) melamine together form (c) a hydrogen bonded monolayer. (d) STM images of the PTCDI-melamine monolayer. Scale bar is 3 nm. From reference 107

These molecules form significantly larger pores than TMA and so a range of experiments could be performed studying host-guest interactions in this network.¹⁷ In particular, it was found that modification of the pore size through the addition of side chains to the PTCDI allowed greater selectivity in adsorption of guest species, and also that the network could act

as a template for deposition of gold-thiol SAMs. Studies also considered deposition from solution, however in this case it was found that formation of the layer became dependent on a variety of factors, with competitive adsorption and binding to solvent molecules meaning that porous-network formation is not always dependable.

Inspired by the range of work on co-crystals of PTCDI, an in-depth study of the mono-component PTCDI monolayer on gold was performed by Mura et al.¹⁰⁸ The mono-component system is of interest as, because PTCDI is approximately rectangular in shape, both close packing and hydrogen bonding interactions favour similar structures so the same structures are reliably observed under a range of deposition conditions. In this case, monolayer formation was performed by sublimation of PTCDI at 335 °C and deposition of the vapour onto an Au{111} surface. The sample was then imaged using a room-temperature STM with no subsequent annealing. Three phases were found to coexist on the surface (Figure 1.18).

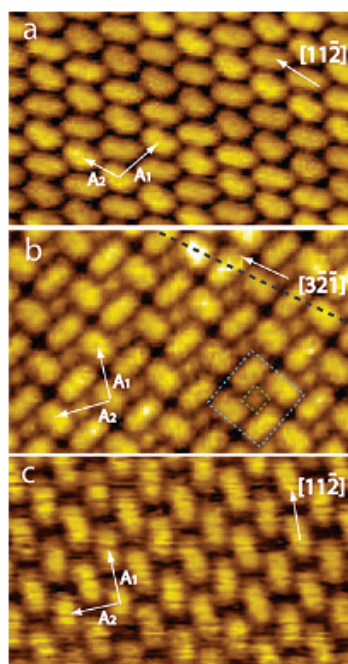


Fig. 1.18 Three phases of PTCDI on gold: canted (a), domino (b), and brick wall (c). From reference 108

The first, and most prevalent, structure was the "canted" structure (Figure 1.18a). This consists of rows of PTCDI aligned along the Au $[11\bar{2}]$ direction. The molecules in one set of alternate rows were measured to be rotated at 12° relative to the row direction, while the molecules in the other set of rows could not be accurately measured, but were presumed to be tilted at a similar angle in the opposite direction. The second "domino" structure (Figure 1.18b) was novel in their work with sets of 4 molecules arranged into squares similar to domino pieces. The final "brick wall" structure (Figure 1.18c) had previously only been

observed on an NaCl surface.¹⁰⁹ This structure consists of identical rows, shifted relative to each other similarly to a brick wall, and aligned with the Au $[11\bar{2}]$ direction. DFT calculations were performed that demonstrated these phases to be among the most stable configurations possible, along with predicting an unobserved "waveform" configuration. According to these simulations the canted phase was predicted to be the most stable of all structures considered, explaining its prevalence. This work helped demonstrate the power of combining both observation and simulation in the study of self-assembly of monolayers.

1.4.7 Halogen-bonded Monolayers

One of the simplest two-dimensional halogen-bonding networks is found within the solid dihalogens. Dihalogen molecules possess both two σ -holes and two belts of high electron density associated with their lone pairs. Thus, each dihalogen molecule can take part in four halogen-bonding interactions. For example in solid Cl_2 , it is found that a lamellar structure forms, with each plane containing adjacent chlorines interacting to form a 2D network with characteristic 90° type II halogen-halogen contact bond angles. (Figure 3.6).¹¹⁰

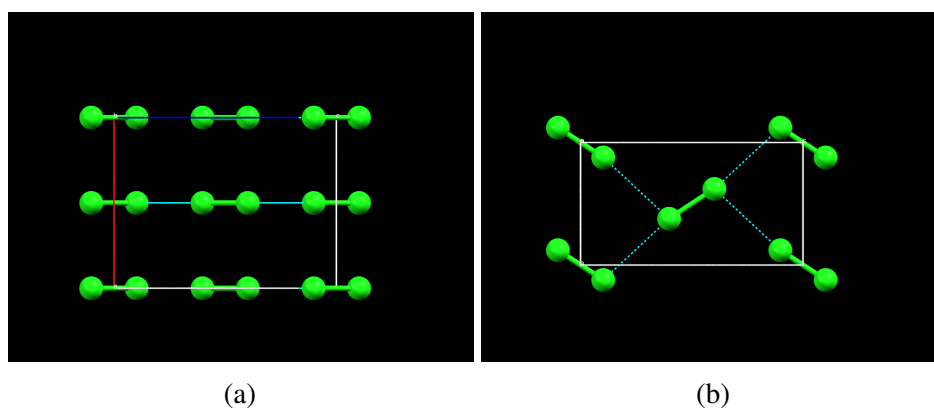


Fig. 1.19 Crystal structure of solid chlorine viewed from the side (a) and from above (b). The halogen bonds between Cl_2 molecules within each layer are indicated. From structure YATKIP in the Cambridge Structural Database²⁹

As with much work on halogen bonding in the 20th century, this was written off as a curiosity and little thought put into designing potential analogues. The explosion of activity in the field of halogen-bonded crystal design in the early 21st century initially passed 2D structures by. The first STM study of a halogen-bonded monolayer was only published by Yang et al. in 2007.¹¹¹ Yang imaged the monolayer formed when 1-dodecyl-imidazole and N-(2,3,5,6-tetrafluoro-4-iodophenyl)hexadecylamine were deposited on a surface of highly orientated pyrolytic graphite (hopg). As shown in Figure 1.20, these molecules form a

lamellar structure held together by the strength of the halogen bond and alkyl chain-alkyl chain interaction.

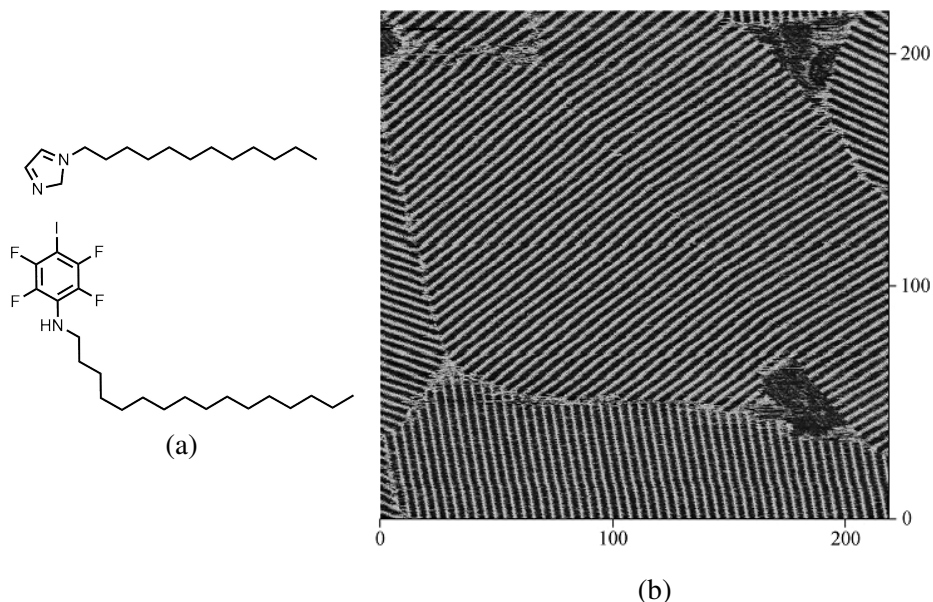


Fig. 1.20 (a) Chemical structure of 1-dodecyl-imidazole (top) and N-(2,3,5,6-tetrafluoro-4-iodophenyl)hexadecylamine (bottom) (b) STM image of a 218.6 nm square area of the surface showing the laminated structure of the monolayer. Based on their size and texture, bright patches were assigned as corresponding to the π -systems. From Reference 111

Based upon their size and texture the bright stripes in the STM image (Figure 1.20b) were assigned as belonging to the two electron-rich π systems joined by a halogen bond. The dark stripes were similarly assigned to the electron-poor interdigitated alkyl chains. The quality of the image indicates the molecules are immobile, even when probed by the tip, suggestive of strong intermolecular interactions. By contrast, a deposited layer containing only 1-dodecyl-imidazole was not well imaged by the tip. This was taken to indicate that Van der Waals interactions alone are insufficient to prevent the molecule being moved by the tip, and so that halogen bonding is key to monolayer formation.

This same motif of halogenated benzene donors and pyridine derivative acceptors was then extended to multifunctional molecules. Clarke et al. used synchrotron X-ray diffraction to image monolayers of 4-4'-bipyridine (BPY) and 1,4-diiodotetrafluorobenzene (TF1) on an HOPG surface.¹¹² These molecules (Figure 1.21a) are both bifunctional, with a 180° angle between their binding sites. As expected from the linear structure of the functional groups, these molecules were found to form long-chains along the surface. The calculated structure is shown in Figure 1.21b.

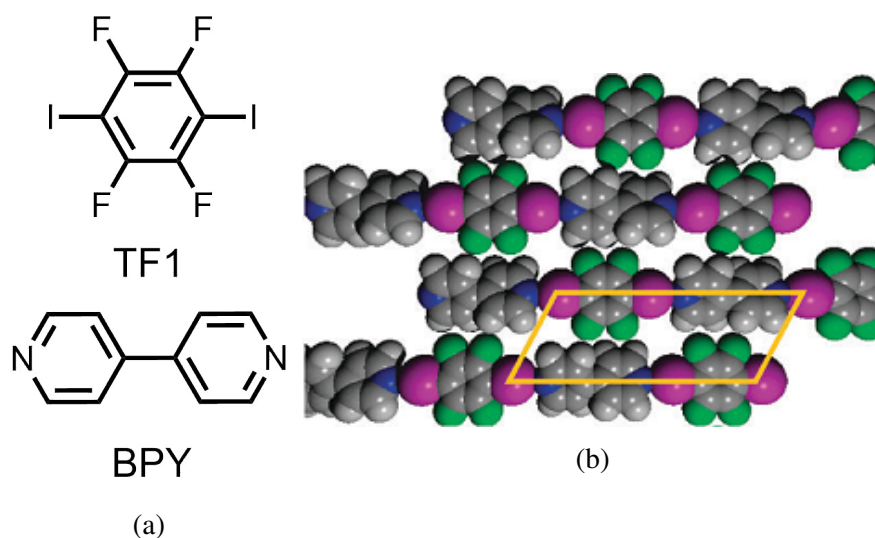


Fig. 1.21 Figures taken from reference 113 showing the structure of a halogen bonded monolayer (a) Chemical structure of TF1 and BPY, the two component molecules (b) Structure of the monolayer calculated from the X-ray diffraction pattern. The monolayer can be seen to consist of parallel linear chains, with each chain consisting of alternating TF1:BPY units.

Later work by Sacchi et al. used a mix of DFT simulation and diffraction data to show that 1,4-diiodotetrafluorobenzene (the non-fluorinated TF1 analogue) does not form a halogen-bonded co-crystal with BPY, instead separating into two phases.¹¹³ This demonstrates the importance of fluorination of the halogen bond donor in promoting the σ -hole and so favouring halogen bond formation. Brewer et al. performed additional investigations, finding that 1,4-dibromotetrafluorobenzene (TF2)(Figure 1.22a) also formed a halogen-bonded monolayer with BPY.¹¹⁴ The structure however was found to be bent slightly from linear (Figure 1.22b). This was attributed to lateral hydrogen bonding interactions between C-H bonds on the BPY and the electron-rich region of the Br. The fact that these interactions have a more significant effect on the structure of the brominated monolayer compared to the iodinated one was taken to be evidence of the comparative weakness of the halogen bond. DFT simulation was performed that supported this hypothesis.

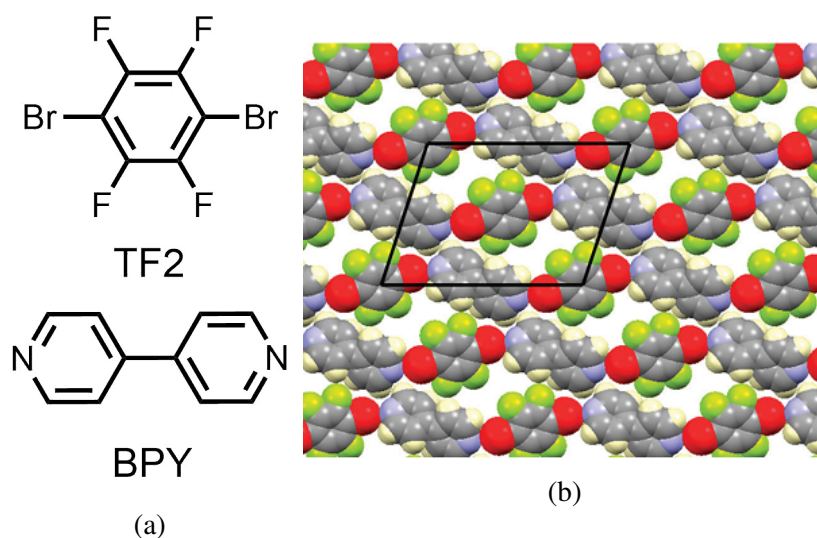


Fig. 1.22 Figures taken from reference 114 showing the structure of a halogen bonded monolayer) Chemical structure of BPY and TF2, the two component molecules (b) Structure of the monolayer calculated from the X-ray diffraction pattern. Unlike in figure 3.12 it can be seen that the BPY:TF2 chains are not linear, but are instead kinked. This has been interpreted as an indicating of the relative weakness of the Br...N halogen bond, compared to the I...N halogen bond contained in the previous figure.

1.5 Scope of this Work

This chapter has provided a brief overview of key concepts in the fields of intermolecular interactions and assembly of molecules at surfaces of relevance to the current work. It is clear that many interactions not covered can also be relevant to molecular assembly, and many further aspects of surface science have not been considered. This work is concerned with the use of hydrogen and halogen bonding interactions to assemble molecules at surfaces, ideally in ordered, crystalline arrays, with the aim of further understanding how these interactions can generate porous monolayer systems with potential further applications in host-guest chemistry.

The key techniques considered will be scanning tunnelling microscopy (STM) and X-ray diffraction (XRD). Chapter 2 discusses key aspects of these experimental techniques. Chapter 3 then presents data collected via STM on a small range of molecules. Chapter 4 provides an overview of the diffraction technique used, as well as containing some analysis specific to this work necessary to model the XRD substrate. Chapters 5 and 6 then consider the use of diffraction on several halogen bonding molecules. Finally, Chapter 7 presents diffraction data collected for two hydrogen bonding systems.

Chapter 2

Experimental Techniques

As has been seen in the previous chapter, scanning tunnelling microscopy is the predominant technique that has been used in the study of monolayers. It is an extremely powerful technique, and an initial portion of this work concerns itself with the use of a high precision STM system. Section 2.1 will consider the aspects of the theory and application of the technique that are of relevance to this work.

An additional technique that has been used in this work is a specific X-ray diffraction (XRD) technique designed to investigate monolayers on graphite. Section 2.2 further describes the background of the technique, while section 4.4 considers additional mathematical derivations that were necessary for the specific diffraction geometry utilised.

2.1 Scanning Tunnelling Microscopy (STM)

2.1.1 Introduction

Scanning Tunnelling Microscopy (STM) was first developed in 1981 by Binnig and Rohrer, mainly as a technique for imaging the surface reconstruction of bulk solids.¹¹⁵ The instrument is part of a family of scanning probe techniques, all of which rely on scanning a sharp probe over a substrate, in order to infer some aspect of the character of the surface. Potential applications in large areas of science were quickly realised after its invention, and the creators were awarded the Nobel Prize in 1986.

STM is one of very few techniques that can regularly achieve atomic resolution, and provides an interesting real-space alternative to diffraction based experimental techniques. STM relies on the quantum effect of electron tunnelling, whereby electrons can be observed to cross potential barriers that classically they would not be expected to. The effect is strongly dependent on separation, and so a high degree of depth sensitivity can be achieved. Through

careful design of the scanning stage on which the tip is mounted, high spatial resolution can also be achieved. These two factors together allow atomic scale resolution images to be obtained.

2.1.2 Theory of Operation

Quantum Tunnelling

In classical mechanics, there cannot be significant conduction through a vacuum under reasonable temperature conditions. This is because there is a large potential difference between solid state electrons and the free electron energy, which the electrons do not have sufficient energy to overcome under experimental temperatures. However, in practice it is observed that electrons can "tunnel" through the potential energy barrier separating two conductors, provided the distance is short enough. If both conductors are at the same potential then their Fermi levels will be equal and so tunnelling in both directions will be equally favoured leading to zero net current. However, if a bias voltage is applied to one conductor, tunnelling from the negative to the positive conductor will become more favoured and so a measurable net tunnelling current (I_t) will be observed. The key result is encapsulated in the equation $I_t \propto e^{-2\kappa d}$.

This equation states that tunnelling current (I_t) is exponentially dependent on the sample separation (d) and a characteristic decay length κ . The decay length term accounts for a large number of parameters such as bias voltage, sample geometry, and electronic configuration, with theories at various levels of detail able to calculate it. However none of these change the key feature of the equation, the exponential dependence of observed current on separation. For physically realistic values of κ , a 1 Å increase in separation causes approximately an order of magnitude drop in I_t . Thus, miniscule changes in separation between two conducting species can be observed readily by a change in observed current.

Experimental Setup

For STM an (ideally) atomically sharp tip is used as a probe to study an almost flat conducting surface. This is performed by applying a bias voltage to the system¹ and then scanning the tip over the sample. Movement of the tip is performed by high precision

¹Instruments can either be tip biased or sample biased, with one component held at the relevant potential, and the other grounded. Most literature considers sample biased instruments, and so the convention is for imaging conditions to be reported as sample biases. The instrument used in this work consists of a biased tip and grounded sample. However bias voltages are reported as sample relative to tip to allow comparison. Thus a reported +1V sample bias in reality equates to a -1 V tip bias and grounded sample for this instrument

piezoelectric crystals. These allow submolecular spatial resolution of tip position within the sample plane. Figure 2.1 shows a schematic of the tip-sample setup.

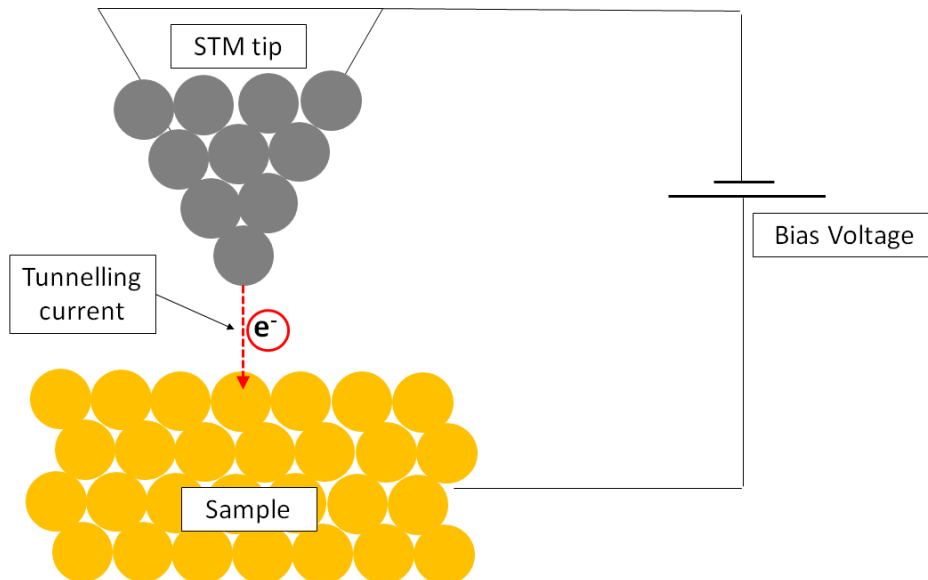


Fig. 2.1 Schematic diagram of an STM tip held above a surface. The applied bias voltage leads to a tunnelling current between the tip and sample.

In its simplest incarnation (constant height mode) the tip is held at a constant height (z) and the variation in tunnelling current measured as the tip scans the surface. Constant height mode is a conceptually simple mode of operation, however seldom used in practice because there is a large risk of a collision between the tip and the substrate (tip crash) if the surface is rough. This can render the tip unusable, and so is to be avoided. For this reason, constant current mode is generally used. Here, a feedback mechanism is used to maintain a constant tunnelling current by modifying the z position of the tip. For a surface with a uniform electronic structure this will coincide with a constant tip-sample separation. Any deviations in electronic structure will then be mirrored by changes in the tip position. By tracking the movement of the STM tip it is then possible to image the surface.

As the feedback loop takes a finite amount of time to move the tip, the tunnelling current still varies somewhat as the tip scans, and so provides an alternate stream of information that can also be observed. Thus, information from STM experiments is obtained through two "channels", the I (current) channel and the z (position) channel. Unless otherwise stated all images in this work are collected by observing the z channel. However chapter 3 presents some unexpected images collected through observation of the I current channel.

Interpretation of Images

Although the theory of STM seems comparatively simple when considering model systems, in reality any solid has a range of electron energy levels, any of which can contribute to the observed tunnelling current. The measured image therefore represents a complex combination of tip and sample electronic and topographic information. To simplify this analysis, several approximations are generally made. These approximations are generally considered valid for low bias voltages and metallic substrates. At higher bias voltages, and when considering semiconductors these approximations break down.

As the tunnelling current is so dependent on the size of the potential energy gap, it can be approximated that only the highest energy electrons i.e. those at the Fermi level, will tunnel. Furthermore, if the tip is atomically sharp, it can be assumed that the tip electronic state is spherically symmetric. Thus, any observed symmetry in the STM image must originate from the surface. These assumptions may seem extreme, and accounting for them can be important in high precision studies, but, suitably interpreted, STM has been shown to be a powerful probe of molecules on surfaces for a variety of systems.¹¹⁶ A more rigorous approach to simulating STM images using the Tersoff-Hamann¹¹⁷ approach is possible but shall not be considered in this work.

2.1.3 Image Processing

Although it would be hoped that STM data could be analysed unaltered, in reality many artefacts such as from thermal drift of the tip control piezos or adsorption/desorption of molecules from the tip can affect the quality of images. Thus, it is common practice to use image processing software to aid in analysis of data. For this work the open source software "gwyddion" was used.¹¹⁸ In all cases such processing is minimised to maintain the integrity of the data. Generally, the only corrections applied were:

Mean plane subtraction Calculates a mean plane and subtracts it from the image, this helps level the image.

Remove polynomial background Calculates a polynomial background function and subtracts it. This helps level more complex images.

FFT filtering Applies a Fourier transform that allows the removal of low frequency noise that is known to be a problem with the particular instrument used in this work.

Stretch colour range Adjustment of the false-colour scale allows highlighting of particular features of interest.

2.1.4 Practical Considerations

Temperature effects

STM can be performed at almost any temperature. However, high temperatures generally lead to undesirable thermal noise in the observed images, as well as thermal drift of the piezos controlling the tip. Also, many monolayer systems will be mobile at room temperature, due to the low energy barrier to surface diffusion. It is thus often desirable to image under low temperature conditions. Generally, either liquid nitrogen (LN2) or liquid helium (LHe) are used as coolants. These can cool the system to a temperature just above their boiling points, 77 K and 4 K respectively.

Ultra-high vacuum

Modern STMs are capable of imaging in a diverse range of environments; images have been produced in ambient atmospheric conditions, and even of solid-liquid phase boundaries. However, for the best image quality, ultra-high vacuum (UHV) conditions are required. This is because adsorption of unwanted molecules from the air can contaminate the sample or tip. The need for "ultra-high" rather than just "high" vacuum can be seen from a consideration of the kinetic theory of gases. It can be shown that the flux (F) of an ideal gas on a surface is given by

$$F = \frac{P}{\sqrt{2\pi mkt}}. \quad (2.1)$$

If one considers carbon monoxide (CO) as a model contaminant, at room temperature and a high vacuum pressure of 10^{-6} mbar the flux will be $2.88 \times 10^{14} \text{ cm}^{-2} \text{ s}^{-1}$. If the surface has a density of $10^{15} \text{ atoms cm}^{-2}$ (typical of a close packed solid substrate), and the sticking probability is 1 (i.e. every collision between CO and the surface leads to irreversible binding), then the time for the surface to be completely covered by CO would be 3.5 seconds, even at this very low pressure. Since the flux is proportional to pressure, lowering the pressure by 4 orders of magnitude to 10^{-10} mbar would raise the time required to cover the surface by 4 orders of magnitude, to 35000 seconds, or just over 9 hours.

In reality, adsorption sticking probability is less than 1 for all but the most reactive molecules, so the pressure constraints are somewhat looser than this, however the need for extremely low pressures to avoid contamination is clear. A secondary consideration of the need for UHV in low temperature (LT) STM in particular is the need to keep the sample cooled. This requires thermally isolating both the sample and cryostat from the surroundings. Placing the instrument in a vacuum chamber is an ideal way to do this, and also avoids any issues with condensation on the cold surfaces.

Achieving UHV

To achieve UHV conditions, the STM is mounted in a vacuum chamber made of stainless steel. Stainless steel is used as even small gas molecules cannot easily penetrate its lattice. All flanges are sealed using single-use copper gaskets. In combination with knife-edge flanges these form a near-impermeable seal. A variety of pumps can be used to achieve UHV pressures. In the equipment used for this study, rotary pumps provide the main initial pumping. Turbomolecular pumps are used once pressure is below 0.1 mbar and ion pumps once pressure is below 10^{-6} .

Once the chamber is evacuated, turbomolecular and ion pumps are then used to maintain UHV conditions. Turbopumps have a higher pumping load but higher energy usage, and have a finite pump life. They can also introduce vibrations which will affect sensitive measurements. Thus, they are only used when large amounts of gas flux are expected. For everyday maintenance of pressure, ion pumps are preferable.

To achieve the best vacuum conditions, baking of the chamber is also required. Many adsorbates from the air, in particular water, adsorb onto the inside of the chamber and only degas very slowly. This slow, steady, flux of gas prevents pressures below about 10^{-8} mbar from being achieved. To remove these in-chamber contaminants the whole chamber can be "baked" by being enclosed in a thermally insulating baking chamber and heating the whole apparatus to $150\text{ }^{\circ}\text{C}$. This increases the rate of desorption of the contaminants and so, after 72 hours of baking and then being allowed to cool, the chamber is capable of reaching UHV conditions.

Tip preparation

A consideration of the theory of STM makes clear that a sharp tip is essential to achieve atomic resolution. Two main methods of achieving sharp tips have been developed: mechanical cutting and electrochemical etching.

- **Mechanical cutting** involves cutting a piece of metal wire at an angle. This leads to a rough tip consisting of multiple "microtips". Since the tunnelling current is so dependent on separation, the longest microtip will be the overwhelming contributor to the measured signal, so other microtips can theoretically be ignored. In practice, it is found that several attempts are required before a satisfactory tip can be produced. As the STM used in this work is mounted in a cryostat, tip transfer is comparatively difficult so a more reliable tip production method is desirable.
- **Electrochemical etching** involves using some electrochemical reaction (dependent on tip material) to shape the tip to a point. The exact details of the technique can vary,

but generally depend on using the meniscus of the etchant solution to form a sharp point. Figure 2.2 shows electron microscopy images of both a mechanically cut and an electrochemically etched tip. As can be seen the etched tip has a much more defined shape.

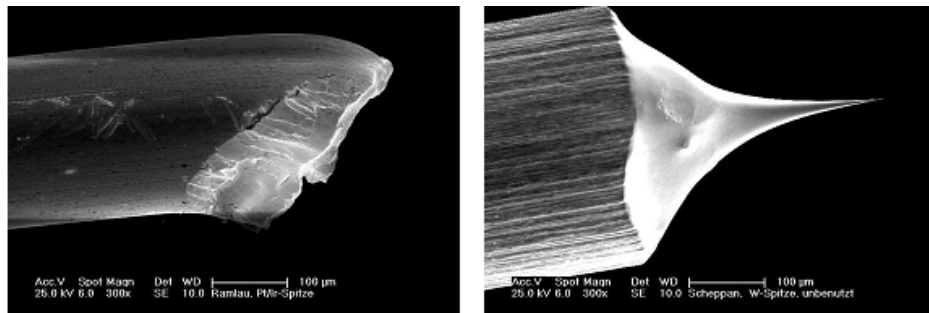


Fig. 2.2 Left: Mechanically cut tip made from Pt80/Ir20 wire; Right: Etched tungsten tip. From reference 119

The tip material used depends on the conditions that shall be used for imaging. For imaging in air, it is important the tip does not corrode, hence an alloy of platinum and iridium is generally used. For imaging in UHV conditions corrosion is less important, hence tungsten tips are generally used due to the ease of etching. In this work, electrochemically etched tips purchased from Scienta Omicron GmbH were used for all images presented. Mechanically cut and self-made electrochemically etched tips were trialled, but gave unsatisfactory imaging results.

2.1.5 Substrate

As discussed above, for STM imaging an extremely flat substrate is required. This is because the limited range of the piezo crystals means that the tip cannot move enough to compensate for large changes in the height of the substrate. Highly polished metal single crystals are a commonly used substrate. These are carefully cut to expose a particular Miller plane of the metal surface. Another commonly used substrate is graphite in the form of highly oriented pyrolytic graphite (HOPG). This is available commercially in a range of grades separated by their mosaic spread angle. In this work an Au {111} single crystal was used for most initial imaging. Several HOPG single crystals of ZYB grade (Mosaic spread $0.8^\circ \pm 0.1$) were used for some STM studies, however these unfortunately could not be completed due to restrictions due to the Covid-19 lockdown.

2.1.6 Substrate Cleaning

As has been seen, even under UHV conditions a surface will still be contaminated after long periods of storage. It is thus desirable to clean the surface prior to monolayer deposition, so that adsorbates are interacting with a known surface.

Metal Surfaces

For metal single crystals, the main methods used to clean the surface are annealing and sputtering. Heating of the surface increases the desorption rate of any adsorbed contaminants, and remove any defects or reconstructions the contaminants may have caused. It is important the substrate is kept well below its melting point, and also below the temperature of any phase transitions which could cause the single crystal to split into domains. For the Au {111} surface considered in this work an annealing temperature of 850 K was used, in keeping with standard literature.¹²⁰

Heating does not always remove all the contaminants from the surface, particularly strongly bound ones. For this reason, it is common to also sputter the surface by bombarding it with Ar⁺ ions. These ions contain a large amount of kinetic energy, which is transferred to the surface atoms upon impact and hence ejects them. Sputtering for approximately half an hour removes the top few layers of atoms to reveal a completely fresh surface. This fresh surface is highly disordered and hence a further annealing step is necessary to obtain an equilibrated surface. In practice multiple sputter-anneal cycles are used to ensure cleanliness of the surface prior to imaging, as impurities diffuse out from the bulk to the surface in the first few annealing steps.

Graphitic Surfaces

The main method of obtaining a clean graphite surface is through cleaving of the crystal using adhesive tape to form a fresh surface. This is the predominant method reported in literature for quickly preparing a fresh substrate in ambient conditions. As this step involves exposing the graphite to ambient conditions every time it is cleaned, it can involve the contamination of the graphite and sample plate. Hence, for this work an additional step of heating the crystal to 900 K in UHV was also performed after every cleavage, to ensure that contaminants were removed prior to dosing and imaging.

Sample dosing

There are multiple methods considered in the literature for forming surface assemblies. For work in UHV conditions, solvent deposition methods are obviously impractical in situ.

Ex situ deposition and fast entry into the instrument can be used, particularly for initial studies, due to its ease of use. However the uncertainty of whether the formed structure still contains solvent molecules means that it is undesirable for high quality data collection.

The generally used method of sample deposition for UHV studies is chemical vapour deposition. In this method, a sample of the adsorbate is sublimed, with the substrate positioned such that the sublimated vapour will impinge on the surface. The doser used in this work is adapted from one previously developed within the group.¹²¹ It consists of a glass capillary held by a ceramic plate attached to three copper screws. The copper screws also function as electrodes for resistive heating by a tantalum coil wrapped around the capillary. The capillary is half open and half solid glass, meaning that the “bottom” of the capillary occurs halfway up its length, and hence all dopant is covered by the heating coil. A thermocouple is attached to the capillary to allow temperature measurement. A schematic of the doser is shown in Figure 2.3. The doser is capable of containing and separately heating two capillaries, however in practice it was found that the thermal isolation between the two capillaries was poor. This caused co-sublimation of both dopants when only one was heated. Hence in all work presented here the component molecules were dosed individually, with the doser being vented and refilled in between changing the molecule being dosed.

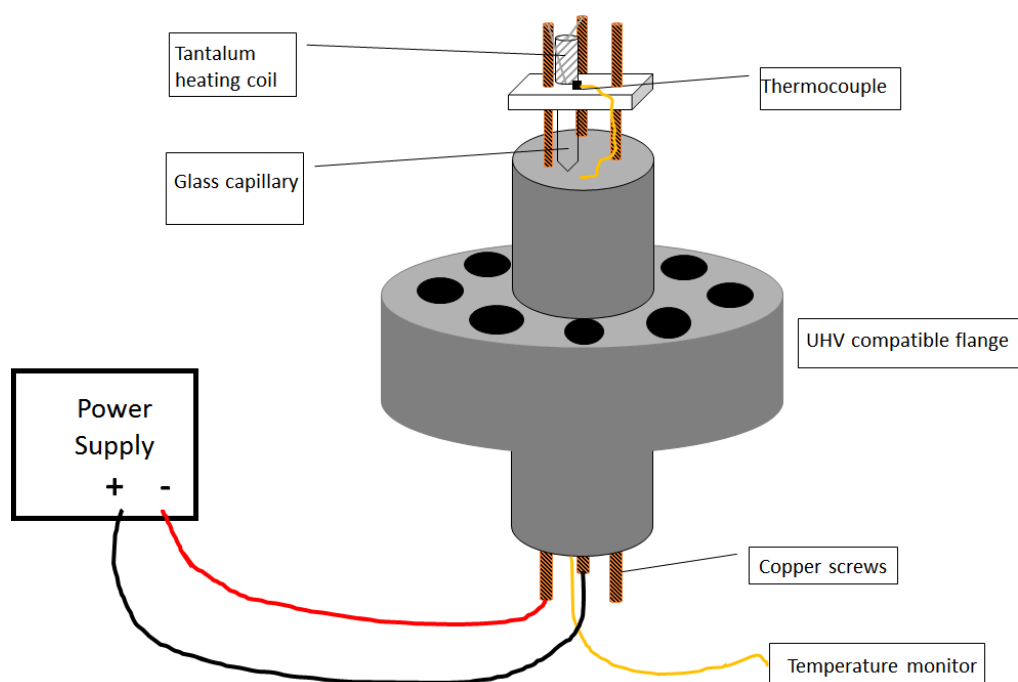


Fig. 2.3 A schematic of the doser used for this work

Once a sample is loaded into the capillary, the doser is attached to the doser chamber and pumped using a combined turbopump and roughing pump. The sample must then be heated

to remove contaminants, particularly water. Previous work had used narrow capillaries fully filled with adsorbate. These were found to only partially degas. It was observed that even after 48 hours of drying, significant quantities of water were detected by the residual gas analyser once the doser was connected to the main vacuum chamber. For this work the capillary holder was adjusted to hold larger, 6 mm capillaries. These are easier to fully degas and are also easier to load and clean. For cases where the sample to be dosed was only available in limited quantity, narrow capillaries can be placed inside the larger capillary to reduce the required sample quantity. These were only partially filled to minimise the total adsorbate mass, and hence improve the rate of degassing. The increased thermal mass of two glass capillaries means that thermocouple readings of sublimation temperature may be affected, however slow heating rates were used to reduce this problem.

2.1.7 STM Instrumental details

The STM instrument considered in this chapter was first used more than 20 years ago.¹²² Prior to the commencement of this phase of work it had been left dormant for three years and so significant effort was required to make it operational again. The instrument is an Omicron LT-SPM with the ability to operate either in STM mode or in AFM mode using a Qplus tip. For this work only simple STM tips were used.

The STM is contained in a vacuum system that consists of two separately pumped main chambers (preparation and STM), with a third separately pumped load lock and a fourth separately pumped doser chamber. Each chamber is separated by gate valves from adjacent chambers. Base pressure in the prep chamber is 10^{-10} mbar under normal conditions while the STM chamber pressure can fall into the 10^{-11} mbar pressure range when cooled, as the cryostats act as a cold trap ('cryopumping'). The apparatus can operate at room temperature, low temperature cooled by LN₂, or ultra-low temperature while cooled by LHe. For this study only liquid nitrogen temperatures were used. A schematic diagram of the apparatus is included (Figure 2.4).

- The load lock consists simply of a small chamber with an easily opened viewport, pumped by a turbopump with backing rotary pump, which can achieve pressures of around 10^{-7} mbar. Sample transfer is achieved using a magnetic transfer arm that can be extended into the prep chamber. This allows samples and new tips to be quickly introduced into the manipulator while introducing minimal atmospheric contamination.
- The preparation chamber consists of an electronically controlled manipulator arm that can move the crystal around different positions within the chamber. This arm can also be extended into the STM chamber. Within the preparation chamber are several

facilities for surface characterisation and cleaning. The first of these is resistive heating within the manipulator. The second is a Hiden quadrupole residual gas analysis mass spectrometer, which can track masses up to 200 amu. A leak valve connected to a gas line allows the introduction of low partial pressures of specific gases. Introduction of argon to the chamber, combined with an ion gun, allows sputtering of the sample to clean the surface as described in section 2.1.6. There is also a set of SPECS LEED/Auger optics. The Auger mode was found to lack sufficient sensitivity to reliably identify adsorbates, while the LEED has not been considered in this work. The preparation chamber also contains a gate valve that connects to the doser chamber.

- The doser chamber consists of a small chamber pumped by a Pfeiffer Turbopump system. The doser described previously is attached to this chamber once loaded. Heating tape allows the doser to be baked independently of the rest of the apparatus. Base pressure after baking is generally 10^{-8} mbar.
- The final chamber is the STM chamber. Once in this chamber the crystal can be manipulated using a wobblestick from the manipulator into either a 6-space carousel for storage, or into the STM sample stage. The entire STM sample stage is encased in two cryostats, an inner and an outer. For ultra-low temperature work the inner can be filled with liquid helium (LHe) and the outer with liquid nitrogen (LN2) to provide thermal shielding. Alternatively both cryostats can be filled with LN2 for operation at low temperature (77 K) with an extremely long (48 hours) temperature hold time. Once the sample is in the STM stage, the doors on both cryostats can be closed to thermally isolate the sample. The entire sample and scanner are both suspended by springs and connected to a magnetic eddy current damping system. This allows isolation of the STM from mechanical vibrations. Coarse and fine-motion piezos are used to control the tip, while the sample is held stationary and grounded.

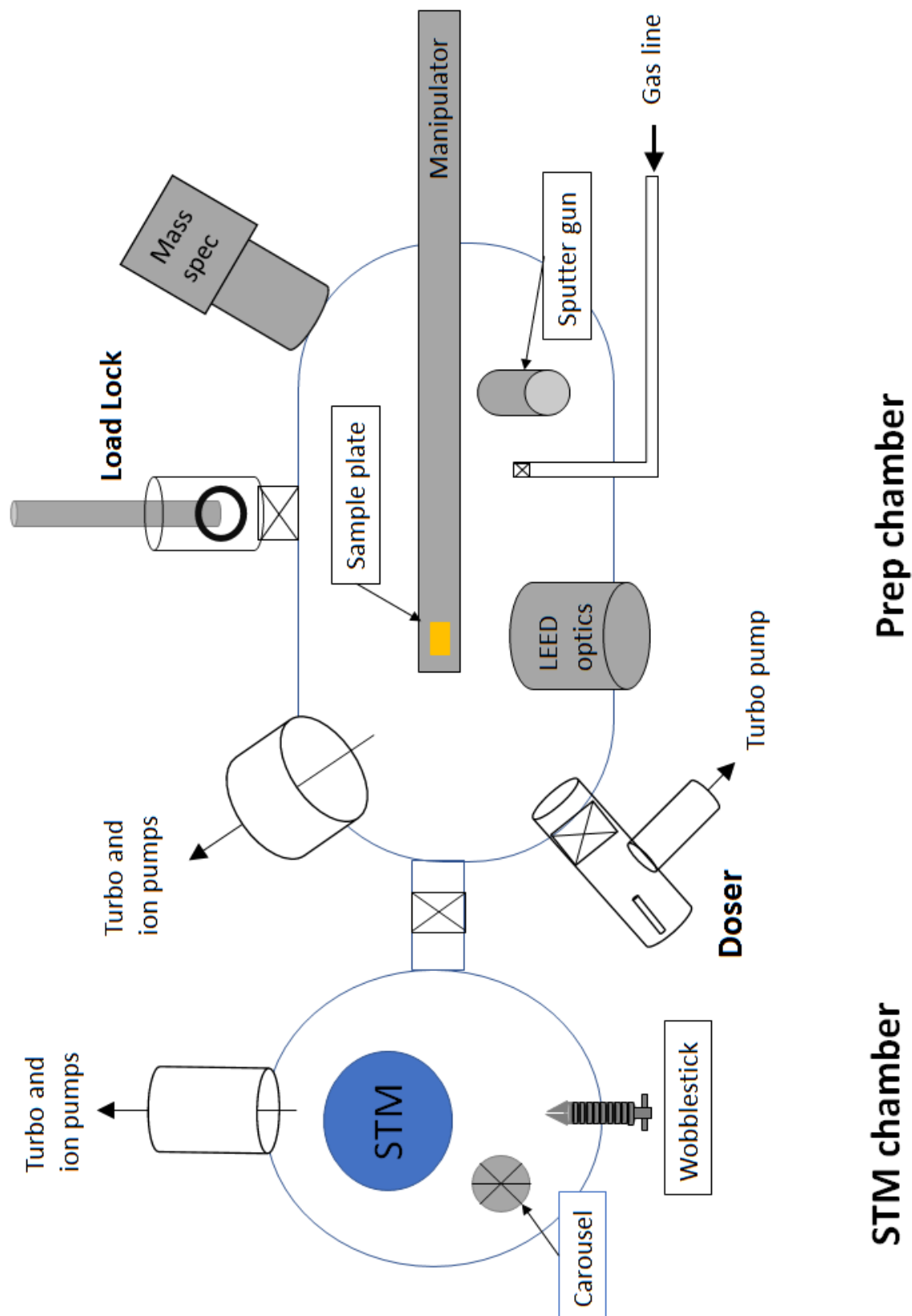


Fig. 2.4 Schematic of the layout of the STM system used to collect the results presented here

2.1.8 Instrument Effects

Near the end of the tenure of the previous user of the STM (Dr Stephen Driver) he reported an issue with large amounts of noise appearing in images in the y scan direction. Despite multiple adjustments and technician visits no satisfactory solution to this issue was found. This issue was reproduced upon commencement of this work to reactivate the instrument.

The method used to remove the effects of this noise is through a Fast Fourier Transform filter, as implemented in the post-processing software described in section 2.1.3. Figure 2.5 shows an atomic resolution scan of a HOPG surface before/after processing.

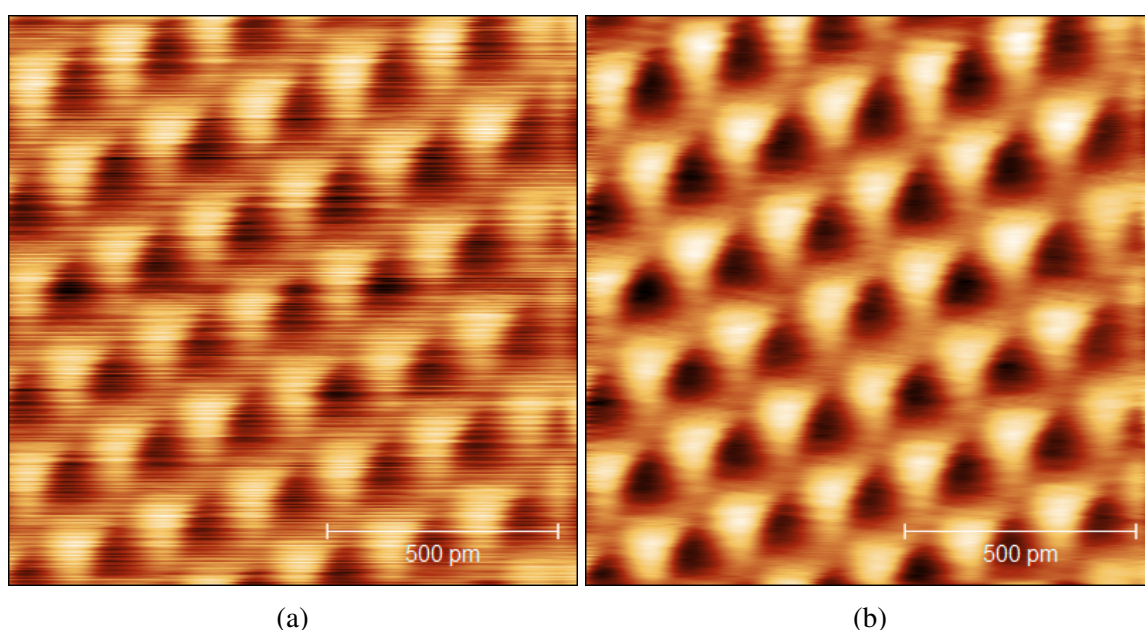


Fig. 2.5 STM image showing an atomic resolution image of graphite before (a) and after (b) image processing

2.2 X-Ray Diffraction (XRD)

X-ray diffraction (XRD) experiments are some of the most powerful structural techniques available for ordered materials. X-rays are part of the high energy range of the electromagnetic spectrum, with wavelengths ranging from about 10nm to 10pm. This lengthscale coincides with typical atomic separations in molecules, thus X-rays are diffracted by solids with systematic atomic separations. The use of X-ray diffraction to determine crystal structures was pioneered by William and Lawrence Bragg.¹²³ With the key result summarised in Bragg's law:

$$2d \sin(\theta) = n\lambda. \quad (2.2)$$

Bragg's law gives the conditions for constructive interference, i.e. a spot in the diffraction pattern. d is an atomic spacing in the crystal, θ is the scattering angle, and λ the radiation wavelength. n is simply an index number for different peaks. By systematically collecting data from different peaks it is possible to obtain a diffractogram of a crystalline material. Careful analysis of the positions and intensities of peaks in the diffractogram allows the solution of the crystal structure. This method has allowed the determination of the structures of a large range of solids.

2.2.1 Substrate

The substrate used in these XRD experiments is papyex, a recompressed exfoliated graphite. Chapter 4 details the methods used to characterise the specific batches used in this work.

Exfoliated graphite is graphite that has been produced industrially through the addition of agents that intercalate between the graphite sheets. On rapid heating these then thermally dissociate in an explosive manner to delaminate the graphite sheets, forming a powder. The intercalation agent used to form papyex is sulphuric acid. The powdered exfoliated graphite is then heat treated to remove the additives, and compressed into a sheet. The compression of the papyex is important as this means that the graphite crystallites exhibit a preferred orientation, being more likely to lie parallel with the plane of the sheet than perpendicular. This allows manipulation of diffraction geometry to maximise the in-plane scattering contribution.⁸²

In general papyex exhibits a surface area of approximately 15-20 m²g⁻¹. This is lower than many nanostructured graphites which can exhibit surface areas in the 1000s of m²g⁻¹ however, it is significantly higher than HOPG crystals. A key feature of papyex is the comparatively large size of the crystallites. It has been characterised that the typical crystallite size in papyex is 20 μm, with the packing of these crystallites generating voids of 500 Å in size.¹²⁴ Papyex is thus a mesoporous material, meaning that the electronic and other properties of the graphite are closer to that of bulk graphite than of nanomaterials. This provides a large, comparatively flat surface that is closer to an ideal "infinite flat plane" than higher surface area carbons which exhibit smaller planes and a higher defect density.

2.2.2 Sample Dosing

Although papyex has been cleaned post exfoliation and is specified as high purity (>99.85% Carbon). Impurities from the atmosphere are known to concentrate on the surface of materials, so it is prudent to further clean the substrate prior to use. Each substrate batch was outgassed by pumping with a turbomolecular pump to 10^{-5} mbar pressure. The batch was then heated to 500 °C and pumped for at least 12 hours until the pressure returned to the 10^{-5} mbar regime. This outgassing temperature is somewhat higher, and pressure somewhat lower, than has been previously used.¹²⁵ This is possible thanks to the use of a metal vacuum system and improved pump in place of the previous glass vacuum system. For the first batch cleaned in this way a liquid nitrogen cold trap was placed between the papyex and pump, however no condensible residue was obtained. The metal-glass joints between the vacuum system and cold trap limited the pressure that could be achieved, so for future cleaning cycles the cold trap was not used.

Once degassed, dosing was generally performed by sublimation within a sealed pyrex glass tube. Section 7.2.3 covers some of the alternate dosing mechanisms that were used for the dosing of trimesic acid which required more complex treatment. For other systems, dosing was performed by placing weighed amounts of graphite and adsorbate within the pyrex tube. This was then evacuated by a trained glassblower using a rotary pump to 0.1 mbar before being sealed. Most adsorbates used are solids with a low vapour pressure, meaning that loss of adsorbate due to initial pumping is negligible. However, for dosing of volatile liquids it is possible that significant quantities of adsorbate could be lost while obtaining vacuum. For this reason when using volatile adsorbates the entire apparatus was submerged in liquid nitrogen shortly before pumping commenced to freeze the adsorbate and hence reduce adsorbate loss.

The sealed tube was then heated to a specified temperature, generally at or just above the literature sublimation temperature. Once this temperature was reached, it was maintained for one hour before being left to slowly cool to room temperature overnight.

The tube was then broken open, and the contents recovered. For study at synchrotrons where a capillary geometry was utilised, the dosed graphite was cut into 3mm diameter discs and stacked into a Lindemann glass capillary. For experiments where a "flat plate" geometry was used, the recovered graphite was simply cut into narrow strips and mounted parallel to the sample pin of a standard crystallography sample mount as in figure 2.6 and used in air. This was appropriate because these additives adhere very strongly to the papyex surface and will not be removed or out competed by atmospheric impurities once on the surface.



Fig. 2.6 Mounted XRD sample for flat-plate transmission. The sample is aligned parallel to the stub pin, and held in place with adhesive putty

2.2.3 X-ray sources

There are several methods of generating X-rays. The quality of the incident radiation is a key determinant of the quality of the end diffractogram. This section will briefly outline essential theory on different methods of X-ray generation and their pros and cons.

Laboratory sources

Conventional laboratory X-ray sources generate radiation using an X-ray tube. These generate radiation through the collision of electrons emitted by a hot cathode with an anode target. Figure 2.7 gives a schematic overview of this process.

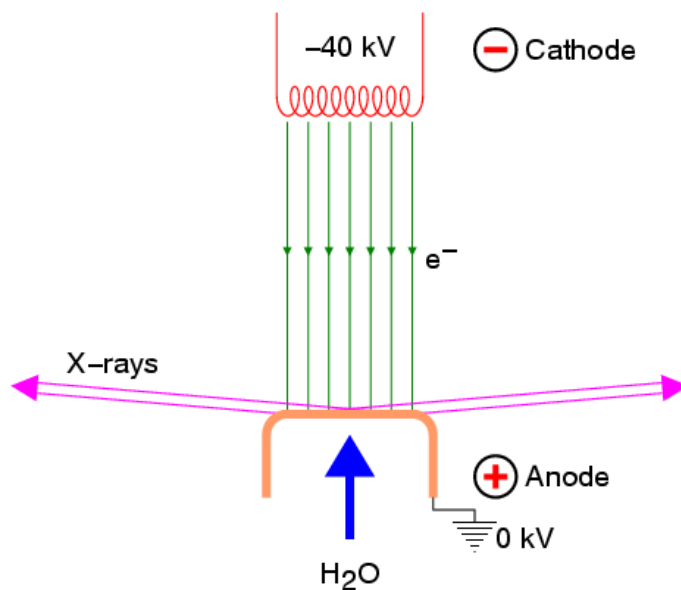


Fig. 2.7 Conventional X-ray source using filament and target. Image is sourced from the Advanced Certificate in Powder Diffraction on the Web Course Material Master Index at Birkbeck university¹²⁶

There are two mechanisms of X-ray production when electrons collide with the target. So called “K-lines” are generated when the incident electron beam excites a low energy core electron from its atomic orbital. The excited electron is ejected and leaves behind a vacancy in a low energy shell. This low energy vacancy is then filled by a higher energy electron, with the energy difference being emitted as a photon. As the core electron energy levels are well defined and quantised, this process ideally leads to production of several discrete wavelengths of radiation, defined by the energy of the core shells of the target. In practice even core electron energy levels vary somewhat between atoms in different electronic environments, leading to some finite peak width, but this effect is generally negligible.

However, a second mechanism of photon production is more problematic for diffraction, as it occurs over a range of wavelengths. As incident beam electrons strike the target, they are deflected and accelerated through interaction with the positive nucleus. When charged particles such as electrons change in kinetic energy, the excess energy is emitted in the form of a photon (see figure 2.8). These photons lead to Bremsstrahlung radiation, a continuous background evident in figure 2.9.

For the optimal diffraction pattern monochromatic radiation is desired. This is because radiation of different wavelengths has a different wavevector (k) and so is diffracted through different angles by the same reciprocal lattice spacing, hence broadening the detected signal. Careful choice of anode material can minimise the number of similar k lines produced,

however the inelastically scattered Bremsstrahlung background is present for all anode materials. Monochromators and other optics can be used to improve the quality of the generated radiation, but these serve to further reduce the available intensity available for analysis. Hence, the trade-off between incident beam intensity and quality is an important choice when running a diffraction experiment.

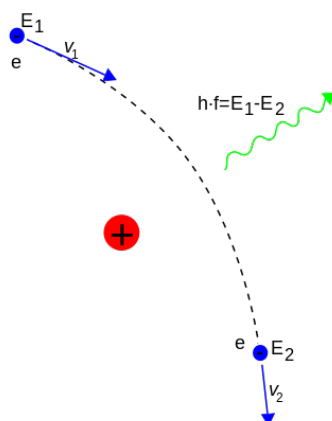


Fig. 2.8 Deceleration of electrons from V_1 to V_2 reduces their energy from E_1 to E_2 . Due to conservation of energy a photon is emitted with energy equal to $E_1 - E_2$. Image is public domain sourced via Wikimedia Commons.

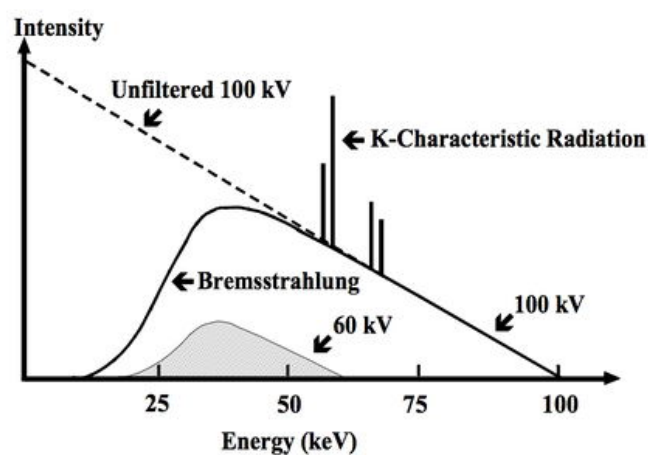


Fig. 2.9 X-ray production from an X-ray tube, showing multiple discrete “K-lines” as well as a continuous bremsstrahlung background. Image is public domain sourced from Kieranmaher, via Wikimedia Commons.

Taken as a whole the process of X-ray generation is highly inefficient, with 1 % of the electrical energy used in the process generating X-rays of any kind, with the rest dissipated as heat. Once the undesired wavelengths have been removed the efficiency of production is

even lower. Overcoming the low X-ray generation efficiency through increasing the power supplied is possible, however the main limitation then becomes the need to dissipate the excess heat generated. It is for this reason that the intensity of lab-based X-ray sources is largely limited by the availability of cooling for the anode target.

A particular development has been the creation of Rotating anode sources. As the name suggests, these utilise an anode that rotates, with only part of the Anode being exposed to the electron beam at any one time. This significantly improves heat dissipation and allows the use of significantly higher emission currents to generate a more intense X-ray beam. However they are still inherently inefficient and cannot reach the highest possible intensities, as well as producing much of the X-ray flux at undesired wavelengths.

Particle accelerators

Generation of highly intense, electromagnetic radiation is important for a multitude of applications, both for its intrinsic intensity, and to allow monochromation and optical manipulation while maintaining acceptable intensity. Particle accelerators were known for some time to be capable of generating electromagnetic radiation through acceleration of electrons, however it took much work for the process to be refined enough to use for analysis.

Synchrotron

Synchrotrons are particle accelerators in which electrons follow a circular path defined by applied magnetic fields. As the electrons are constantly being diverted they are constantly accelerating and hence constantly emitting radiation (in this case magnetobremstrahlung radiation). In practice modern synchrotrons utilise more complex modes of operation including undulators and linear sections, but the principle of acceleration of electrons via a magnetic field remains the mechanism of X-ray generation.

This process is significantly more efficient in terms of energy usage than the process described above, and through the use of superconducting electromagnets heat dissipation issues can be almost eliminated. This allows significant manipulation of the generated radiation to produce highly collimated, highly monochromatic radiation of unprecedented intensity. Synchrotron radiation is highly tunable and can range from far IR to hard X-ray energies depending on the user requirements.

Monochromators

Monochromators are often used to limit the radiation that gets to the sample to a narrow range of wavelengths. This is done in an analogous method to that used to split white light

into its component parts, through a prism. The materials used as monochromators are single crystals, where the crystal lattice spacings act as lines on a diffraction grating. Ideally they should be resistant to X-ray damage, as they are constantly exposed to the full intensity of the incident beam. Crystal choice is determined by a variety of factors, including the presence of intense Bragg peaks and low absorbance to maximise the transmitted intensity. For the instrument used in this work, a graphite monochromator is used. This maximised the beam intensity at the cost of a relatively larger wavelength distribution.

2.2.4 Instruments Used

Diamond light source

Some of the diffraction patterns presented in this work were obtained at Diamond Light Source (DLS). This is a third generation synchrotron with 39 beamlines available. Different beamlines are setup for different experimental techniques and can utilise electromagnetic radiation of a range of wavelengths, and with a range of detector and sample geometries. For this work the dedicated powder X-ray diffraction beamline I11 was used. This beamline is equipped with a MYTHEN multidetector¹²⁷ which allows collection of a large angular range simultaneously, greatly reducing acquisition time. The minimum accessible scattering angle was 1° (limited by a beamstop used to prevent detector damage) and the maximum angle collected was 90° , however for the systems of interest here most peaks occurred at $2\theta < 30^\circ$. The X-ray wavelength chosen was approximately 1 \AA , chosen to coincide with the maximum available flux. Previous experiments had shown that beam damage was not significant for systems of this type, and comparison of patterns after several hours of exposure confirmed this to be the case for the systems studied. A silicon standard was used to calibrate the exact incident wavelength (0.998421 \AA).

The sample environment required mounting of the samples in capillaries. This was done by cutting circular discs of the papyex substrate, and stacking them upright, keeping the aligned planes of the papyex parallel. Figure 2.10 presents a schematic of the setup. The red arrows indicate the incident and diffracted beam scattered by the blue \mathbf{Q} vector.

3mm diameter capillaries were obtained to maximise the illuminated sample volume, along with custom stubs to allow mounting of the extra-large capillaries to the standard sized sample holder. The sample environment is equipped with a nitrogen cryostream (Oxford cryostream) that can range from 80 K to 500 K.

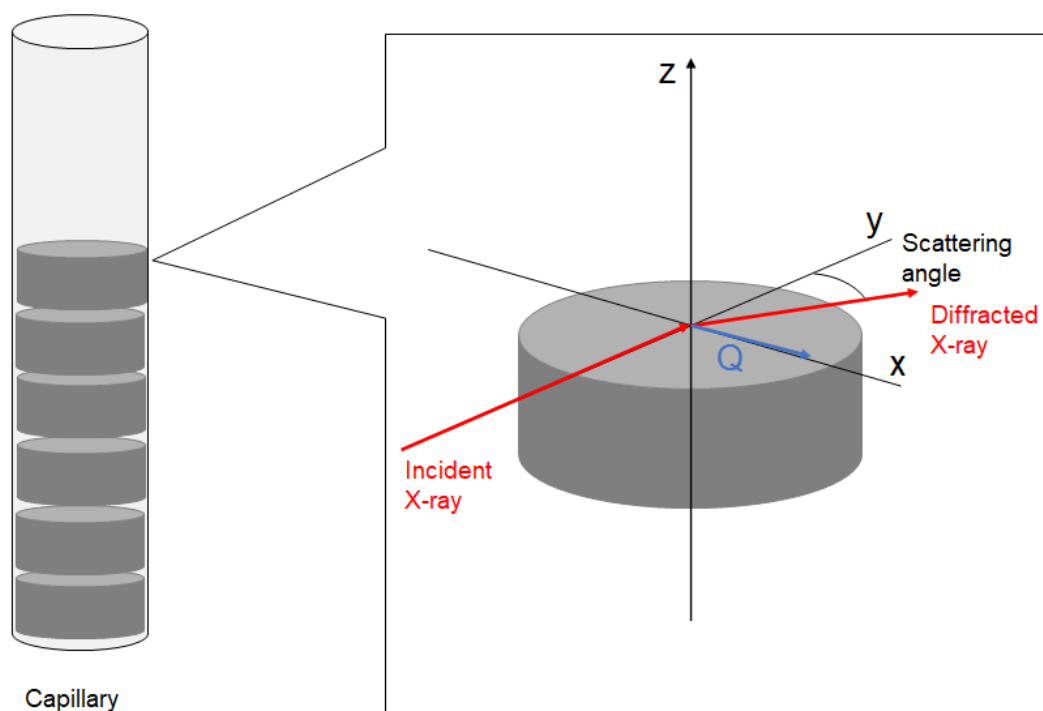


Fig. 2.10 Schematic diagram of the capillary geometry. Stacked discs of papyex are placed in the capillary, with the detector oriented such that \mathbf{Q} is oriented within the aligned planes

Lab-sources

Although synchrotrons emit the highest possible X-ray intensity, they are of only limited availability. Due to the large numbers of systems that have been studied in this work, most data has instead been collected from lab-based sources.

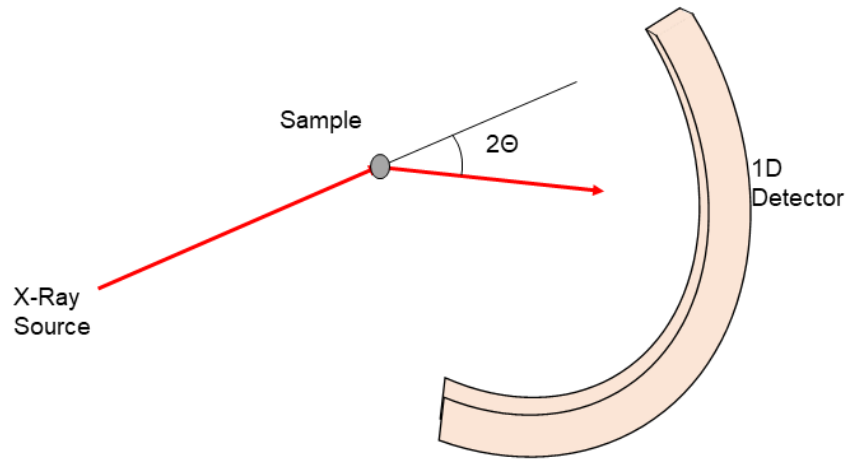
Some screening data was collected using a Panalytical Empyrean powder diffractometer at the Department of Chemistry. The diffractometer has a fixed copper anode leading to low incident beam intensity. Because of this no monochromator was used so as to maximise incident intensity. Despite the lack of intensity loss due to monochromation, data collection was still extremely slow, and collected diffractograms of low quality. It was however useful for simple studies of strongly scattering systems to determine if any crystalline monolayer was present.

Unless otherwise stated all X-ray data was obtained from a Rigaku FR-E+ superbright located at the MRC laboratory of Molecular Biology. This system contains a rotating copper anode and so is significantly more intense than the Panalytical. A graphite monochromator was used to improve beam quality and despite reducing beam intensity improved the quality of diffractograms that could be collected. Acceptable diffractograms could be obtained with just a ten minute exposure. The monochromator ensures generated radiation wavelength

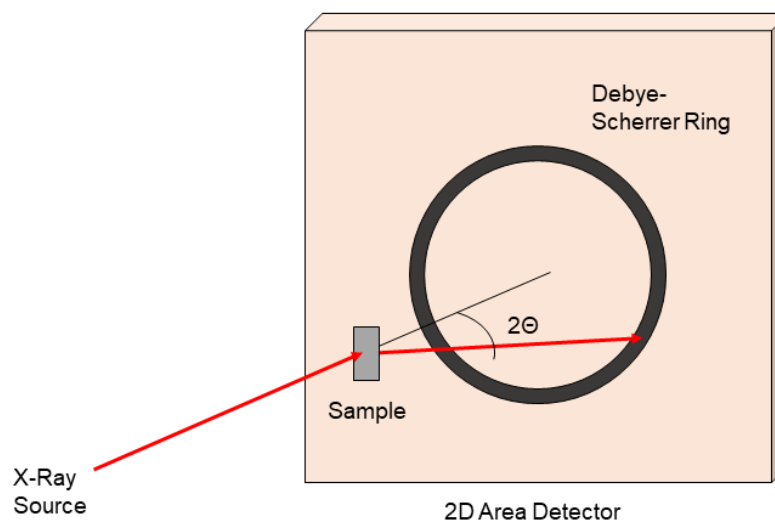
is tightly distributed around 1.54179 Å. The beam size is 200- μm in diameter and highly collimated with knife edge slits, further improving the collected diffraction pattern quality.

The detector used with this instrument is a MarDTB 2D area detector. An area detector allows the collection of the whole powder ring, rather than just a segment as in 1D detectors. This can provide information on the distribution of crystallites in the sample if the powder ring is not uniform, or can be radially integrated and used to produce a conventional PXRD intensity- 2θ plot with improved counting statistics compared to a conventional detector.

To make best use of this detector the sample geometry was adjusted to flat plate so that the whole monolayer powder ring would be detectable. This involved some differences in analysis compared to capillary geometry, which are presented in section 4.4, but the order of magnitude gain in measured intensity makes it worthwhile. Figure 2.11 compares the capillary geometry used with a 1D detector as at Diamond I11 with the flat plate geometry used for the area detector at the LMB. The area detector is able to capture the whole of the powder ring, while the 1D detector collects only a fraction of the total scattered radiation.



(a) Capillary Geometry



(b) Flat plate geometry

Fig. 2.11 Schematic diagrams of the experimental setup for the two geometries considered. The incident and diffracted X-ray beams are represented by red arrows, while the sample is grey. For the capillary geometry the view is from above, looking down on the capillary. Hence, all scattering occurs in the plane of the page. In the flat plate geometry data is collected from scattering in three dimensions

The LMB instrument is also equipped with a nitrogen cryostream (Oxford Cryostream) with a range from ambient to 100 K. Cooling diffraction samples helps reduce intensity

drop-off at higher Q due to thermal motion (Debye-Waller factor) and so unless otherwise states samples were run at 100K.

2.2.5 Theory

Bulk crystallography and diffraction are well established fields with many comprehensive standard texts. However it is useful to discuss some basic concepts and results here, that will translate to more specialised cases later.

Crystallography

In a three dimensional crystalline material the periodicity of the crystal can be represented by a maximum of three lattice vectors \mathbf{a} , \mathbf{b} and \mathbf{c} . Two symmetrically equivalent points can then be represented by a combination of these three vectors.

Any plane in the unit cell can then be represented by three Miller indices; h, k , and l where the plane intersects the points \mathbf{a}/h , \mathbf{b}/k , and \mathbf{c}/l . A Miller index of 0 indicates that the plane is parallel to the corresponding axis. Any plane can be represented by the values of the Miller indices in the format $\{hkl\}$, for example the $\{111\}$ plane is the plane formed from the three points \mathbf{a} , \mathbf{b} , and \mathbf{c} , while the $\{110\}$ plane would intersect \mathbf{a} and \mathbf{b} while being parallel to the \mathbf{c} lattice vector.

Reciprocal space is a concept that is extremely useful when considering diffraction. In reciprocal space, rather than considering the lattice vectors \mathbf{a}, \mathbf{b} , and \mathbf{c} ; three reciprocal lattice vectors \mathbf{a}^* , \mathbf{b}^* , and \mathbf{c}^* are defined such that

$$\begin{aligned}\mathbf{a}^* &= \frac{2\pi(\mathbf{b} \times \mathbf{c})}{\mathbf{a} \cdot (\mathbf{b} \times \mathbf{c})}, \\ \mathbf{b}^* &= \frac{2\pi(\mathbf{c} \times \mathbf{a})}{\mathbf{b} \cdot (\mathbf{c} \times \mathbf{a})},\end{aligned}\tag{2.3}$$

and

$$\mathbf{c}^* = \frac{2\pi(\mathbf{a} \times \mathbf{b})}{\mathbf{c} \cdot (\mathbf{a} \times \mathbf{b})}.$$

The above equations define \mathbf{a}^* , \mathbf{b}^* , and \mathbf{c}^* in such a way that the lattice vector \mathbf{a}^* has a magnitude of $\frac{2\pi}{a}$ and points in the direction perpendicular to both \mathbf{b} and \mathbf{c} , with equivalent relationships for \mathbf{b}^* and \mathbf{c}^* . The reciprocal lattice shall be used in section 2.2.6

X-ray Scattering

All electromagnetic radiation is to some extent scattered by matter. Two main types of scattering are of relevance to X-ray diffraction.¹²⁸

- **Compton scattering** involves a change in the energy of the scattered radiation. This generally occurs where a charged particle (such as an electron) absorbs some of the energy of the radiation, reducing the energy of the incident photon and hence increasing its wavelength.
- **Thompson scattering** involves no change in the energy and hence wavelength of the scattered radiation. It occurs for all charged particles, however the intensity of the scattering varies inversely with the square of the mass of the particle.

As Thompson scattering does not change the energy or wavelength of the radiation the scattered photons are coherent with each other. This means that when multiple scatterers are present the coherent scattered photons constructively and destructively interact to produce diffraction patterns that contain information on the structure of the scatterer.

By contrast, because of the change in photon energy photons scattered by Compton scattering are incoherent (have random relative phase differences) meaning they do not interact repeatably to give diffraction patterns. Because of this, Compton scattering is undesirable for diffraction experiments, as the incoherent background obscures the information from the coherent, Thompson scattered, photons. Compton scattering is minimised when the photon energy is small relative to the mass energy of the scatterer. Thus for a scatterer of a fixed mass, Compton scattering is minimised when the lowest possible X-ray energy (longest wavelength) is used.

2.2.6 Atomic Scattering Factors

As X-rays are scattered by electrons, the intensity of scattering from an atom must depend on the number of electrons it contains. This means that heavy atoms with a higher atomic number (and hence more electrons) scatter significantly more strongly than lighter atoms. The information on the strength of scattering for an atom, n , is contained in the atomic scattering factor f_n , given by

$$f_n = \frac{\text{amplitude of wave scattered by atom}}{\text{amplitude of wave scattered by free electron}}. \quad (2.4)$$

An initial approximation would be that scattering of X-rays by many electrons is independent of each other and additive. With this approximation the above equation would reduce

to $f_n = Z$ where Z is the atomic number, the number of electrons in a particular atom. In practice there is destructive interference due to scattering from nearby electrons, particularly at higher scattering angles. This means that for a given element the value of f_n vary with X-ray wavelength and scattering angle - the so called atomic scattering factor. Tabulated values are available for all wavelengths and elements that shall be considered in this work.¹²⁹

Single Scattering

Diffraction occurs when waves are scattered by two or more points. This results in a path length and hence phase difference between the scattered waves. This phase difference leads to both constructive and destructive interference at different points away from the two scatterers.

As X-rays are only weakly attenuated by matter, a general assumption is single scattering, that each transmitted beam has only been scattered by a single pair of points. In this case there is will be a path length difference between the beams scattered by each point. Constructive interference occurs only when this path length difference equals $n\lambda$. Figure 2.12 shows a schematic of this process. Although these calculations can be performed using the real separation of the scatterers, it is useful to introduce the concept of reciprocal space, as this greatly simplifies analysis.

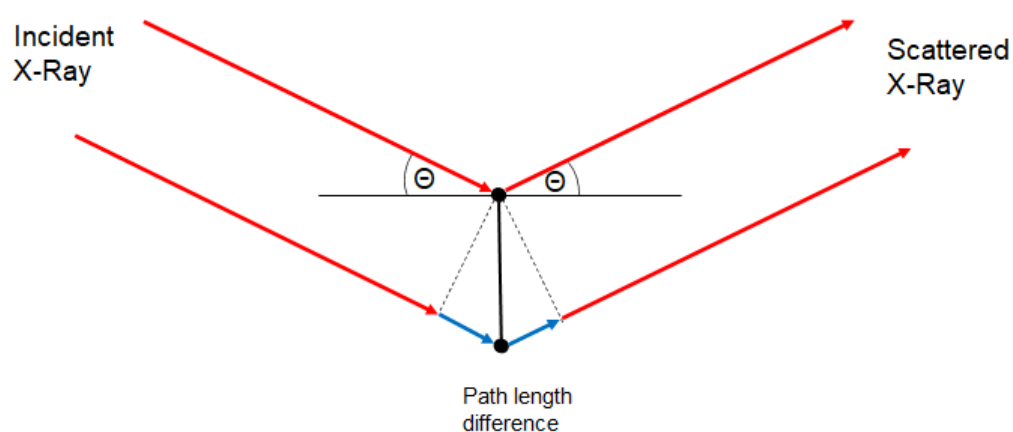


Fig. 2.12 Schematic diagram of single scattering, when an X-ray beam (red) is scattered by two points, there is a phase difference (blue) between the beams scattered by each point. Constructive interference occurs when this phase difference = $n\lambda$

Scattering Using the Reciprocal Lattice

Using reciprocal space, rather than considering the radiation as a wave with a wavelength λ , it is instead considered to consist of a wavevector \mathbf{k} with a length $\frac{2\pi}{\lambda}$. The incident

beam is denoted \mathbf{k}_i , while the final, diffracted beam is denoted \mathbf{k}_f . For elastic scattering the energy and hence wavelength of the radiation is unchanged, meaning the magnitude of the wavevectors is constant. The change in direction between the initial and final wavevectors can be represented as occurring due to a scattering vector \mathbf{S} as in figure 2.13.

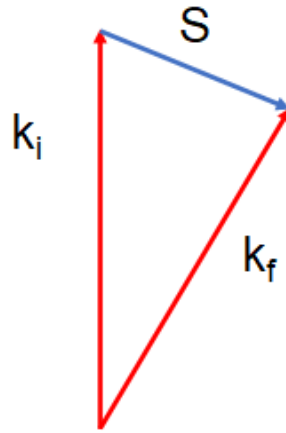


Fig. 2.13 Schematic diagram of scattering in reciprocal space. The wavevector \mathbf{k}_i is deflected by the scattering vector \mathbf{S} and ends up with a different direction as in \mathbf{k}_f .

In general, the intensity of radiation with a scattering vector \mathbf{S} is given by the square of the modulus of the structure factor \mathbf{F} . \mathbf{F} is given by the sum over all n atoms in the unit cell as shown in the equation

$$\mathbf{F}(\mathbf{S}) = \sum_n f_n \exp(\mathbf{r}_n \cdot \mathbf{S}). \quad (2.5)$$

Where \mathbf{r}_n is the position vector of atom n , while f_n is the atomic form factor of the same atom.

Because of the form of the above equation, it is found that significant scattering intensity is found only when \mathbf{S} is a point on the reciprocal lattice, i.e. when

$$\mathbf{S}_{hkl} = h\mathbf{a}^* + k\mathbf{b}^* + l\mathbf{c}^*. \quad (2.6)$$

Where $h, k, l \in \mathbb{N}$.

The diffraction pattern of a perfect crystal can thus be considered as a series of wavevectors pointing towards all the points on the reciprocal lattice, each with a unique set of h, k and l values. The intensity of each peak is given by the square of the modulus of the structure factor defined in previously.

2.2.7 Powder Diffraction

A related treatment of X-ray scattering is often considered when the sample is an isotropic powder. In this instance it is assumed that all possible orientations of the crystallites are possible in the sample, and that hence the individual diffraction “spots” evident for a single crystal above instead appear as “rings”. It is then convenient to project the pattern onto a single dimension, a radial integration of the powder rings. In this case the scattering can best be modelled using a single scattering vector \mathbf{Q} , related to the observed scattering angle 2θ by the equation

$$\mathbf{Q} = 2\mathbf{k} \sin \theta. \quad (2.7)$$

Here, \mathbf{k} is the wavevector of the incident beam, related to the X-ray wavelength by

$$\mathbf{k} = \frac{2\pi}{\lambda}. \quad (2.8)$$

For diffraction from a crystal, the conditions for a ‘spot’ or a ring to appear on the detector can be demonstrated to occur when \mathbf{Q} is equal to the reciprocal lattice vector so that

$$\mathbf{Q} = \frac{2\pi}{d}. \quad (2.9)$$

The integration of the rings into one dimension necessarily means that significant amounts of structural information are lost, particularly from the overlap of adjacent peaks. However, the relative ease of obtaining random powders as opposed to perfect single crystals mean that powder diffraction is frequently the most accessible technique for difficult-to-crystallise samples. Typically, structural solutions of powder diffraction are not possible *ab initio*. However, using intuition and working from a trial structure, it is possible to use powder diffraction to solve atomic structures.

Generally, this is automated using a Rietveld-type refinement that systematically varies unit cell sizes and atomic positions to obtain the best fit from a given trial structure, with operator intuition guiding the selection of trial structures and discounting clearly incorrect refinements. Data must be interpreted with care however, as solutions are not unique. It has been shown to be perfectly possible to achieve a well refined structural fit to a powder pattern with a completely wrong structure.¹³⁰

2.2.8 Temperature Effects

Although the above treatment is applicable for a perfect powder with all atoms perfectly at rest, in a real crystal there is atomic motion driven by thermal effects (and, even at low

temperature, by zero point energy). The end result of this thermal motion is to reduce the (useful for diffraction) elastic scattering, and increase the inelastic scattering (visible as a diffuse background).

The overall effect of the thermal motion is that higher \mathbf{Q} peaks are suppressed with increasing temperature, making the low \mathbf{Q} peaks appear more prominent in real experimental data than in the modelled data.

This can be taken into account by the addition of a temperature factor, generally called the B or Debye-Waller factor. This factor represents a scaling term for the intensity of diffraction peaks of a given \mathbf{Q} . The B factor can be calculated from the equation

$$B = \langle e^{i\mathbf{Q}\cdot\mathbf{u}} \rangle^2, \quad (2.10)$$

where \mathbf{Q} is the scattering vector and \mathbf{u} is the displacement of the atoms at a given time. The B factor is calculated by taking the square of the time average $\langle \dots \rangle$ of $e^{i\mathbf{Q}\cdot\mathbf{u}}$.

As it is impossible to know \mathbf{u} for a newly characterised system, fitting of B to the experimental data is another step that is performed to fully fit experimental data to a model. Because of the comparatively small number of peaks available for systems considered in this work, Debye-Waller factors have been set to unity to reduce the number of fitting parameters. This is justifiable as experimental data was collected at low temperatures (100K) and (for most systems) the component molecules are extremely rigid, meaning that \mathbf{u} varies over only a small range. These assumptions were also used in previous work considering similar systems and proved valid.^{113,114}

2.2.9 Diffraction From 2D systems

A key reason for the usefulness of X-rays in bulk structural studies is their comparatively weak attenuation. The scattering cross section of atoms for X-rays is of the order of 10^{-6} \AA^2 meaning that X-rays penetrate deep into the material. Hence, observed diffraction patterns can be taken to be representative of the bulk structure, and not of reconstructions and impurities concentrated at the surface. However, the ability of X-rays to probe deep into the bulk of a material is problematic for those who wish to study the reconstructions, impurities and other phenomena localised at the surface. Grazing incidence can be used to enhance the surface selectivity of a wide range of techniques, including diffraction. Indeed, this technique has been used for the study of heavy elements at surfaces, however the weak attenuation of light elements mean that it is generally not possible to use it for organic molecules at surfaces.

Powder diffraction as a surface sensitive technique

An alternative way to achieve surface sensitivity is to maximise the signal from the surface relative to bulk by using a powder or other high surface-area substrate. By comparing a dosed and clean diffraction pattern it is then possible to "subtract out" the signal from the substrate. The residual pattern after subtraction can be approximated as being due simply to diffraction from the monolayer structure. This is significantly more facile to set up than grazing incidence. However, even for a high surface area substrate, the scattering signal from the surface will still be comparatively tiny. Hence, a large flux of incident radiation is required to obtain usable data.

The subtraction of the substrate signal is also generally imperfect, so that features close to substrate diffraction peaks will be lost. The masking effect of significant substrate peaks limits the technique to applications where the surface peaks of interest do not significantly coincide with diffraction peaks observed for the substrate. For physisorbed monolayers the peaks of interest are those identified with long range periodicity within the layer, as the molecular structure is already known. From the theory of diffraction it is clear that these long range features will appear at significantly lower scattering angles than the peaks due to the short interatomic distances, due to the inverse relationship between scattering angle and real-space separation. Thus, study of self-assembly of molecules is well suited to surface sensitive powder diffraction.

Differences from 3D

Diffraction from 2D crystals such as monolayers bears much similarity with diffraction from bulk materials. However, there are also key differences that must be addressed before proceeding. A key difference is the behaviour in the perpendicular plane. As 2D materials have no periodicity in the third dimension, they have no reciprocal lattice spacing in this direction. Instead the in-plane reciprocal lattice points become reciprocal lattice rods, extending infinitely out of the plane of the surface. Within the plane, the spacing of these rods relates to the real-space lattice parameters of the 2D crystal in the same way as the bulk.

There are significant repercussions to the existence of these rods. In a bulk diffraction pattern, the diffraction condition for a particular reciprocal lattice spacing are satisfied only when the scattering vector aligns with the reciprocal lattice point separation. Figure 2.14 shows how, due to their infinite extent, the Bragg rods of any misaligned planes will eventually intersect with the scattering vector, at some higher Q . This means that diffraction peaks from 2D systems are highly asymmetric, with slightly misaligned planes contributing significant intensity to the high-angle side of the peak.

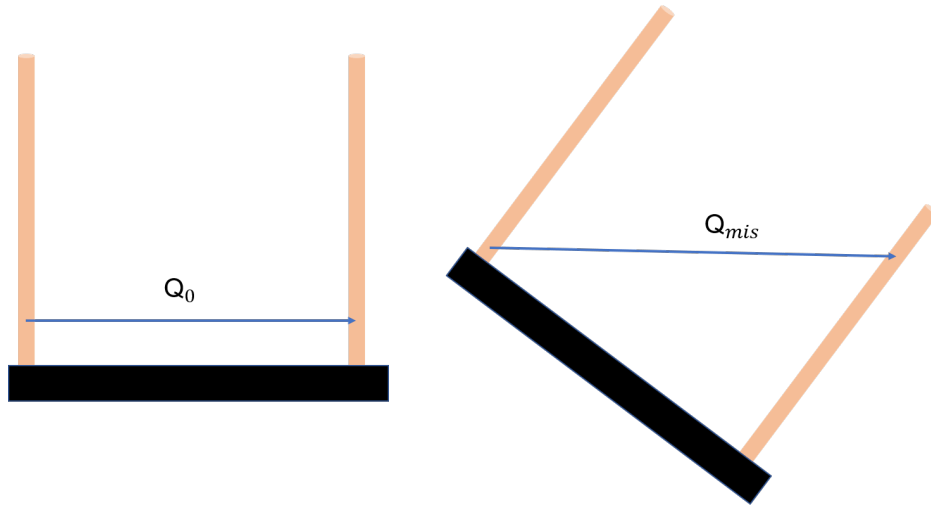


Fig. 2.14 When planes are misaligned from the scattering plane, the diffraction condition for a Bragg rod spacing of Q_0 is met not only when the Bragg rod spacing and scattering vector align, but also for larger scattering vectors

The Bragg rods would ideally be considered as being entirely one-dimensional objects, with no size within the plane. However in reality the Bragg rod obtains some broadening due to various factors such as the limited coherence length of the real-space lattice. This broadening can be modelled using either Gaussian or Lorentzian terms. The forms of these two model cross sections are presented in the below equations. The form of any specific Gaussian/Lorentzian is determined only by the relevant constant α or β , which are related to the full width at half maximum of the Bragg rod by a set of equations shown below. The term calculated for Gaussian line broadening is

$$Gaussian = \exp\left(-\frac{(uQ - Q_0)^2}{\alpha^2}\right), \quad (2.11)$$

while for Lorentzian line broadening the term is

$$Lorentzian = \frac{\beta_{Lorentz}}{1 + \beta_{Lorentz}(uQ - Q_0)^2}. \quad (2.12)$$

An alternative term utilises a squared Lorentzian and is given by

$$Lorentzian^2 = \frac{\beta_{Lorentz}^2/\pi}{\left(1 + \beta_{Lorentz}(uQ - Q_0)^2\right)^2}. \quad (2.13)$$

The α and β constants in the above equations are related to the full width half maxima (FWHM) of the Bragg rod. For the Gaussian term the constant α is given by

$$\alpha = \frac{FWHM}{2\sqrt{\ln 2}}. \quad (2.14)$$

For the Lorentzian terms there are two subtly different β factors given by

$$\beta_{Lorentz} = \frac{4}{FWHM^2}, \quad (2.15)$$

and

$$\beta_{Lorentz^2} = \frac{4(\sqrt{2}-1)}{FWHM^2}. \quad (2.16)$$

Lineshape

The shape of diffraction peaks from monolayers of this type has been analysed by Schildberg and Lauter for scattering from samples in capillary geometry.¹³¹ Section 4.4 covers some subtly different details relevant for the novel geometry used in this work, however the bulk of the analysis is identical to that put forward by Schildberg et al. The key points are reproduced here for clarity.

When considering diffraction from substrates with a range of orientations, it is necessary to consider the distribution of substrate/crystallite orientations. It is useful to define a dummy variable u that varies $0 < u < 1$. u defines how parallel a plane is to the scattering vector where $u = 1$ indicates they are parallel and $u = 0$ indicates they are perpendicular. It is then possible to integrate over all possible orientations (all possible u) to determine the predicted diffractogram from a given sample.

An important quantity in the case of samples with preferred orientation is the probability distribution $P(u)$. Schildberg et al. considered solutions for no preferred orientation, as well as preferred orientation perpendicular to the scattering vector as used in capillary geometry.

Combining the preferred orientation term with the appropriate term (Gaussian, Lorentzian etc.) for the decay of the Bragg rods gives the set of equations below. These describe the intensity variation with Q of a peak at Q_0 .

For the Gaussian shaped Bragg rods, the calculated intensity profile is given by

$$I_{gauss}(Q) \propto \frac{1}{\sqrt{QQ_0}} \int_{u=0}^{u=1} P(u) \frac{\sqrt{u}}{\sqrt{1-u^2}} \exp\left(-\frac{(uQ-Q_0)^2}{\alpha^2}\right) du. \quad (2.17)$$

The equivalent expression for the Lorentzian term is

$$I_{Lorentzian}(Q) \propto \int_{u=0}^{u=1} P(u) \frac{u}{\sqrt{1-u^2}} \frac{1}{\sqrt{B^2-C^2}} \arccos\left(\frac{C}{B}\right) du, \quad (2.18)$$

while that for the squared Lorentzian is

$$I_{Lorentzian^2}(Q) \propto \int_{u=0}^{u=1} P(u) \frac{u}{\sqrt{1-u^2}} \frac{1}{B^2-C^2} \left(\frac{B}{B^2-C^2} \arccos\left(\frac{C}{B}\right) - \frac{C}{B} \right) du. \quad (2.19)$$

In the above equations B is given by

$$B = 1 + \beta (Q_0^2 + Q^2 u^2), \quad (2.20)$$

and C is given by

$$C = -2\beta Q_0 Q u. \quad (2.21)$$

2.2.10 Data fitting

Data processing

As discussed in section 4.2, collected diffraction data has a graphite background subtracted in order to isolate the monolayer diffraction peaks from that of the graphite bulk. However, in addition to Bragg peaks from the graphite there is also significant intensity at low angles due to Porod scattering. This is a form of low-angle scattering caused by the interfaces between particles.¹³² The scattered intensity (I) can be calculated from the surface area of the component particles (S) and the scattering vector (Q) through the equation

$$I = \frac{S}{Q^4}. \quad (2.22)$$

Although S is not easily available, it is possible to fit a term for Porod scattering and subtract it from the data to achieve a flat low-angle baseline. This is helpful in identifying low angle peaks and this correction is applied to all processed data presented in this work.

Theory

Analysis of diffraction data is the subject of many standard texts.¹²⁸ Concepts will only be discussed briefly here, and the reader is directed to a specialised text for a complete understanding of the concepts and techniques outlined.

Initial analysis of diffraction data involves indexing the peaks to identify a unit cell of the crystal. The smallest possible unit cell is termed the primitive unit cell, and contains just one lattice point within it. However, as shall be discussed in section 2.2.10 unit cells with symmetry groups can be easier to populate with atomic positions. Generally the highest symmetry unit cell possible is used for indexing. Indexing is performed by identifying the positions of diffraction peaks, and comparing them to those expected for trial unit cells. It is essentially a trial and error method, involving intuition to identify patterns such as regular patterns in the peak positions. Automated brute force methods have also been developed to aid in this process for larger unit cells.

Once a unit cell has been identified, it must be populated with atomic positions. Information on the distribution of scatterers (electron density for X-rays) is contained within the intensities of the observed diffraction peaks. However, analysis of the diffraction data is complicated by the so called phase problem. This problem occurs because the collected data consists only of the diffracted intensity, ($\propto |\mathbf{F}_{\mathbf{hkl}}|^2$) and not the actual value of the structure factor. This means it is impossible to mathematically invert the structure factor equation to directly obtain the atomic positions, as would be possible if the actual structure factors were measurable.

A variety of methods have been used to overcome this limitation for single crystal X-ray data. These generally consist of obtaining initial estimates for the phase of the diffracted beams, and then refining these estimates to then invert the diffraction data and directly obtain the electron density. This electron density can then be related to a chemical structure.

An example method often used for initial analysis of diffraction data is the Patterson method. This involves calculation of a function called the Patterson function. This is the Fourier transform of the measured intensities, rather than the structure factor. This ignores the phase term but creates a function that still has a relationship to the crystal structure. The Patterson function ($P(u, v, w)$) is calculated by summing over all the indexed peaks the equation

$$P(u, v, w) = \sum_{h,k,l} |\mathbf{F}_{\mathbf{hkl}}|^2 \exp(-2\pi i (hu + kv + lw)). \quad (2.23)$$

Where $\{hkl\}$ are the indices of the peaks, and u, v, w are the indices of the position vector within the unit cell. The Patterson function is thus a scalar field within the unit cell, with a value at each u, v, w point. It can be shown that the Patterson function has the property of having a maximum at the same distance and magnitude from the origin of every interatomic displacement in the atomic structure.

Figure 2.15 visualises the Patterson function for a simple model of atoms in a unit cell. The key property of the function is that the peak maxima have an intensity that is the product

of the atomic numbers of the two atoms related to a particular separation. This makes them ideal for constraining the relative positions of the heaviest atoms in the unit cell, and hence providing a starting point for further trials.

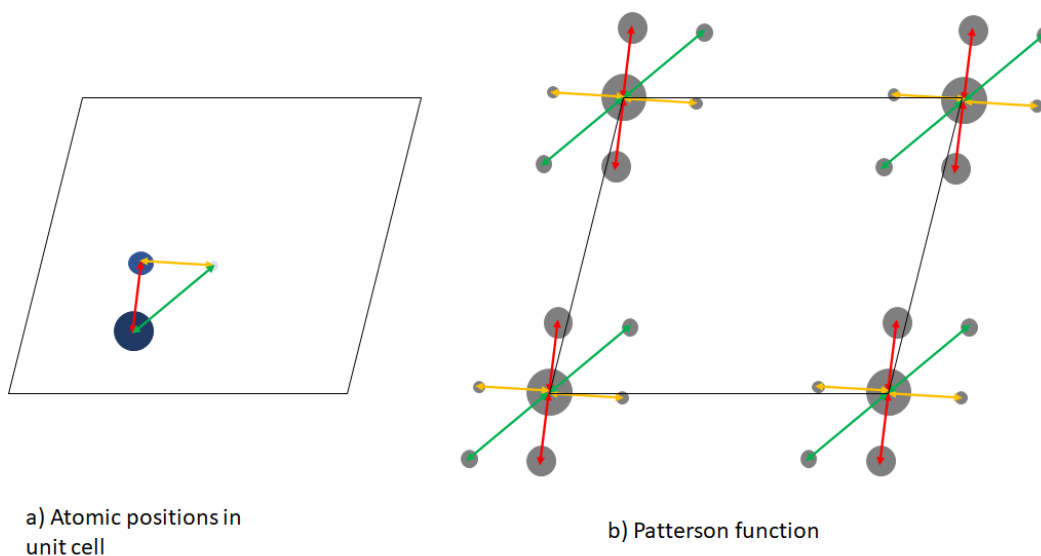


Fig. 2.15 schematic indicating how the Patterson function (b) relates to the interatomic separation in the unit cell (a). Patterson peaks have an intensity equal to the product of the atomic numbers of the two atoms. Thus it is dominated by the atomic separations of the heaviest atoms.

Powder diffraction data compresses the three-dimensional information obtained for diffraction from a single crystal into just one scattering angle. This loss of information means that peaks often overlap, and hence it is challenging to obtain accurate estimates for peak intensities.¹³³ This, combined with the low number of peaks observed in the systems studied here, meant that Patterson functions were not as useful as first hoped in structural analysis.

Rietveld Refinement

The simplest powder diffraction analysis technique is one of simple trial and error. That is, making a trial structure, predicting its diffraction pattern, and comparing that with the observed pattern. The trial structure is then refined to minimise difference between the predicted and experimentally collected diffractogram. This is implemented in a variety of software packages, generally using some variation of a Rietveld refinement method.

Rietveld refinement was first performed in 1969 by Hugo Rietveld.¹³⁴ In this method a theoretical whole diffractogram profile is built for the trial structure, based on theoretical peak positions and intensities, and quantities accounting for experimental factors such as line

broadening. This profile is then compared to the experimentally obtained profile. The various parameters, both structural (unit cell size, atomic positions...) and experimental (experimental line broadening, zero angle offsets...) for the trial structure are then optimised to obtain a best fit for the experimental pattern. Although there are many parameters to optimise, careful use of the Rietveld refinement process has been extremely successful in solid powder diffraction studies, and the technique is extremely well established.^{135,133} However, care must always be taken in validating the results, as due to the number of parameters it is quite possible to overfit the model to an incorrect structure.¹³⁰

Software

Although bulk powder diffraction techniques are well established, and integrated into both commercial and open source analysis packages, all of these software packages are designed for bulk X-ray crystallography and utilise a mixture of Gaussian and Lorentzian lineshapes (convoluted into a Voigt lineshape) to model the lineshape of bulk powder diffraction. None of the software packages were able to be modified to accept the significantly more complex forms of the "sawtooth" lineshapes obtained from monolayer diffraction. For this reason it was not possible to utilise automated structural refinement, instead such optimisation was performed manually, and using chemical intuition on likely structures.

As discussed in section 4.2, the powder diffraction method is only able to capture peaks that do not overlap with the diffractions peaks of the graphite substrate. For this reason, only relatively low angle peaks can be collected. These peaks containing information on the large scale atomic structure of the monolayer, but relatively little on the internal structure of molecules within the layer. For this reason, and to constrain the fitting, it is assumed that the internal molecular structure of the component molecules remains constant, and that they can be treated as rigid bodies. Combined with constraints of symmetry and disallowing atomic overlap, this greatly limits the possible structural solutions to the data.

A package "patternNx" was previously coded in python 2.7 by Dr Chris Richardson, Dr Stuart Clarke and Dr Adam Brewer (BP Institute, University of Cambridge).¹²⁵ This package utilises the standard Schildberg lineshapes discussed in section 2.2.9 however is invaluable for obtaining predicted peak positions and intensities for trial structures. To take account of the slight differences due to the alternate geometry used in flat plate a series of scripts were written in Matlab. These scripts fit peak positions and intensities to the experimental data independently of any structural model. This aids in optimising the unit cell parameters, as well as adjusting for the minor relative intensity differences between the two geometries.

Symmetry

Symmetry is a powerful tool in interpreting diffraction data, both of monolayers and of bulk systems. The details and origins of the effects of symmetry on diffraction are well covered in any standard diffraction text. In two dimensions there are just four crystal families: oblique, rectangular, square, and hexagonal. When combined with symmetry operations these generate 17 two-dimensional plane (or wallpaper) groups. Full details of all of these groups are available from the International Tables for Crystallography.¹²⁹

The key reason these groups are of interest is because they contain symmetry elements (mirror planes or rotation axes) that constrain the positions of molecules. This is especially useful for small unit cells where it is known that only a limited number of a given molecule is present. In this case the symmetry elements of the molecule must line up with that of the cell. For example an aromatic molecule such as 1,3,5-triiodotrifluorobenzene has three 2-fold rotation axes (running through the iodines and fluorines), but only one 3-fold rotation axis. If this is to be tiled using a unit cell with a 2-fold rotation axis, it is necessary that the molecule must be “standing upright” on the surface, with either an iodine or a fluorine pointing directly towards the surface. By contrast if it is to be tiled on a unit cell with a 3 fold rotation axis, it is necessary that it is lying flat on the surface, with the molecular centre coinciding with the centre of the cell.

The correct wallpaper group to use for a given fitting can be identified through the presence of systematic absences in the experimental diffraction pattern. These are families of Bragg peaks (e.g. 00l where l is odd) that are absent in diffraction patterns from a particular wallpaper group. The origin of these absences comes from detailed diffraction theory, but the relevant absences are tabulated with each group in the International Tables for Crystallography.

Fitting Strategy

The fitting strategy used in this work has been validated for many different monolayers systems of varying degree of structural complexity.^{78, 82, 83, 84, 86, 112, 113, 114, 136, 137, 138, 139, 140, 141} Due to the low number of available peaks, and novel lineshapes of monolayer systems it is found that conventional powder diffraction analysis such as Rietveld refinement cannot be applied. Instead structural models are refined manually.

The fitting begins with indexing of peaks through identification of peak positions and matching these with the expected peak positions for possible unit cells. Any “missing peaks” from a unit cell can either be due to symmetry, or simply a lack of scatterers at appropriate

points in the cell. However any peaks present not predicted by the unit cell cannot be due to that trial structure.

Once a trial unit cell is obtained the peak intensities must then be matched. Matching is done by comparing the predicted pattern from a placement of molecular rigid bodies within the identified unit cell. A great deal of chemical intuition is required to identify sensible structures, with structures that maximise adsorbate-substrate interactions (e.g. being flat-lying) and adsorbate-adsorbate interactions (e.g. halogen bond donors and acceptors adjacent) being obvious starting points.

In addition to the intensities, the peakshape parameters (chiefly the coherence length, L) and Bragg rod shape (Gaussian, Lorentzian etc.) are also optimised to best fit the experimental data. These factors do not vary the peak shapes or intensities and so can be varied almost independently of unit cell size and atomic positions.

The fitting process is labour intensive, and the limitations of manual optimisation mean that it is not an exhaustive search of the possible solution space. For this reason it is preferable to have alternative techniques available to build confidence in the accuracy of the solution. Collaborators have performed DFT simulations to aid in structural validation, and relevant DFT work is presented in relevant chapters.

2.2.11 Neutron diffraction

Although the majority of the diffraction experiments in this work consider diffraction of X-ray photons, several experiments in chapter 7 consider scattering of neutrons.

Neutron scattering is a complementary techniques to X-ray scattering with much of the physics being superficially similar. However the nature of the interaction between neutrons and atoms, and photons and atoms differ, meaning there are some key differences that must be taken into account.

Theory of neutron scattering

One key difference is that neutrons are scattered through interactions with the nucleus, rather than charged electrons like X-rays. Because of this, the scattering strength of a given nucleus depends on detailed interactions that go beyond the work considered here. The scattering strengths are observed vary wildly between atoms and isotopes, with no simple trend analogous to that of “increased electron density equates to increased scattering” as is the case for X-rays. It is also notable that, unlike X-ray scattering factors which are nearly angle independent, neutron scattering factors decrease with increased scattering vector \mathbf{Q} . Although this adds additional complexity, detailed tabulations of the scattering strengths

of different nuclei (both different elements, and even different isotopes) and how they vary with Q are available.¹²⁹ Upon application of the appropriate atomic scattering factors, the analysis and interpretation of X-ray and neutron data is analogous, with similar issues due to the phase rule and fitting procedures using a structural model.

The utility of neutron scattering is that, because of the different atomic scattering factors, it is possible to change the relative peak intensities due to scattering from different centres. Combining the results of X-ray and neutron scattering thus provides additional information that can aid in fitting, by eliminating structural solutions that appear similar. Neutron experiments are also useful because, while hydrogen atoms interact only weakly with X-rays. Hydrogen nuclei are extremely significant neutron scatterers. ^1H nuclei are problematic due to their large incoherent scattering component, however ^2D nuclei exhibit a large coherent scattering cross-section and so give strong diffraction signal. Hence, to avoid a large incoherent background in the diffractogram generally only deuterated molecules are utilised for neutron scattering experiments.

Neutron sources

The neutron experiments reported in chapter 7 were performed on beamline D20 at the Institut Laue-Langevin. This is a nuclear reactor neutron source with one of the strongest neutron fluxes available anywhere in the world. The layout and availability of the equipment is similar to that of I11 synchrotron considered earlier, although because of the relatively weak interaction of neutrons with matter the samples are significantly bigger (2cm in diameter). These are held in aluminium sample holders in a geometry otherwise analogous to the glass capillaries utilised for the synchrotron experiments.

Chapter 3

STM data

3.1 Introduction

The Low-Temperature Scanning Tunnelling Microscope (LT-STM) apparatus described in chapter 2 is potentially extremely powerful. It can image surfaces to atomic scale precision at temperatures from liquid helium to ambient. However, it had been out of operation for several years by the time the research in this project began, and institutional knowledge of how to use the equipment was sparse. As such the focus of the early stage of my PhD was gaining familiarity with this equipment. Initial testing was performed on a Au{111} single crystal, as this is an extremely well characterised surface. It exhibits a characteristic "herringbone" reconstruction that is frequently lifted upon addition of adsorbates.¹⁴² Figure 3.1 presents STM images showing the reconstructed gold surface. The "zig-zag" patterns are characteristic of the herringbone reconstruction.

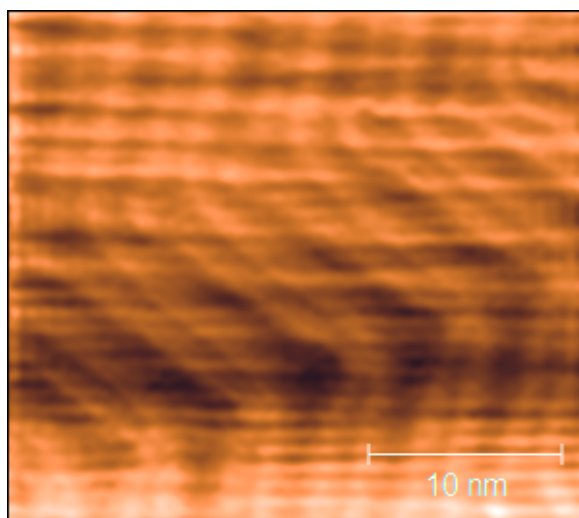


Fig. 3.1 Herringbone reconstruction of the Au $\{111\}$ surface. ($V_{\text{bias}} = -0.5$ V, $I_{\text{set}} = 0.2$ nA)

As this surface is well known it is able to be used for calibration of the STM tip. The bulk lattice parameter of gold is 4.08 Å. As bulk gold has a face-centered-cubic unit cell, the step change between adjacent layers is $\frac{a_0}{2}$ which is equal to 2.04 Å. The surface unit mesh consists of a hexagonal lattice with unit vector $a_1 = \frac{a_0}{\sqrt{2}}$ or 2.88 Å. The herringbone reconstruction then consists of a rectangular lattice with parameters $22a_1$ and $\sqrt{3}a_1$ or 63.50 Å and 5.00 Å respectively.¹⁴³ These distances can be used to provide a known benchmark to calibrate measured distances in the STM. This is necessary after each tip exchange, as the relationship between applied potential and displacement of the piezoelectric crystals used for tip control will be weakly affected by the weight of the tip.

3.2 PTCDI

Once some degree of familiarity with the equipment was achieved, an appropriate test monolayer to study had to be chosen. The goal was to deposit a well-known monolayer structure to confirm the equipment and experimental procedures were working effectively. As seen in the literature review, perylenetetracarboxylic diimide (PTCDI) (Figure 3.2) has been well studied under similar deposition conditions and the monolayers it forms are known to be robust. Hence it was chosen for this initial study.

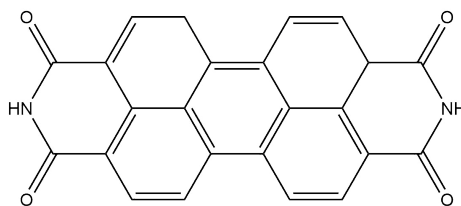


Fig. 3.2 Chemical structure of the PTCDI molecule

3.2.1 Experimental

PTCDI was purchased from TCI chemicals, (>95 % purity), and used without further purification. It was loaded into a capillary and placed in the doser setup described in section 2.1.6. The entire doser assembly was then baked for 4 hours at 150 °C using both heating tape and resistive sample heating through the tantalum coil. After being left overnight to cool, the pressure stabilised at around 3×10^{-8} mbar, the lowest achievable pressure in this setup. The PTCDI was observed to change colour from red to dark purple, possibly an indication of dehydration.

Upon opening the gate valve to the main chamber, a small increase in pressure to 2×10^{-8} mbar was recorded in the main chamber, alongside large peaks from water (18 amu), N_2/CO (28 amu) and CO_2 (44 amu) in the mass-spec residual gas analyser. These peaks grew upon heating of the PTCDI, until at 490K it was observed to visibly sublime. At this point an extra peak at 64 amu appeared in the RGA signal, likely a fragment peak of PTCDI (390 amu). This sublimation temperature is lower than that which has been reported (608 K). This variance could be due to different pressure/impurity conditions to the previously reported work, or due to insufficient thermal contact between the thermocouple and the sample due to the thick capillary. Visual inspection of the sample indicated a large excess of adsorbate had been deposited. To remove some of this excess, as well as any small molecule contaminants from the raised background pressure, the sample was gently annealed to 373 K before being transferred to the STM chamber, and left for one hour to allow thermal equilibrium to be established.

3.2.2 Initial images

Initial images followed the previous studies in using a comparatively low tunnelling current of 0.3 pA and a large applied potential of -1.8 V. These conditions lead to a comparatively large tip-sample separation and so minimise the risk of destruction of the monolayer by the tip. However, this comes at the cost of reduced precision of measurements.

The initially observed images are shown in Figure 3.3. Under these conditions the image resolution is relatively poor, however it can be seen that there is a complete tiling of the surface. There also appears to be a partially formed layer on top of this underlying base layer. No area of bare substrate is visible so it is not possible to measure the thickness of the base layer and determine if it is monolayer or multilayer. The underlying base layer appears to be arranged similarly to the canted phase observed by Mura,¹⁰⁸ this alignment implies a strong interaction between the base layer and the surface, implying the observed layer is likely a monolayer.

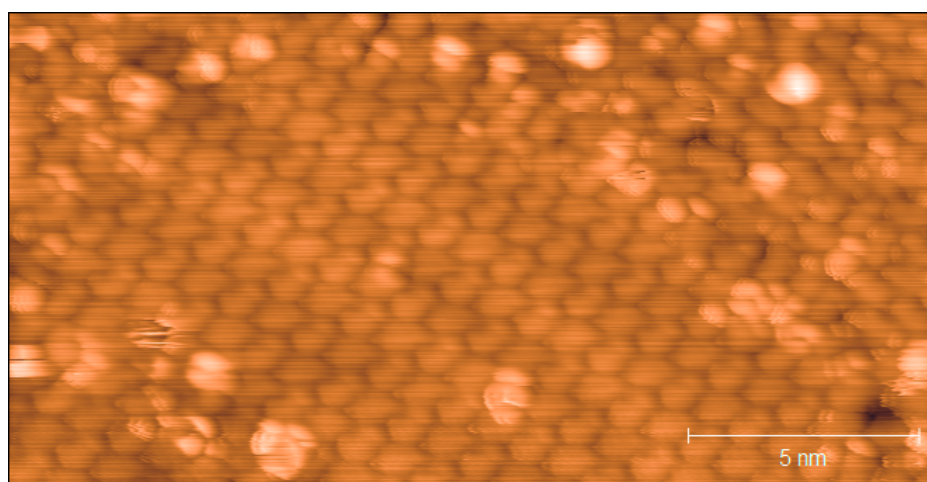


Fig. 3.3 Initial STM image of PTCDI on Au{111}. A regular tiling pattern can be seen. ($V_{\text{bias}} = -1.8$ V, $I_{\text{set}} = 0.3$ nA)

In order to remove the unwanted excess molecules, the tunnelling current was raised to 2.0 nA, and bias voltage lowered to +1.2 V. This has the effect of moving the tip nearer to the surface, allowing it to scrape off any weakly bound adsorbates.

From Figure 3.4 this approach does indeed produce a clearer image, where the structure of the overlayer can be clearly equated to the canted structure suggested by Mura. At no point was any non-canted phase imaged during study of the surface, likely due to the annealing step equilibrating the monolayer. The images obtained under these conditions are of comparable quality to those seen by Mura, with no internal molecular structure visible. The top of the image shows a disordered region that forms the boundary between two different grains of the canted phase.

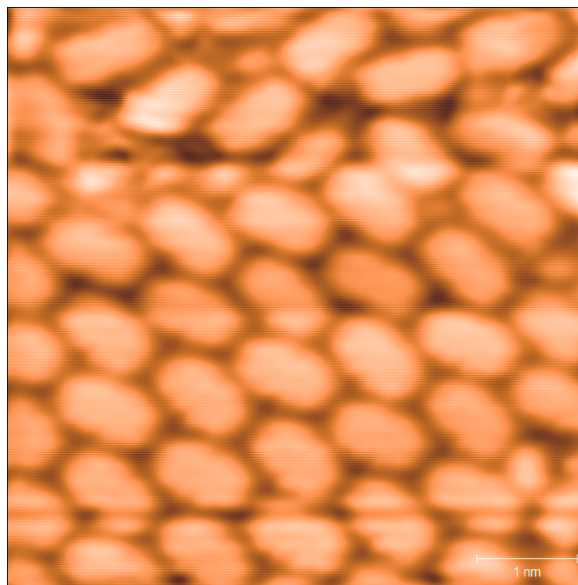


Fig. 3.4 STM image of the PTCDI base layer. Individual molecules can be identified, but with no submolecular resolution. ($V_{\text{bias}} = -1.2 \text{ V}$, $I_{\text{set}} = 2.0 \text{ nA}$)

It is possible to compare these results with those obtained by Mura et al. They characterised the canted phase as consisting of parallel rows of molecules along the Au $[11\bar{2}]$ direction. The molecules in one set of rows were measured to be canted (rotated about the z axis) at approximately 12° relative to the row direction, while the other set could not be reliably measured. DFT work suggested the most stable tilt angle was 10.4° for an isolated row, and 11.5° for a set of rows. Using Figure 3.5a, it is possible to more precisely measure the angle of tilt of the molecules relative to the rows. In confirmation with Mura it was found that one set of alternate rows had molecules tilted at approximately 12° relative to the row direction. The other set however were measured to be tilted at a somewhat lower angle of about 10° . This is closer to the DFT calculated tilt of an isolated row, but lower than the 11.5° tilt calculated for rows with parallel neighbours.

3.2.3 High Resolution Images

Adjustment of tunnelling conditions allowed better resolution images to be obtained. Figure 3.5a shows the image produced when a high bias voltage (in this case -3 V)¹ and an extremely high tunnelling current (12 nA) were used. Under these conditions the tunnelling current (I) channel exhibited very good quality images, as shown in figure 3.5. Each molecule

¹It is worth restating that, in keeping with convention, all bias voltages are reported as sample biased, despite the fact that the instrument is tip biased. A reported bias of -3 V thus corresponds to a grounded sample and a tip of $+3 \text{ V}$ relative to ground. Tunnelling is thus occurring from the sample to the tip.

can be seen to have two planes of symmetry, similar to the PTCDI molecular structure. There are 4 lobes on each side of the molecule, with the atomic structure not discernible. Figure 3.5b shows a simple calculation of the structure of the PTCDI HOMO. Although there are differences between these images, there are also some similarities, such as the 4 lobes on each side of the molecule.

The structure of the STM image does not exactly correlate with the HOMO because tunnelling from other orbitals will also be significant. As well as this the interaction with the gold surface will modify the form of the molecular orbitals. A full theoretical treatment of the tunnelling would be possible using the Tersoff-Hamann approach,¹¹⁷ but this has not been performed. Nevertheless, the form of Figure 3.5a is of the type that would be expected for high resolution STM images, with imaging revealing the internal electronic structure of the molecule.

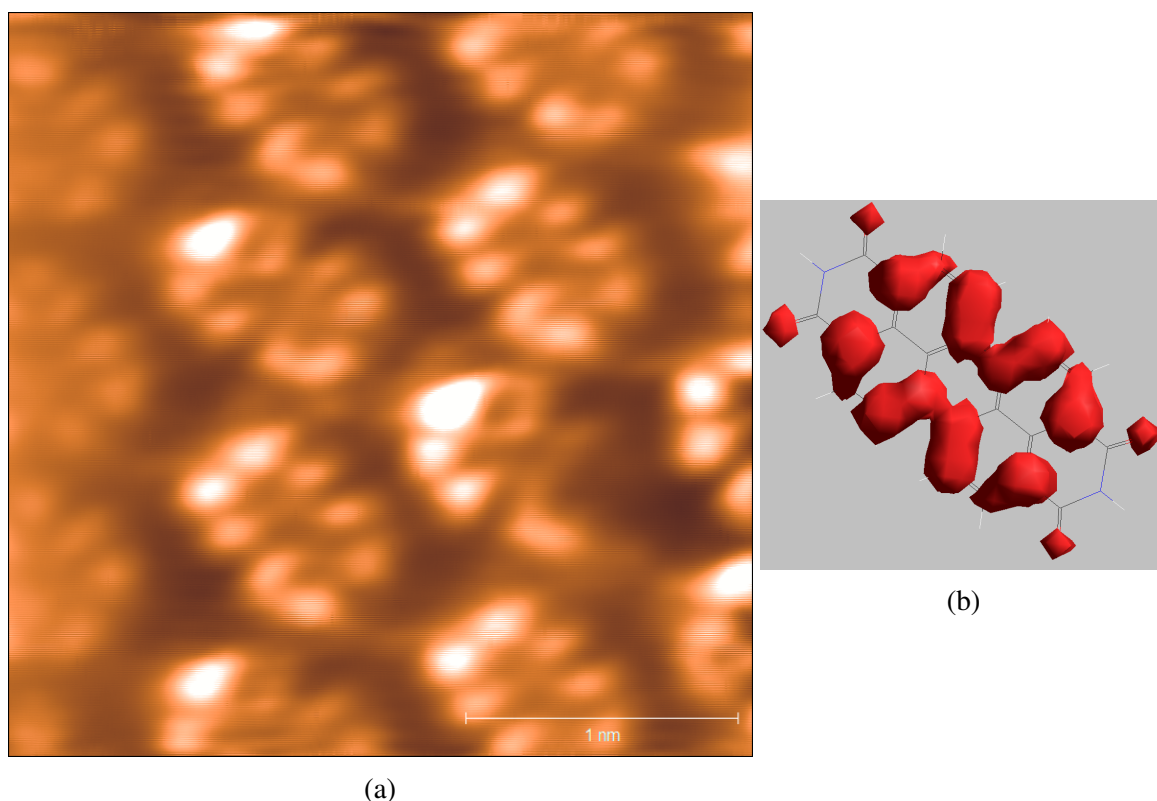


Fig. 3.5 (a) STM image showing orbital resolution of the PTCDI monolayer. ($V_{\text{bias}} = -3$ V, $I_{\text{set}} = 12.0$ nA) (b) Ψ^2 of the PTCDI HOMO calculated using the semi-empirical PM3 basis set on hyperchem

When different tunnelling conditions were tested, they delivered an extremely unexpected result. While still observing the current channel, images appeared to map out the geometric connectivity of the molecule. Figure 3.6a was the result of optimisation of these conditions;

the tip feedback mechanism was reduced to minimum setting give a pseudo-constant height image, while the tunnelling parameters were set to $V_{\text{bias}} = 900$ mV, $I_{\text{set}} = 7.0$ nA. This image does not correlate with any frontier orbitals of the molecule, appearing instead to map out the σ framework. This is an extremely unusual result for STM.¹⁴⁴

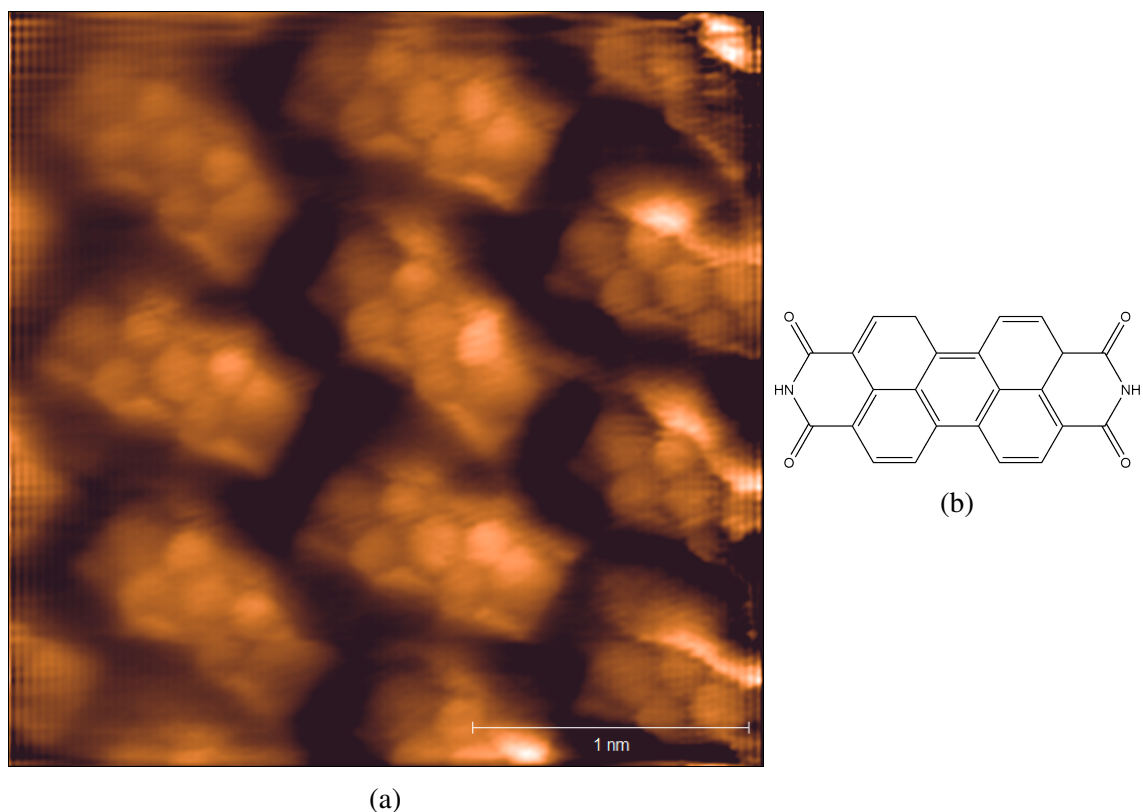


Fig. 3.6 (a) STM image showing geometric resolution of the PTCDI monolayer ($V_{\text{bias}} = 900$ mV, $I_{\text{set}} = 7.0$ nA). Compared with (b) the atomic structure of PTCDI. Limited thermal drift has occurred between this and the previous image.

If the contrast of these images is suitably adjusted it is also possible to discern faint features, in at least some locations one would identify hydrogen bonds as occurring. However, as figure 3.7 shows, not all expected hydrogen bonds coincide with these lines.

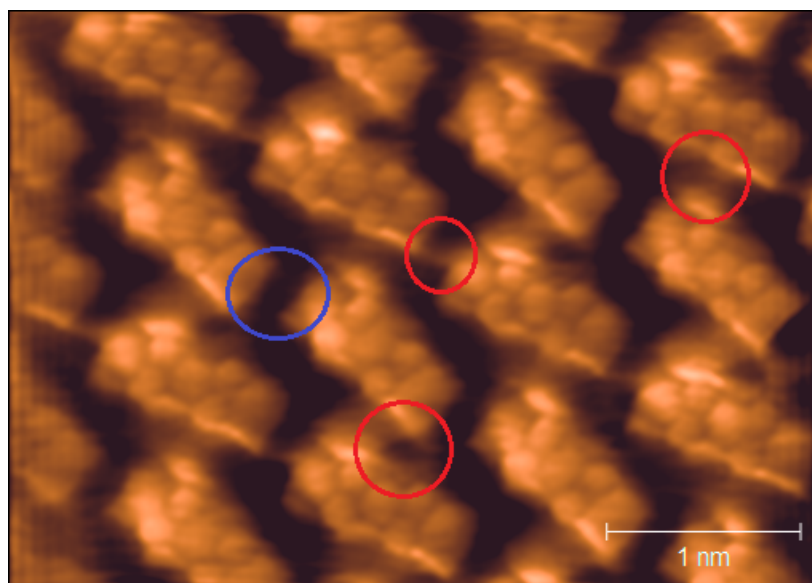


Fig. 3.7 STM image of PTCDI with adjusted contrast to highlight intermolecular "features". Areas where "features" coincide with expected hydrogen bonds are circled in red. Circled in blue is an area expected to show hydrogen bonds, but with no feature visible. $V_{\text{bias}} = 600\text{mV}$, $I_{\text{set}} = 2.4\text{ nA}$

3.2.4 Discussion

The STM images presented in the previous section appear similar to high-quality atomic force microscopy (AFM) measurements of organic monolayers, as AFM maps out atom positions rather than electron density, and has also been shown to image "features" that correlate with intermolecular interactions.¹⁴⁵ However, since these images were taken under pseudo-constant height conditions, it would be thought the images must be due to purely electronic effects.

The most similar images to these in the STM literature are those captured at ultra-low temperatures, and with tips functionalised using a gas molecule. This phenomenon was first shown by Temirov et al.¹⁴⁶ in a study of perylenetetracarboxylic dianhydride (PTCDA). This is a very similar molecule to PTCDI, differing only in the replacement of the two terminal imide groups with anhydride. Temirov et al. used temperatures of 20 K, along with a tip pre-dosed with H_2 to obtain images showing atomic resolution. Figure 3.8 shows a selection of images obtained using this method under varied tunnelling conditions.

Further refinement to this technique found that Xe and CO could also act as good "probe" molecules to functionalise the tip. The best quality images even seemed to highlight intermolecular bonds, for example in Figure 3.9a.

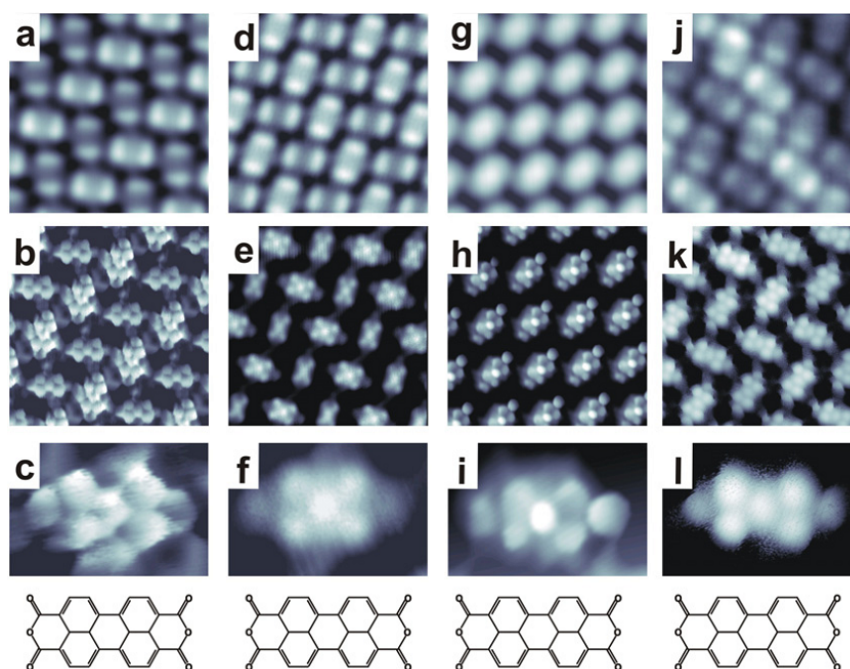


Fig. 3.8 STM images taken with a H_2 dosed tip of PTCDA (the acid anhydride analogue of PTCDI) on a variety of silver and gold surfaces. The top two rows are 5×5 nm, while the bottom row is 1×1.5 nm. V_{bias} varies from -0.01 to -0.3 V while I_{set} varies from 0.03 to 2.1 nA. See reference 146 for full details.

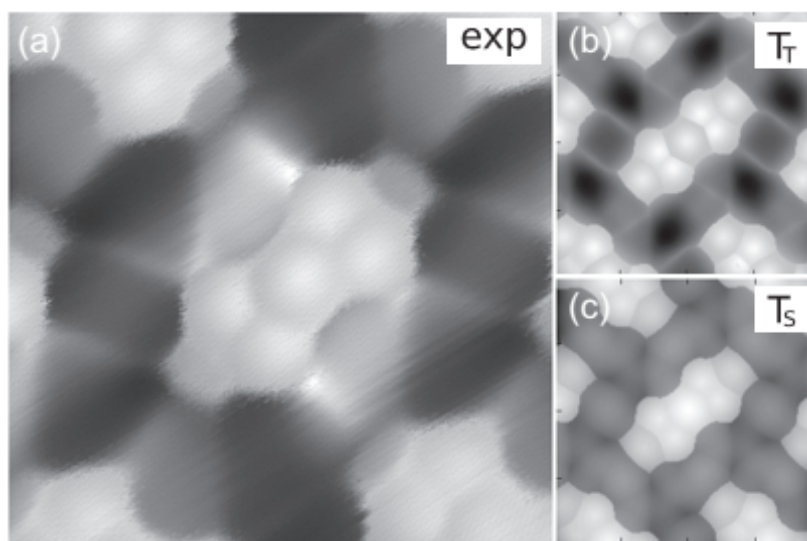


Fig. 3.9 (a) STM image of PTCDA taken at 5 K using a Xe functionalised tip. $V_{\text{bias}} = -0.004$ V, $I_{\text{set}} = 0.1$ nA. (b) Simulated images considering only the tip-probe tunnelling current T_T (c) Simulated images considering only the probe-surface tunnelling current T_S . Image From reference 147

Previous work attempted to explain these images by modelling a three component tip-probe-surface system. This enables consideration of contributions to the tunnelling current from both tunnelling between the tip and "probe" (T_T) and tunnelling between the "probe" and the surface (T_S). The work suggested the sub-molecular resolution could be explained by the extremely small tip-sample separations meaning that the probe molecule, at the surface of the tip, was affected by Pauli repulsion. Over atoms and σ bonds the probe is pushed away from the surface, due to the high total electron density. This then moves the probe closer to the tip, raising the T_T and lowering the T_S components of the tunnelling current. For the intermolecular features it was considered that a short separation between atoms (which generally coincides with where hydrogen bonds would be expected to be) would repel similarly to an atom/covalent bond, with similar effects on the T_S and T_T tunnelling currents. It was then thought that different probes would show different weightings between T_S and T_T allowing either sub-molecular or intermolecular features to dominate.

No previous images showed both good sub-molecular and intermolecular resolution in one image, thus it is difficult to reconcile the collected images with the T_S, T_T theory. An alternate theory contended that sub-molecular resolution was due to the probe being pushed closer to the tip and Pauli repulsion lowering the local density of states at the tip.¹⁴⁸ This theory did not attempt to explain any intermolecular features however, and any theory will struggle to explain why areas with a large degree of Pauli repulsion can show either lowered (atoms and σ bonds) or raised (intermolecular contacts) tunnelling currents.

It is also notable that all previous images were taken at lower bias voltages, and much lower temperatures, than were utilised here. The tip used in this work was also not intentionally dosed with a "probe" molecule, however it is commonly known that even in UHV conditions it is possible for molecules to adsorb on the STM tip, and these will often prefer to bind to the apex of the tip due to this atom's low co-ordination number. Thus, the presence of a probe cannot be discounted.

3.2.5 Summary

In this section we have present a number of STM images of the bare gold substrate and of a well-studied organic molecule adsorbed on the surface. In both these respects we are able to both repeat observations in previous literature, as well as provide obtain high quality images through an unknown mechanism. However, the most significant conclusion we draw here is that we have successfully reinitialised the experimental LT-STM facility and obtained data that gives us some confidence that we have appropriate working methods to address these very challenging 2D adsorbed layer systems. This facility is now suitable to investigate other systems which have not been presented in the literature.

We will now present a number of STM systems investigated, some have been previously studied in the literature, however, significant further work was required, and other previously uninvestigated systems

3.3 Trimesic acid on gold

This section presents an STM study of trimesic acid (TMA) on gold. This is complementary to the diffraction study presented in section 7.2.

3.3.1 Experimental

In keeping with previous dosing conditions used for deposition onto graphite, TMA was sublimed from a capillary at 573 K.⁹³ As in the previous section, a clean Au{111} single crystal held at room temperature was the substrate. Similarly to PTCDI, despite 24 hours degassing at 120 °C large amounts of water and CO₂ were detected on the RGA during deposition, indicating degassing was not quite complete. No significant fragment peaks of TMA (210 amu) were detected in the RGA, indicating either that the amount sublimed was minute compared to the volatile molecules observed, or that the sublimed TMA was immediately and strongly bound to the prepared surface and very few TMA molecules reached the RGA which is offset from line-of-sight of the capillary.

The crystal was annealed post deposition at 330 K before being imaged, in order to reduce the presence of the aforementioned volatile impurities on the surface.

3.3.2 Results

Figure 3.10 presents an initial image of what was observed. A number of terraces of Au {111} are visible, and on large terraces there are irregular islands of an ordered layer. The areas around the islands consist of bare gold, with the herringbone reconstruction faintly visible.

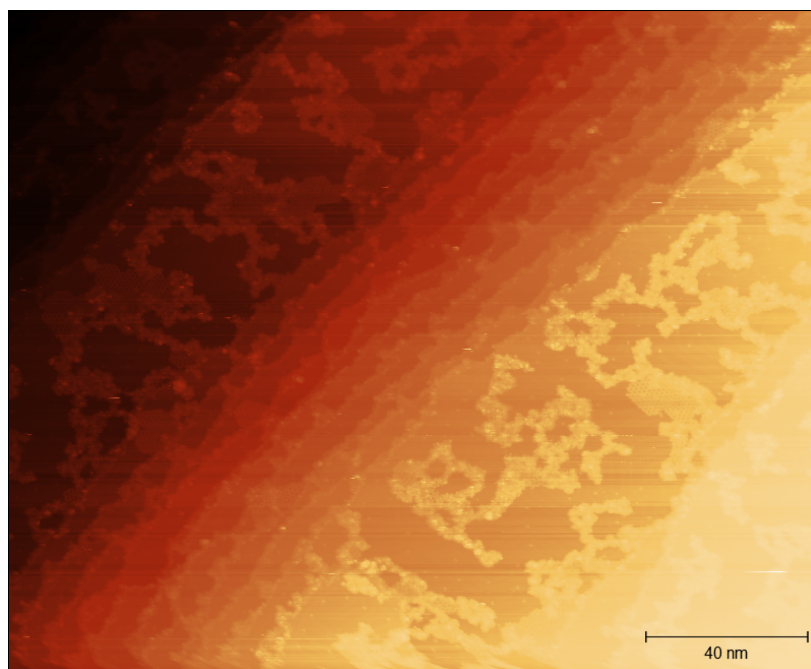


Fig. 3.10 STM image of trimesic acid deposited on Au {111}. Taken at 77 K, $V_{\text{bias}} = 3$ V, $I_{\text{set}} = 0.1$ nA.

Figure 3.16 presents a high resolution image of the ordered layer. Examination of the periodicity of the layer allows this layer to be identified with the "chickenwire" structure previously reported. No other ordered structures could be observed. Previous research has reported coexistence of flower with chickenwire. The observation of just the chickenwire phase could be due to the low coverage, as the flower phase is significantly more dense (area per molecule $\approx 100^2$ for the flower phase compared to $\approx 120^2$ for chickenwire). This means the flower phase will be more favoured at higher coverages when denser packing is favourable. Alternatively the annealing step used in preparation of this sample may have caused the less thermodynamically stable "flower" phase to reform into the thermodynamically more stable chickenwire phase.

Attempts to repeat the same conditions as described in the previous section to achieve "atomic resolution" were unsuccessful, implying that the imaging conditions used for PTCDI are not generally applicable.

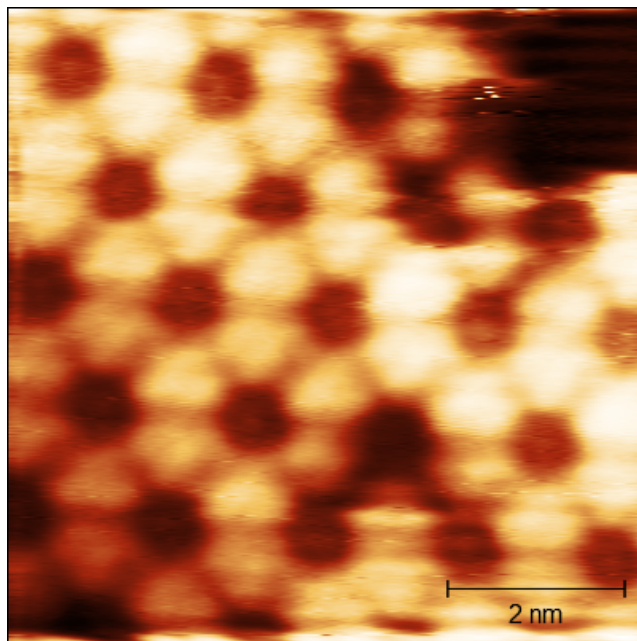


Fig. 3.11 High resolution STM image of the ordered structure observed after trimesic acid was deposited on Au {111}. Taken at 77 K, $V_{\text{bias}} = 5$ V, $I_{\text{set}} = 0.05$ nA.

3.3.3 Summary

In this section another previously reported monolayer structure has been successfully reproduced, further supporting confidence in the integrity of the equipment and experimental procedure. Due to the prodigious body of literature already existing, no further STM study of trimesic acid was considered necessary.

3.4 Halogen Bonded layers

Having successfully imaged two previously studied hydrogen bonding systems, the next step was to investigate the behaviour of novel, halogen bonding, systems. 1,4-diiodotetrafluorobenzene (TF1) is frequently studied as a halogen bond donor, and its co-crystal with 4,4'-bipyridine on graphite previously reported via X-ray diffraction.¹¹² The chemical structures of these molecules is presented in figure 3.12. A related molecule, 1,3,5-triiodotrifluorobenzene is also of interest due to its potential for forming more complex, porous, layers.

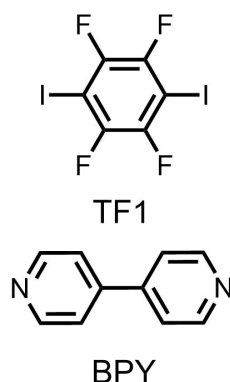


Fig. 3.12 Chemical structure of 1,4-diiodotetrafluorobenzene (TF1) and 4,4'-bipyridine (BPY)

3.4.1 Experimental

4,4'-Bipyridine (Alfa Aesar, 97%), 1,4-diiodotetrafluorobenzene (Sigma Aldrich, 90%), and 1,3,5-triiodotrifluorobenzene (Acros Organics, 97%) were obtained commercially and used without further purification. These molecules were dosed using the sublimation system reported previously, with deposition temperatures of 100 °C utilised for both BPY and 1,4-diiodotetrafluorobenzene, while a temperature of 60 °C was sufficient for 1,3,5-triiodotrifluorobenzene. These initial experiments utilised the same Au{111} single crystal surface utilised above as the substrate.

3.4.2 4,4'-Bipyridine

Literature

Assembly of 4,4'-Bipyridine (BPY) into a crystalline lattice on graphite has been previously characterised through diffraction experiments.¹³⁷ In these instances the BPY was seen to lie flat on the surface, forming a monolayer with regular unit cell $a = 11.26 \text{ \AA}$, $b = 11.45 \text{ \AA}$, and $\gamma = 90.0^\circ$.

Meanwhile assembly of BPY on gold {111} surfaces under aqueous perchlorate solution has been by two authors using electrochemical STM¹⁴⁹ and a combination of electrochemical STM and AFM.¹⁵⁰

Cunha et al. found several different monolayer structures dependent on electrochemical potential of the electrolyte solution, however the structure at ground potential was indexed to an overlayer lattice, $a = 12.55 \text{ \AA}$, $b = 13.20 \text{ \AA}$ and $\gamma = 72.5^\circ$. Within this mesh the BPY molecules were modelled as upright with a nitrogen molecule facing the gold surface.¹⁵⁰

Mayer et al. similarly reported several different structures dependent on electrochemical potential, with the structure at ground potential also identified as consisting of upright BPY molecules, but with a subtly different lattice parameters $a = 11.5 \text{ \AA}$, $b = 13.2 \text{ \AA}$, $\gamma = 71^\circ$.¹⁴⁹

Results

Figure 3.13 presents a typical STM image obtained after BPY was deposited onto the Au {111} crystal. A suggested unit mesh and structural assignment is overlain on the image. The tentatively assigned unit mesh is a centered mesh with cm symmetry. Mesh parameters are $a = 13.9 \text{ \AA}$, $b = 6.5 \text{ \AA}$, and $\gamma = 88^\circ$. The topography of the image is extremely flat, with the difference in height between the dark and light regions being only approximately 30 pm. As discussed in section 2.1.2, care must be taken in interpreting this number, however it strongly supports a flat-lying BPY structure, unlike the upright structures observed in solution by Cunha and Mayer.

If it is assumed that the BPY molecules are flat lying, the logical structural interpretation of figure 3.13 is of a series of offset chains. Each chain consists of a unit approximately 12 \AA in length, with these units appearing to consist of two roughly circular “caps” of 2 \AA in length, and an elongated unit of approximately 7 \AA in length. The initial interpretation of these observations is of a BPY molecule, lying flat on the surface, with two gold adatoms coordinated to each of the BPY molecule’s nitrogens.

As this was a preliminary study in molecular imaging, designed purely to confirm the presence of BPY prior to deposition of halogen bond donors onto the surface, no complementary techniques were conducted to test this interpretation. However, it is clear that the structure is unlike that which has been observed in solution phase.

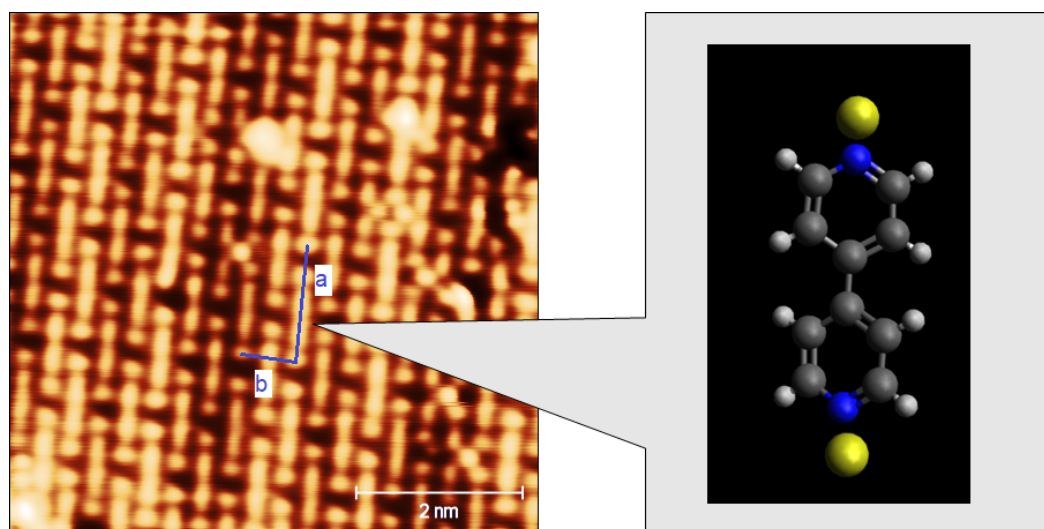


Fig. 3.13 STM image of 4,4'-Bipyridine deposited on Au {111}. Taken at 77 K, $V_{\text{bias}} = 1$ V, $I_{\text{set}} = 1$ nA. The centered unit mesh has parameters are $a = 13.9$ Å, $b = 6.5$ Å, and $\gamma = 88^\circ$. The structural interpretation of the image is of offset chains of BPY coordinated to two gold atoms.

1,4-diiodotetrafluorobenzene

Deposition of aromatic molecules containing both iodine and gold has not previously been reported. Deposition of TF1 was attempted, however no clear structural signal was identified. In some images a consistent pattern could be identified. An example of these is shown in figure 3.14. The structure is amorphous with irregularly shaped indents with an apparent depth of 0.15-0.2nm. However, the signal is extremely noisy and variable, making it difficult to draw solid conclusions from these images. Multiple attempts at depositing TF1 with different dosing/annealing procedures were attempted, as well as deposition of TF1 onto a gold surface precoated with BPY. However, none of the experiments yielded non-amorphous images.

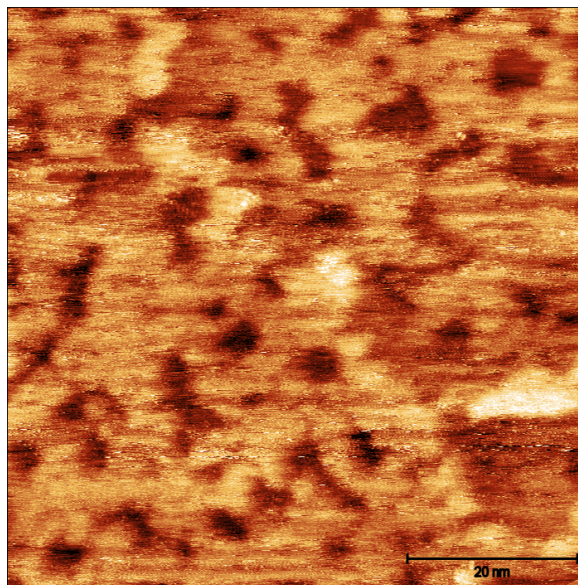


Fig. 3.14 STM image of 1,4-diiodotetrafluorobenzene deposited on Au {111} post annealing to 340 K. Image collected at 77 K, $V_{\text{bias}} = -0.3$ V, $I_{\text{set}} = 0.6$ nA.

The nature of the STM images indicates that no crystalline monolayer structure was formed upon TF1 deposition onto gold. Ullmann coupling, where a surface adatom atom inserts into the C-I bond, followed by coupling of adjacent molecules through C-C bond formation, has been observed in similar non-fluorinated molecules. This was originally thought to chiefly occur with more reactive metals than gold, and at elevated temperature, but more recent work has shown it to occur on gold {111} at room temperature.¹⁵¹ These initial experiments are not sufficient to confirm the occurrence of a reaction of this type, however it provides a plausible mechanism for the generation of amorphous material from the deposited TF1 molecule.

1,3,5-Triiodo-2,4,6-trifluorobenzene

1,3,5-Triiodo-2,4,6-trifluorobenzene (TITFB) is a putative halogen bond donor that will be further explored in chapter 5. The structure of the molecule is presented in figure 5.3b

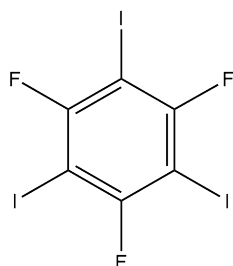


Fig. 3.15 Chemical structure of 1,3,5-Triiodo-2,4,6-trifluorobenzene (TITFB)

Deposition of TITFB onto the gold surface generally gave similar poor quality images as for TF1 above, likely for similar reasons. However, in one run of experiments a low coverage of TITFB was deposited, followed by a post deposition annealing step to 373 K. After this stage images of the surfaces found evidence of assembly on the edges of the gold {111} terraces. Figure 3.16 illustrates the observed assembly.

The features are 1 Å in height with a size of approximately 4.0 Å by 7.1 Å. The height of 1 Å is of the order of size that may be expected for TITFB lying flat on the surface, while 7.1 Å is similar to the I...I bond length in the crystal structure.

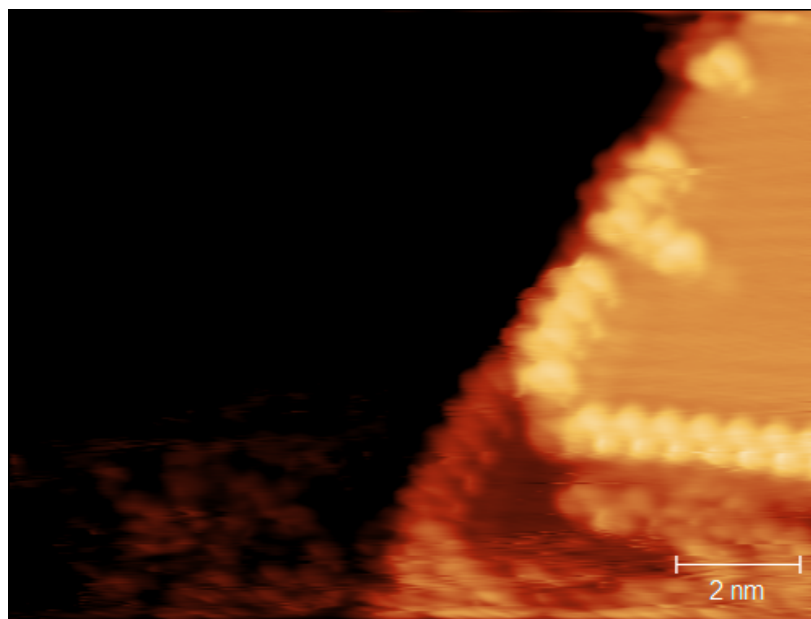


Fig. 3.16 STM image of 1,3,5-triiodo-2,4,6-trifluorobenzene deposited on Au {111}. Taken at 77 K, $V_{\text{bias}} = -0.8$ V, $I_{\text{set}} = 0.04$ nA.

Conclusion

Initial STM experiments with BPY were able to identify the formation of a crystalline monolayer with a structure different to that which has been identified under solution. However, initial experiments depositing halogen bond donors onto the gold surface yielded chiefly amorphous or impossible-to-image samples, aside from a single low coverage TITFB sample. The few samples attempted co-deposition of BPY with TF1 or TITFB were all unsuccessful in obtaining images of any sort. Given the previously discussed likelihood of Ullmann coupling or other interaction of the surface metal atoms with the halogen-bond donors, it was decided to change substrate from the metallic Au{111} surface, to an HOPG graphite surface. This would also have the benefit of improving the transferability of the structural conclusions from the STM data to the diffraction data and vice versa.

3.5 Graphite

Graphite and monolayer assemblies on graphite have been commonly studied via STM. However, the instrument used in this work had not previously been used to image graphite. Initial experiments focused on imaging a clean graphite surface. This was aimed to be a prelude to further investigations of adsorbed molecules on graphite. However, the poor quality of the recovered images, and constraints due to the Covid-19 pandemic led to this subsequent phase of work not being completed.

3.5.1 Experimental

Commercially available HOPG crystals were obtained from Merck. These were of ZYB grade, with a mosaic angle of $0.8 \pm 0.2^\circ$. This is of sufficient grade to be generally recommended for STM imaging. The samples were freshly cleaved in air and then quickly transferred into the vacuum system. Once in the chamber they were heated to 900 K to be outgassed before imaging.

3.5.2 Results

Imaging quality of the bare HOPG surface was extremely poor, despite using the sample conditions recommended by the system operation manual prepared by the instrument manufacturer Omicron ($V_{\text{bias}} = 0.5 \text{ V}$, $I_{\text{set}} = 500 \text{ nA}$). Alternative tunnelling conditions were attempted, however image quality remained poor. A typically recovered image is shown in figure 3.17

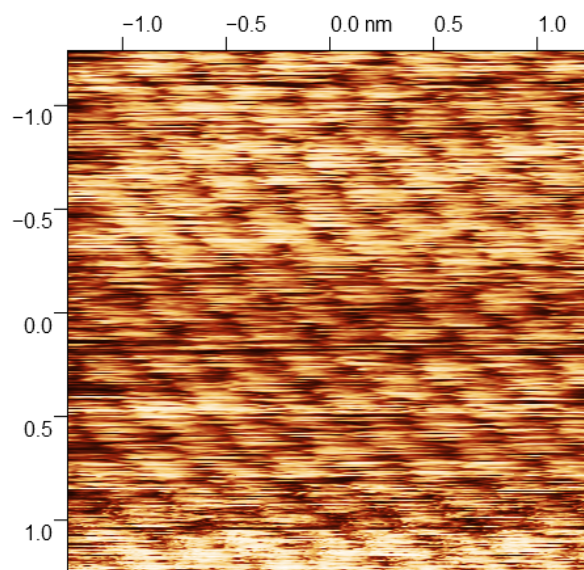


Fig. 3.17 STM image of bare HOPG surface taken at 77 K. $V_{\text{bias}} = 0.5$ V, $I_{\text{set}} = 0.5$ nA.

Although the image appears to simply be random noise, it is possible to discern some regularity in the pattern. The Gwyddion software package used for image processing post scan allows the filtering of frequencies in a collected image using a Fast Fourier Transform (FFT). If this is performed it can be seen that there are regularities in the scan with a hexagonal symmetry (see figure 3.18).

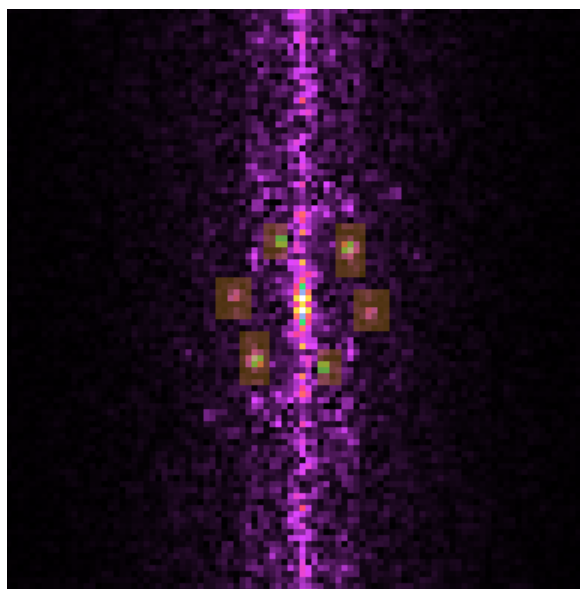


Fig. 3.18 2D FFT of the image presented in figure 3.17 obtained using the “Fourier filter” option in Gwyddion. The six peaks highlighted represent periodicity close to that of a graphite lattice.

From these points it is possible to fit a lattice with parameters $a = 2.505(6) \text{ \AA}$ and $b = 2.663(8) \text{ \AA}$, and a γ value of 57.09° . The expected lattice constant of graphite is $a = b = 2.459 \text{ \AA}$ with $\gamma = 60^\circ$.¹⁵² As there is a reasonably close match between the regularity detected in the STM images and the actual lattice constant of graphite it is likely that the graphite surface is being successfully imaged, however that noise in the collected scan is so significant that it can barely be detected. As discussed in the experimental section, high frequency noise was known to be a problem with this instrument from the previous operator, Dr Stephen Driver. When using the instrument 5+ years ago there had been multiple technician visits and instrument modifications to attempt to eliminate the noise, to no avail. It had been accepted as a minor nuisance when imaging on metal surfaces, and easily isolated from sample signals using image processing software. It is unknown why noise appears drastically worse when imaging HOPG.

After a tip exchange it was possible to obtain more successful images of graphite. However, the noise was still evident, and had to be removed using software adjustment as in section 2.1.8. Because of the difficulties in imaging on graphite, as well as repeated equipment failures and leaks in the vacuum system it was decided to deprioritise STM investigations in the present work. Because of this de-prioritisation, and the effects of the COVID-19 pandemic no more STM data was collected in this work.

Chapter 4

Substrate Analysis

4.1 Introduction

In this work the focus is on the intermolecular interactions of adsorbed molecular species. The substrate, to first order, is simply a support for the 2D layers. The interactions of the molecules with the substrate, ideally should be weak and not exhibit any significant in-plane periodicity, as this may favour commensurate layers, determined by the substrate periodicity, rather than overlayer molecular structure. Graphite has been demonstrated to be a reasonable model in these criteria. The interactions are mainly weak van der Waals and although there is some substrate corrugation, it is relatively weak. Hence, we hope that adsorption onto the basal plane of graphite will enable us to explore the adsorbate-adsorbate interactions without significant perturbation from the substrate.

4.1.1 Highly Oriented Pyrolytic Graphite (HOPG)

It is very difficult to obtain single crystals of graphite. The closest material is Highly oriented pyrolytic graphite (HOPG) such as that produced by Merck. This material consists of highly oriented graphite basal planes stacked onto each other with a single exposed basal plane. These are ideal for STM (see section 3.5) but do not have a high surface area appropriate for surface diffraction studies, the contribution from the adsorbed layer is too weak to observe relative to the much larger amounts of graphite.

4.1.2 Powdered Graphites

There are a large number of high surface area graphitic materials, produced in a number of ways. In this work we have used papyx, a commercially available material from Mersen.

Papyex is a weakly compressed, exfoliated graphite with the graphite basal planes preferentially oriented. It has been previously used successfully as a relatively high surface area graphite substrate for scattering experiments. As discussed in section 4.2, the properties of papyex are key, as the high surface area allows maximisation of the signal from molecular assemblies at the surface. At the same time, many higher surface area graphite substrates contain significant micropores and high defect density, meaning they are far from the ideal infinite flat plane necessary for adsorbate-substrate interactions to be negligible. Papyex thus falls into a "goldilocks zone" that allows the study of behaviour at macroscopic surfaces. The structure of papyex was characterised by Gilbert et al.¹²⁴ They found that papyex consists of highly crystalline flakes of graphite of thickness $10\mu\text{m}$ and radius $20\mu\text{m}$. These flakes are randomly stacked with a tendency to align parallel to the sheet direction. This tendency is quantified by the mosaic spread angle which shall be further covered in section 4.3.3. The preferred orientation, as discussed below, is a significant benefit in optimising scattering studies.

Each flake of graphite is not a single crystal, but instead consists of multiple domains. X-ray analysis indicates a coherence length of 600\AA in-plane and 300\AA out of plane in the graphite lattice. This indicates that there is no long-range order beyond these distances, and so is closely related to the average size of a graphite domain in the substrate.

Papyex is significantly less dense than single-crystal graphite, consisting of approximately 60% void space. In-depth analysis of nitrogen adsorption isotherms indicates that the pores are macro-scale. Precise quantification of the pore sizes was difficult, but there is strong evidence the dimension of the pores is similar to that of the graphite domains (300\AA).

In summary papyex can act as a good model substrate suitable for these experiments mainly due to its preferred orientation and significantly larger surface area than HOPG single crystals.

Although different batches of papyex are not found to deviate significantly from the aforementioned properties. It is prudent to fully characterise the particular papyex substrate used in these scattering experiments. The key quantities that must be considered for each individual batch are the specific surface area (usually characterised by BET isotherm), the preferred orientation of the crystallites (mosaic spread), and the fraction of unoriented crystallites (determined by rocking curve analysis). The batches of papyex utilised in experiments reported in this work are: BPI004L (0.5mm thickness) and JAD01 (2mm thickness). The batch of substrate used will be clearly displayed in the results chapters. Because none of the diffraction experiments with the 2mm substrate were successful, a rocking curve analysis has not been performed for this substrate.

4.2 BET

4.2.1 Theory

Measurement of the surface area of high surface area and porous materials is not a straightforward task. The most commonly used method is the Brunauer-Emmett-Teller (BET) method.¹⁵³ This method involves characterising the adsorption of nitrogen onto the surface. The method is an application of the BET isotherm model, which is itself an extension of the Langmuir model.

In the Langmuir model the surface is assumed to consist of a discrete number of adsorption sites. Each site can either be unoccupied or occupied by one molecule. The binding energy of a molecule to a site is termed the enthalpy of adsorption and is the same for all sites, regardless of their neighbour's occupancy. This model can be used to derive an expression relating the surface coverage (θ_A) of a gas A to the partial pressure of A (p_A) and the equilibrium constant of the single site binding of A to an adsorption site (K_{eq}^A). The Langmuir expression for the surface coverage (θ_A) is

$$\theta_A = \frac{K_{eq}^A p_A}{1 + K_{eq}^A p_A} \quad (4.1)$$

and leads to an adsorption isotherm as in figure 4.1.

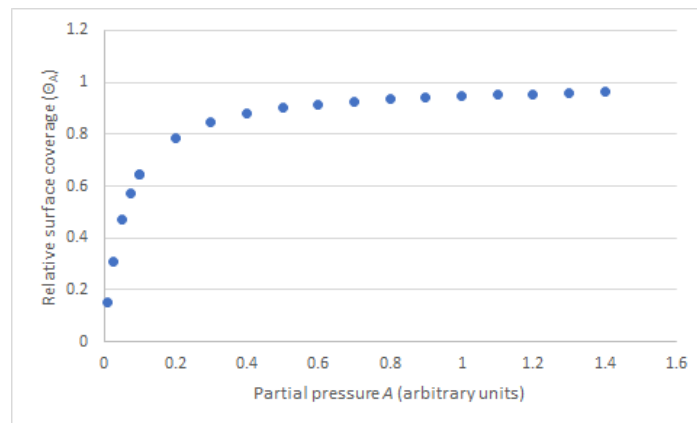


Fig. 4.1 Model data of the Langmuir isotherm. Surface coverage initially increases near linearly with partial pressure of A . But as pressure increases the rate of change of coverage decreases until reaching a maximum (saturation of the surface).

The BET model is an extension to the above Langmuir model to account for the fact that additional gas molecules can adsorb on top of already adsorbed molecules. Similar to the Langmuir model the enthalpy of adsorption is modelled as being independent of the occupancy of neighbouring sites, however a distinction is drawn between the first adsorbed

layer (binding to the surface), and the enthalpy of subsequent layers (binding to other gas molecules). Figure 4.2 provides a schematic of the model. The first layer binds with an enthalpy E_1 equivalent to the Langmuir binding enthalpy, while the subsequent layers bind with enthalpy E_L equivalent to the enthalpy of liquefaction of the adsorbate. These values are used to define a quantity c which is called the BET constant and quantifies the difference in strength of interaction of the adsorbate with the surface versus itself. The BET constant can be calculated using the equation $c = \exp \frac{E_1 - E_L}{RT}$. The form of the BET isotherm then also depends on the vapour pressure of the adsorbate p_o , leading to a more complex expression for relative surface coverage of

$$\theta_A = \frac{cp}{(p_o - p)(p_o + p(c - 1))}. \quad (4.2)$$

This equation leads to behaviour exhibited in figure 4.3, the initial behaviour of the system is Langmuir like, but at high partial pressures of A multilayers of adsorbed gas start to form as fewer unoccupied sites become available.

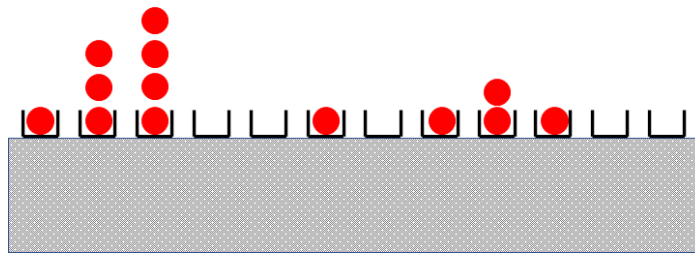


Fig. 4.2 Schematic diagram of the BET model. The surface is subdivided into a number of sites, each of which can have any number of gas molecules adsorbed. In the BET model each layer is assumed to follow the Langmuir model, with the first layer having a greater enthalpy of adsorption, and all subsequent layers have the same, lesser, adsorption enthalpy.

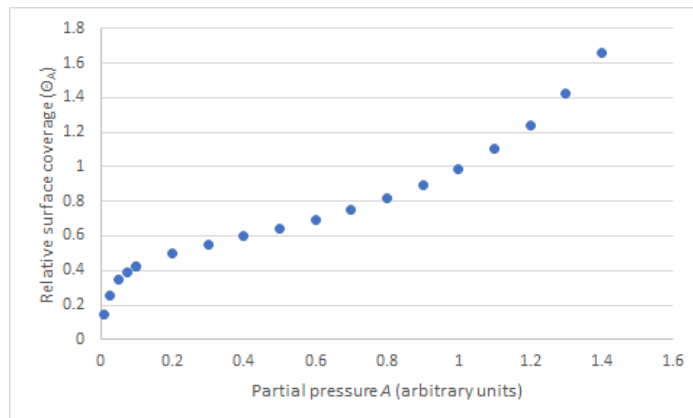


Fig. 4.3 Model data of the BET isotherm. Initial behaviour exhibits Langmuir-like behaviour with an initial linear increase in coverage, followed by a levelling off as the initial layer becomes saturated. However, as partial pressure of A continues to increase additional adsorption occurs to form subsequent layers. This allows surface coverage to go above 1 (the amount required to completely cover one monolayer)

The BET theory is useful because it better reflects the adsorption properties of gases at high partial pressures near the vapour pressure than the Langmuir model. This is relevant because to precisely measure the surface area of a substrate it is ideal to have as much gas adsorbing onto the surface as possible so that the change in number of molecules in the gas phase (the quantity measured) is as large as possible.

4.2.2 Method

To calculate the surface area of a substrate, a weighed amount of the substrate is placed inside a vessel. Another vessel of the same volume is left empty as a control for all subsequent steps. Both vessels are then degassed by being pumped at elevated temperature. The aim of this step is to ensure that the entire surface area of the substrate is free of any adsorbates. Once the chamber is fully evacuated, a quantity of an inert gas such as He is added to measure the dead volume of both vessels, with inert substrate such as glass beads added to the control vessel to ensure a similar dead volume in both vessels.

Once the two vessels are evacuated, nitrogen is then added to both vessels and the pressure change measured as a function of the quantity of nitrogen added. In the control vessel, all the nitrogen will remain in the gas phase, and so the pressure will vary purely as a function of the ideal gas law ($PV = nRT$). For the vessel containing the substrate, a quantity of nitrogen will become adsorbed on the substrate, meaning for a given amount of nitrogen added, the pressure will be less than for the control vessel.

Analysis of the variance in adsorption with pressure and temperature can be used to measure the surface area of the substrate, as well as providing information on the distribution of pore sizes. In this work all analysis was performed by Antonio Exposito in the group of Dr Laura Torrente in the Department of Materials Science in the University of Cambridge, using commercial equipment.

4.2.3 Results

BET surface area measurements were performed on both two recompressed papyex batches (2 mm and 0.5 mm thickness), and a sample of uncompressed papyex powder. The uncompressed powder was found to have a surface area of $31.53 \text{ m}^2\text{g}^{-1}$.

Compression of the graphite powder to form papyex sheets will be expected to reduce the surface area somewhat, Gilbert et al. reported a BET area of approximately $18 \text{ m}^2\text{g}^{-1}$ for a 0.5 mm thickness sheet. From past experience the surface area within batches is fairly similar, but can vary between batches due to slight changes in the manufacturing conditions. For the 0.5 mm batch BPI004L a surface area of $15.72 \text{ m}^2\text{g}^{-1}$ was found. The 2 mm thick batch JAD01 had a BET surface area of $22.88 \text{ m}^2\text{g}^{-1}$. Both of these surface areas are lower than for the uncompressed powder, indicating compression into papyex reduces the available graphite surface area as expected. It is likely that the faces of the strips are more compressed than the centres, thus it is possible to justify why the thicker batch (which will have a lower ratio of face to centre) exhibits a higher BET surface area.

The value of the BET surface area is used in the determination of the amount of adsorbate required to give a desired coverage. Since all systems studied in this work are at sub-monolayer coverage, to ensure no multilayer structures, the precise value is not of particular importance, however it is necessary to confirm that the adsorbates are indeed at the sub-monolayer coverage regime. As discussed in chapter 2, substrates were dosed to approximately 0.8 of a monolayer coverage. This represents a trade-off between maximising the coverage to obtain a strong scattering signal, while providing a safety factor reflecting the possible differences in accessible surface area between N_2 molecules used in the BET isotherms and the larger molecules considered later in this work.

4.3 Rocking curve

The distribution of graphite crystallites is an important parameter in the determination of the monolayer diffraction lineshape, and as a means to optimise the experimental geometry of the scattering experiments. As discussed in section 2.2.9 the lineshape is determined by

both the properties of the monolayer (in particular the crystallite size, L) and the distribution of orientations of the crystallites $P(u)$. In all previous work the orientation of the crystallites to obtain $P(u)$ has been modelled as the superposition of an isotropic fraction (f) and an oriented fraction ($1-f$) whose orientation is described using a Gaussian, with a characteristic spread angle θ_{mosaic} which equated to the full-width at half maximum of the Gaussian.

L is a function of the monolayer crystallite and so will vary between different monolayer systems and so must be fit as part of the curve fitting procedure for each sample studied. However f and θ_{mosaic} are functions of the substrate and so can be measured separately. This is useful as it helps to constrain the monolayer pattern fitting procedure by reducing the number of free variables. Previous literature has reported on a number of different experiments on papyex substrates, reporting values of $\theta_{mosaic} \approx 30^\circ$ and $f \approx 0.3$.^{124,154,155} However, these references give little detail of how these values were obtained. Adam Brewer's PhD thesis goes into greater detail of the method employed, obtaining similar values to the above.¹²⁵

In keeping with Brewer's previous work, the diffraction pattern of a blank papyex strip was measured and the intensity of the inter-basal plane diffraction peak (001) was recorded as a function of sample orientation. By analysing the change in intensity with rotation angle it is possible to extract information about the orientation of the papyex crystallites and hence obtain values for f and θ_{mosaic} .

4.3.1 Geometric correction

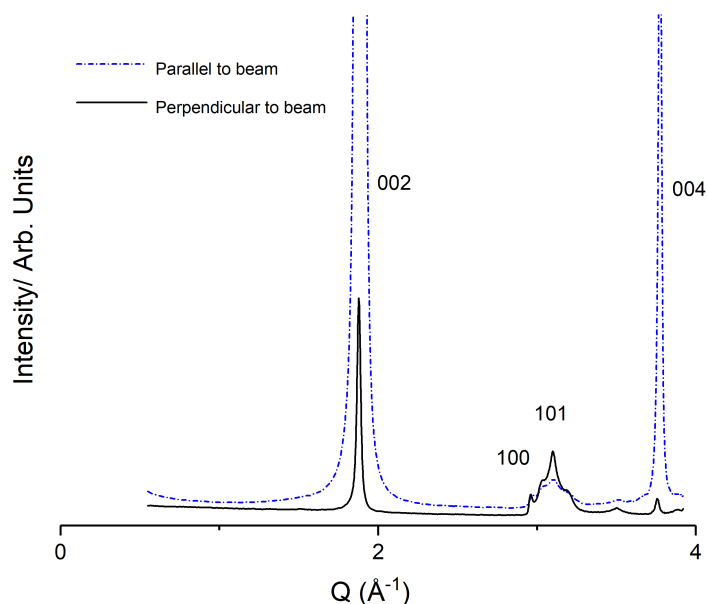


Fig. 4.4 Two diffractograms for a papyex sample at two orientations relative to the incident X-ray beam: a) the plane of the papyex sample parallel to incident beam (blue) or b) perpendicular (black). It can be seen the relative intensities of peaks vary drastically, with the out of plane $\{002\}$ and $\{004\}$ peaks being orders of magnitude more intense with the incident beam parallel rather than perpendicular to the sample.

Figure 4.4 shows the experimentally measured X-ray intensity as a function of the scattering vector \mathbf{Q} of an undosed papyex sample for the two extremes of sample orientation relative to the incident beam of a) beam parallel to the graphite planes (blue) or b) beam perpendicular to the graphite planes (black). Relevant peaks are labelled. Due to the symmetry of the stacking of the graphite sheets the $\{00l\}$ reflections are systematically absent for odd l . The $\{002\}$ and $\{004\}$ are thus the only interlayer peaks visible within this \mathbf{Q} range. As can be seen, the intensities of these peaks vary drastically with sample orientation. This is partly a function of the distribution of graphite crystallite orientations within the papyex, but also a function of several other factors which must be corrected for.

Path Length

Carbon has a low Z number so there is a relatively weak attenuation of the X-rays on passage through the sample. Nevertheless for best results it is necessary to account for changing path length of the beam as the sample rotates.

Figure 4.5 shows the key geometries for consideration of transmission path length. The sample is modelled as a cuboid of infinite extent in the direction normal to the plane of the paper. Within the paper plane the sample has a long dimension (width, w) and a short dimension (thickness, t). The angle β is defined as the angle between the long axis of the graphite strip and the incident beam. The beam is modelled as an incident beam of no thickness entering the strip and scattering from its centre. Critical values of β can be identified that correspond to maxima in path length and discontinuities in path length change with angle. These critical angles denote where the incident or transmitted beam switches from exiting through an edge to a face, or vice versa.

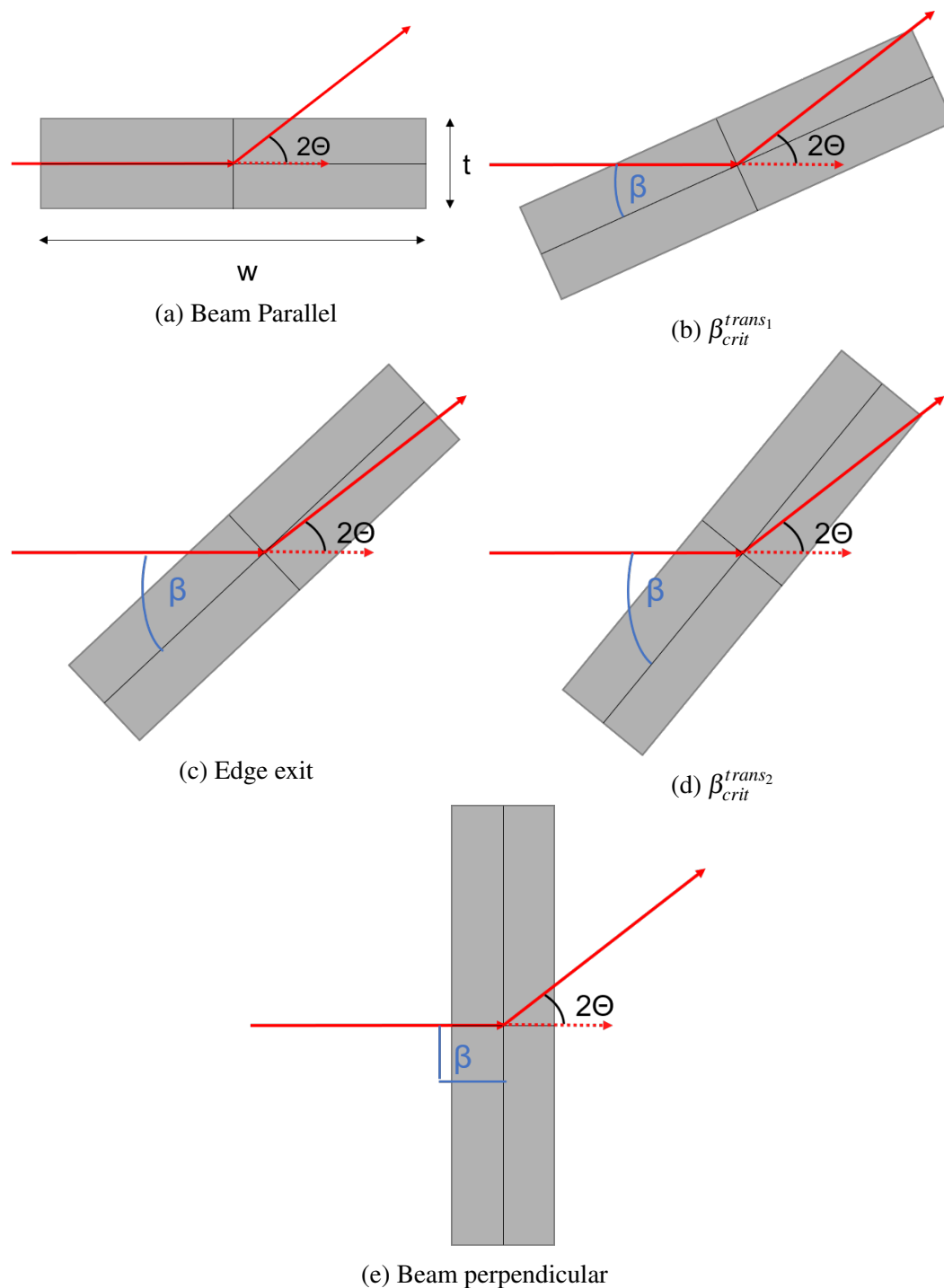


Fig. 4.5 Schematic diagram of the key geometries in the rocking curve. The sample strip has a thickness of t , and a width of w . The red arrows represent the incident and diffracted X-ray beams, with scattering modelled as being localised entirely from the centre of the substrate. β is defined as the rotation angle of the substrate from beam parallel. Two critical values of β , labelled β_{crit}^{trans1} and β_{crit}^{trans2} denote changes in regime as the beam exits through different faces of the sample.

The path length of the incident and transmitted beams for the geometries shown in figure 4.5 can be calculated through simple trigonometry. The below equations can be used to calculate the transmitted beam path length l_t .

When β is less than β_{crit}^{trans1} the beam falls in regime (a) from figure 4.5 and the transmitted path length is given by

$$l_t^{topface} = \frac{t}{2 \sin(2\theta - \beta)}. \quad (4.3)$$

When β is greater than β_{crit}^{trans1} but less than β_{crit}^{trans2} the geometry is in regime (c) and the transmitted path length is

$$l_t^{edge} = \frac{w}{2 \cos(2\theta - \beta)}. \quad (4.4)$$

Finally, when β is greater than β_{crit}^{trans2} but less than 180° the geometry is in regime (e) and the path length is

$$l_t^{bottomface} = \frac{t}{2 \sin(\beta - 2\theta)}. \quad (4.5)$$

Once $\beta = 180^\circ$ the geometry becomes equivalent to regime (a). The values of the critical angles β_{crit}^{trans1} and β_{crit}^{trans2} are given by the equations

$$\beta_{crit}^{trans1} = 2\theta - \arctan\left(\frac{t}{w}\right), \quad (4.6)$$

and

$$\beta_{crit}^{trans2} = -2\theta + \arctan\left(\frac{t}{w}\right) \quad (4.7)$$

respectively.

Figure 4.6 shows how the path length calculated using the above set of equations changes with rotation angle β for a sample with dimensions of thickness = 0.5 mm and width = 2mm. As can be seen, the minimum transmitted path length is 0.25 mm (half of the strip thickness) while the maximum path length is 1.03 mm (exiting diagonally through a corner of the strip at one of the critical angles). In between these two extremes the transmitted beam path length varies smoothly with derivative discontinuities at the critical angles.

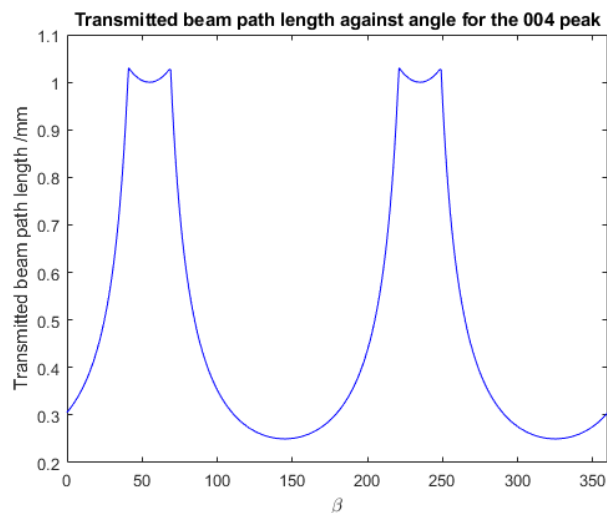


Fig. 4.6 Transmitted beam path length for the $\{004\}$ reflection of X-ray of 1.54179 \AA wavelength for a strip of papyex 0.5mm by 2mm in size. $\beta = 0^\circ$ equates to the strip being parallel to the incident beam as in figure 4.5a, while $\beta = 90^\circ$ equates to the strip being perpendicular to the beam as in figure 4.5e

Similar analysis was also performed for the incident path length. Due to the simplified geometry only one critical angle is required ($\beta_{crit}^{incident}$), determining whether the incident beam enters through the face or edge. This critical angle is given by

$$\beta_{crit}^{incident} = \arctan\left(\frac{t}{w}\right). \quad (4.8)$$

When β is below this critical angle the incident path length is

$$l_i^{face} = \frac{w}{2 \cos(\beta)}, \quad (4.9)$$

while above the critical angle the incident path length is equal to

$$l_i^{edge} = \frac{t}{2 \sin(\beta)}. \quad (4.10)$$

Figure 4.7 shows how the incident beam path length changes with rotation angle β . As can be seen the minimal incident beam path length occurs at $\beta = 90^\circ$ when the strip is perpendicular to the incident beam and so the incident path length is 0.25 mm , half the thickness of the strip. The maximum path length occurs when the beam enters diagonally at $\beta_{crit}^{incident}$ ($\beta \approx 14^\circ$).

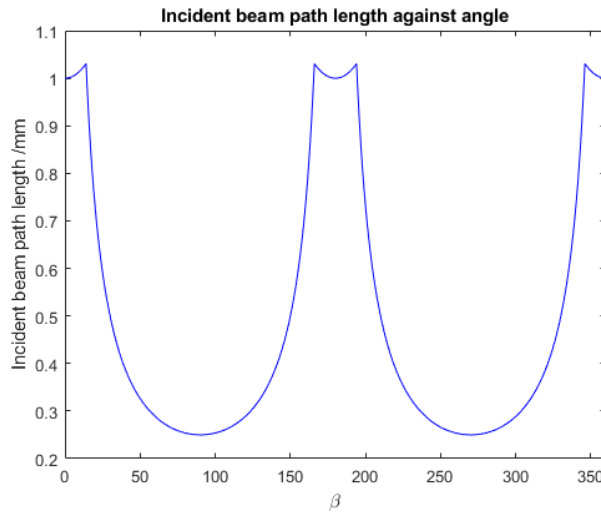


Fig. 4.7 Incident beam path length for a strip of papyex 0.5mm by 2mm in size. $\beta = 0^\circ$ equates to the strip being parallel to the incident beam as in figure 4.5a, while $\beta = 90^\circ$ equates to the strip being perpendicular to the beam as in figure 4.5e

Attenuation

The X-ray attenuation coefficient α is a key quantity when considering X-rays passing through matter. It is the reciprocal of the distance through the sample at which the X-ray beam decays by a factor of e from its original intensity. For a sample of thickness d , the intensity of the attenuated beam is given by $I(d) = I_0 e^{-\alpha d}$.

The attenuation of a given wavelength of radiation by an atom of a given element is fixed and can be obtained from literature values.¹²⁹ However, the value for a particular sample depends on the number of atoms of that kind per unit length of beam path, and hence the density of the atoms in the sample.

For photons of wavelength 1.54179 Å, the attenuation coefficient of carbon is 4.576 cm^2g^{-1} .¹⁵⁶ The density of papyex can be estimated through weighing of samples of known dimensions. The density is found to be variable between 0.4 and 0.6 g cm^{-3} . For a density of 0.5 g cm^{-3} a value of $\alpha \approx 2.3 \text{ cm}^{-1} = 0.23 \text{ mm}^{-1}$ is obtained. This means the attenuation length (the path length required for beam intensity to drop to $1/e$ of the original intensity) is $\approx 5\text{mm}$. 5mm is significantly larger than the thickness of the papyex (0.5-2 mm) and so attenuation is negligible for these samples.

It is desirable to have a more exact value for the attenuation coefficient for the particular sample of graphite being scanned in the rocking curve. This could be done by observing how the intensity of the direct through beam varies with sample orientation. The direct beam is highly intense, and so a beamstop is used to prevent the beam from damaging the detector.

However, despite the beamstop there is still a residual beam detectable in the detector area shadowed by the beamstop.

However, attempts to relate the intensity of the residual beam to the rocking curve of the papyex were unsuccessful, with no discernible relation between sample thickness and direct beam intensity. Figure 4.8 shows how the through beam intensity changes with β . If attenuation was significant a periodicity of 90° would be expected as the sample rotates. No discernible trend can be seen likely indicating that random fluctuations in intensity of the residual "through beam" are more significant than attenuation by the graphite.

Because it was not possible to measure a value for α , the literature value of 0.2 mm^{-1} was used. However it is important to note that the structural interpretation of the rocking curve results, the focus of this work, were largely insensitive to the absolute values of α (or attenuation neglected entirely).

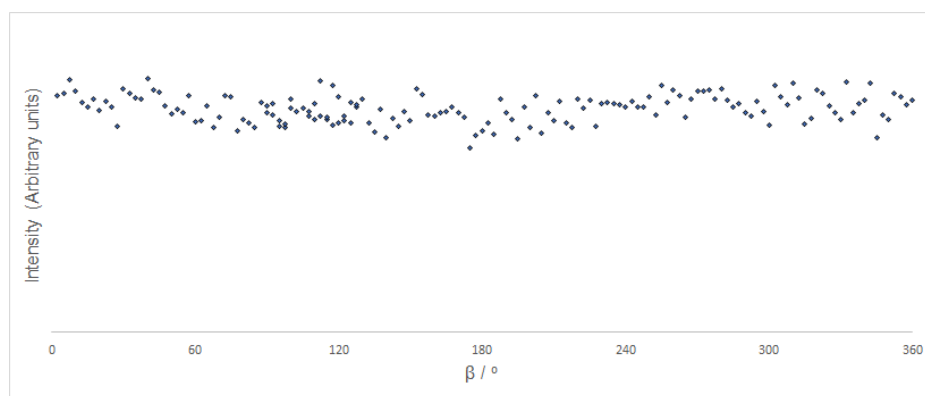


Fig. 4.8 Intensity of the through-beam showed no significant periodicity with sample rotation angle β . This means that random fluctuations in beam intensity were more significant than any attenuation by the graphite sample.

Illuminated volume

The second geometric effect that must be accounted for is the changing volume of the sample illuminated by the beam as the sample rotates. The incident beam is of a fixed beamwidth and illuminates all of the sample in its path. Assuming the papyex is of uniform composition the intensity of a diffracted beam should be directly proportional to the illuminated volume. The illuminated volume is simply the incident beam path length multiplied by the beamwidth (a constant). Thus the illuminated volume correction simply takes the form of a multiplication by $I_{incident}$.

Total Geometric Correction

The final form of the geometric correction term is given by an overall correction factor I_c . This factor is obtained from the equation

$$I_c = I_i \times e^{-\alpha l_i} \times e^{-\alpha l_t}. \quad (4.11)$$

The form of this correction factor is plotted in figure 4.9. The correction factor takes a value of one for maximum intensity (large illuminated volume, little attenuation) and is smaller for conditions that serve to lower collected intensity. The measured intensity must therefore be divided by the I_c to give the corrected intensity. The form of the total geometry correction is extremely similar to figure 4.7. As discussed previously attenuation is almost negligible for this system and so the illuminated volume term provides nearly all of the variance in diffracted intensity with angle.

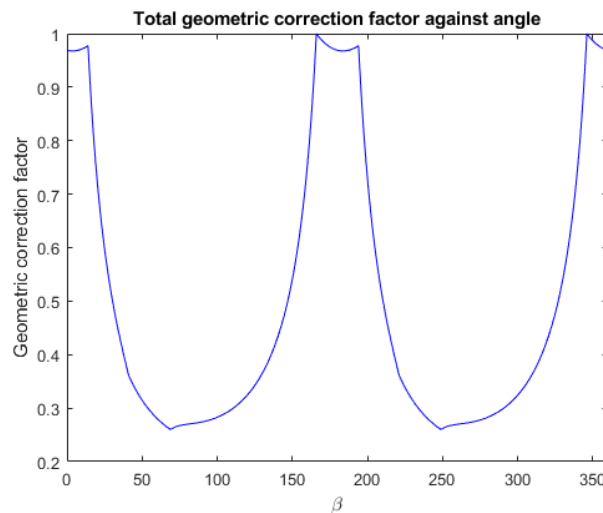


Fig. 4.9 Correction factors calculated using the above equations for a strip of papyex 0.5 mm by 2 mm in size and with density 0.4 gcm^{-3} ($\alpha = 0.2 \text{ mm}^{-1}$). The form of the correction is dominated by the illuminated volume term as in figure 4.7, with a slight asymmetry due to the attenuation terms. As the correction factor accounts for factors influencing the intensity other than crystallite orientation, the correction factor is a number the measured intensity must be divided by to obtain a "corrected intensity".

4.3.2 Experimental

Data was collected at the Laboratory of Molecular Biology (LMB) on the rotating anode diffractometer discussed in section 2.2.4. A sample of papyex from batch BPI004L was cut to form a strip. The dimensions of this strip were thickness of 0.5mm, width 2mm and

length 30mm. The sample was mounted lengthwise along the sample pin, such that only the sample's width and thickness are relevant for diffraction. The goniometer was adjusted so that the sample could fully rotate while remaining in the beam. The diffractometer was setup to rotate the sample by 2.5 degrees between diffractograms, with each data collection step taking 20 seconds. A comparatively short sample-detector distance of 105 mm was used to allow collection of higher angle peaks.

The 160 scans collected were integrated using a fit2D macro script to produce an intensity- 2θ scan for each value of β . A Matlab script was then used to extract from each scan a single value for the 004 peak intensity. This was done by first taking a linear background using the peakfit function to identify the centre of the 004 peak and fitting a linear background between the points 4 peak halfwidths before and after the peak. The total peak intensity was then calculated using the trapezium rule to sum the area under the curve.

Both the {002} and {004} peaks can be used to perform a rocking curve. However in practice the high intensity of the {002} reflection leads to significant issues with detector saturation. This was also reported in previous work.¹²⁵ As such, the change in {004} peak intensity is considered in this analysis.

4.3.3 Analysis

The sample was rotated through a full 360°. Due to the symmetry of the sample the 180-360° range can be mapped onto the 0-180° range. When performing rocking curves it has previously been found that despite the geometric correction, intensity when the beam and graphite planes are close to parallel is still significantly higher than is expected. This is thought to be due to the papyex strips not being perfectly flat and aligned.¹²⁵ Hence, the data has been removed for $\beta < 20^\circ$ and $\beta > 160^\circ$.

As outlined above in section 4.3.3 the shape of the rocking curve can be modelled by an isotropic component of unoriented graphite crystallites that give scattering that has the same intensity across the angular range, and an oriented component of crystallites that has a Gaussian form to the intensity. Figure 4.10 shows the intensity of the {004} peak against rotation angle of the papyex strip, mapped to the 0-180° range. In red is a modelled intensity pattern optimised to the experimental data. The optimised parameters are the isotropic fraction, f and the spread angle of the oriented component θ_{mosaic} .

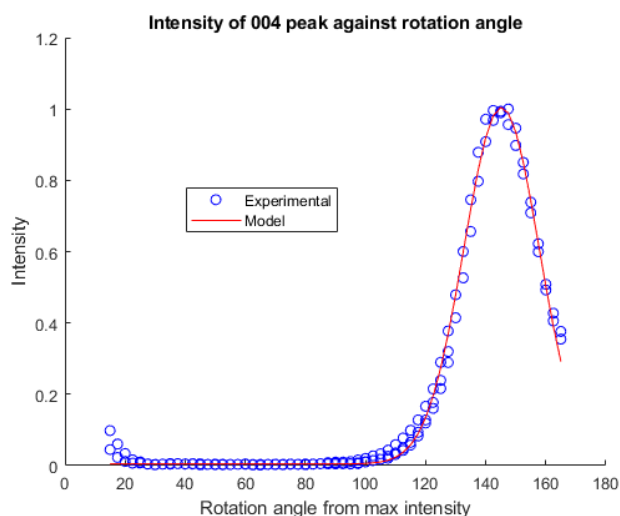


Fig. 4.10 Rocking curve of papyex. The geometrically corrected intensity against rotation angle is plotted in blue, while red represents a modelled intensity from a fraction, f , of isotropic component and a fraction $1-f$ of oriented component. Optimised parameters for this sample are $f = 0.025$ and mosaic spread angle = 29.42°

Previous work has reported several different values of f and θ_{mosaic} for the papyex substrate. In Dr Adam Brewer's PhD thesis the two batches of papyex gave θ_{mosaic} values of 29.1 ± 0.1 and 31.8 ± 0.1 respectively, with f values being 0.32 ± 0.01 and 0.37 ± 0.01 respectively. However the large f values reported in that work are largely impacted by a poor fit of the oriented crystallite component to a Gaussian, with the reported f value clearly overestimating the fraction of crystallites oriented far $> 50^\circ$ from the z axis. This can be seen in figure 4.11 which is reproduced from Dr Brewer's thesis.¹²⁵

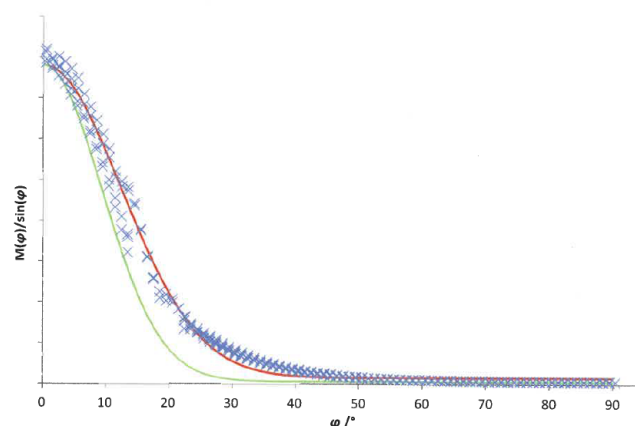


Fig. 4.11 Reproduced from reference 125. The rocking curve has been translated such that a rotation angle (ϕ of 0 equates to a maximum in the intensity). The crystallite distribution modelled using $\theta_{mosaic} = 29.1$ and $f = 0.32$ is shown in red, while the experimental data is shown in blue crosses. The green line is a model based on previous, badly fitting, parameters. The model (red line) shows a good match with the experimental data at low ϕ , but the Gaussian is a poor match for the tail of the experimental curve at around $\phi = 30^\circ$. I hypothesise that the relatively large value of f Adam Brewer obtained was due to the fitting attempting to account for this mismatch.

Due to these experiments being collected on an area detector it is possible to utilise single scans to visualise the distribution of crystallites. This data is uncorrected for geometric effects but provides a useful sanity check of the low value of f (and hence high degree of preferred orientation) calculated above. Figure 4.12 is an image of the diffraction data collected when the papyex sample was tilted at 57.5° to the incident beam, approximately the same angle as the 2θ value of the $\{004\}$ peak. This would be expected to maximise the intensity of the $\{004\}$ peak from crystallites aligned with the preferred orientation.

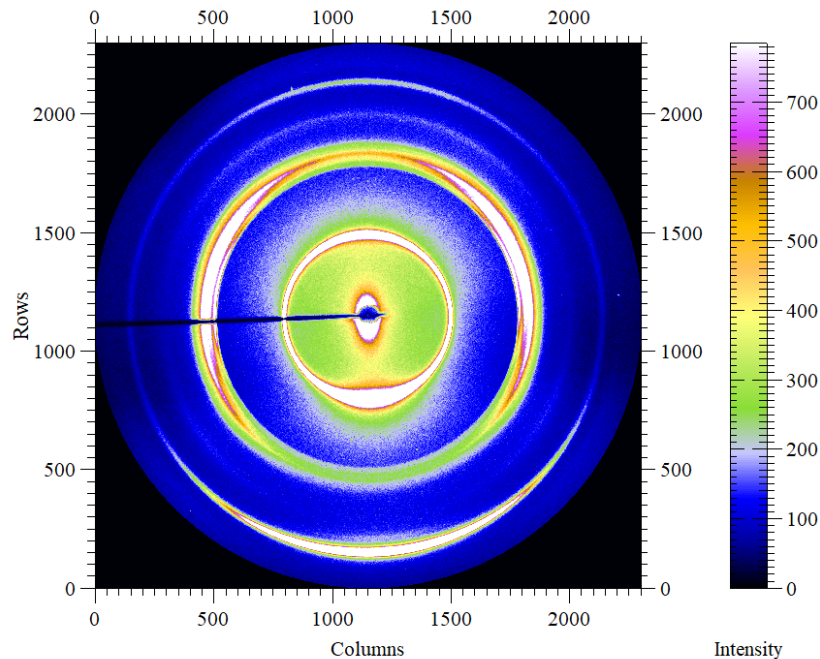


Fig. 4.12 Image of the unprocessed data from the area detector. This run was taken when the papyex was at an angle to the detector optimised for scattering from the 004 peak to be optimised pointing downwards. As expected the maximum intensity in the outer ring (the 004 Bragg peak) is directed downwards. There is some spread azimuthally, but far from the maximum the Bragg peak intensity is significantly less.

In figure 4.12 the outermost ring in the diffractogram represents the $\{004\}$ peak of the graphite, with a clear maximum in intensity towards the bottom of the ring. Looking azimuthally around the ring it can be seen that the intensity becomes less significant. It should be noted that the intensity again increases directly opposite the maximum (at the top of the detector). The top of the ring equates to diffraction from crystallites that are perpendicular to the direction of preferred orientation. The second maximum may be an artefact of the lack of geometric correction to this data (as the transmitted path length will be shortest for this direction) or represent an over-representation of crystallites directly perpendicular to the axis of preferred orientation. Detailed textural analysis of the papyex substrate would theoretically be possible using this data, but is beyond the scope of this work.

Ideally, an alternative mathematical function that more precisely represents the experimentally measured crystallite probability distribution would be used in the expression for $P(u)$ introduced in section 2.2.9. However, any move away from a Gaussian expression would significantly complicate the derivation and drastically increase the expense of the computational calculations. The experimental patterns reported in chapters five and six are all consistent with the small f value of 0.025 calculated here, and not with the higher f value

reported in Brewer's work. Other than the divergent values of f the determined value of θ_{mosaic} falls within the range of values reported previously.

4.3.4 Summary

Hence in summary, this section has carefully examined the graphite crystallite orientation distribution in a typical Papyex sample. The details of the analysis of the experimental data requires some care to ensure geometric effects and transmission are correctly included. The results are to be employed in structural determination of the physisorbed overlayers.

4.4 Flat Plate Geometry

The software tools used to analyse the monolayer diffraction patterns previously use lineshapes based on the mathematical treatment by Schildberg and Lauter.¹³¹ Their work considered an experimental setup where the incoming radiation is orthogonal to the principal axis of the crystallite preferred orientation, as used in capillary experiments at synchrotrons. This geometry removes any dependence of the scattered intensity on the mosaic spread angle of the papyex, simplifying analysis of the data. However it means that only a small fraction of the incident beam is scattered by the monolayer. For experiments at synchrotron beamlines this is acceptable, as generally only a one-dimensional detector is used, and incident beam intensity is extremely high. However, when using lab based sources incident beam intensity is significantly lower, and it is desirable to maximise the fraction of the beam that is scattered by the in-plane periodicity of interest.

The lab-based source used in this work utilises a two-dimensional area detector allowing collection of scattered intensity from the full Debye-Scherrer ring. The data from this ring can then be compressed into a single radial dimension similar to that obtained from a one-dimensional detector, but with better detection statistics. For this reason it was found optimal to orient the samples in a flat plate geometry, with the preferred orientation of the graphite sheets aligned with the incident beam. Figure 4.13 presents schematic diagrams of the two scattering geometries.

The use of this flat plate geometry for study of monolayer samples is completely novel and has allowed drastically improved collection times, allowing a lab X-ray source to collect high-quality monolayer diffraction patterns with measurement times on the order of minutes rather than multiple hours. However, it requires a new mathematical treatment to model the lineshapes.

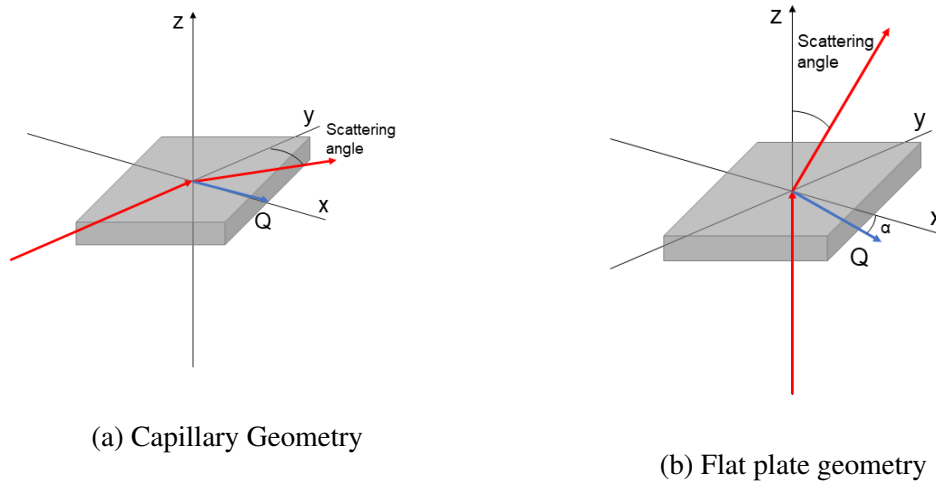


Fig. 4.13 Schematic diagrams of the two geometries considered. The cuboid represents the graphite substrate, with preferred orientation along the z axis. The incident and diffracted X-ray beams are represented by red arrows, while the scattering vector \mathbf{Q} is represented by a blue arrow. For the capillary geometry scattering occurs entirely in the x - y plane, while in the flat plate geometry the scattering vector has some z component that varies with \mathbf{Q} . In keeping with the derivation, the scattering angle has been titled "scattering angle" rather than the more usual 2θ to avoid confusion

4.4.1 Setup

The aim of this section is to derive an expression which, given a set of monolayer diffractions peaks and intensities, returns the scattering intensity detected at given \mathbf{Q} . This will involve structural terms considering the structure factor of the monolayer, as well as geometric terms based on the experimental setup. It is these geometric terms which will be different from those previously calculated due to the new sample orientation. For completeness, figure 4.14 defines the standard polar coordinate system that shall be used.

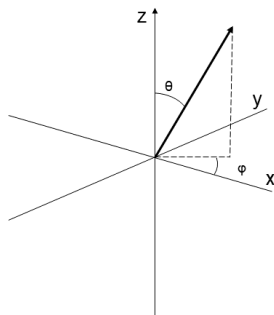


Fig. 4.14 Standard spherical polar coordinates used in this derivation θ defines the angle relative to the z axis, while ϕ defines the angle relative to the x axis

Figure 4.13 relates the two scattering geometries to the coordinate system. In all that follows the preferred orientation of the graphite planes of the papyex is considered to point directly along the z axis. This preferred orientation takes the form of a Gaussian weight factor of the form $\exp\left(-\frac{\theta^2}{\sigma^2}\right)$, where σ defines the mosaic spread angle (θ_{mosaic}) of the graphite as obtained in section 4.3.3 through the equation

$$\sigma = \theta_{mosaic} \frac{\pi}{360\sqrt{\log 2}}. \quad (4.12)$$

For the capillary geometry the incident beam enters along the y axis, and the scattered beam exits on the other side of the sample at some angle to the y axis. This angle is generally called 2θ , however to avoid confusion with the coordinate system shall in this case be simply be referred to as the scattering angle. The scattering vector \mathbf{Q} is localised within the x-y plane. Utilising this geometry greatly simplifies the derivation, as \mathbf{Q} is always at the same value of θ (90°).

For the flat plate geometry the incident beam enters along the z axis, and the scattered beam exits on the other side of the sample having been deflected by an equivalent 2θ scattering angle to the capillary geometry. As shown in figure 4.13b this means the scattering vector \mathbf{Q} is oriented at an angle α to the x-y plane, where α is equal to half the scattering angle, and is related to \mathbf{Q} by the equation

$$\alpha = \arcsin\left(\frac{\mathbf{Q}\lambda}{4\pi}\right). \quad (4.13)$$

Because of this, different values of \mathbf{Q} are located at different values of θ , meaning there is a \mathbf{Q} dependence of the intensity that distinguishes the flat plate geometry from the capillary geometry.

4.4.2 Derivation

The sample consists of many crystallites with different orientations. The orientation of a particular crystallite can be fully described using the surface normal vector \mathbf{n} to describe the orientation of a crystallite, as well as the quantity ω to describe the rotation of the sample about \mathbf{n} .

In polar coordinates, \mathbf{n} is given by

$$\mathbf{n}(\theta, \phi) = \begin{bmatrix} \sin(\theta) \cos(\phi) \\ \sin(\theta) \sin(\phi) \\ \cos(\theta) \end{bmatrix}. \quad (4.14)$$

ω represents the orientation of an individual 2D crystallite within the plane defined by \mathbf{n} . As the system is a 2D powder consisting of a large number of randomly oriented crystallites it is assumed that all values of ω are equally probable. In that case there is no ω dependence on the probability of a particular orientation.

To obtain an expression for how the total scattered intensity varies with \mathbf{Q} it will be necessary to sum over all possible orientations. Due to the preferred orientation of the papyrex substrate not all values of \mathbf{n} have equal probability. Thus a weight factor must be derived to account for the different probabilities of certain orientations of crystallite to the total scattered intensity.

Distribution of Orientations

The scattering of X-rays from a system depends on the interaction of the reciprocal lattice of the system with the scattering vector \mathbf{Q} . For a monolayer system it can be shown that the reciprocal lattice consists of a series of Bragg rods oriented perpendicular to the plane of the surface. As the rods are uniform along their length, the scattering does not depend on the component of \mathbf{Q} parallel to the rods (\mathbf{Q}_{\parallel}) but only on \mathbf{Q}_{\perp} , which is perpendicular to the rods and thus within the surface plane.

It is thus convenient to define a quantity u , which is a function of θ , ϕ and α and describes the contribution of a particular orientation of crystallite to the scattering at a given \mathbf{Q} . This is derived in a method analogous to that used by Schildberg. This quantity is the flat plate

equivalent of the Schildberg u and is given by the equation

$$u_{fp}^2(\theta, \phi, \alpha) = (\sin(\alpha) \sin(\theta) \sin(\phi))^2 + (\sin(\alpha) \sin(\theta) \cos(\phi) - \cos(\alpha) \cos(\theta))^2 + (\cos(\alpha) \sin(\theta) \sin(\phi))^2. \quad (4.15)$$

This equation can then be rearranged to find ϕ as a function of u_{fp} , θ and α in an analogous way to the literature. If this is done it is found that there are four roots of the equation. Two of the roots are simply reflections in the x-z plane (i.e. ϕ in the range $0-\pi$ is symmetrically equivalent to ϕ in the range $\pi-2\pi$). However, two of the roots (ϕ_1 and ϕ_2) consider values of ϕ between 0 and $\pi/2$, and $\pi/2$ and π respectively. These are equivalent for $\alpha = 0$, but are distinct for non-zero values of α , so must both be considered separately. The first root of the equation (ϕ_1) is

$$\phi_1(u_{fp}, \theta, \alpha) = \arccos\left(\csc(\theta) \sec(\alpha) \sqrt{1-u^2} - \cot(\theta) \tan(\alpha)\right), \quad (4.16)$$

while the second root (ϕ_2) is

$$\phi_2(u_{fp}, \theta, \alpha) = \arccos\left(\csc(\theta) \sec(\alpha) \sqrt{1-u^2} + \cot(\theta) \tan(\alpha)\right). \quad (4.17)$$

It is possible to obtain the probability density of u_{fp} by integrating between the equipotentials $\phi(u, \theta, \alpha)$ and $\phi(u + \Delta u, \theta, \alpha)$. If this is done the expression obtained for the probability density of u_{fp} is

$$P(u_{fp}) = \int_{lowerlim}^{upperlim} (\phi(u + \Delta u, \theta, \alpha) - \phi(u, \theta, \alpha)) \sin(\theta) d\theta. \quad (4.18)$$

The $\sin(\theta)$ term in the above equation accounts for the spherical nature of the polar coordinates being integrated over. The term in brackets is simply the derivative of $\phi(u, \theta, \alpha)$ with respect to u .

To obtain the total $P(u_{fp})$ two integrals must be performed separately, for both ϕ_1 and ϕ_2 . These shall be denoted $P_{\phi_1}(u_{fp})$ and $P_{\phi_2}(u_{fp})$. The limits for the integration can be obtained by considering the possible values of θ when $\cos(\phi) = -1$ and $\cos(\phi) = 1$ respectively. The equations for these limits are

$$upperlim_{\phi_1} = \arccos\left(\frac{-u \sec(\alpha) - \sqrt{1-u^2} \sec(\alpha) \tan(\alpha)}{1 + \tan^2(\alpha)}\right), \quad (4.19)$$

$$lowerlim_{\phi_1} = \arccos \left(\frac{u \sec(\alpha) - \sqrt{1-u^2} \sec(\alpha) \tan(\alpha)}{1 + \tan^2(\alpha)} \right), \quad (4.20)$$

$$upperlim_{\phi_2} = \arccos \left(\frac{-u \sec(\alpha) + \sqrt{1-u^2} \sec(\alpha) \tan(\alpha)}{1 + \tan^2(\alpha)} \right), \quad (4.21)$$

and

$$lowerlim_{\phi_2} = \arccos \left(\frac{u \sec(\alpha) + \sqrt{1-u^2} \sec(\alpha) \tan(\alpha)}{1 + \tan^2(\alpha)} \right). \quad (4.22)$$

It can be shown that defining a new variable t and substituting such that $t = \arccos(u)$ aids numerical solution of the integral. A weighting term $\exp\left(-\frac{\theta^2}{\sigma^2}\right)$ must also be added to reflect the preferred orientation of the crystallites around the z axis. This finally gives two integrals below that must be summed to obtain the total probability distribution of possible u_{fp} . The first equation, for the probability density of u_{fp} related to ϕ_1 , is

$$P_{\phi_1}(u_{fp}) = \int_{lowerlim_{\phi_1}}^{upperlim_{\phi_1}} \frac{\cot(t) \csc(\theta) \sec(\alpha) e^{-\frac{\theta^2}{\sigma^2}}}{\sqrt{1 - (\csc(\theta) \sec(\alpha) \sin(t) + \cot(\theta) \tan(\alpha))^2}} d\theta. \quad (4.23)$$

The second equation, for the probability density related to ϕ_2 , is

$$P_{\phi_2}(u_{fp}) = \int_{lowerlim_{\phi_2}}^{upperlim_{\phi_2}} \frac{\cot(t) \csc(\theta) \sec(\alpha) e^{-\frac{\theta^2}{\sigma^2}}}{\sqrt{1 - (\csc(\theta) \sec(\alpha) \sin(t) - \cot(\theta) \tan(\alpha))^2}} d\theta. \quad (4.24)$$

These integrals added together give a non-normalised value of $P(u_{fp})$. Integrating over the values $0 < u_{fp} < 1$ gives a normalisation constant, used to ensure the total probability density equals unity.

It is instructive to see the difference that the alternate geometry makes to values of $P(u_{fp})$ compared to Schildberg and Lauter's $P(u)$. For Schilderberg and Lauter's $P(u)$ the distribution is found to increase rapidly to a maximum at $P(u_{fp}) = 1$.

Figure 4.15 compares the normalised probability distributions for both the capillary geometry $P(u)$ and the derived $P(u_{fp})$ for the case that $\mathbf{Q} = 0$. When $\mathbf{Q} = 0$, it can be seen that α is also zero. This means that the scattering vector lies within the x - y plane and so is an equivalent to the capillary geometry case. This is confirmed by figure 4.15, which shows that the $P(u)$ distribution calculated using the two methods is identical.

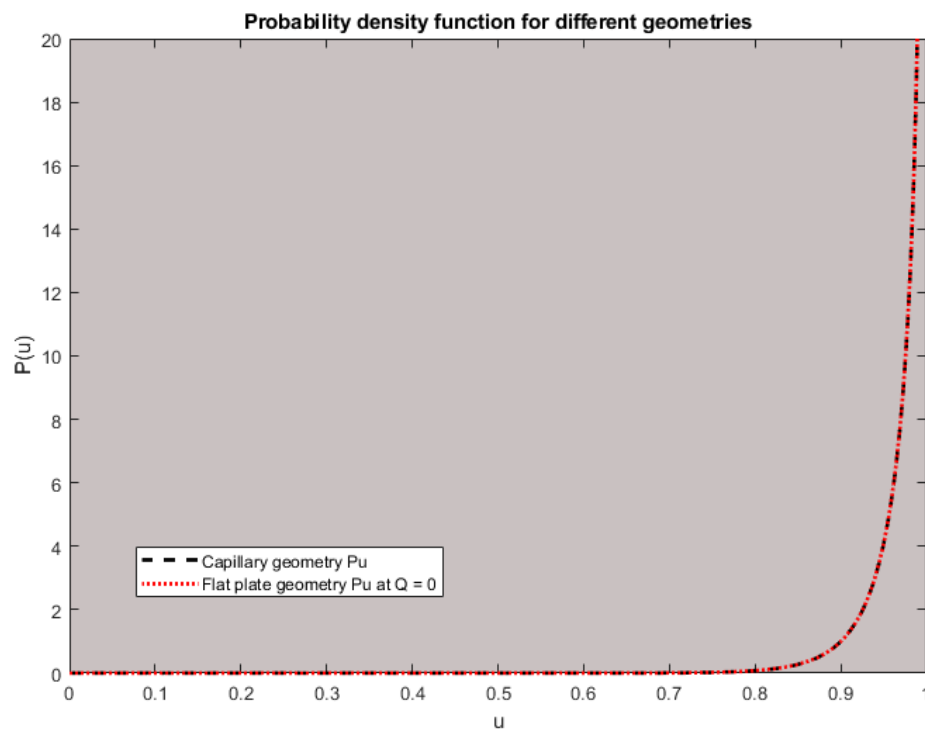


Fig. 4.15 Figure comparing the $P(u)$ distributions obtained using the previously published equations for the capillary geometry and those newly derived for the flat plate geometry. When $Q = 0$ the two geometries are identical.

When Q is non-zero, the angle α between the scattering vector and the x-y plane is also non-zero. This means that the distribution $P(u_{fp})$ will shift. Figure 4.16 shows how $P(u_{fp})$ changes with different values of Q .

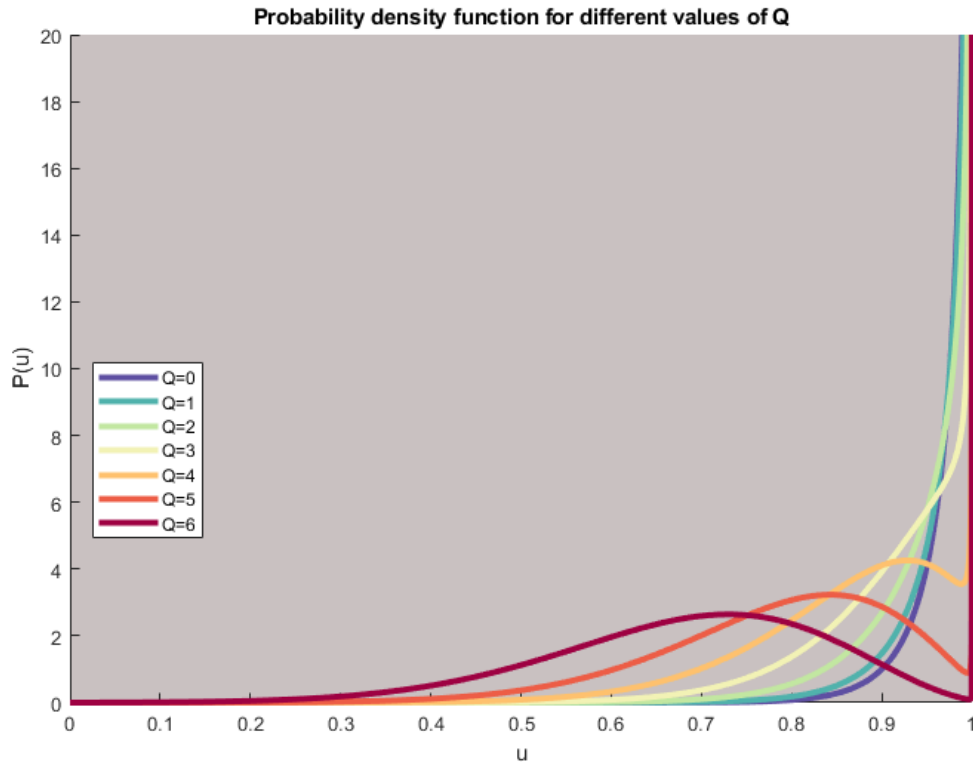


Fig. 4.16 Figure showing how the $P(u_{fp})$ distributions change with changing scattering vector Q . The distributions are similar to those seen in the capillary geometry for low Q , but change significantly for higher Q

The distributions are similar to those seen in the capillary geometry in figure 4.15 for low Q , but change significantly for higher Q . When considering monolayer patterns, generally only peaks below the 002 graphite peak ($Q = 1.8$) are considered. Hence the changes in the lineshapes will be minimised for the systems studied.

The overall effect of the alternate geometry can be seen in figure 4.17. This figure has been prepared for a hypothetical diffraction pattern with peaks at $Q = 0.5, 1, 1.5, 2, 2.5 \text{ \AA}^{-1}$ all having equal intensity of unity. For both geometries the measured peak maximum decays with increasing Q due to the effect of the atomic form factor. However, the flat plate geometry exhibits a more rapid decrease in intensity with Q due to the geometric effects discussed. The peak at $Q = 2.5 \text{ \AA}^{-1}$ is approximately half the intensity of the same peak in a capillary geometry diffractogram.

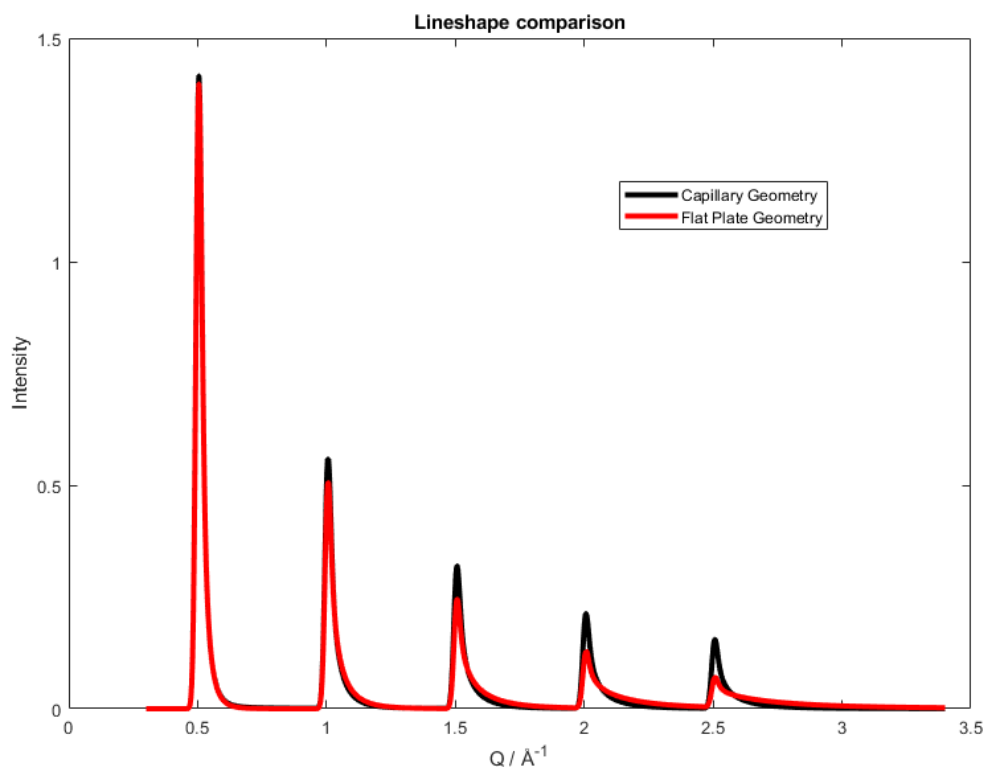


Fig. 4.17 Figure showing the modelled diffractograms for a hypothetical pattern with five peaks with unit intensity at $Q = 0.5, 1, 1.5, 2, 2.5 \text{ \AA}^{-1}$. The flat plate geometry is seen to have a sharper drop-off in peak intensity with Q , as well as marginally broader peaks at higher Q

This loss of intensity from the flat plate geometry relative to the capillary at first implies this to be a sub-optimal geometry for data collection. However, it becomes more useful with the addition of an area detector that can collect scattered beams from the whole Debye-Scherrer ring. In a capillary geometry experiment only a small segment of the ring is captured. Exact calculation of the improvement in detection efficiency requires detailed knowledge of a particular sample. However, it is at least 6x, as the mosaic spread angle of the graphite means that at most two 30° regions give in plane scattering in a capillary geometry, meaning that $60/360 = 1/6$ of the total detector area is utilised. Thus overall the flat plate geometry remains more favourable for collecting diffraction data at low angles.

The other noticeable difference in figure 4.17 is that, especially at higher values of Q the flat plate geometry lineshapes exhibit longer tails. Again the effect is relatively small for the low values of Q considered, but this is an important correction to consider when fitting coherence lengths of diffraction patterns to experimental data.

The nature of the flat plate geometry means that several mathematical approximations made by Schildberg and Lauter are no longer valid. This means that the flat plate lineshapes are significantly more computationally expensive to calculate. Typically they take 1000 times as long to calculate as the equivalent capillary geometry lineshapes, even when fully parallelised. As such, and considering the comparatively minimal differences in form, the classic capillary geometry lineshapes were largely used for initial structure calculation and optimisation, with the flat plate lineshapes only being used for a final fitting step. Throughout this work the lineshape being presented will be made clear in the figure caption.

Chapter 5

Triiodotrifluorobenzene

In this section the X-ray diffraction technique discussed in chapter 3 shall be used to identify and characterise the monolayer assembly of triiodotrifluorobenzene (TITFB). Initially the monolayer structure will be identified, and then in subsequent sections the behaviour of TITFB when co-deposited with two halogen bond acceptors will be reported. These experiments were designed to better understand whether TITFB has the capability to form porous monolayer structure.

5.1 Introduction

As discussed in Chapter 1, nearly all work considering the formation of halogen bonds at surfaces has utilised aromatic halogen bond donors. This is because of the comparatively strong (for a physisorbed system) interaction between aromatic systems and most surfaces, as well as the planarity inherent in the 2D nature of an aromatic system. Clarke et al. reported the assembly of a co-crystalline monolayer of 1,4-diiodotetrafluorobenzene with 4,4'-bipyridine on graphite,¹¹² while Brewer et al. further investigated the effect of substitution of fluorine with hydrogen¹¹³ or of iodine with bromine.¹¹⁴ Interestingly despite the strong evidence for crystalline monolayer formation no 2D structure could be deduced for the monocomponent monolayer of 1,4-diiodotetrafluorobenzene (DITFB).

To form a porous network it is necessary that at least one component have a coordination number greater than two. Building upon the previous work one potential candidate molecule to study is 1,3,5-triiodo-2,4,6-trifluorobenzene (TITFB). The structure of TITFB is shown in figure 5.3b. This molecule can be considered to be a the three-fold analogue of DITFB. In bulk supramolecular systems TITFB has been shown to interact with halogen bond bases to form co-crystals.^{45,46}

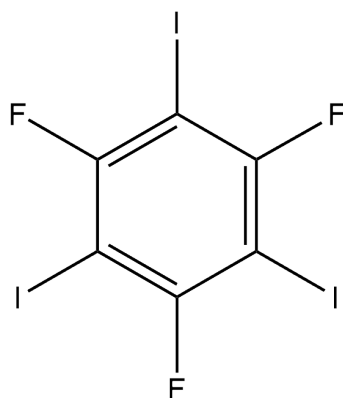


Fig. 5.1 Chemical structure of 1,3,5-triiodotrifluorobenzene (TITFB)

At a liquid-graphite interface, TITFB has also been observed to form halogen bonds, Zheng et al. found that TITFB could interact with halogen-bond bases to form ordered structures. Intriguingly, several of these systems were only observed to form after application of a high voltage pulse from an STM tip. Several of these layers are reported to be porous, but as they were observed under a phenyloctane solution the pores are likely to be at least transiently occupied by solvent molecules.¹⁵⁷ Assembling similar systems at the solid-air interface would indicate that halogen bonds are capable of supporting porous monolayer structures even in the absence of guest solvent molecules occupying the pore.

5.2 Monocomponent

5.2.1 Introduction

Before considering the interaction of TITFB with halogen bond accepting groups on other molecules, it is instructive to first study the behaviour of the monocomponent system on graphite. This helps to provide a point of comparison for any co-crystal structures that may be observed, as well as being an interesting topic of investigation in its own right. In the monocomponent system the lack of strongly basic atoms means that any layer formed can only be stabilised by halogen-halogen interactions. As discussed in section 1.2.3 halogen-halogen contacts come in two types; type I and type II.⁴² These are defined by the angles shown in figure 5.2a. Type I contacts exist where $\theta_1 \approx \theta_2$ and are simply the result of the VdW close-packing of large, polarisable, halogen atoms.

Type II contacts are equivalent to a halogen bonds containing an electron-rich halogen atom as the halogen bond acceptor. They ideally have $\theta_1 = 180^\circ$ and $\theta_2 = 90^\circ$, though can vary from this geometry.

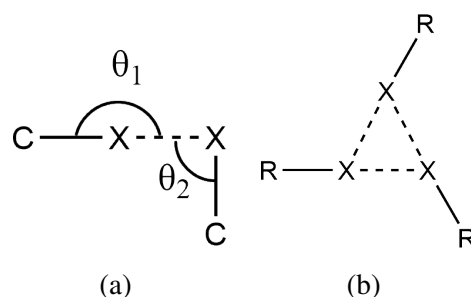


Fig. 5.2 (a) Schematic of the key parameters θ_1 and θ_2 used to characterise halogen-halogen contacts. If $\theta_1 \approx \theta_2$ the contact is type I and not considered halogen bonded. Type II contacts typically exhibit $\theta_1 \geq 150^\circ$ and $\theta_2 \leq 120^\circ$. For an ideal halogen bond $\theta_1 = 180^\circ$ and $\theta_2 = 90^\circ$. (b) Schematic of the X_3 motif, which consists of three type II contacts in a trigonal geometry.

In systems of this type, a particularly interesting motif is the X_3 shown in figure 5.2b. This motif was first identified in the bulk crystal structure of trihalomesitylene molecules,¹⁵⁸ and has since been recognised in several other halogen bonding systems.^{159,160,161} The motif consists of a trigonal arrangement exhibiting three type II contacts, with each halogen atom acting both as a halogen bond donor and acceptor.

The significance of this motif is that it contributes a versatile three-fold symmetric vertex for the construction of supramolecular scaffolds. Molecules exhibiting structural and chemical similarity to the trihalomesitylene compounds are therefore of significant interest, as they may also give rise to exploitable X_3 motifs in their intermolecular interactions. X_3 motifs have been observed in bulk crystal structures isomorphic to triiodomesitylene such as 1,3,5-triiodo-2,4,6-trichlorobenzene and 1,3,5-triiodo-2,4,6-tribromobenzene.

Interestingly however bulk TITFB does not exhibit this motif. Instead it has been observed to adopt a corrugated structure with multiple type II contacts to adjacent out-of-plane TITFB molecules (see figure 5.4). The fact that bulk TITFB differs from its chloro and bromo analogues, as well as triiodomesitylene, in not exhibiting a planar structure based around a X_3 halogen bonding motif is initially surprising due to these molecules' structural similarity. The apparent anomaly was ascribed by Reddy et al. to the destabilising effect of large voids that would be left in the TITFB-based structure due to the significantly smaller size of fluorine atoms relative to bromine, chlorine or methyl groups.¹⁶²

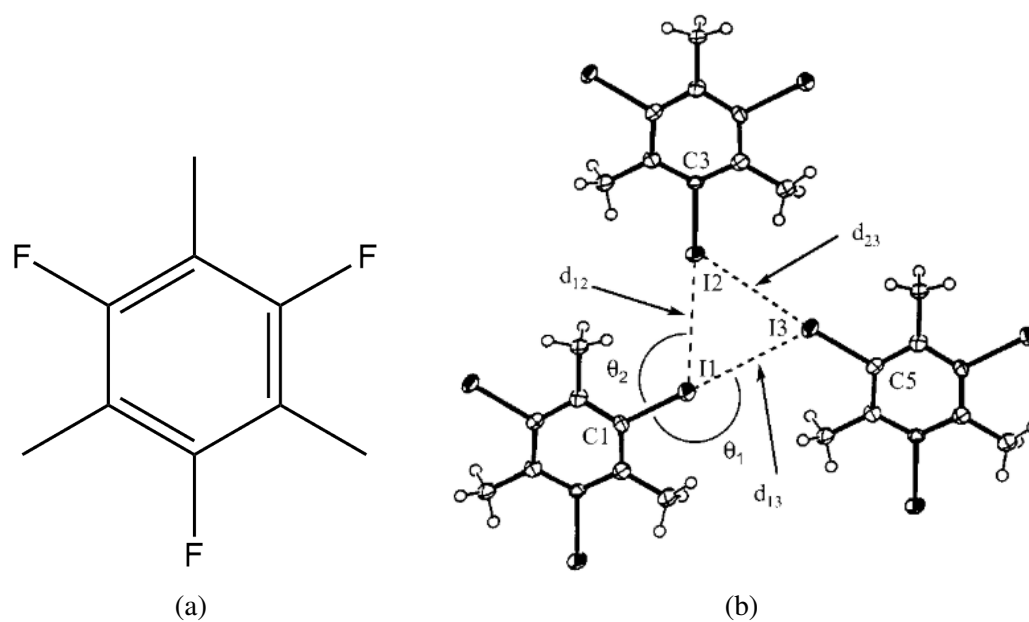


Fig. 5.3 (a) Chemical structure of triiodomesitylene, the first species shown to exhibit the X_3 halogen bonding motif. (b) Figure taken from 158 showing the bulk structure identified for this molecule

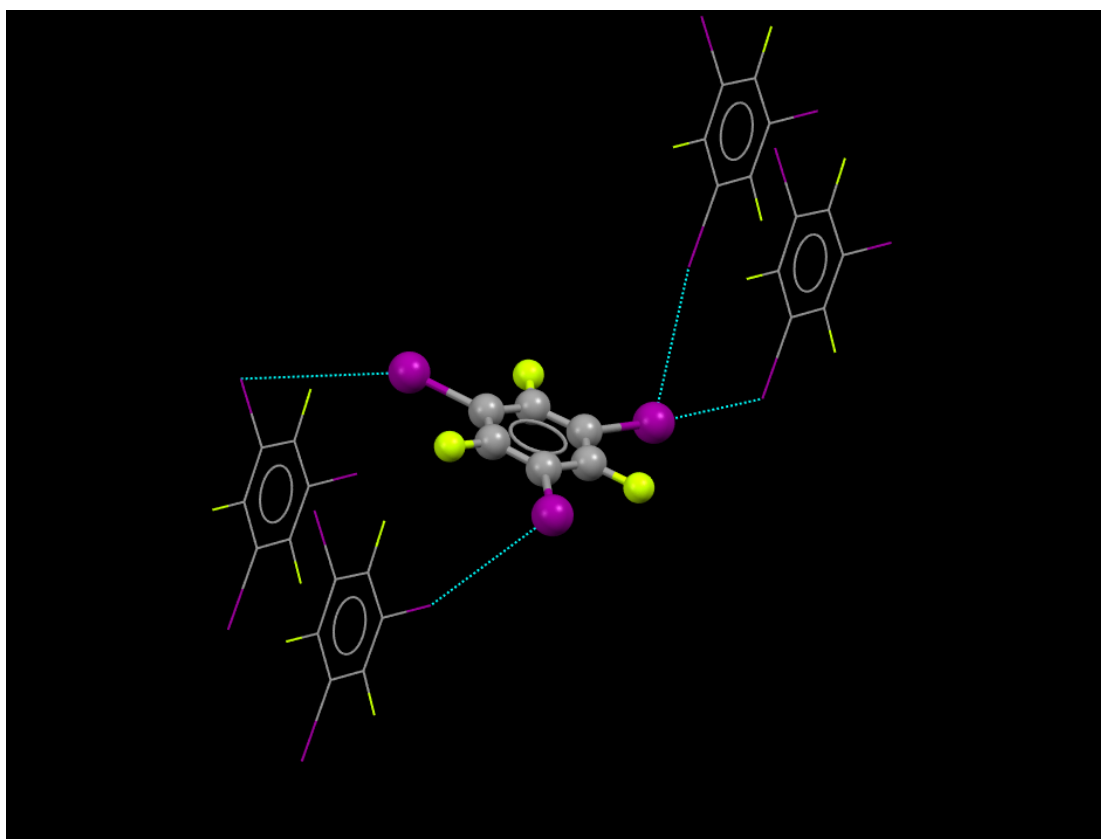


Fig. 5.4 Visualisation of the bulk structure of TITFB collected by Reddy et al, deposited in the CSD as UCEPEY. 162

Although the bulk structure of TITFB has been reported, intriguingly the structure of the single component TITFB monolayer has thus far resisted analysis. When studied under phenyloctane solution using STM in ambient conditions Zheng et al. were able to report on imaged co-crystals but could not obtain an image from the monocomponent TITFB system.¹⁵⁷ This was attributed to the effect of solvent displacement of the TITFB from the surface. A later DFT simulation found that planar adsorption was predicted to be more favourable, though considered only interactions between a single TITFB molecule and a very small flake of hydrogen terminated graphene, not graphite.¹⁶³

Although no previous study has identified the monolayer structure of TITFB, related molecules have been successfully imaged using low temperature STM on metal surfaces. Hexabromobenzene on gold (77K)¹⁶⁴ and hexafluorobenzene on silver (5K)¹⁶⁵ have both been found to adsorb in a planar geometry, with close halogen-halogen contacts between adjacent molecules. F-F contacts have been identified to be type I (close packing) in nature, while Br-Br contacts are type II (halogen bond). This is consistent with expectations, as the F atom's low-energy orbitals mean that the σ -hole is not present. However, metal surfaces exhibit stronger interactions with adsorbates than graphite surfaces, so care must be taken in generalising these results to monolayers on graphite or other weakly adsorbing substrates. No STM images of small perfluorinated aromatic molecules on graphite have previously been reported. It is possible that this is due to comparatively weak binding to the surface that renders the layer prone to perturbation by the STM tip, or that the electronic properties of molecules of this type are unfavourable for high-resolution STM imaging.

5.2.2 Experimental

Diffraction data was collected as described in section 2.2.4 using the rotating anode diffractometer at the LMB. Patterns were collected at a cryostream temperature of 100K to freeze any layer and minimise thermal motion, and a detector-sample distance of 250 mm to optimise the scattering angle range accessible. TITFB (Acros Organics, 97%) was dosed onto the papyex at 523 K under reduced pressure and allowed to cool to room temperature before being retrieved and mounted for study.

5.2.3 Results

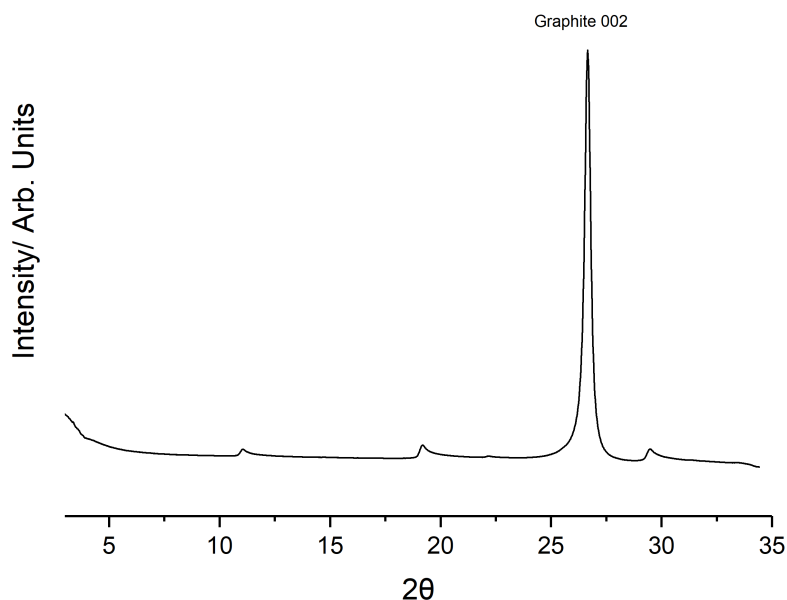


Fig. 5.5 Collected diffractogram of papyex dosed with TITFB, the Graphite {002} peak is labelled. Below 5° small-angle scattering is significant. In addition to the bulk graphite peak several additional "sawtooth" peaks of much lower intensity can be seen.

The raw collected diffractogram for graphite dosed with TITFB is presented in figure 5.5. There is a large symmetric peak at $2\theta = 27^\circ$ consistent with the 002 reflection of the graphite substrate. In addition to this, there are several asymmetric "sawtooth" type peaks evident only in the dosed graphite diffractogram. The most significant of these peaks occur at $2\theta = 11^\circ, 19^\circ$ and 30° . As discussed in section 2.2.9 this sawtooth shape is indicative of monolayer diffraction peaks, the peak asymmetry originates from the presence of Bragg rods from the 2D periodicity of the monolayer. Below 5° small-angle Porod scattering is evident. As discussed in section 2.2.10 this scattering can be subtracted using a fitted function varying as Q^{-4} . After subtraction of the Porod scattering term it was not possible to identify any further peaks at lower angles.

As discussed in chapter 2 subtraction of the pattern of a bare graphite allows isolation of the monolayer peaks. By examining the locations of these peaks it is possible to index them to a 2D unit mesh. High symmetry unit meshes are preferred to constrain the fitting. For this system the peak positions were indexed to a relatively high symmetry hexagonal unit mesh with $p3$ symmetry ($a = b = 9.28(7) \text{ \AA}$, $\gamma = 60^\circ$).

It is important to note that this cell is not commensurate to the underlying graphite hexagonal lattice $a = 2.461 \text{ \AA}$, meaning that the overlayer lattice cannot be represented by linear transformations of the underlying graphite unit mesh. The overlayer not being commensurate indicates that inter-adsorbate molecular interactions are dominant over molecule-substrate interactions in determining the periodicity of the layer. The area of the overlayer cell is 74.7 \AA^2 which is only slightly larger than the summed areas of the Van der Waals radii of the component atoms of a TITFB molecule (62.7 \AA^2). The slight increase in unit mesh area compared to molecular area would be consistent with imperfect packing of TITFB in the layer. The interpretation of a flat lying TITFB monolayer structure is further supported by the 3-fold symmetry of the unit mesh (since the rotational symmetries of the molecule and of the unit cell can match only if the molecule lies flat on the surface). This symmetry greatly constrains the position of the TITFB molecule, and indeed treating TITFB as a rigid body leaves rotation within the plane of the substrate as the only remaining degree of freedom. This degree of freedom can be represented by means of a rotation angle, ω , defined relative to the molecular orientation in which iodine atoms from adjacent TITFB molecules point directly along the primitive lattice vectors.

Using the lineshape prediction method described in chapter 2 the best fit to the experimental data is achieved when $\omega = 11.5^\circ$, leading to the monolayer structure depicted in figure 5.6a. Figure 5.6b compares the predicted diffraction pattern for this model to the experimentally collected data after substrate subtraction. An excellent match can be seen between the experimental data (black) and the modelled data (blue). Rotation of just a few degrees in either direction dramatically worsened the peak intensity fit. The slight underestimation of intensity in the first peak is likely due to the absence of Debye-Waller temperature factors in this model. As discussed in the experimental chapter these are ignored so as to constrain the fitting. As TITFB is a fairly rigid molecule, the magnitude of these temperature effects would be expected to be minimal.

The structure presented in 5.6a shows the iodine atoms of adjacent TITFB molecules adopting the distinctive X_3 motif discussed in section 5.2.1. The small size of the fluorine atoms leads to some empty space in the structure, though at approximately 3.25 \AA the pore size is too small to be of interest for guest occupancy. Within the X_3 motif each C-I bond points very nearly directly towards an iodine atom in a neighbouring molecule, yielding values of $\theta_1 = 163.2^\circ$ and $\theta_2 = 103.2^\circ$ and suggesting a Type II (halogen bond) interaction. In contrast, the C-I bonds point quite wide of the fluorine atoms on neighbouring molecules, yielding $\theta_1 = 148.2^\circ$ and $\theta_2 = 148.0^\circ$ and suggesting a Type I interaction (non-halogen bonded) between the I and F atoms. This is expected due to the high electronegativity

System	lattice vector (a) / Å	$\omega / ^\circ$	C-I...I		
			$\theta_1 / ^\circ$	$\theta_2 / ^\circ$	$d(I...I) / \text{Å}$
TITFB expt	9.29	11.5	163.2	103.2	4.08
Bulk triiodomesitylene ¹⁵⁸	9.59	18.9	170.7	119.4	3.90
Bulk triiodotrichlorobenzene ¹⁶²	9.44	17.61	169.5	115.6	3.83

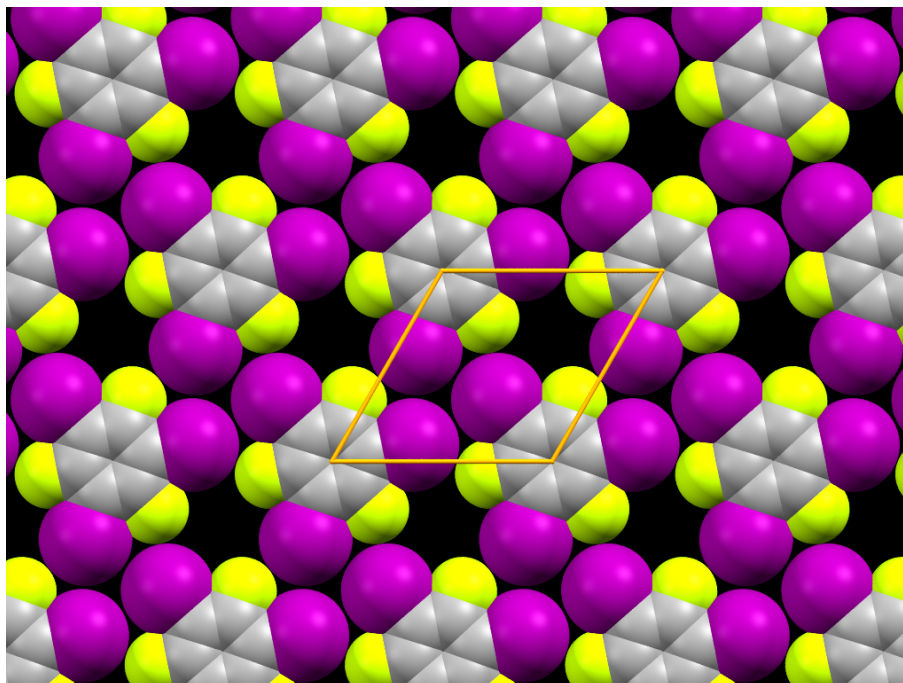
Table 5.1 Key geometric parameters for several relevant systems. θ_1 and θ_2 are defined in figure 5.2a. The literature structures were not symmetrically constrained, and so the average of the three distinct values for the X_3 motif are used.

and low polarisability of the F atoms making them poor halogen bond donors or acceptors respectively.

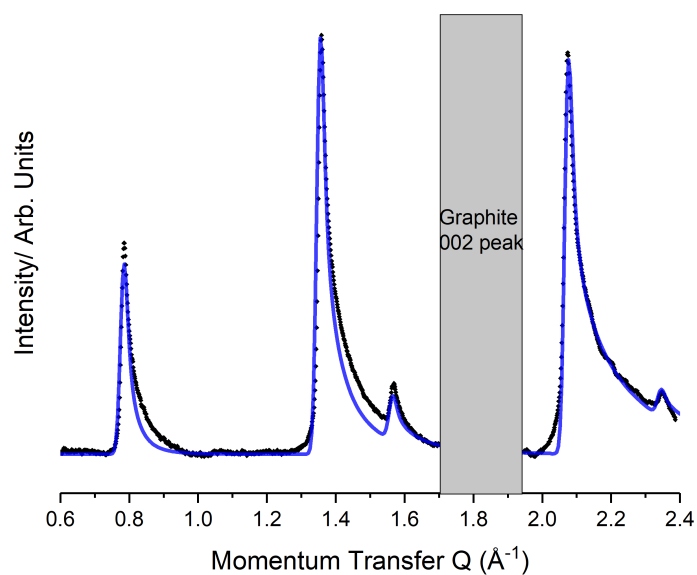
The structure displayed in figure 5.6 can be compared to planes of the bulk lamellar structures reported for 1,3,5-triiodomesitylene¹⁵⁸ and 1,3,5-triiodotrichlorobenzene.¹⁶² Table 5.1 compares a few key parameters for these systems. As the literature reported structures were not symmetry constrained and there is some minor variation in the angles, the reported values are the average of the three distinct contacts of the X_3 motif.

The distance between adjacent molecules is slightly smaller for the TITFB monolayer than the methyl and chloro equivalents. This is consistent with the structures compensating for the small size of the fluorine atoms by "squeezing together" to minimise the void space in the structure. Interestingly although the lattice constant of the TITFB layer is smaller, the I...I separations are slightly larger (4.1 Å vs 3.9 Å). The ω value for the TITFB is also smaller (11.5° vs 17.5°). Since ω is defined as the angle relative to the lattice vectors this indicates that the iodines in the TITFB molecule point further away from each other than in the analogue bulk structures. This is consistent with the small size of the fluorine atoms modifying the packing, causing the molecules to both squeeze together and twist to minimise the void space. Thus, even for this strongly polarised halogen bond donor, the X_3 motif is insufficiently strong to entirely override close-packing effects.

In summary, we have successfully obtained the 2D diffraction pattern from TITFB monolayer and fitted the data with a high symmetry, highly constrained 2D crystal structure with X_3 halogen bonded motif.



(a) Optimised experimental structure for the TITFB monolayer. The unit mesh is hexagonal with lattice parameters $a=9.28(7) \text{ \AA}$ $\gamma = 60^\circ$.



(b) Comparison between the X-ray diffraction pattern of TITFB at 100K after background subtraction (black) with the modelled pattern (blue) for the structure shown in figure 5.6a using the flat plate geometry lineshape derived in chapter 3.

Fig. 5.6 Comparison between the experimental (black) and modelled (blue) diffraction pattern for the TITFB monolayer structure shown in (a)

5.3 Co-deposition of TITFB with Bipyridine

5.3.1 Introduction

As discussed above there is much interest in bi-component halogen bonded systems. Here we consider TITFB and the previously studied bitopic halogen bond acceptor bipyridine.

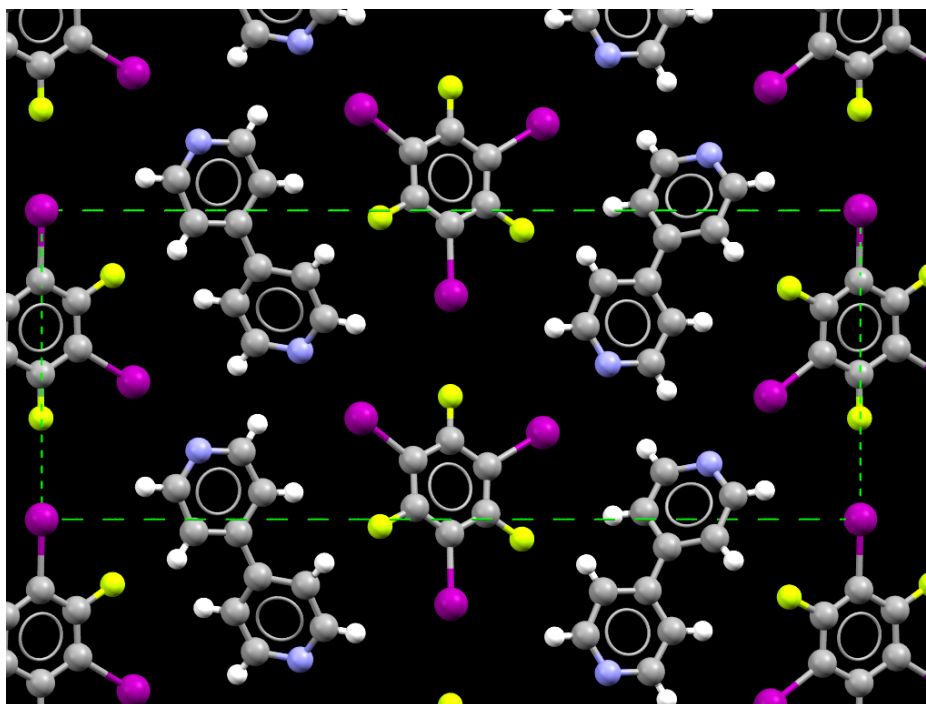


Fig. 5.7 Visualisation of a single plane of the lamellar co-crystal structure found by Lucassen et al. upon evaporation of a chloroform solution of 2:3 TITFB and BPY in the bulk.¹⁶⁶ Each TITFB molecule forms two halogen bonds, with a third type I I...F contact. The in-plane lattice constants are $a = 27.396 \text{ \AA}$, $b = 9.056 \text{ \AA}$, $\gamma = 90^\circ$

The tritopic halogen bond donor TITFB might be expected to form a hexagonal co-crystal with large pores when present in a 2:3 ratio with a bitopic linear halogen bond acceptor. Such behaviour would require a large deviation from close-packing behaviour, but is an intuitive advance from the 1,4-diiodotetrafluorobenzene:BPY system considered previously.¹¹²

Lucassen et al structurally characterised the bulk co-crystal from TITFB with BPY in the bulk. They found crystallisation from evaporated chloroform yielded a lamellar 1:1 cocrystal with two halogen bonds and a close-packed I...F type I contact.¹⁶⁶ Figure 5.7 shows a visualisation of one plane of the lamellar crystal. The in plane lattice constants are $a = 27.396 \text{ \AA}$ and $b = 9.056 \text{ \AA}$, while $\gamma = 90^\circ$.

It was unclear whether the 1:1 chain structure was favoured over a lamellar structure due simply to close packing, or if charge transfer led to a build-up of negative charge on the TITFB, reducing the σ -hole. Lucassen et al performed some initial DFT results which indicated that there was some weakening of the third halogen bond, but that it would still be thermodynamically favourable to form.

Co-deposition of TITFB with BPY on graphite was also previously performed by Adam Brewer¹²⁵ in a 2:3 ratio. The deviation from close-packing in forming three halogen bonds would be expected to be lessened in two dimensions compared to three. The analysis in the thesis consisted solely of demonstrating that the collected pattern was not consistent with the desired hexagonal porous pattern. In this work a more detailed treatment is performed, and a monolayer structure determined.

5.3.2 Experimental

Experiments combining TITFB with bipyridine were some of the first diffraction experiments performed during this work. As such the samples were prepared using the remaining papyex substrate code BPI004J utilised by Adam Brewer.¹²⁵ This graphite is 1 mm thick, and had already been characterised by Dr Brewer as having a mosaic spread angle of 29.1° and an isotropic fraction (f) value of 0.32 and so it was considered unnecessary to re-characterise it. Samples were prepared in keeping with the method described in section 2.2.4 using graphite substrate code BPI004J, TITFB (Acros Organics, 97%) and BPY (AlfaAesar, 97%). The components were dosed at 353 K in the apparatus described previously and cooled for study.

Collection of the diffraction data was performed by Dr Tom Arnold at the Diamond Light Source using beamline I11. A wavelength of 0.8266 Å was used and verified by a silicon standard. The data was collected in capillary geometry.

5.3.3 Results

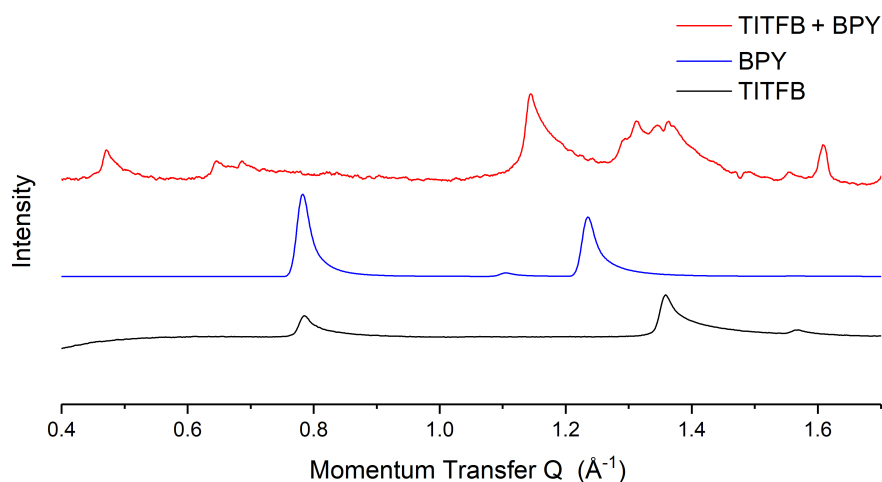


Fig. 5.8 Comparison of the obtained diffraction pattern for graphite co-deposited with TITFB and BPY, with those of the monocomponent systems. The co-deposited layer can be seen to exhibit distinct peaks, indicating it consists of a novel phase and not simply phase separated domains of BPY and TITFB

Figure 5.8 presents the diffraction pattern obtained when TITFB and BPY were co-deposited on graphite in a 1:1 ratio and compares it to that collected for TITFB and BPY alone. Most significantly the collected pattern from the combination is novel and not simply an addition of the two monocomponent diffraction patterns, indicating formation of a new co-crystal phase. It is especially notable that the lowest angle peaks of the co-deposited layer occur at lower Q values than for either individual component. This indicates the co-crystal unit mesh is larger than either monocomponent unit mesh as expected. Interestingly it was not possible to index the co-crystal peaks to the expected three-fold symmetric mesh. Instead the pattern was indexed to a unit mesh with parameters $a = 26.795 \text{ \AA}$, $b = 9.749 \text{ \AA}$ and $\gamma = 90^\circ$. From the indexing it is notable that there is an additional peak that doesn't match this unit cell. The peak occurs around $Q = 1.6 \text{ \AA}$ and is symmetrical rather than sawtooth in shape, as can be seen in figure 5.8. This peak occurs due to formation of bulk crystalline ice on the outside of the capillary. This is an often unavoidable artifact of data collection at low temperatures, and the peak shall be ignored in all subsequent analysis.

This indexed mesh is close, but slightly different to that measured from analysis of a single lamellar plane of the structure deposited in the CSD by Lucassen et al ($a = 27.396 \text{ \AA}$, $b = 9.056 \text{ \AA}$, $\gamma = 90^\circ$). It is likely that the main driving forces determining the plane structure are similar, but that the absence of adjacent lamella, and presence of the graphite modify the structure slightly.

Although low-angle peaks are difficult to determine as they are superimposed onto the small angle scattering caused by the size of the crystallites, there is no evidence of the $\{10\}$ peak which would be expected from the indexed mesh at $Q = 0.23 \text{ \AA}^{-1}$. The $\{30\}$ reflection at 0.703 \AA^{-1} is also weak or absent. These systematic absences are consistent with a Pg symmetry with glide planes parallel to the a lattice vector (Pg_a). As expected from Brewer's work, this symmetry is inconsistent with the "chickenwire" type monolayer structure that might be expected from a porous three fold mesh.

The best fit to the observed experimental diffraction pattern is consistent with a chain structure analogous to that found in the bulk.¹⁶⁶ This structure is shown in figure 5.9 and the comparison of the experimental and predicted diffraction patterns in figure 5.10. The fit is not perfect, however no sensible alternate structure gave as close a fit. The inconsistencies between the experimental and modelled diffraction patterns are likely due to the rigid body assumption made in the fitting, and discussed in chapter 2.

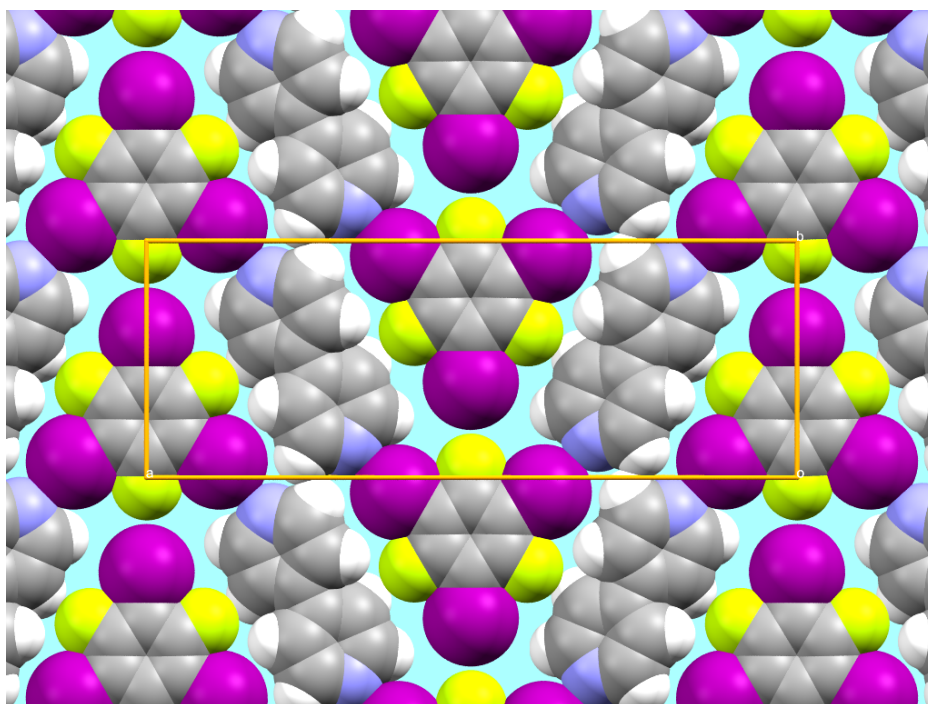


Fig. 5.9 Visualisation of the modelled structure of the cocrystal formed between TITFB and BPY

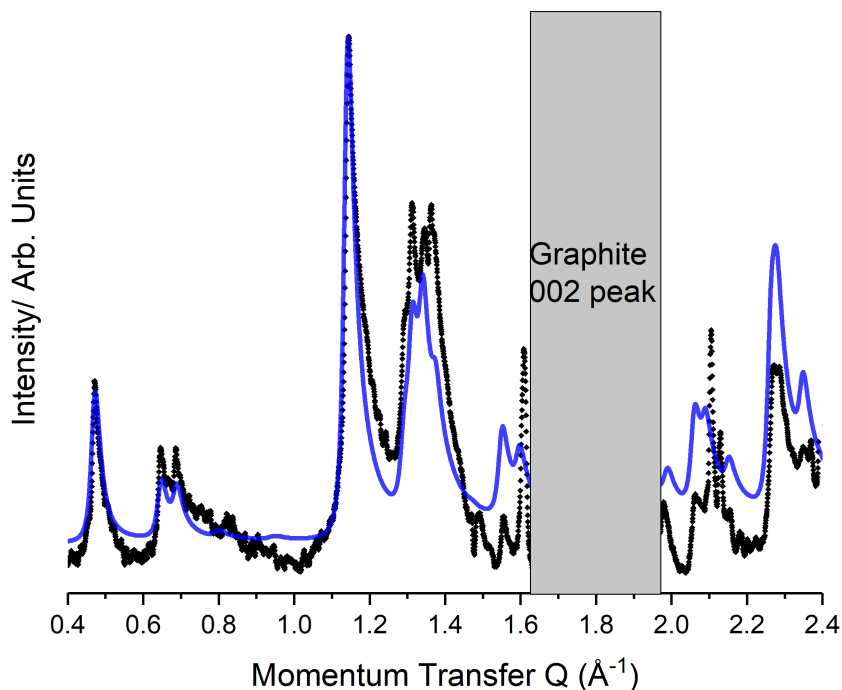


Fig. 5.10 Comparison between the experimental (black) and predicted (blue) diffraction pattern for the TITFB:BPY co-crystal

5.3.4 Conclusion

Although it is often observed that monolayer co-crystal structures can differ significantly from the bulk structure, for the case of TITFB+BPY it seems the same factors preventing the bulk structure from forming a porous lamellar structure also prevents formation of a porous monolayer structure. The loss of binding energy in not forming a third halogen bond must be more than compensated in the close packing of the chains.

5.4 Co-deposition of TITFB with Triazine

5.4.1 Introduction

The fact that the TITFB:BPY system formed a close-packed system rather than an open porous structure indicates the high cost of forming porous networks due to the reduction in Van der Waals interactions. If a three-fold symmetric halogen bond acceptor is used

alongside TITFB, this would minimise the size of the pores and so potentially reduce the energetic cost of forming a porous mixed layer.

5.4.2 Experimental

Experiments combining TITFB with s-triazine were performed on papyex batch BPI004L. Samples were prepared in keeping with the method described in chapter 2.2.4 using TITFB (Acros Organics, 97%) and triazine (AlfaAesar, 97%). The components were dosed at 323 K and slowly cooled to crystallise any layer for study in the apparatus described previously. Diffraction experiments were performed on the rotating anode instrument described in chapter 3, with the cryostream set to a temperature of 100 K.

Results

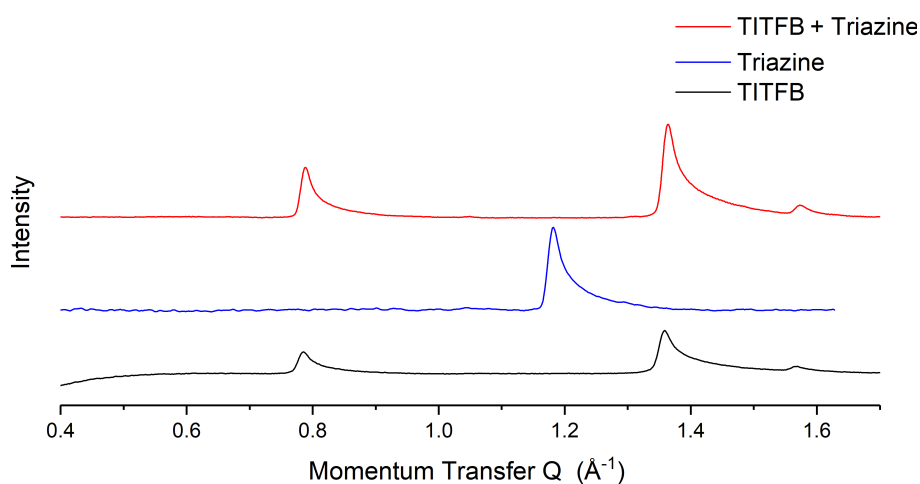


Fig. 5.11 Comparison between the experimental patterns of TITFB, triazine, and a TITFB+triazine co-deposited sample. The three patterns are scaled to be the same intensity. The co-deposited sample is near identical to the TITFB monolayer pattern. (The experimental triazine monolayer structure will be analysed in the next chapter).

Figure 5.11 compares the diffraction pattern obtained when TITFB and triazine were co-deposited with the diffraction patterns for the components individually. It can be seen that the diffraction pattern of the co-deposited layer is almost identical to that of the TITFB monolayer. It should be noted that in this figure the patterns are scaled to be approximately the same intensity. In reality the scattering power of TITFB is significantly greater than triazine, due to the larger number of heavy elements. Figure 5.12 utilises the modelled patterns of TITFB and triazine, so that the absolute magnitude of scattering from the two

systems can be compared. It can be seen that the observed co-deposited diffraction pattern is consistent with a simple addition of the diffraction patterns of the two components. This indicates phase separation has occurred and means that the binding energy of the respective pure monolayers is greater than that of any possible co-crystal structure.

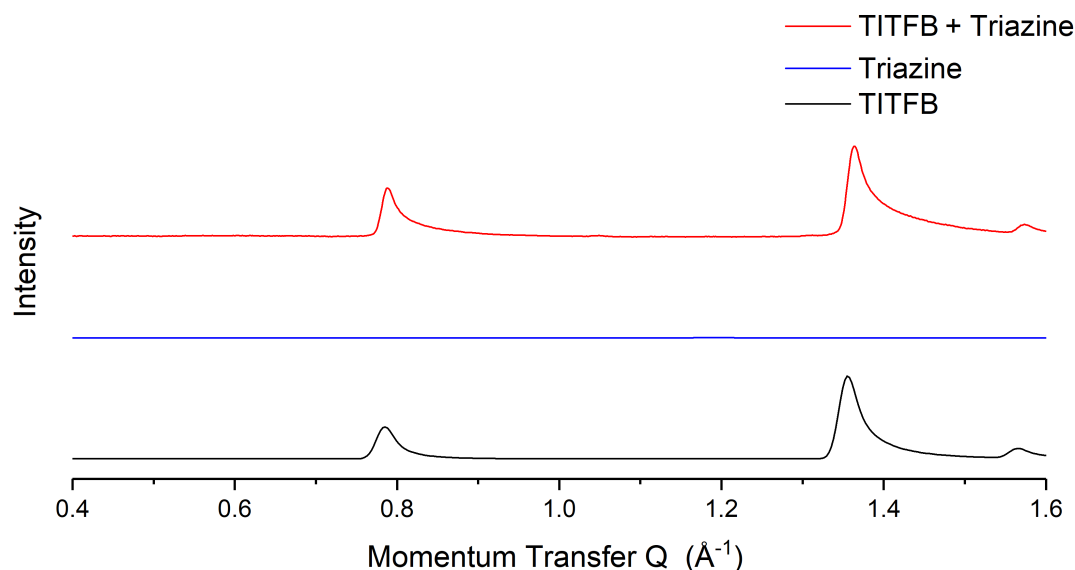


Fig. 5.12 Comparison between the experimental TITFB+triazine co-deposited sample and the modelled patterns of triazine and TITFB plotted in absolute magnitude. The scattering power of triazine is orders of magnitude less than TITFB and so the TITFB scattering dominates the scattering of the co-deposited layer.

5.4.3 Conclusion

The crystalline structure of a monolayer of 1,3,5-triiodotrifluorobenzene (TITFB) on graphite has been structurally characterised. The monolayer is found to consist of flat-lying TITFB with threefold X₃ halogen-halogen contacts between adjacent molecules.

When TITFB and the putative halogen bond acceptor triazine were co-deposited on graphite, it was found that they do not mix and instead phase separates. This indicates that the binding energy from the formation of a putative halogen bonded co-crystal is less than that of the respective monolayers.

Chapter 6

Perfluoroalkane Halogen Bond Donors

6.1 Terminally Iodinated Perfluoroalkanes

6.1.1 Introduction

As discussed in section 1.4.7 the previous work on halogen bonding at surfaces has to date utilised solely aromatic halogen bond donor molecules. The reason for this is the strong interaction between the aromatic system of the adsorbate and the graphite substrate. Strong adsorbate-substrate interactions help to promote crystalline monolayer formation by maximising the total binding strength of a crystalline monolayer. However, as seen in the previous chapter it has not been possible to use these aromatic halogen bond donors to form a porous layer. Published literature has also observed difficulty in using halogen bonding to predictably assemble desired monolayer structures. Some systems were successful in forming desired structures, but the structures were observed to only be stable when the pores were filled with solvent or guest molecules, so in this sense are not truly porous layers.¹⁶⁷

Given the failure of several hypothesised porous networks to form, detailed previously, changing the nature of the halogen bond donor represents a logical next step in rational design of a porous layer, and also builds on the growing fundamental basis as more halogen bonded co-crystals are added to the literature.

α,ω -diiodinated perfluoroalkanes have been previously used in a range of bulk halogen bonding systems.^{168,169,37,170} The high fluorination of the molecule means that the terminal iodines have a substantial affinity for nucleophiles, though the magnitude of the sigma hole is generally estimated to be somewhat less than in perfluorinated aromatic systems. As shall be discussed in the next section, the nature of the perfluoroalkane chain means that the packing property of this class of molecules is subtly different to the previously explored aromatic systems. In this work we shall designate the α,ω -diiodinated perfluoroalkanes with a name

of the formula $C_nF_{2n}I_2$ (e.g. $C_4F_8I_2$) where n indicates the number of carbon atoms in the alkyl chain.

Nature of the perfluoroalkyl chain

A key difference between aromatic halogen bond donors and those with a perfluoroalkyl chain is the nature of the backbone. Aromatic systems have an intrinsically rigid sp^2 hybridised backbone, minimising degrees of freedom and the ability of the molecule to contort. By contrast, hydrocarbon alkyl systems are generally thought of as flexible, with only a weak preference for the all-trans thermodynamic minimum geometry. Fluoroalkyl chains, though similar to hydrocarbon analogues, exhibit a different, helical, thermodynamically most stable state. The origin of this helical twist in perfluoroalkyl chains has been identified to be a mixture of steric and coulombic repulsion, with coulombic repulsion identified as the most significant.¹⁷¹ The fluoroalkyl chain can also be identified to be more rigid than hydrocarbon analogues¹⁷² indicating a greater preference for this helical thermodynamically most stable state and affecting the strength of intermolecular interaction.¹⁷³

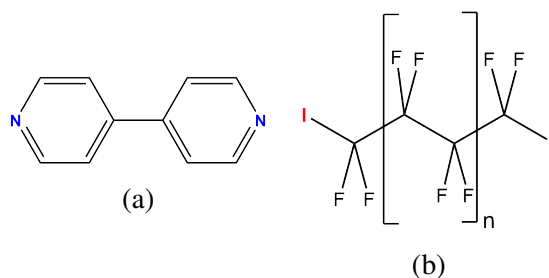


Fig. 6.1 Chemical structure of (a) 4,4'-Bipyridine (BPY) and (b) the family of terminally iodinated perfluoroalkanes used in this study. $n=1,2,3$ were studied. Halogen bond donating and accepting motifs are indicated

The assembly of perfluoroalkane monolayers on graphite has been previously reported by Parker et al. perfluoroalkanes from C6-C16 were studied, all of which formed crystalline monolayers at the low temperatures studied (10K). For all of the systems studied these crystalline layers were incommensurate with the underlying graphite lattice and consisted of the carbon backbone chain lying flat on the surface.⁸⁰ Additional calorimetry measurements of some of the layers found a range of melting temperatures from 189 K for C6 to 392 K for C14.¹⁷⁴ The interaction between the layers and the underlying graphite was observed to be relatively weak, exemplified by the displacement of the perfluoroalkane monolayer by stronger binding hydrocarbon alkane layers.¹⁷⁵ This low adsorption energy is symptomatic of the low polarisability of Fluorine, and hence the weak van der Waals (vdW) interactions

present between the chains. This relative weakness of the interchain interactions is key to crystal design, as it would be hoped to reduce the energetic cost in deviating from close-packing when forming a porous system.

Bulk Co-crystals

The assembly of halogen bonded co-crystals between 4,4'-bipyridine and short chain α,ω -diiodinated perfluoroalkanes has been previously reported in the bulk. It was found that the chains remained in the low energy linear conformation, and segregation between the hydrocarbon and perfluorinated segments was evident.¹⁷⁰ Figure 6.2 is a visualisation of the structure of the C₆F₁₂I₂:BPY cocrystal as deposited by the authors in the CSD structure QANRAS and visualises the segregation. The authors found the structures of the co-crystals of C₂,C₄,C₆,C₈, and C₁₀ α,ω -terminally iodinated perfluoroalkanes with BPY to be analogous, with increasing chain length serving only to enlarge the size of the unit cell.

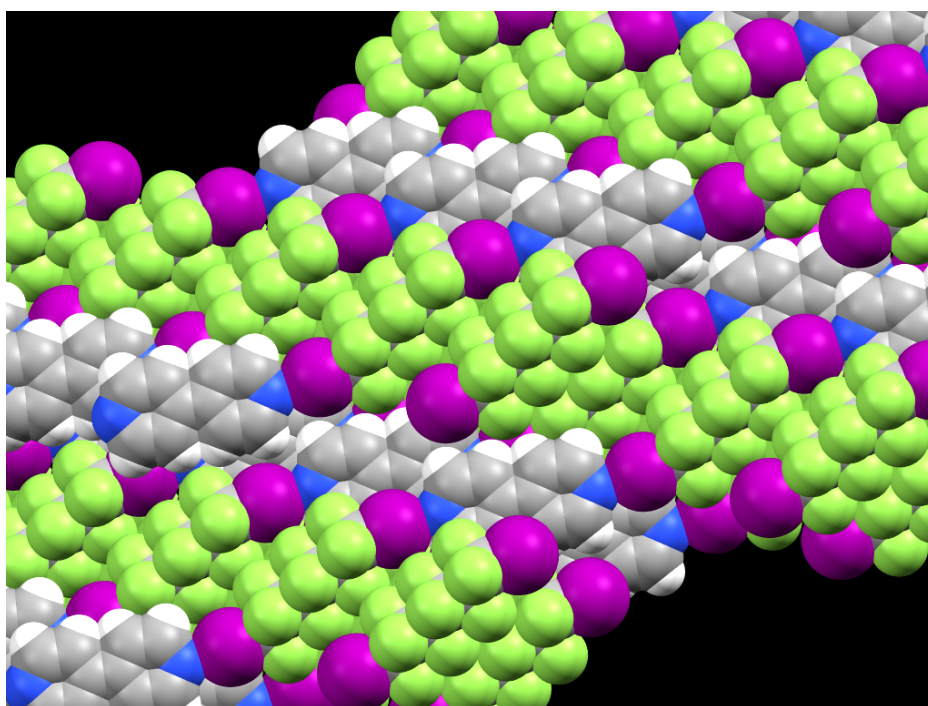


Fig. 6.2 Structure of the C₆F₁₂I₂:BPY cocrystal (CSD structure QANRAS) from reference 170. Segregation between the aromatic hydrocarbon BPY and perfluorinated C₆F₁₂I₂ chains is evident, assigned to the weak nature of C-H...F interactions

6.1.2 Experimental

Diffraction experiments were performed using the LMB rotating anode diffractometer described in chapter 2. The batch of Papyex used in this work was BPI004L. As characterised in section 4.2. The adsorbates used were purchased from commercial suppliers and used without further purification. Stated purities were 98% for 4,4'-Bipyridine (Alfa Aesar), 97% for C₄F₈I₂ (Fluorochem), 97% for C₆F₁₂I₂ (Alfa Aesar) and 98% for C₈F₁₆I₂ (Sigma Aldrich). Dosing was performed through the vapour phase as detailed in section 2.2.2

6.1.3 Monocomponent 2D systems

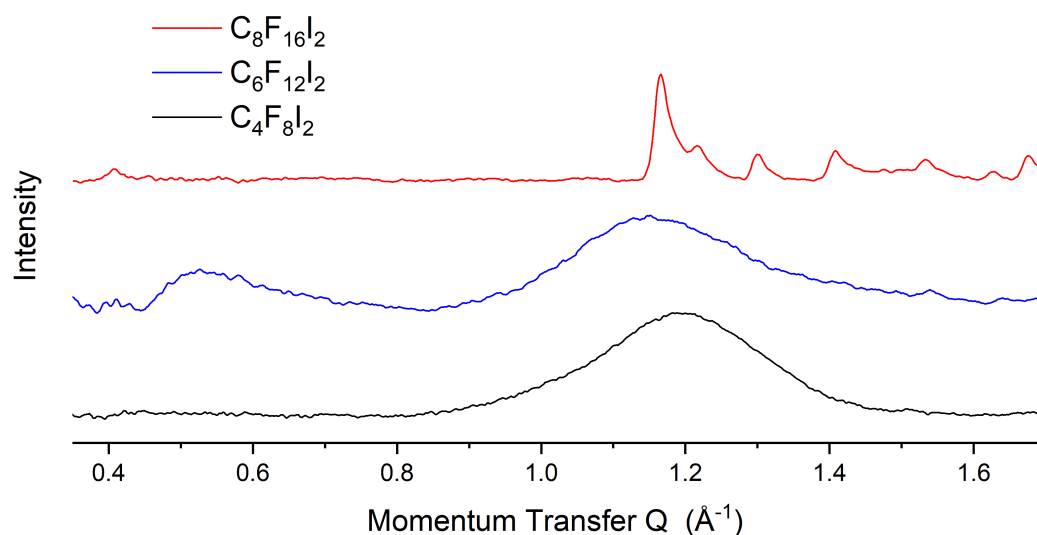


Fig. 6.3 Comparison of the diffraction patterns obtained for graphite dosed with the series of Halogen bond donors used in this study. Only the C₈F₁₆I₂ pattern shows evidence of crystalline monolayer

Before two-component systems can be studied, it is first necessary to understand the behaviour of the single-component systems on graphite. This can help confirm whether or not mixing has occurred in the multicomponent system, as well as providing information on the behaviour of the adsorbates as a single phase.

Figure 6.3 presents the low temperature (100K) diffraction patterns after background subtraction for graphite dosed with sub-monolayer coverage of three halogen bond donors. Incomplete subtraction of the strong 002 graphite peak at $Q = 1.8 \text{ \AA}^{-1}$ limits the high Q range of the pattern. Small angle Porod scattering limited the low Q range. However no significant diffraction features were observed below $Q = 0.3 \text{ \AA}^{-1}$.

For the graphite dosed with C₈F₁₆I₂ it is possible to discern “sawtooth” peaks in the observed pattern. The main features are at approximately $Q = 0.4$ and 1.2 \AA^{-1} with a good number of weaker features. The pattern can be indexed to a unit cell with pg symmetry, with a glide plane parallel to the a lattice parameter. The unit cell has lattice parameters $a = 31.38(2) \text{ \AA}$, $b = 5.52(5) \text{ \AA}$ and $\gamma = 90^\circ$. This is similar but slightly longer than the high symmetry Phase I centred structure previously reported for perfluorooctane.⁸⁰ The peak intensities are well fit by a flat-lying structure with chains lying at an angle of approximately 7° to the a lattice parameter. Figure 6.4 compares the modelled intensities (black) with the experimental data (grey), while figure 6.5 illustrates the model structure.

At room temperature this pattern was observed to melt to give a pattern typical of an amorphous structure, indicating the melting point of the monolayer structure lies somewhere between 100K and 298 K. Initial DSC experiments failed to identify a significant monolayer melting peak to support this hypothesis. However, the monolayer melting enthalpies are very small and hence the monolayer melting peaks would be expected to be difficult to observe.

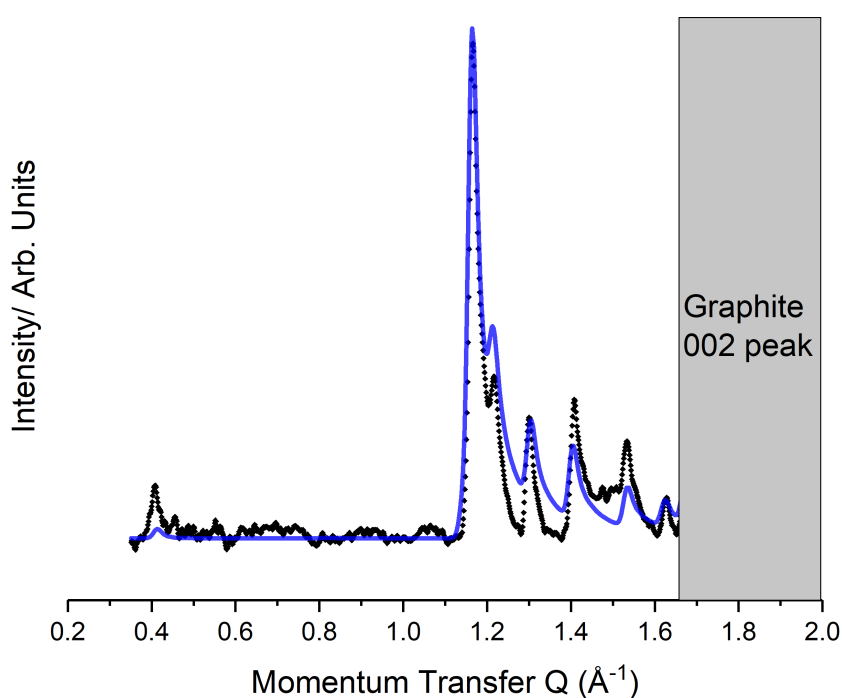


Fig. 6.4 Comparison between the experimental (black) and predicted (blue) diffraction pattern for the crystalline C₈F₁₆I₂ monolayer

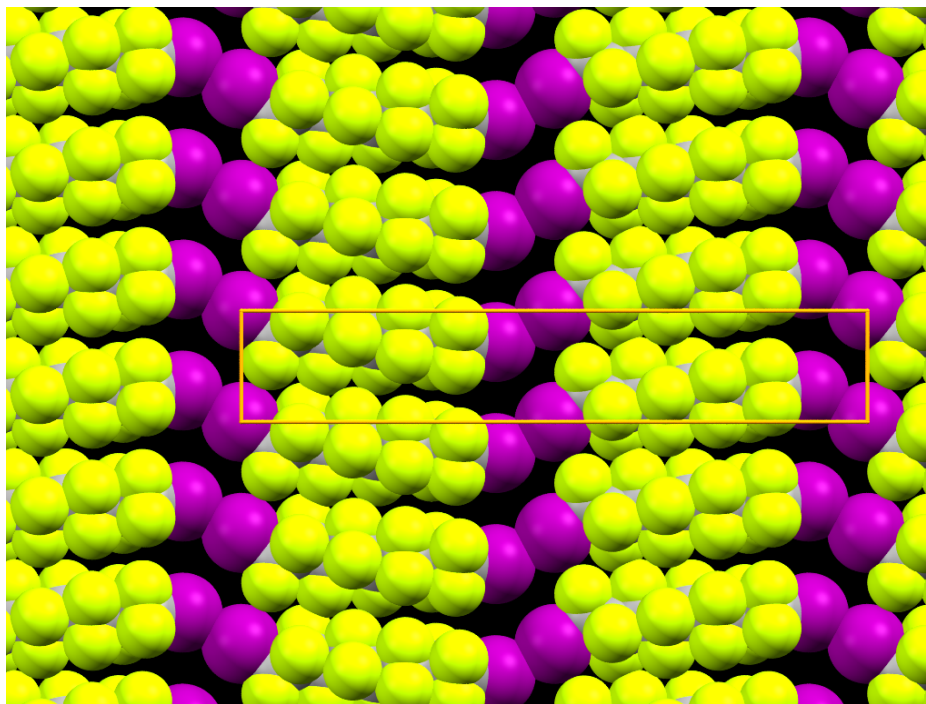


Fig. 6.5 Visualisation of the crystalline monolayer structure modelled for C₈F₁₆I₂. The pg symmetric unit cell is marked.

For the diffraction pattern of both pure samples of C₄F₈I₂ and C₆F₁₂I₂, no sharp diffraction peaks were detected, even after extended time to equilibrate in the 100K cryostream. Broad amorphous features are observed at approximately $Q = 1.2 \text{ \AA}^{-1}$ and 1.1 \AA^{-1} respectively, with a secondary feature for C₆F₁₂I₂ observed at $Q = 0.5 \text{ \AA}^{-1}$. This is initially surprising, as the bulk melting temperatures of these compounds are 270 K and 302 K respectively.¹⁷⁶ The monolayer melting temperature would be expected to be of the order of 3/4 of the bulk (i.e. >200 K), and so significantly above the experimental temperature.¹⁷⁴

To confirm the sample's purity, differential scanning calorimetry (DSC) was performed on the purchased samples. The experimentally determined melting point did match the literature bulk melting temperatures. However, a large hysteresis in melting and freezing temperatures was observed for the bulk samples. For example, C₄F₈I₂ melted at 270 K, yet only froze at 245 K in the DSC. This thermal hysteresis is indicative of difficulty crystallising in the bulk and may indicate that kinetic trapping could also be problematic in monolayer crystallisation. Given the lack of crystallisation an unambiguous structural assignment for these layers is not possible.

Overall there is minimal evidence of crystalline monolayer formation under the experimental conditions for the C₄F₈I₂ and C₆F₁₂I₂ molecules. The larger C₈F₁₆I₂ system forms a crystalline monolayer on graphite that can be identified at low temperatures, but which melts

at ambient temperatures. As expected this indicates the α,ω -diiodinated perfluoroalkanes only weakly interact with both the substrate and each other.

6.1.4 Co-deposition of α,ω -terminally iodinated perfluoroalkanes with Bipyridine

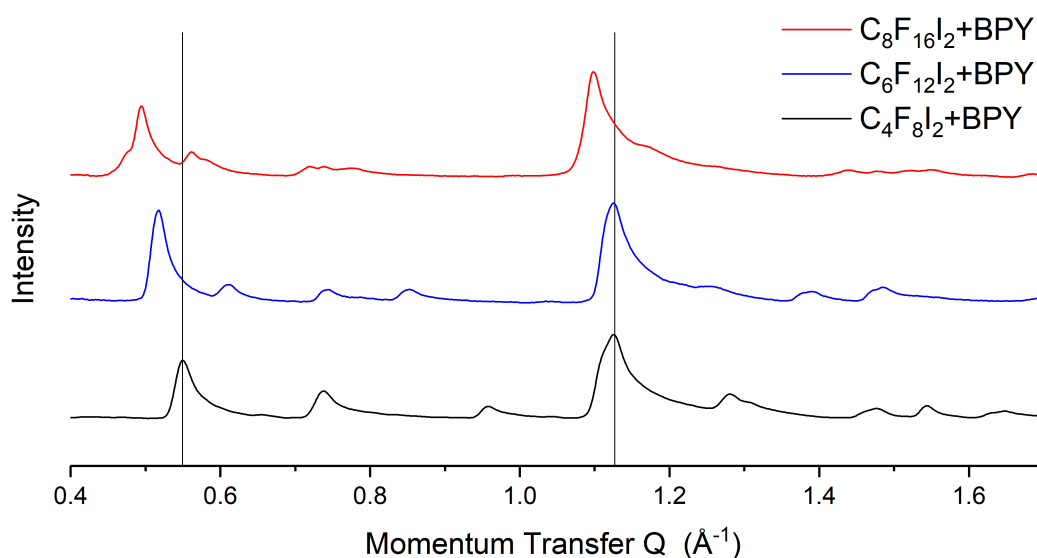


Fig. 6.6 Comparison of the diffraction patterns obtained for graphite dosed with BPY alongside the series of Halogen bond donors used in this study. The first peak (indexed as 01) shows a progression to lower Q with increasing chain length.

Fig 6.6 presents the diffraction pattern observed for 1:1 ratios of the $C_4F_8I_2$:BPY, $C_6F_{12}I_2$:BPY and $C_8F_{16}I_2$:BPY systems. From initial observation it is clear that these systems exhibit diffraction patterns that are distinct from those of the individual components, indicating the formation of new phases. The observed peaks all exhibit the characteristic “sawtooth” shape characteristic of monolayer diffraction peaks. Hence, it can be concluded that monolayer crystal structures have formed. For each system, if an excess of one component was added, the collected pattern was a superposition of the bicomponent diffractogram from figure 6.6, and the excess monocomponent phase. It is thus clear that the mixed phase contains each component in an approximately 1:1 ratio. This is in agreement with the expectations if the halogen bond is key to co-crystal formation.

It is evident there are two major peaks in the diffraction patterns of all three co-crystals, around the approximate positions indicated by the two lines on figure 6.6. Observing the progression of peaks, it is evident that the first peak shifts to lower Q with increasing length

of halogen bond donor. Assuming the structures are homologous this suggests the molecules may be partially aligned in the lattice direction associated with this peak, as that would cause longer α, ω -terminally iodinated perfluoroalkanes to extend the lattice in this way.

Data Fitting

The diffraction patterns were analysed as described in section 2.2.10. Molecular rigid bodies for the structural optimisation were taken from the corresponding bulk crystal structures¹⁷⁰ to constrain the fitting as much as possible. In keeping with previous work, and to limit the number of degrees of freedom of the model, the Debye-Waller factors have been set to unity. Qualitatively, this term would be expected to suppress the intensity of higher Q peaks, and so our fitting will slightly underestimate the intensity of low Q peaks. The peakshapes were modelled using the Gaussian peakshape models of Schildberg and Lauter.¹³¹

C4F8I2+BPY

Figure 6.7 compares the observed diffraction pattern for a sample dosed with a 1:1 combination of C4F8I2 and BPY with the modelled pattern. The pattern was indexed to an oblique unit cell with lattice parameters $a = 20.47(8) \text{ \AA}$, $b = 9.99(0) \text{ \AA}$ and $\gamma = 34.20^\circ$. This is incommensurate with the underlying hexagonal graphite lattice $a = 2.4589 \text{ \AA}$, $\gamma = 60^\circ$, indicating that intermolecular interactions are more important than the substrate in determining monolayer structure. The area of the cell (115 \AA^2) matches well with the expected size of a 1:1 C4F8I2:BPY complex from consideration of the atomic VdW radii ($\approx 117 \text{ \AA}^2$). Similarities can be identified between the identified unit cell and that previously observed for the co-crystalline monolayer formed from a mixture of 1,4-diiodotetrafluorobenzene and BPY.¹¹²

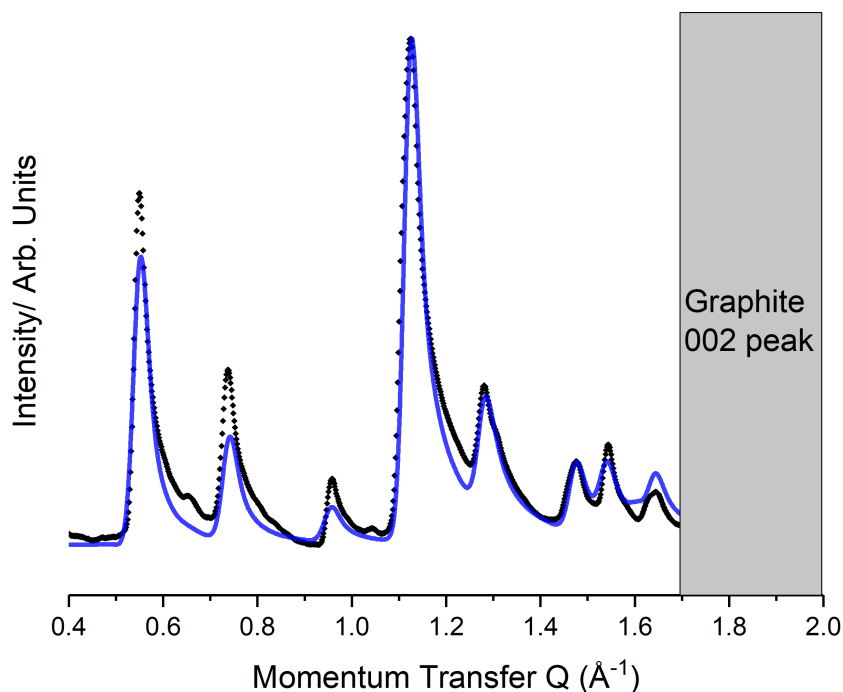


Fig. 6.7 Comparison between the experimental (black) and predicted (blue) diffraction pattern for the C₄F₈I₂:BPY co-crystal

Given the dimensions of the cell, and similarity to the DITFB:BPY pattern, a logical trial structure is one based around linear chains of alternating molecular species. It is found that the pattern is well fit by such a structure consisting of the I atoms of the C₄F₈I₂ molecule and two N atoms of BPY lying along the same axis. Deviation from this linearity by only a few degrees dramatically worsened the fit, strongly supporting a linear structure.

Figure 6.8 illustrates the determined monolayer structure. Interestingly, this structure shows the perfluorinated species and non-fluorinated species adjacent to each other in the lattice with no evidence of the segregation between hydrocarbon and perfluorinated tectons that has been observed in the bulk.¹⁷⁰ It has previously been noted that mixing of dissimilar components occurs more readily in 2D than in 3D, as a function of the decreased dimensionality of the system.¹⁷⁷

The low-Q peak intensities in figure 6.7 are somewhat underestimated in the model relative to the experiment. This is likely a function of significant Debye-Waller factors (previously observed to be insignificant in our studies of aromatic systems) which act to suppress the intensity of high Q peaks in the experimental pattern, and hence make the low

Q peaks appear somewhat larger. A greater effect of Debye-Waller factors is somewhat expected, as less constrained fluorocarbon chains are less rigid than aromatic rings, and so exhibit a greater degree of thermal motion. As discussed in section 2.2.8, the low number of reflections observed means that more detailed modelling of the Debye-Waller factors would be extremely challenging and require collection of data from a wide range of temperatures, which was not available on the instrument in this work.

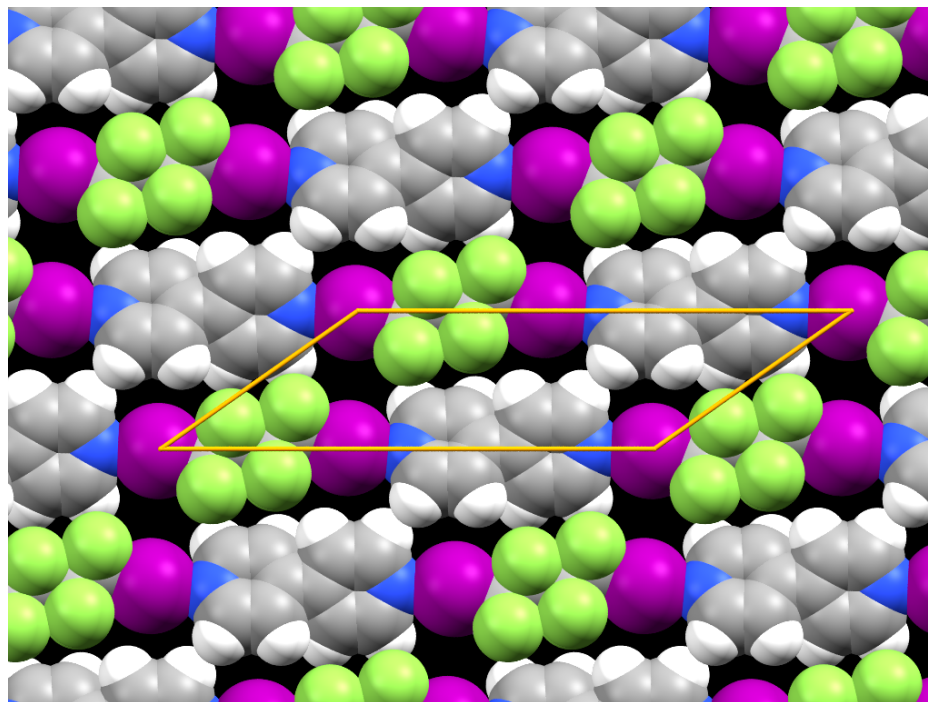


Fig. 6.8 A visualisation of the modelled structure of the C₄F₈I₂:BPY co-crystalline monolayer.

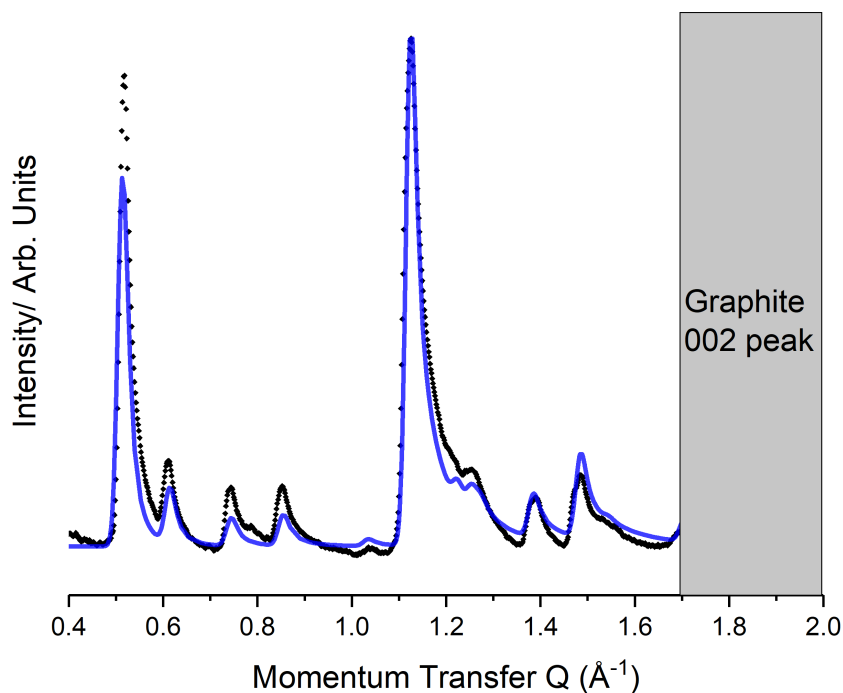
C6F12I2+BPY

Fig. 6.9 Comparison between the experimental (black) and predicted (blue) diffraction pattern for the C6F12I2:BPY co-crystal

Figure 6.9 compares the experimental and modelled structure of the C6F12I2:BPY co-crystal. Upon indexing unit mesh parameters were found to be $a = 22.71(5) \text{ \AA}$, $b = 10.44(3) \text{ \AA}$ and $\gamma = 32.53^\circ$. Again, this indicates an incommensurate unit cell, implying strong intermolecular interactions. The experimental intensities were fit to a linear chain structure similar to that observed for the short chain C4F8I2. Figure 6.10 visualises the determined monolayer structure. Similar to the previous system, it seems the low angle peak intensities are under predicted in our model, as discussed above. Again, any deviation from a linear chain structure dramatically worsened the fit.

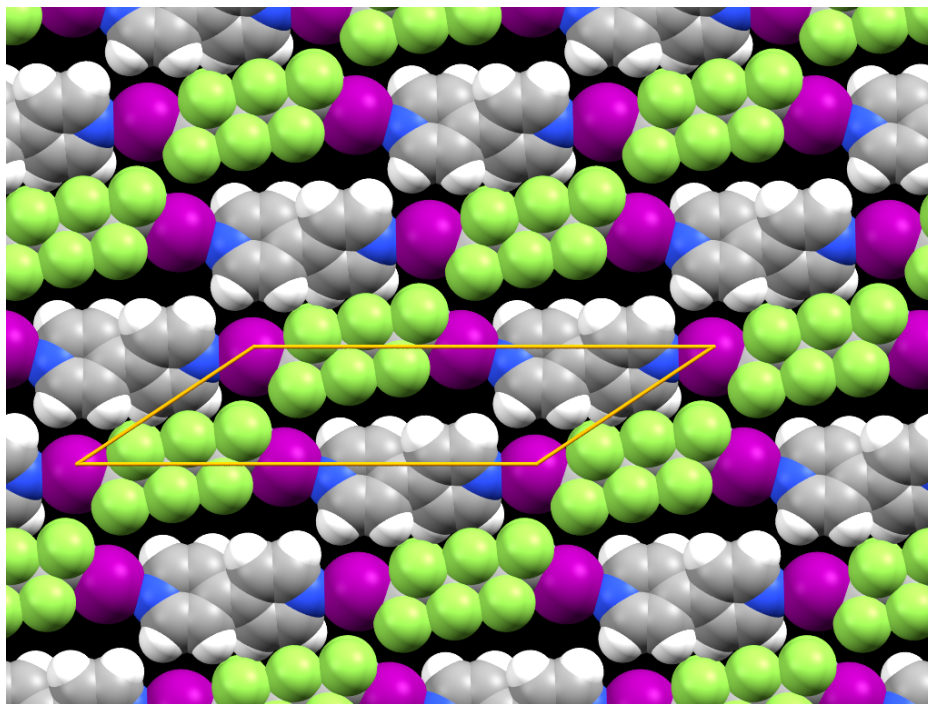


Fig. 6.10 A visualisation of the modelled structure of the C₆F₁₂I₂:BPY co-crystalline monolayer.

C₈F₁₆I₂+BPY

The diffraction pattern of the C₈F₁₆I₂:BPY system was indexed to an incommensurate cell with parameters $a = 25.27(4) \text{ \AA}$, $b = 11.29(3) \text{ \AA}$ and $\gamma = 30.61^\circ$. However, upon fitting of the intensities to a pattern it was considerably more difficult to obtain a satisfactory fit. Figure 6.11 presents the best obtainable fit using the rigid bodies taken from the bulk structure published by Catalano et al. It can be seen that the intensities of the peaks at $Q = 0.7\text{--}0.8 \text{ \AA}^{-1}$ (indexed as the [11] and [31]) are underestimated, while the relative intensity of the higher Q peaks are not correct and in contrast to the previous structures there is no underestimation of the [10] peak. Although the broad form of the structural assignment matches well with the data, with a physically realistic chemical structure, it is clear that at least some atomic positions are significantly incorrect. In an effort to remedy this problem with the structural fit, the nature of the rigid bodies was reconsidered

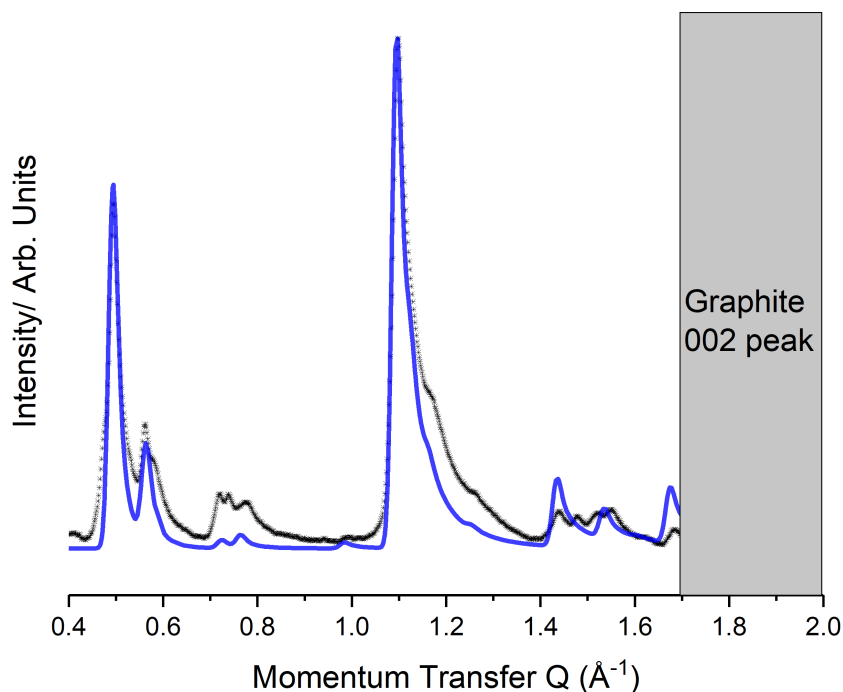


Fig. 6.11 Comparison between the experimental (black) and best obtainable predicted diffraction pattern (blue) for the C₈F₁₆I₂:BPY co-crystal utilising a rigid body containing a near all trans perfluoroalkyl chain.

Upon reexamination it is notable that the rigid bodies taken from the published work by Catalano et al. all contained near all trans conformations for the perfluoroalkyl chain. This is despite perfluoroalkyl chains being notable for their helical twist, as discussed in 6.1.1. For example, in the diffraction structure of perfluorohexane the C-C-C-C torsion angle is observed to be between 163 – 165°. ¹⁷⁸

Similar torsion angle values have been reported across the fluorocarbon literature. ¹⁷¹ In an attempt to better understand the distribution of perfluorocarbon helical torsion angle a CSD search was performed. The search utilised the "crystal packing feature search" utility in the Mercury software program to collect the C-C-C-C torsion angles of any structures containing acyclic -C₄F₈- motifs up to May 2020 in the CSD. Structures with errors, disorder, or not 3D coordinates were excluded using the utility options. 378 hits were detected, of which a surprisingly large proportion feature perfluoroalkyl chains with a torsion angle of exactly 180°. Figure 6.12 presents a polar histogram of the C-C-C-C torsion angles observed across the 378 structures identified. 37 submissions exhibit a torsion angle of exactly 180°,

with 96 submissions exhibiting torsion angles $>175^\circ$. The remaining torsion angles are more distributed, with a maximum occurring at 162° , consistent with that expected for helically twisted chains.

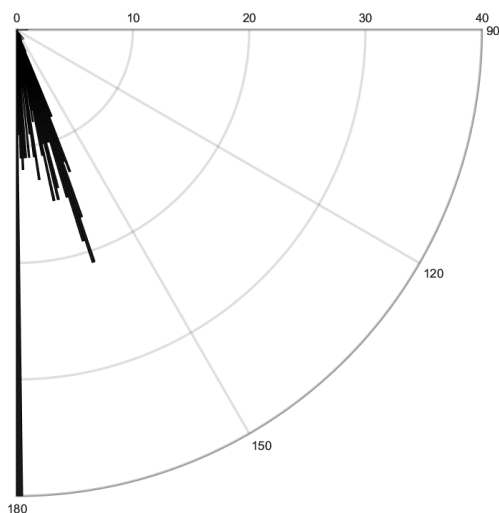


Fig. 6.12 Polar histogram showing the frequency of various torsion angles in perfluoroalkyl chains submitted to the CSD. A large number of submitted structures exhibit torsion angles of exactly, or close to, 180° . The maximum at lower torsion angles is centered around 162°

From this it is clear that, although many CSD structures do exhibit the expected behaviour, many do not. From examination of the structures none seem to be particular outliers, instead it seems that there is great difficulty in obtaining the correct torsion angle in perfluoroalkyl chains, even via single crystal x-ray diffraction, meaning that many authors simply leave the chain torsion angles constrained in the fitting procedure. Considering the more limited information available from powder diffraction of monolayer systems it was determined that fully optimising the torsion angle in the monolayer systems considered in this work would be impossible. Instead, an alternative trial rigid body molecular structure was obtained that exhibited the expected helical twist.¹⁷⁹

Figure 6.13 compares the optimised model diffraction pattern using this twisted perfluoroalkyl chain to the experimental data for the $C_8F_{16}I_2$ system. The unit cell remains identical to that of the previous figure ($a = 25.27(4) \text{ \AA}$, $b = 11.29(3) \text{ \AA}$ and $\gamma = 30.61^\circ$) but the peak intensities exhibit a better match to the experimental data. Figure 6.14 visualises the structure of this model. As can be seen the structure exhibits similarities to the C_4 and C_6 monolayer structures, consisting of linear halogen bonded chains, with no evidence of segregation of perfluorocarbon and hydrocarbon motifs. The chief difference is the perfluoroalkyl chain

helical twist, which means that the F atoms are not equally displaced from the horizontal lattice vector.

Following the previous discussion helical chain structures were trialled for the C4 and C6 monolayer fittings, but no significant difference was noted. Because a fitting of the exact torsion angle would be impossible with the limited information available from powder monolayer diffraction experiments, it was decided to keep the rigid bodies from the corresponding bulk crystals for these systems, while acknowledging the exact torsion angle may be different to this.

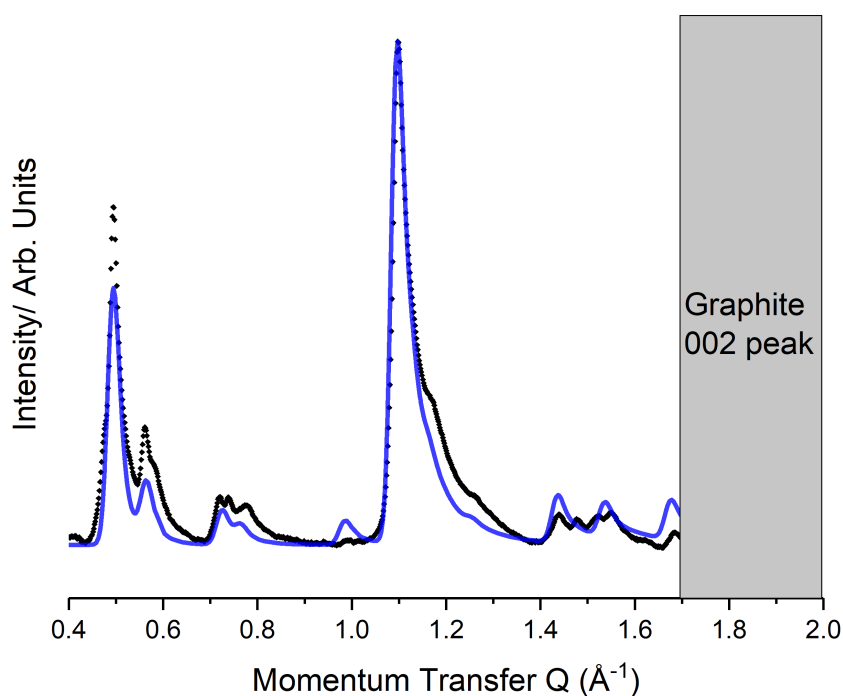


Fig. 6.13 Comparison between the experimental (black) and predicted (blue) diffraction pattern for the C8F16I2:BPY co-crystal utilising a helical chain structure of C8F16I2 obtained from reference 179

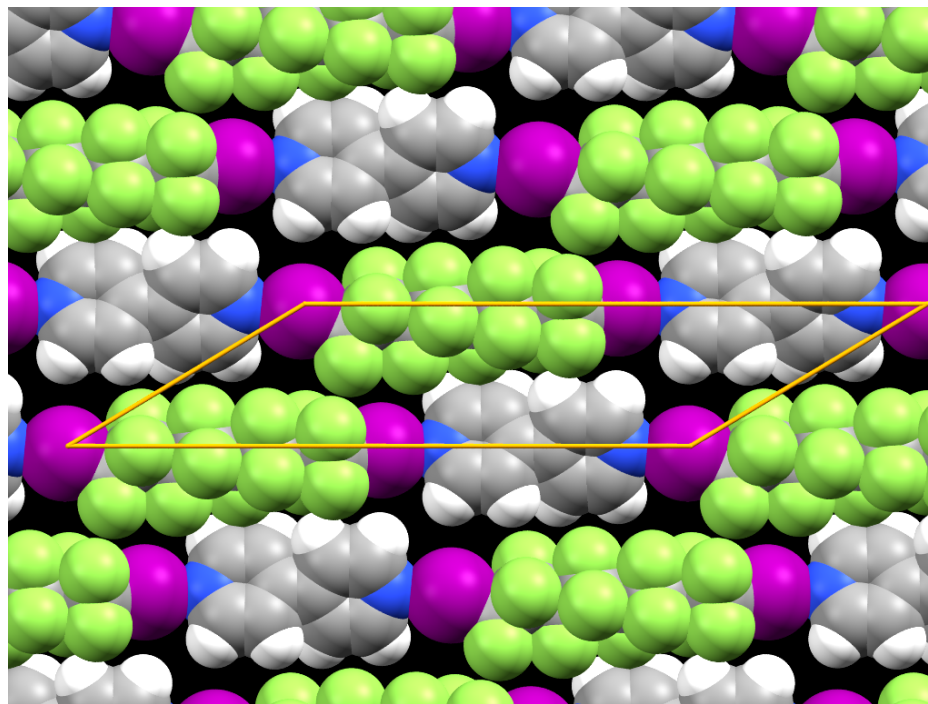


Fig. 6.14 A visualisation of the modelled structure of the C₈F₁₆I₂:BPY co-crystalline monolayer.

6.1.5 Conclusion

Pure C₈F₁₆I₂ was successfully observed to form a crystalline monolayer on graphite at low temperature (100K). At room temperature this was melted, but due to limitations of the equipment it was not possible to exhaustively perform temperature scans to determine the monolayer melting point. Neither C₄F₈I₂ nor C₆F₁₂I₂ showed evidence of crystalline monolayer formation in the absence of a halogen bond acceptor. This is somewhat surprising as such monolayers if formed generally exhibit a monolayer melting temperature of approximately three quarters of the bulk melting point. It may be that these systems exhibit unusually low monolayer melting temperatures, or that kinetic trapping could be significant in the experimental setup used or they may be glass formers.

When co-deposited with the halogen bond acceptor BPY, all three molecules successfully showed clear evidence of new monolayer co-crystalline phases. For the three systems studied, the diffraction patterns could be indexed to a similar set of unit meshes. Hence in this sense all three co-crystals were fitted by homologous structures which gives more confidence in the determined structures. Peak intensities were fit to this set of homologous structures containing linear chains of halogen bonded molecules. These meshes were significantly

different to any planes of the bulk crystal structures, indicating the monolayer structures are novel and not simply a plane of the corresponding bulk co-crystals.

The damping of higher Q intensities of the experimental patterns compared to the modelled structures may indicate that the structures are slightly less rigid than the previously studied aromatic systems. For the longest chain halogen bond donor, the helical nature of the perfluorinated chain had a significant effect on the observed pattern, but using a helical or trans chain structure had limited effect on the predicted diffraction behaviour of the shorter chain systems. Because of the limited information available from the collected data, a precise fitting of the torsion angle was not possible.

6.2 Terminally Brominated Perfluoroalkanes

Due to the strong halogen bonding observed in the series of α,ω -diiodinated perfluoroalkanes just discussed, a logical next choice was to examine what effect substituting iodine for bromine would have on the monolayer structure. Compared to iodine, bromine has higher energy electron orbitals, and hence brominated molecules exhibit a reduced σ -hole compared to the corresponding iodinated molecules, this means they generally exhibit somewhat weaker halogen bonds. For example, 1,4-dibromoperfluorobenzene was found to form a halogen bonded monolayer co-crystal with BPY similarly to its iodinated analogue. However, the halogen bonds were found to be significantly non-linear, with DFT results confirming the bond as being significantly weaker than for DITFB with BPY.¹¹⁴

Figure 6.15 presents the experimental patterns collected for C₈F₁₆Br₂ and C₈F₁₆Br₂ + BPY, alongside the calculated pattern for a BPY monolayer collected by Clarke et al.¹³⁷ 1,8-dibromoperfluorooctane on graphite yielded a broad amorphous diffraction signal indicative of a liquid or amorphous monolayer pattern.

The pattern from the co-deposited material can be clearly identified as a simple addition of the broad amorphous peak of the dibromide with the well defined BPY sawtooth peaks. This is indicative of phase separation and indicates that, unlike for the aromatic system, the brominated perfluoroalkane does not form a halogen bonded co-crystal monolayer.

This interesting results also qualitatively supports the initial hypothesis that brominated halogen bonds are weaker than iodo and that is why although co-crystals are identified above for the di-iodo species, the di-bromo combinations phase separate.

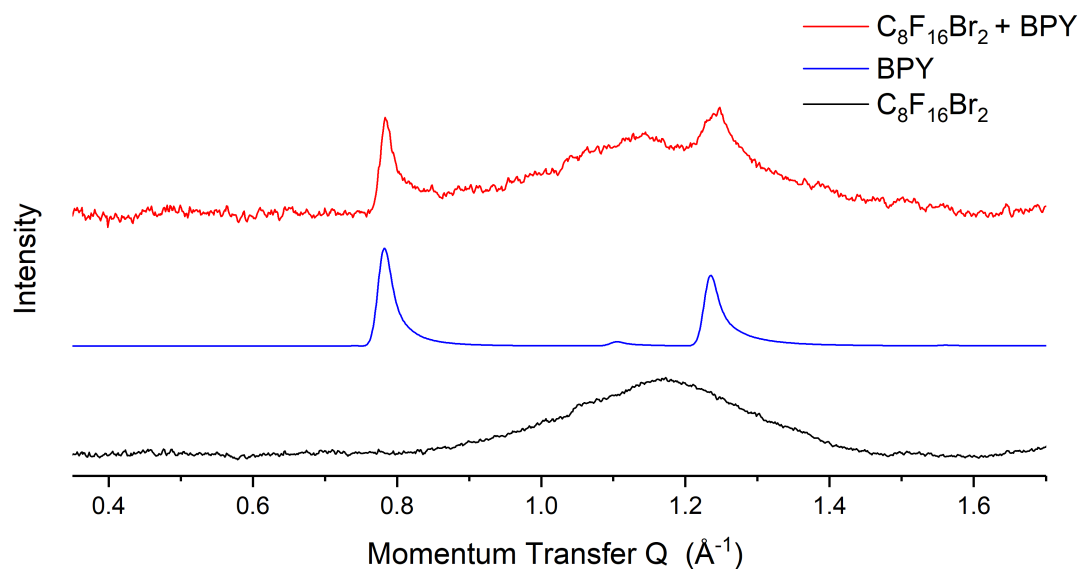


Fig. 6.15 Stacked plot of the diffractograms of the graphite deposited with C₈F₁₆Br₂, BPY, and a 1:1 ratio of both. C₈F₁₆Br₂ can be seen to exhibit only a broad scattering feature consistent with an amorphous structure, while the sample co-deposited with BPY exhibits a combination of the aforementioned broad feature with the sawtooth peaks of the crystalline BPY monolayer. This is consistent with phase separation and indicates no mixing of the two components.

6.3 Computational

Alongside the experimental work performed by myself, parallel computer simulation studies have also been performed by both Marco Sacchi (University of Surrey) and Stephen Jenkins (University of Cambridge). Much of the evolution of this area of work in our group has exploited the synergy of experiment and DFT calculations. All simulations were performed by Dr Sacchi and Prof. Jenkins, with interpretation of the results being performed jointly with myself. The results of these simulations are complementary to the above experimental results and so are presented below. Note that without the detailed crystallographic data collected by myself and presented in this thesis, the DFT is generally unable to find the true monolayer crystal structure and hence determine the appropriate energetics. This is because the molecules on the surface live in a very rough potential energy surface where there are lots of local minima. Without the diffraction to precisely guide the DFT, the simulations would likely end up in the wrong minimum.

6.3.1 TITFB Simulation

Simulation of the TITFB monolayer presented in chapter 5 was performed by Professor Stephen Jenkins using both uncorrected DFT, and DFT using two popular corrections for Van der Waals forces. The comparison of results obtained using different DFT methods helps elucidate the contribution of different interactions to the monolayer binding.

Computational details

First-principles DFT calculations, was performed at the University of Cambridge by Professor Stephen Jenkins using the CASTEP computer code.¹⁸⁰ Previous experience with similar systems^{113,181} has confirmed that interactions between halogen-bonded overlayers and the underlying graphite substrate are weak enough that the substrate can be ignored.

Hence, the TITFB was modelled as a raft of molecules, applying periodic boundary conditions consistent with a supercell with height of 12 Å (perpendicular to the raft) and lateral dimensions conforming initially to a hexagonal lattice constant of 9.30 Å (chosen close, but not identical, to the experimentally determined value). The lateral lattice constant was permitted to relax, along with the internal structure of the TITFB molecule replicated within each supercell, in response to the calculated forces, subject only to the constraint that the lattice was to remain of simple hexagonal type.

Sensitivity of the results to Van der Waals (VdW) interactions, which are not satisfactorily described within the standard DFT approach, was tested by comparing the effects of two semi-empirical correction schemes, namely the Tkatchenko-Scheffler (TS) scheme¹⁸² and Grimme's D2 scheme.¹⁸³ These schemes utilise either fixed polarisability terms for each element (D2) or terms that vary depending on atomic environment (TS), to correct for dispersion interactions. The most appropriate correction for each case can be difficult to determine, hence the use of several corrections in this work.

Intermolecular interaction energies were estimated by comparing total energies computed in the fully relaxed supercells (for each scheme) against energies computed for molecules relaxed within supercells artificially fixed at twice the equilibrium lateral lattice constant (in which circumstances the interactions between neighbouring molecules are expected to be negligible). Calculations performed in such "expanded" cells (but with frozen local molecular geometries) were also the source of reference electron density distributions, which could be subtracted from the electron density obtained at the equilibrium lateral lattice constant to provide "electron density difference" maps that reveal spatial information on the formation of intermolecular bonds.

Method	Lattice Vector (a) /Å	$\omega /^\circ$	C-I...I		
			$\theta_1 /^\circ$	$\theta_2 /^\circ$	$d(I...I)/\text{Å}$
Experimental	9.29	11.5	163.2	103.2	4.08
No VdW correction	9.40	15.1	171.4	111.4	3.92
TS correction	9.31	14.1	168.4	108.4	3.90
D2 correction	9.26	13.9	168.1	108	3.90

Table 6.1 Key geometric parameters for a TITFB monolayer determined by experimental or DFT simulation methods. θ_1 and θ_2 are defined in figure 5.2a

Discussion

Optimisation of the DFT model structure in the absence of VdW corrections yielded a lateral lattice constant of 9.40 Å, which is 1.2% greater than the experimental value. Inclusion of the TS correction reduced this to 9.31 Å (0.2% higher than experiment) while the D2 correction led to a value of 9.26 Å (0.3% smaller than experiment). This means that the TITFB lattice constants obtained from four different methods (experimentally in this work, and via three different DFT calculations) fall within 1.5% of another.

Because the internal structure of TITFB was allowed to relax in the calculations, values of ω are not strictly comparable to the experimental value ($\omega = 11.5^\circ$). By taking the rotation of the aromatic carbon ring it was possible to obtain values for ω that are reported in table 6.1.

The calculated geometries all feature an X₃ motif similar to that deduced from the experimental data. The key parameters are collected in table 6.1, and it can be seen they are broadly consistent with the experimentally determined values.

By artificially doubling the lattice constant and comparing the calculated binding energy for the initial and doubled systems it is possible to estimate the magnitude of the intermolecular interactions. In the non VdW corrected calculation this binding energy was found to equate to 0.16 eV per molecule. By comparison the TS VdW corrected calculation found a binding energy of 0.34 eV, and a value of 0.44 eV was found for the D2 corrected calculation. These results suggest that halogen-bonding (present even without VdW corrections) amounts to between one third to one half of the total intermolecular interaction, the remaining contribution being dispersive in nature.

To further investigate the nature of the intermolecular interaction it is possible to compare the shift in electron density between the doubled and initial calculations. This was conducted for the D2 corrected calculation. Figure 6.16 presents an isosurface visualisation of the electron density difference for this calculation. In this figure red equates to an increase in

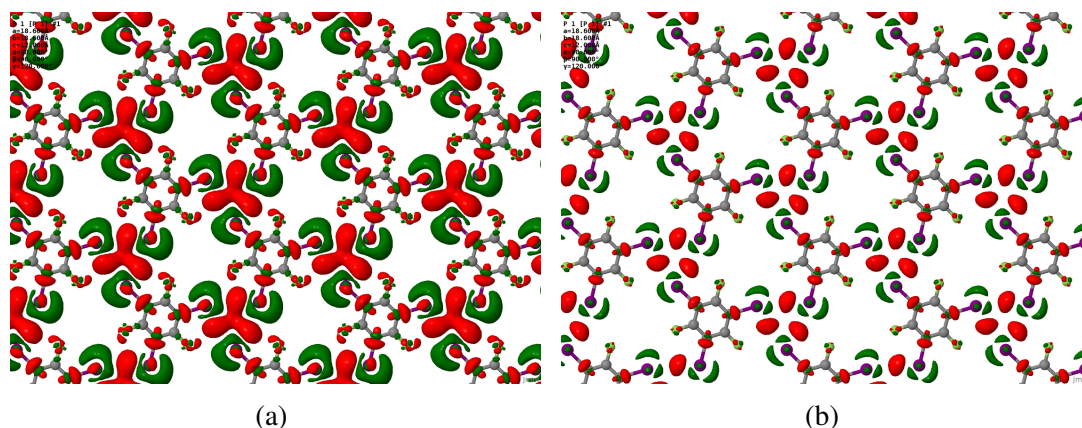


Fig. 6.16 Maps of electron density accumulation (red) and depletion (green) for the condensed TITFB monolayer, relative to the electron density of isolated molecules constrained to the same local geometries but with doubled lateral lattice constant. Isosurface thresholds are set at (a) $\pm 2 \times 10^{-3}$ electrons. \AA^{-3} , and (b) $\pm 4 \times 10^{-3}$ electrons. \AA^{-3} .

electron density, and green to a reduction in electron density in the monolayer relative to the unbound state. It can be seen that there is a threefold symmetric increase in electron density equating to the X_3 motif, with a corresponding depletion in the vicinity of the iodine atoms. Such a pattern is entirely consistent with the previously published work on aromatic halogen bonding systems.^{113,181}

6.3.2 Terminally Iodinated Perfluoroalkanes

Similar computational work was performed by Dr Marco Sacchi at the University of Surrey for the α,ω -diiodinated perfluoroalkanes discussed earlier. The method used was similar to that used by Stephen Jenkins using the CASTEP code to simulate a raft of molecules without any substrate.

Computational details

As previously discussed, simulations were performed using the CASTEP code.¹⁸⁰ For these simulations only the Tkatchenko Scheffler (TS) dispersion force correction¹⁸² was applied to account for VdW interactions. These empirical functionals are necessary due to the plane-wave basis of the CASTEP code and have proven to be robust for these types of system.¹¹⁴

In order to estimate the contribution of different interactions to the total binding energy, the binding energy of a complete tiling can be compared to that of a system with doubled b

lattice size. This will (almost) eliminate the interchain interactions, and hence the calculated binding energy will represent the strength of the two intra-chain halogen bonds.

Discussion

Table 6.2 Results of the DFT-optimised unit meshes for the co-crystals studied, alongside binding energy and estimated halogen bond and interchain interactions strengths. For each system the total binding energy consists of two halogen bonds plus the total interchain interaction energy. Data previously reported for 1,4-diiodotetrafluorobenzene (DITFB) has been reproduced for comparison.¹¹³

Species	a /Å	b /Å	γ	B.E /eV	X-bond /eV	Interchain /eV
C4F8I2 +BPY	20.29	9.89	34.99	1.199	0.255	0.627
C6F12I2 + BPY	22.81	10.54	33.51	1.168	0.256	0.658
C8F16I2+ BPY (twisted)	25.46	11.34	30.96	1.130	0.253	0.624
C8F16I2+ BPY (trans)	25.60	11.44	30.515	1.051	-	-
DITFB + BPY	19.36	12.45	31.73	1.078	0.249	0.580

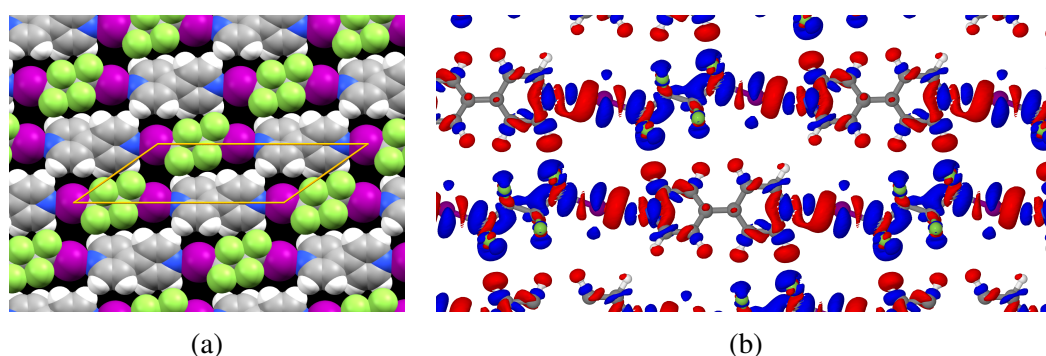


Fig. 6.17 Optimised structure of the C4F8I2+BPY system. **Figure (a)** shows the structure visualised using spacefill atomic models. **Figure (b)** shows a plot of the electron density difference of the monolayer relative to the separate molecules. Blue indicates an increase in electron density while red indicates a loss of electron density relative to the separate molecules (isosurface level $0.005 \text{ e}/\text{\AA}^3$). Shifts in electron density due to the halogen bond are clearly visible, with there mainly being an increase in iodine and decrease in nitrogen electron density

As in previous work DFT optimisation used the experimentally modelled unit cell as the starting point. Geometry optimisation saw less than a 1.5% change in unit mesh for all three structures, with little change in the atomic structure. This helps support the experimental structures as being reasonable.

Figure 6.8 presents a visualisation of the simulated structure of the C₄F₈I₂:BPY layer. Mixing of the perfluorinated and hydrocarbon tectons is evident, as in the experimental structure.

The total binding energy of the structure can be found by artificially double the unit cell parameters. Here it is calculated that the total intermolecular interactions equate to 1.120 eV (115.7 kJmol⁻¹) per unit cell. It is possible to estimate the interchain and intrachain components by doubling the *b* parameter to effectively remove interchain interactions, leaving only the halogen bonds (two per cell) intact. Each halogen bond can then be estimated as having a strength of 0.255 eV (24.6 kJmol⁻¹), which is similar to that previously reported for an aromatic halogen bond donor (0.249 eV).¹¹³ The lateral hydrogen bond and vdW interactions can then be estimated as having a total strength of 0.627 eV. This is slightly larger than the previously simulated interaction for the aromatic halogen bond donor 1,4-diodotetrafluorobenzene. In 3D crystal engineering perfluorinated aromatic molecules are considered to be more strongly interacting than their perfluoroalkane equivalents. In two dimensions it is evident that this ordering is reversed, as the exposed edge of a perfluorinated aromatic system consists of fewer, less polarisable, sp₂ fluorine atoms than the perfluoroalkyl chains considered in this work.

Within the plane of the layer, the only relevant interaction with the fluorine is weak C-H bonds to the aromatic protons of BPY. Although generally considered inert, fluorine is capable of acting as a hydrogen bond acceptor, with sp³ C-F motifs being better acceptors than sp².¹⁸⁴ Such bonds are rare however, and due to their weakness generally only occur where no other interaction is possible.¹⁸⁵

The electron density difference between the bound and free molecules is a useful proxy for the nature of interactions. The plot in figure 6.17b shows the difference in electron density in the co-crystal relative to the component molecules. Blue indicates an increase in electron density and red a decrease. Significant charge transfer is characteristic of halogen and hydrogen bonds, while minimal electron density difference indicates that dispersion forces are the chief method of binding. As observed previously, the halogen bond is evidenced by the increased electron density on the iodine and reduced density on the nitrogen. Hydrogen bonds are also evident in the lateral interactions, with particularly large degree of charge transfer evident between the α and β fluorine atoms and their adjacent BPY protons.

Similar optimisation was performed for the C₆F₁₂I₂+BPY system (figure 6.18). Again very good agreement is found with the experimental structures where the simulated unit cells are within 1.5 % of the experimental lattice, and minimal change in molecular geometry is observed. The electron density difference plot shows a similar pattern to that observed in the shorter C₄ system.

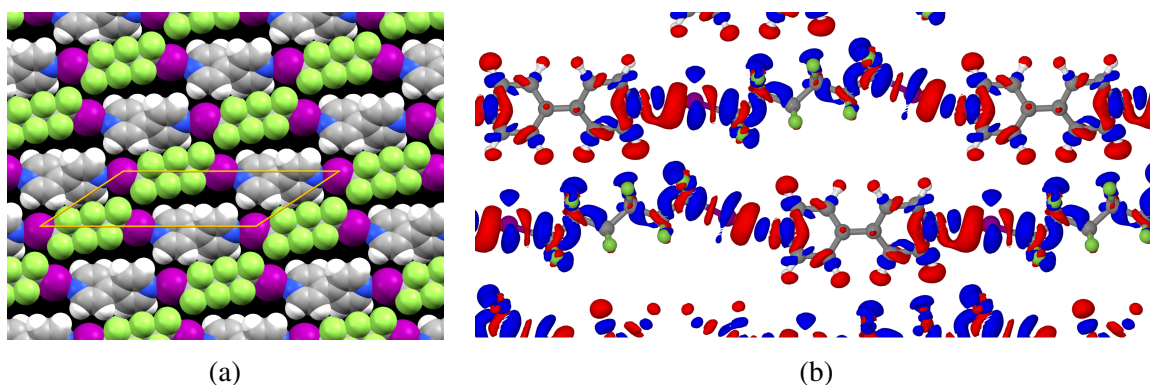


Fig. 6.18 Optimised structure of the C₆F₁₂I₂+BPY system. **Figure (a)** shows the structure visualised using spacefill atomic models. **Figure (b)** shows a plot of the electron density difference of the monolayer relative to the separate molecules. Blue indicates an increase in electron density while red indicates a loss of electron density relative to the separate molecules (isosurface level $0.005 \text{ e}/\text{\AA}^3$). Charge transfer between the chains is evidence of interchain hydrogen bonding between C-H and F atoms.

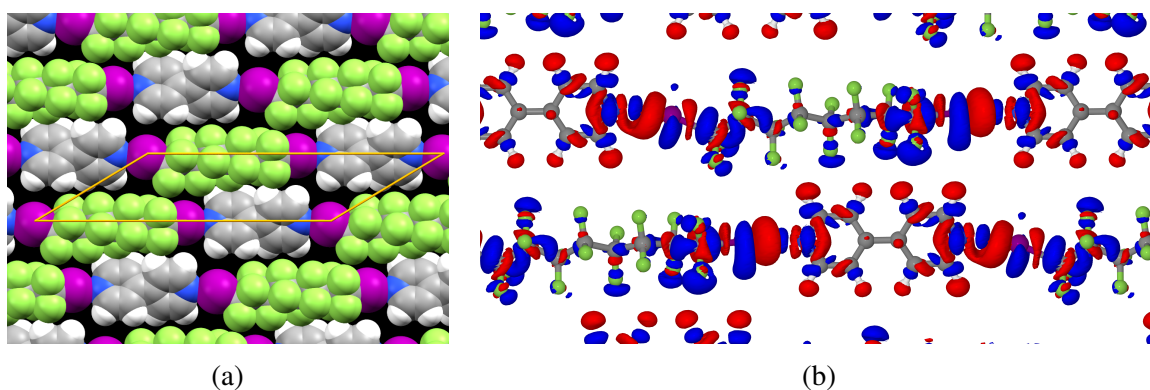


Fig. 6.19 Optimised structure of the C₈F₁₆I₂+BPY system. **Figure (a)** shows the structure visualised using spacefill atomic models. **Figure (b)** shows a plot of the electron density difference of the monolayer relative to the separate molecules. Blue indicates an increase in electron density while red indicates a loss of electron density relative to the separate molecules (isosurface level $0.005 \text{ e}/\text{\AA}^3$). Aside from one putative hydrogen bond, the central fluorine's are relatively uninvolved with charge transfer, explaining the small energy differences between conformers

For the C8F16I2+BPY system, optimisation was performed on both an all-trans alkyl chain analogous with the previous systems, and a twisted-chain structure more consistent with the experimental data. When considering the C8F16I2 molecule individually, the twisted-chain conformer is 0.0488 eV (4.7 kJmol⁻¹) more stable than the trans conformation. However, for the co-crystal the twisted conformer is 0.128 eV more stable. This means that the twisted-chain conformer exhibits a stronger binding energy to BPY than the trans conformer by 0.0790 eV (7.6 kJmol⁻¹)

The optimised unit cell parameters obtained for the two conformers are extremely similar, with a being 0.5% and b 0.8% larger for the trans conformer. As the twisted conformer is lower in energy and was the configuration that best matched the experimental data, it is the structure presented in figure 6.19. The twisting of the chain largely affects the position of the fluorine atoms in the middle of the chain, however as can be seen in the electron density difference (figure 6.19b) these atoms are relatively uninvolved in charge transfer, with only one δ fluorine exhibiting a charge increase consistent with hydrogen bonding. This helps explain the comparatively small binding energy difference.

Table 6.2 summarises the simulated geometry of the three unit cells, as well as the calculated binding energies. For comparison, the previously calculated data for 1,4-diiodotetrafluorobenzene (DITFB) is included. It can be seen that the halogen bonds in all three systems reported here are of similar strength to that previously calculated for DITFB. The two halogen bonds together account for almost half of the total binding energy in each case, and thus make a significant contribution to the mixing of these otherwise dissimilar components.

The total binding energies for the three systems are remarkably similar. A doubling of the carbon chain length between C4F8I2:BPY and C8F16I2:BPY leads to a slight *reduction* in inter-chain interaction. This indicates the vast bulk of the interchain interactions originate from hydrogen bonds to the BPY, with little contribution to the binding from non-hydrogen bonding atoms. The strength of these interchain interactions has important implications for future rational design of monolayers containing perfluorinated motifs.

6.4 Conclusion

In this chapter the assembly of a series of bicomponent halogen bonded monolayers between terminally iodinated perfluoroalkanes and 4,4'-bipyridine on a graphite surface has been observed and characterised. The monolayers exhibit homologous structures, with longer perfluoroalkane chains leading to a longer unit cell but minimal other change. The bicomponent monolayers are more robust than monolayers formed from the iodinated perfluoroalkanes alone, maintaining their crystallinity even above the bulk melting point. Compared

to the corresponding bulk co-crystals, the monolayers exhibit novel packing with a greater degree of mixing between dissimilar components.

Although previous work has observed monolayers that exhibit similar structures whether the halogen bond donor is iodinated or brominated, for the α,ω -disubstituted perfluorooctane system at least, only the iodinated chain was observed to form a co-crystalline layer, with the brominated system phase separating instead.

Through the use of DFT simulation performed by collaborators it has been possible to collect validating evidence behind the structural interpretation of the diffraction data. There is a close match between the DFT optimised geometry, and the experimentally refined structural model for all the co-crystals identified. This analysis has also allowed a better understanding of the driving force of mixing between the two components, with interchain interactions proving to give a substantial contribution to mixing, with important lessons for rational design of potential porous systems.

Chapter 7

Hydrogen Bonded systems

7.1 Triazine

7.1.1 Introduction

In the previous chapter s-triazine (Figure 7.1) was introduced as a tritopic halogen-bond acceptor for potential co-crystals. For completeness, the diffraction pattern of the monocomponent system was also collected and is reported here. S-triazine is interesting because it consists solely of light atoms, which have been a challenge to study using lab based diffractometers in the past. The ability of the rotating anode diffractometer to collect a usable diffractogram from a light atom monolayer is a useful test of its capabilities, and opens the door to further studies of light atom molecules without requiring synchrotron beamtime.

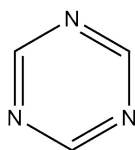


Fig. 7.1 Chemical structure of 1,3,5-triazine

The study is also important in its own right. The formation of co-crystals is always a balance of the energy of the co-crystal compared to the energy of the two separate monocomponent monolayers. An understanding of the energies of the pure components can help to understand why mixing did not occur for the TITFB:triazine system.

7.1.2 Experimental

A monolayer of s-triazine on graphite was produced using the method described in Chapter 3. A weighed amount of S-triazine (Alfa Aesar, 97%,) was deposited onto papyex graphite from batch BPI004L under reduced pressure and then annealed at a temperature of 423 K before slow cooling to room temperature. Data was collected at the rotating anode X-ray source detailed in chapter 3 using a cryostream with a temperature of 100K.

7.1.3 Results

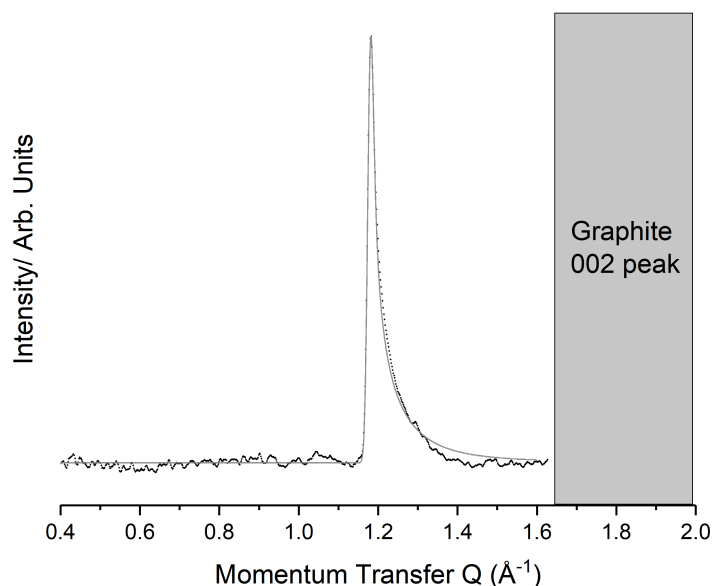


Fig. 7.2 Comparison between the experimental data (black) and predicted pattern (grey) for the proposed structure of the triazine monolayer.

Figure 7.2 presents the diffraction pattern obtained from the substrate and adsorbate after subtraction of the graphite background. As in the previously analysed patterns incomplete subtraction of the graphite peaks limit the range of high Q peaks that can be reliably observed. Below $Q = 0.4$ small angle 'Porod' scattering is evident arising from the small angle scattering of the graphite crystallites. However, no significant 2D diffraction peaks were observed in this region so it has not been considered further. Figure 7.2 illustrates that there is just one feature, a peak with "sawtooth" lineshape at $Q = 1.18 \text{ \AA}^{-1}$. The sawtooth lineshape of the single feature does indicate that a 2D crystalline layer has been formed. However, a single

peak suggests a small unit cell (that might be expected for such a small molecule) and/or a high symmetry unit cell.

When interpreting powder diffraction data it is generally held that the highest symmetry structures should be considered first, with lower symmetry structures considered only if no satisfactory high-symmetry assignment is possible. Given the symmetry of the triazine molecule the single peak is interpreted as being due to a hexagonal unit mesh, which is consistent with previous STM results.¹⁸⁶ If a hexagonal unit mesh is assumed, it is possible to fit this peak to obtain the monolayer lattice parameter. For this structure there is only a single parameter (cell length) that completely defines the lattice. The angle between the 2D unit cell axes is fixed at 120 degrees. The grey line in Figure 7.2 presents the best fit for the monolayer structure. The lattice size was fit as $a = b = 6.161(5) \text{ \AA}$.

The coherence length was fit to be 405 \AA . It is typical for monolayers of this type to exhibit coherence lengths on the order of magnitude of the coherence length of the substrate (ca. 600 \AA).¹²⁴ Previous authors, using the periodicity of Moire patterns imaged using STM have reported lattice constants of 6.14 \AA at 40K.¹⁸⁷ This value is approximately 0.3% smaller than that found here, which may be due to thermal contraction, or evidence of a structural effect of STM tip perturbation.

As outlined above, there is only one identifiable peak in the region of the diffraction pattern observed, so it is impossible to assign relative peak intensities, and thus atomic positions within the unit cell. This is a limitation of the diffraction technique, as overlap with graphite peaks and the low intensity of the monolayer signal means interpretation is reliant on interpretation of a few, strong signals. Particularly for triazine which has a low scattering power, only the most strongly scattering diffraction peaks can be observed. However, the previous STM results as well as the area and symmetry of the cell are all consistent with the molecule lying flat on the surface. Assuming this is the case, the only remaining structural characteristic is the orientation of the molecule about the 3-fold molecular axis.

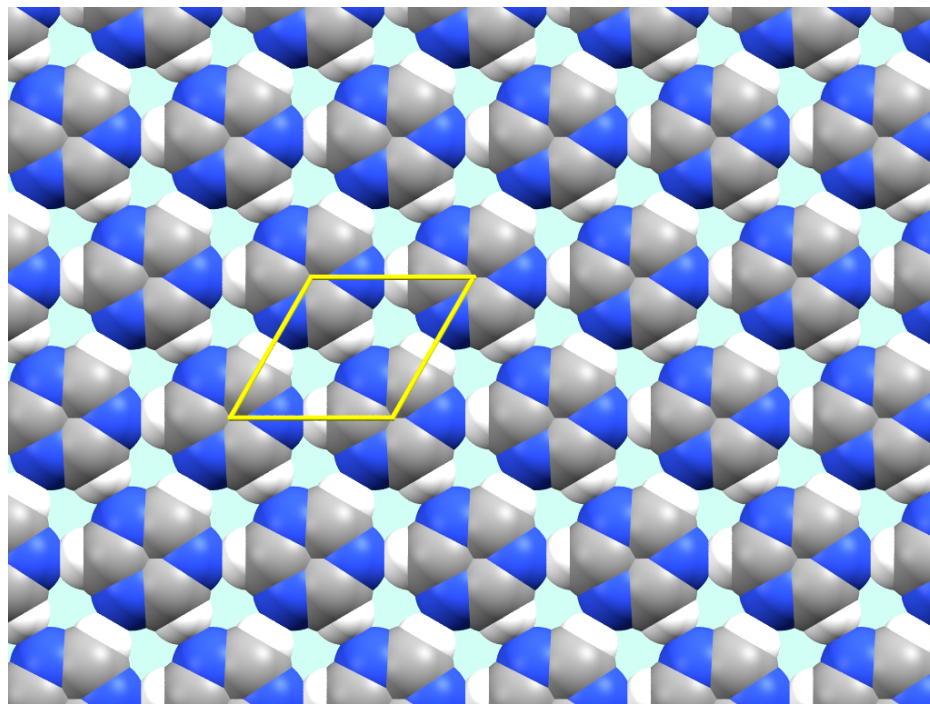


Fig. 7.3 Proposed structure of the triazine monolayer, based upon logical placement of s-triazine molecules onto the experimentally determined lattice

In the past, monolayer structures have been generated by assuming that internal molecular structures are unchanged from the single crystal structure deposited in the CSD. These molecular structures can then be placed on the experimentally determined lattice. The bulk structure of s-triazine has been previously deposited in the CSD as TRIZIN¹⁸⁸ However, it is often found that the positions of light atoms such as hydrogen can be imprecise when using bulk diffraction data. Knowledge of the hydrogen atom positions is important for interpretation of the strength of the hydrogen bonding in the monolayer.

For this reason it is desirable to obtain an alternative experimental model for the internal structure of triazine. A literature molecular structure derived from electron diffraction data¹⁸⁹ has previously been benchmarked against DFT simulations, showing good agreement with the simulations.¹⁹⁰ The carbon and nitrogen backbone of the structure is similar to that of the structure listed in the CSD, however the electron diffraction structure has significantly different C-H bond lengths. Because the scattering power of electrons by hydrogen is significantly stronger than that of X-ray photons, it is reasonable to assume this structure will better represent the H atom positions.

If the aforementioned electron diffraction derived triazine structure is placed upon the experimentally determined monolayer unit mesh, the produced monolayer is sensible, with no overlapping atoms. The exact angle of the triazine molecules on the lattice points is

impossible to determine from a single diffraction peak. However, a logical placement would be such as shown in figure 7.3. This conformation maximises the potential hydrogen bonding interactions between the C-H and N motifs of adjacent molecules.

In this conformation there is a distance of 2.383(3) Å between the hydrogen and nitrogen of adjacent molecules. This is a comparatively short distance, but not physically unrealistic for a system expected to exhibit comparatively strong C-H...N hydrogen bonds. The separation equates to 14% below the combined VdW radii of the two elements. For reference, in the bulk TRIZIN structure the H-N separation is offset in the z direction and is comparatively large at 2.799 Å.

Figure 7.4 depicts the frequency distribution of various C-H...N distances found in the CSD for aromatic protons interacting with aromatic nitrogen-containing rings. As can be seen the experimental C-H...N separation is within the range of observed values, but towards the low separation extreme.

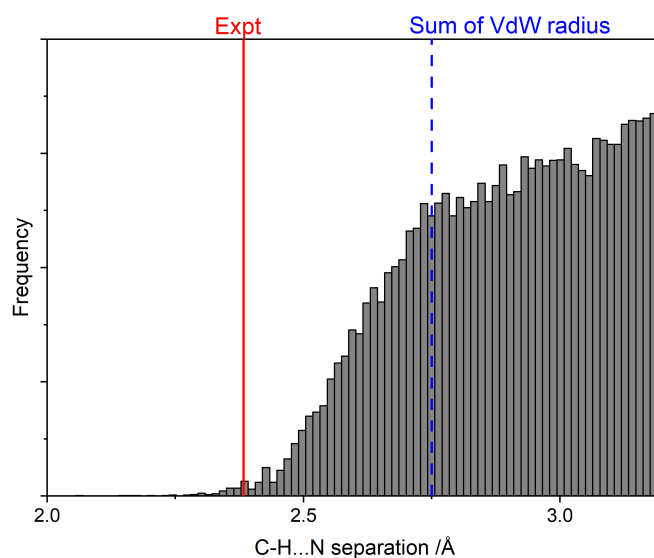


Fig. 7.4 Frequency of various C-H...N distances in the CSD. The distance of the proposed structure is highlighted ('Expt'), and is found to be within the range of experimentally identified separations for a hydrogen bonded system, if towards the shorter end of the distribution.

7.1.4 DFT analysis

In order to further support the experimental findings, DFT simulation was performed by Professor Stephen Jenkins. All calculations were performed by Professor Jenkins, however all interpretation is my own.

Methods

The first-principles density functional theory (DFT) calculations were carried out using periodic boundary conditions, as implemented in the CASTEP computer code.¹⁸⁰ In view of the expected lack of any strong interaction between graphite and the adsorbed molecules, the substrate was omitted from the adopted model. Instead, an isolated triazine raft was modelled within a supercell of height 12 Å, with lateral dimensions initially conforming to a lattice constant of 6.15 Å (based upon an early estimate of the experimental value). Atomic positions and the lateral lattice constant were then refined according to the calculated forces.

In order to test the sensitivity of the results to Van der Waals (VdW) interactions, beyond the capacity of standard DFT, two semi-empirical correction schemes were compared, namely Grimme's D2 scheme¹⁸³ and the Tkatchenko-Scheffler (TS) scheme.¹⁸²

Discussion

Initial DFT simulations in the absence of VdW corrections obtained a monolayer unit mesh of 6.15 Å. This is in very good agreement with the experiment being only 0.2% smaller than the experimental value (6.16 Å) and thus supports the experimentally proposed structure. Similarly to the halogen bonded systems discussed earlier inclusion of VdW correction schemes saw a reduction in the simulated unit cell to 6.08 Å using the D2 correction, and 6.07 Å using the TS correction.

The molecular structure in all three cases was effectively unchanged, with minor changes seen in the C-H bond length. In an analogous method to that used to estimate halogen bond strength, by comparing the simulated energy of the modelled monolayer to that of a hypothetical monolayer with doubled separation it is possible to estimate the total binding energy of the layer. Table 7.1 presents the relevant parameters for both the experimental and DFT simulated structures. Due to the uncertainties in hydrogen atom position discussed in the previous section, C...N separation is sometimes used as a proxy for hydrogen bond length, and is reported for completeness.

As can be seen from table 7.1 all three simulations find a similar or smaller hydrogen bond separation, supporting the experimental analysis. The availability of binding energy information allows an estimation of hydrogen bond strength. Electronic effects (that are

Table 7.1 Results of the unit meshes determined for the triazine monolayer via experimental or DFT methods. Relevant geometric parameters are broadly consistent, with the C-H...N hydrogen bond length varying between 2.3-2.4 Å for the different methods. Binding energy (B.E.) is 0.27 eV for the DFT with no VdW correction, and approximately 0.13 eV stronger for both the cases with VdW corrections.

Method	a /Å	C-H Bond length /Å	C-H...N Hydrogen bond length /Å	C...N Inter-molecular separation /Å	Binding Energy /eV
Experimental	6.16	1.11	2.38	3.49	-
DFT No VdW correction	6.15	1.09	2.39	3.48	0.27
DFT + D2 correction	6.08	1.11	2.31	3.42	0.40
DFT+TS correction	6.07	1.07	2.33	3.40	0.41

predominantly hydrogen bond related) equate to 0.27 eV per triazine molecule, or 0.09 eV per close hydrogen contact. VdW effects will originate from a mix of hydrogen bonds and other atomic contacts, and account for only an additional 0.13-0.14 eV of binding energy. It can thus be seen that electronic effects (which can predominantly be ascribed to the hydrogen bonds) make up the bulk of the binding energy of this system, and hence the triazine monolayer can be confidently described as a hydrogen bonded system, despite consisting only of C-H...N contacts.

7.1.5 Summary

In this section we have presented experimental evidence for the formation of a 2D layer of triazine on graphite at sub-monolayer coverages. The experiments were successful despite the experimental challenges in collecting light-atom scattering data using only a lab-based X-ray source. A high symmetry, hexagonal unit cell is consistent with the data and previous STM reports. The single molecule in each unit cell is flat on the surface. With minimal diffraction data to exploit, a combination of chemical insight and quantitative DFT, was used to locate the atoms in the unit cell and extract the interatomic energies of the layer. We conclude that this molecular layer is dominated by C-H...N hydrogen bonded contacts with a surprisingly high strength.

7.2 Trimesic acid

7.2.1 Introduction

As discussed in chapter 2, Trimesic acid (TMA) was the first porous organic monolayer to be identified. The initial studies were performed using UHV STM,⁹³ with many subsequent studies utilising ambient solution phase STM.⁹⁸ In these studies the TMA monolayer system is found to exhibit interesting behaviour; with several different phases existing on the surface, as well as host-guest behaviour with both itself and other molecules. For all these reasons it was felt it would be a useful additional system to study using monolayer diffraction. In particular the fact that nearly all previous experiments studying TMA monolayers were performed using scanning probe techniques, meant that it was a prime candidate to showcase the complementarity of diffraction based techniques.

7.2.2 Bulk diffraction

Before discussing surface diffraction studies it will be useful to first consider the diffraction pattern of bulk TMA. This provides a standard to confirm distinct features of monolayer diffraction, relative to bulk crystallites. This can be relevant when adsorbates do not like to wet the surface and prefer forming 3D crystallites to 2D layers.

Data was collected at Diamond light source on beamline I11. A cryostream was employed to access a range of sample temperatures.

Figure 7.5 compares the diffractogram obtained for protonated TMA at 80 K, the lowest temperature studied, with the calculated predicted powder diffraction pattern based on the single crystal structure BTCOAC.⁹⁴ A reasonable agreement between the recorded unit cell and collected data is seen, with some agreement between the literature structure and initial diffraction experiments. However, attempts at indexing the observed pattern were not able to converge on a good unit cell fit.

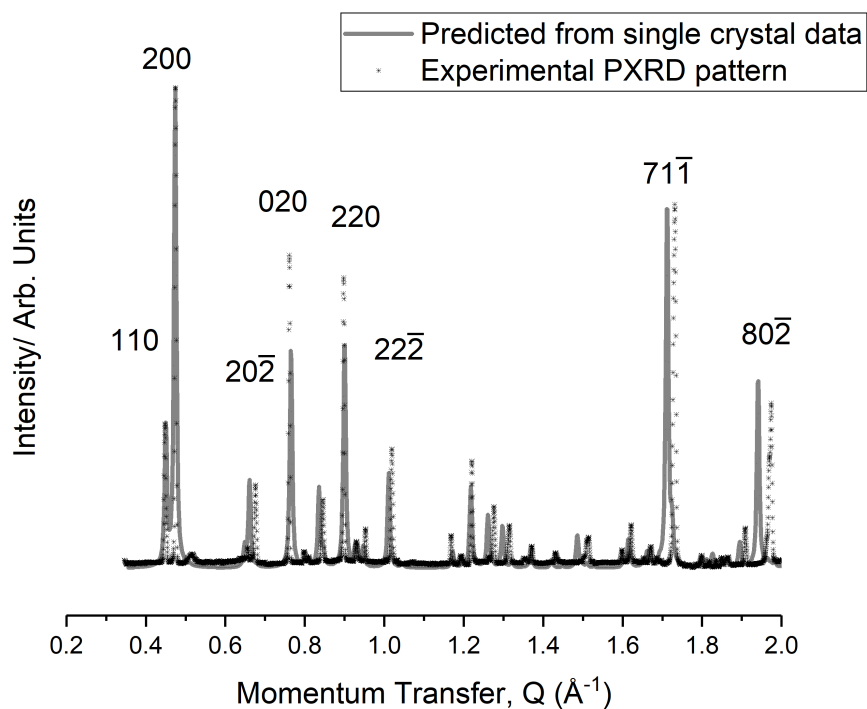


Fig. 7.5 Comparison between the powder diffraction pattern predicted from the single crystal bulk structure of TMA (grey) with the collected powder diffractogram from Diamond Light Source (black). In general there is good agreement between the two patterns, with some offset at higher angles. This could be due to thermal effects, and will not be relevant for comparison to the low angle monolayer diffractograms.

7.2.3 Dosing Monolayer Samples

Previous diffraction studies of monolayers on papyex have used a sublimation method to coat the molecules on the substrate. As described in chapter 3, carefully weighed samples of clean substrate and adsorbate are placed into a glass ampule, which is then sealed under a modest vacuum (10^{-2} mbar). The ampule is then placed in a furnace and annealed at an appropriate temperature. During this step the adsorbate is sublimed and then deposited from the vapour phase over the whole surface area of the closed system within the ampule. Due to the high surface area of the graphite, deposition onto this surface is predominant.

This method had been found to work well for a very wide range of molecules including alkanes,⁷⁸ fatty acids⁸⁴ fluoroalkanes⁸⁰ haloalkanes⁸⁶ and halogen bonding aromatic molecules,^{112,114} as well as the systems previously considered in this work. However, for trimesic acid it was found that the annealing step led simply to growth of solid TMA crystals

on the walls of the glass ampule, or even on the graphite itself, rather than dispersion of the adsorbate equally over the surface area of the system. This can be seen in figure 7.6, where white bulk TMA can be seen to have grown on the wall of the container (blue circle) and the papyex strip (red circle).

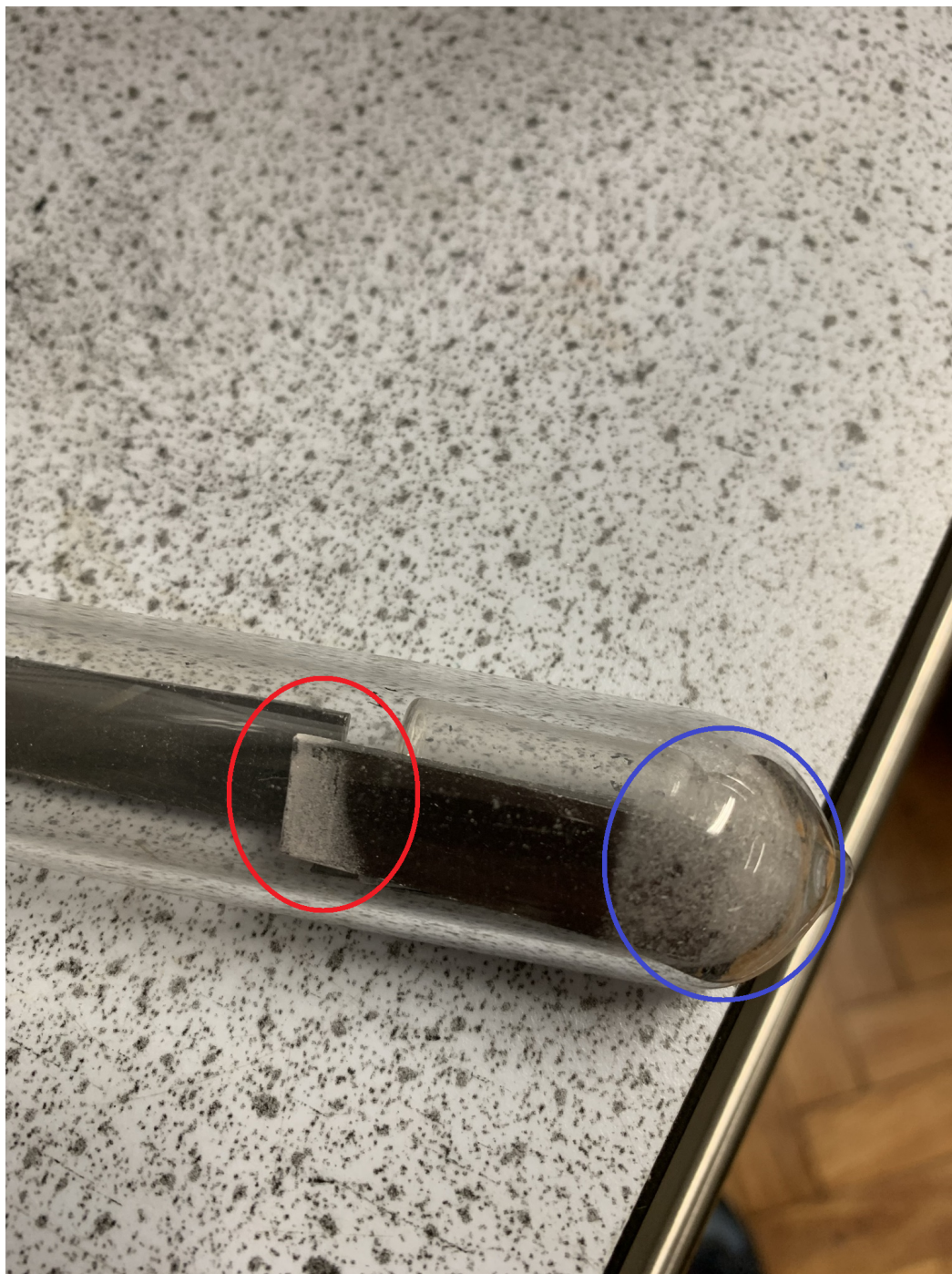


Fig. 7.6 Photo showing the contents of the glass ampule following a failed TMA dosing experiment. Solid TMA crystals can be seen growing on the papyex strip (red circle) and end of the ampule (blue container). For previously studied systems this was not observed, with dosed molecules being uniformly distributed on the internal surface area of the vessel.

Very great care and time was spent to optimise the dosing procedure for this molecule, however it was not possible to distribute the TMA over the internal surface area of the vessel using the previously successful method.

There are a number of possible origins to this challenge, it may be attributed to a comparatively small difference between the bulk and monolayer binding energies of TMA. Alternatively the hydrophilic nature of the glass ampule surface (the location of most of the bulk crystallites) may be templating the formation of the bulk TMA phase. There is a possibility that TMA does not wet the graphite substrate at all and at equilibrium the stable phase is a 3D crystal, rather than a 2D layer. However, previous studies have examined TMA monolayers on graphite in UHV conditions using a sublimation based technique, so it is clearly possible to form the desired monolayer by deposition from the gas phase. Due to the difficulty in obtaining monolayer samples using the established dosing technique, a significant number of novel approaches were trialled to dose TMA onto the papyex substrate.

Solution Dosing

Deposition from solution has been used to create monolayers in many studies conducted using ambient STM. Generally a volatile solvent is chosen, and a solution of less 10^{-6} M concentration formed. This is then deposited onto the substrate and allowed to evaporate before data collection. This is a facile method of deposition, though has the disadvantage of introducing another component to the system. It is possible that the added solvent used may not fully evaporate from the surface. In addition, any addition of a 'bulk' amount of sample can lead to minute impurities becoming significant and modifying the behaviour of the system. Despite these drawbacks, it was the first alternate deposition method attempted.

TMA is soluble in a range of polar organic solvents. Solubility is particularly good in fatty acids, and assembly of chickenwire and flower monolayer patterns has been observed under solution STM in long chain fatty acids.⁹⁸ For this reason acetic acid was chosen as a more volatile analogue of these solvents. Ethanol and Acetone are two other ubiquitous volatile polar organic solvents that TMA is sparingly soluble in that were also trialled.

Figure 7.7 presents the diffraction patterns that could be obtained using these solvents to deposit TMA onto papyex, and compares them to the diffraction pattern of bulk TMA. The patterns have been scaled for comparison, however it should be noted that the intensity of the peaks for the acetic acid dosed sample were significantly lower than for the other two samples, hence the greater background noise.

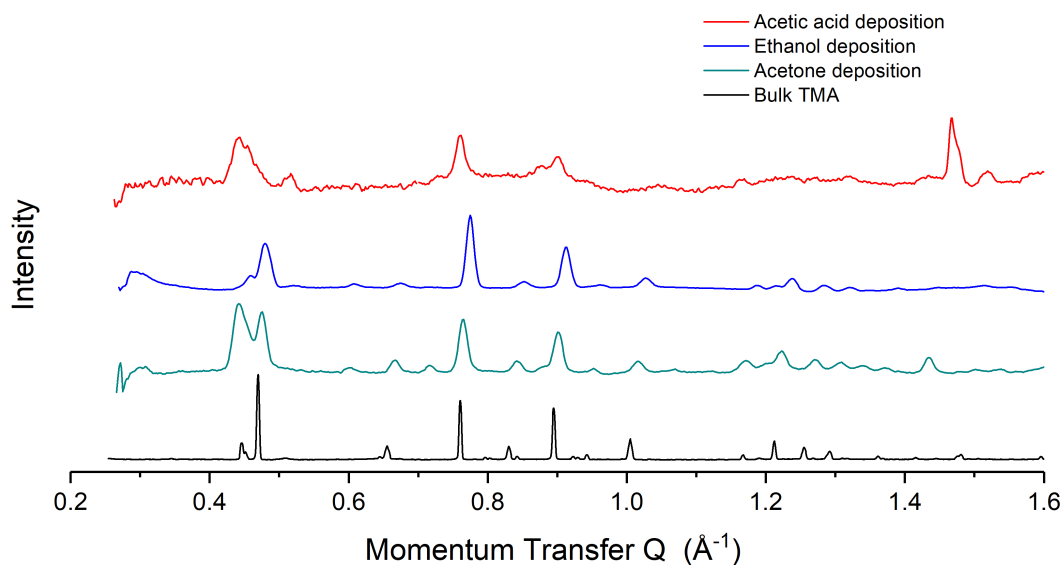


Fig. 7.7 Figure showing the diffractograms obtained for papyex dosed with a measured amount of TMA solution equating to 0.8ML compared to that obtained for bulk TMA. Intensities are scaled to ease comparison of relative peak intensities.

The observed diffraction patterns for ethanol and acetone dosing are fairly similar, though with some differences in relative intensities. In particular the lowest angle peak at $Q = 0.44\text{\AA}^{-1}$ is significantly more intense for the acetone deposited sample. The peaks all show a symmetrical broadening that is more consistent with a 3D periodicity than the asymmetric "sawtooth" peakshape expected for 2D periodic systems. Assuming the observed peaks are all from crystals of bulk TMA, the changes in relative peak intensity can be assigned to some preferred orientation of the formed crystals, possibly induced by the graphite substrate. However, the symmetry of the peaks, strong intensity of the diffraction peaks, and strong similarity to the diffraction pattern of bulk TMA all indicate that a pure monolayer phase has not been formed.

The acetic acid dosed sample exhibits significantly weaker peak intensities than for the other two solution deposited samples. Interestingly and significantly the lowest angle peak exhibits a quasi sawtooth asymmetric lineshape - characteristic of a 2D layer. However the relatively intense peak at $Q = 1.5\text{\AA}^{-1}$ was not observed in any other samples, and likely indicates the presence of additional phases (such as remaining acetic acid on the surface). Because of this, and the comparatively low peak intensity acetic acid was not pursued further as a reliable dosing method.

An alternative method of dosing to measured addition of solution is immersion in a concentrated solution, followed by removal and drying. This provides limited control of coverage, but should provide a more uniform, equilibrated, assembly than from rapid drying

of volatile solvents. Generally control of the solution concentration and exposure time allows conditions to be adjusted to obtain monolayer thick layers of surfactants. Korolkov et al. have reported on the behaviour of TMA in water for a range of concentrations and exposure times.¹⁹¹ Exposure to a 50 μ M solution for 100 seconds was reported to yield a monolayer, with further exposure building up islands of multilayers.

To mimic the referenced technique for this work, a freshly cleaned sample of papyex was immersed in a 50 μ M solution of TMA in ultrapure (18 M Ω cm⁻¹) water for 100 seconds, before being removed and dried using a nitrogen gas line. Unfortunately when the diffraction pattern for this sample was collected, no features of any kind could be seen beyond those of bare graphite.

Sublimation onto a cold finger.

Deposition in UHV experimental chambers is generally performed by heating the adsorbate in a source crucible and then depositing it onto a room temperature substrate, essentially driving the deposition with a thermal gradient. In an attempt to emulate this method, a separate vacuum system was created. (see figure 7.8) This contains a cold finger to keep the graphite cool, while a heat gun is used to heat the surrounding glass and sublime the TMA. In order to maintain vacuum this system has to be continuously pumped, a cold trap is visible to the right of the image to collect any TMA vapour lost from the chamber, as well as to protect the pump.



Fig. 7.8 Cold finger dosing of TMA on graphite

Using this dosing method it was possible to ensure that none of the weighed amount of TMA introduced into the vessel remained on the glass after dosing. No measurable amounts of TMA could be identified in the cold trap, indicating negligible losses to the vacuum system and pump. However the problem of evenly distributing the deposited TMA remained. As can be seen in figure 7.9. The visible fringes on the deposited graphite indicate the layer thicknesses are of the order of the wavelength of visible light (100s of nm). This is significantly thicker than the expected monolayer thickness (0.3 nm). It is also clear from the image that only a fraction of the exterior surface area of the graphite is coated and, due to the thickness required for the refractive fringes, likely only a fraction of the interior surface area of the porous graphite.



Fig. 7.9 TMA deposited on graphite using the cold finger method. The red circle highlights fringes of high refractive index. Although not captured well by camera, these fringes indicate significantly greater than monolayer deposition

Diffraction patterns of samples taken from along the length of the graphite are shown in figure 7.10. These show that along the strip there are only reflections consistent with the bulk structure of TMA. The intensities of these peaks decreases in sections taken from further up the strip, but no new peaks that would be expected of a monolayer structure were seen

to develop. From this it can be concluded that the deposition led to the formation of a bulk phase partially covering the graphite, with no monolayer or other novel phases detected.

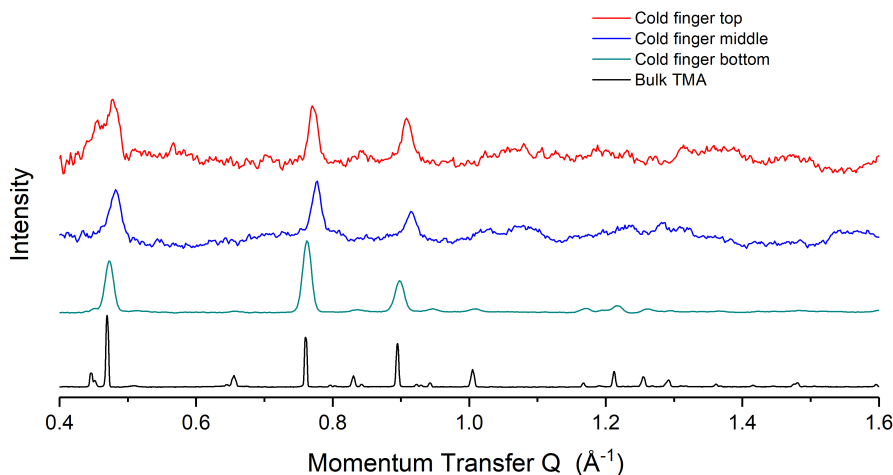


Fig. 7.10 Diffraction patterns of graphite samples taken from the cold finger deposited graphite shown in figure 7.9. Patterns are normalised in intensity, but as can be seen from comparison of the background noise, the intensity of the peaks decreases as samples are taken from further up the strip. All peaks observed are well matched by those expected from bulk TMA.

Warm substrate deposition

UHV experiments previously performed using this molecule have been successful and encountered few dosing problems. This may be attributed to the monolayer forming only on the external face of the substrate. Attempts to replicate this type of setup using a cold finger were unsuccessful, as the molecule simply condensed directly onto the outside face of the papyex, and did not penetrate into the whole of the substrate sample. To prevent this and facilitate more uniform adsorbate distribution it was thought to try a “warm finger” type dosing. Here, the entire glass ampule and graphite were heated to 150°C, just under the normal TMA sublimation temperature. The apparatus was then removed from the furnace, and a hot air gun used to locally heat the outside of the ampule (and attached TMA) above the TMA sublimation temperature, so that it deposited onto the warm graphite. It was observed that the TMA did not form any macroscopic crystals or photoactive thin layer, which indicates some difference from the cold finger method.

Diffraction data of this sample is presented in figure 7.11. The pattern does indicate quasi-2D lineshapes, including some peaks at scattering vectors not present in the bulk phase. Hence, we tentatively conclude that this was the first sample studied to be unambiguously identified as successfully demonstrating formation of a monolayer TMA system

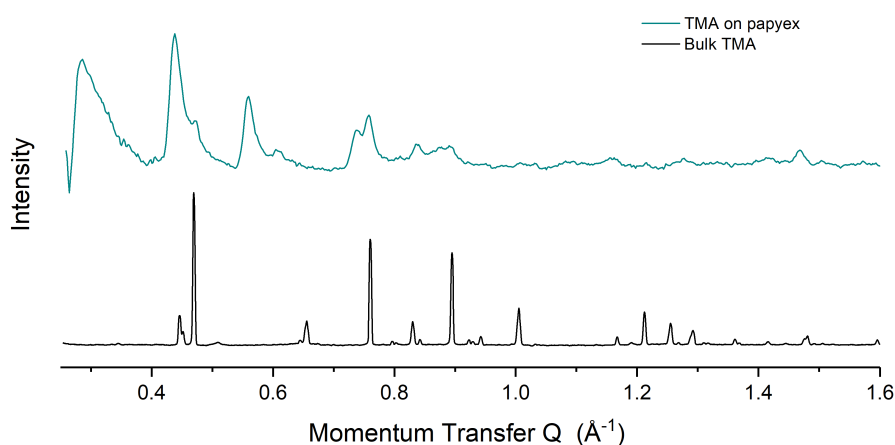


Fig. 7.11 Comparison of the diffraction pattern collected of bulk TMA with that of TMA deposited on papyex using the warm finger dosing technique described above. Significant differences in lineshape as well as several additional "sawtooth" peaks indicate that the warm finger technique led to the formation of monolayer TMA on the surface. Unfortunately subsequent attempts to repeat this dosing technique were unsuccessful in achieving a comparable pattern.

Altogether, this method delivered good results on the first attempt. However, subsequent attempts to repeat this method were unsuccessful, with bulk TMA crystallising on the far side of the ampule, or only on the outer surface of the graphite.

Annealing in Metal Vessel

As all the above deposition techniques have proven to be problematic, it was thought that the energy balance between bulk and monolayer phase formation must be extremely finely balanced, with undetectable temperature/humidity/purity fluctuations causing inconsistency in results. For this reason it was decided to attempt to use a metal reactor vessel to perform a slow anneal. Due to limited access to furnaces with slow enough controllers some of these samples were prepared by Professor Markus Lackinger at TU München. Unless otherwise stated the samples were prepared by myself. For samples prepared by Professor Lackinger all work from when the vessel was opened and data analysis was also performed by myself. The vessel was first pumped and heated to 500 °C to clean it. It was then removed and weighed amounts of freshly cleaned graphite and TMA placed inside. The vessel was then attached to a turbopump and heated at 120 °C for at least 12 hours, until the pressure levelled off within the 10⁻⁵mbar range. This was done in order to degas as much water/other contaminants as possible, without loss of TMA.

After the pressure had levelled off, the reactor was sealed and wrapped in aluminium foil to distribute heat evenly. It was then placed in a furnace with the following setting

- Fast ramp to 250°C
- Hold for one hour
- Cool at 2K hour⁻¹ to 90°C
- Power Off



Fig. 7.12]

Metal reactor after being used for TMA deposition. Graphite residue (grey) from ablation of the papyex strips can be seen inside the reactor along with bulk TMA (white)

When the reactor was opened it was evident that there was some bulk TMA crystals on the walls of the reactor. Despite this the first sample attempted (TMA sample z) which was dosed by Professor Lackinger showed extremely promising results. The diffractogram was extremely similar to that previously obtained using the "warm finger" method described above. Figure 7.13 presents the diffraction pattern obtained.

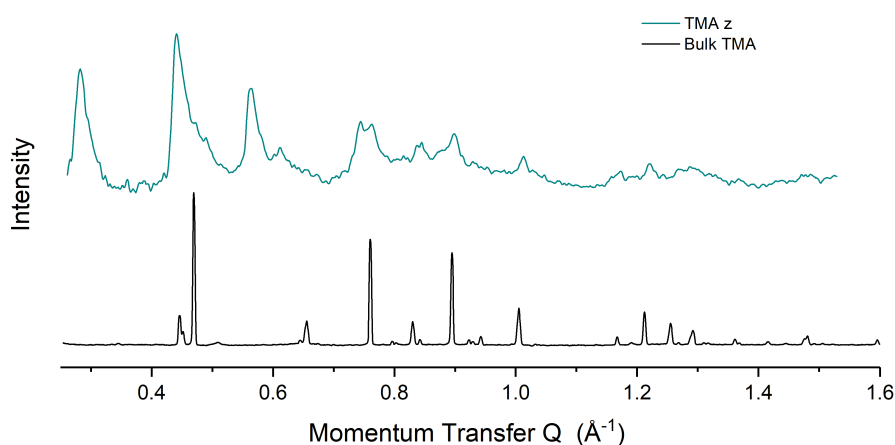


Fig. 7.13 TMA diffraction pattern collected after using the procedure described above. The pattern is comparable to that obtained using the "warm finger" method and show several unique peaks such as at $Q = 0.28$ and 0.56 \AA^{-1} compared to the bulk TMA pattern.

The diffractogram of this and other samples will be further studied in the next section. However, it must be noted that many more samples were dosed than achieved acceptable diffractograms. The quantity of TMA residue remaining in the reactor varied substantially with runs, despite no apparent difference in preparation method.

A limitation of the method was that even at these slow cooling rates some bulk TMA remained, so the absolute coverage of the monolayers could not be precisely determined or controlled.

Modified metal vessel

Neutrons interact with matter significantly less strongly than X-rays. For this reason samples for Neutron experiments must be orders of magnitude larger to give measurable scattering. The geometry of the neutron source also means that the capillary geometry rather than the flat plate geometry must be used. For this reason a different batch of papyex, JAD01 that is 2mm in thickness was used for the preparation of samples for neutron diffraction experiments. In preparation for beamtime at the D20 crystallography beamline at the Institut Laue Langevin (ILL) in Grenoble a larger dosing reactor setup was created to allow larger amounts of this thicker papyex to be dosed.

To test the validity of the setup an initial batch (dTMA II) was dosed at the Department of Chemistry in the University of Chemistry. This batch was then examined using the LMB rotating anode diffractometer. The diffractogram from this sample is shown in figure 7.14. It

can be seen that the pattern is similar to that observed for the smaller metal vessel deposition, providing confidence that both metal vessels perform similarly.

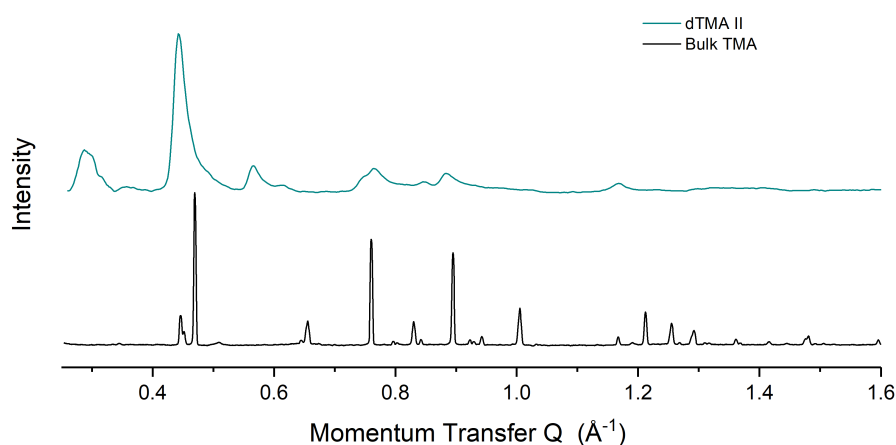


Fig. 7.14 Diffraction pattern collected of batch dTMA II using the larger dosing chamber described above. The relative intensities of some peaks are modified compared to those of protonated TMA as shall be described in the next section, however the positions and shapes of the peaks all indicate formation of a monolayer dTMA system.

Sample d-TMA II was then sealed and shipped to the ILL, alongside the dosing equipment two weeks before the beamline experiment. At the ILL the deposition method was repeated utilising a locally sourced turbopump and furnace, with the same vacuum system as before. This created sample d-TMA III.

Unfortunately, during the beamline experiment, when the vessel containing d-TMA III was opened, it was immediately apparent that dosing had been unsuccessful, with large quantities of bulk d-TMA clearly visible inside the vessel. The absence of monolayer dosing was confirmed upon inspection of the neutron diffraction results, with no differences observed between the dosed papyex and undosed background. At this point sample d-TMA II (which had exhibited a strong monolayer diffraction signal two weeks previously) was inspected, figure 7.15 presents the collected diffractogram and compares it to the data collected using X-ray diffraction on the same sample two weeks prior.

Some peaks in the collected neutron data bear some resemblance to diffraction peaks in the expected positions, however even after accounting for the different scattering properties of neutrons, the relative intensities of the peaks don't match with the collected X-ray data. As well as this, features are also present in completely different scatter vector positions, further reducing the credibility of any attempted peak identification. It is believed that some deterioration of the sample must have taken place between the X-ray and neutron diffraction

experiments. This is actually, an interesting result implying some limitations to the stability of the TMA monolayer under ambient conditions. Further experiments to explore the long term stability of the TMA layers were planned, but were unable to be performed due to the disruption of the Covid-19 pandemic.

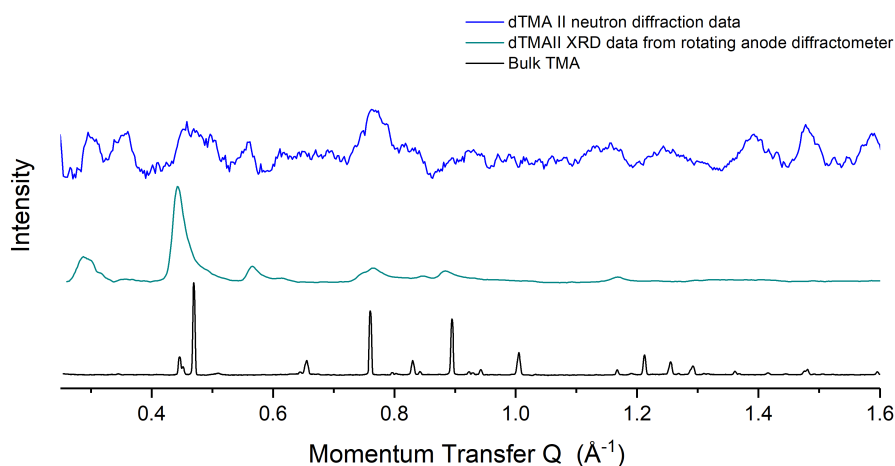


Fig. 7.15 Figure comparing the neutron collected data for sample dTMA II with that previously collected for the same samples using XRD. Some features are visible in the neutron diffraction pattern that bear some relation to peaks in broadly the expected positions, however the data is extremely noisy and the reliability of these features is questionable.

Summary

This section presents the first 2D monolayer diffraction patterns of TMA on graphite. This represents a considerable success given the experimental challenges of dosing the graphite and the propensity of 3D crystallite formation to frustrate 2D layer forming. A significant number of experimental approaches were considered and discarded, before three successful approaches were identified. However, even these still suffer from poor reproducibility.

7.2.4 Monolayer Diffraction Results

As discussed in the previous section, multiple methods were attempted to dose monolayer quantities of TMA on the papyex substrate. Overall, three diffractograms can be regarded as successes (Figures 7.11, 7.13 and 7.14), with the diffraction patterns being unambiguously identifiable as two dimensional in nature due to their very clear sawtooth lineshape. These patterns came from a) the first sample dosed using the "warm finger" technique, b) several samples deposited in the slow annealing metal chamber technique, and c) the deuterated pattern dTMA-II. Figure 7.16 compares representative diffractograms from samples dosed

using each technique to the diffraction pattern of bulk TMA. The patterns identified as successful in generating monolayers can be seen to be broadly alike, with asymmetric lineshapes and several different peak positions to bulk TMA. Some detailed differences can be observed between the three monolayer diffractograms, notably the relative intensities of several of the peaks. This will be discussed in the next section. Of the three dosing methods the use of a metal chamber was the most repeatable, and hence initial diffractogram analysis was performed on this pattern.

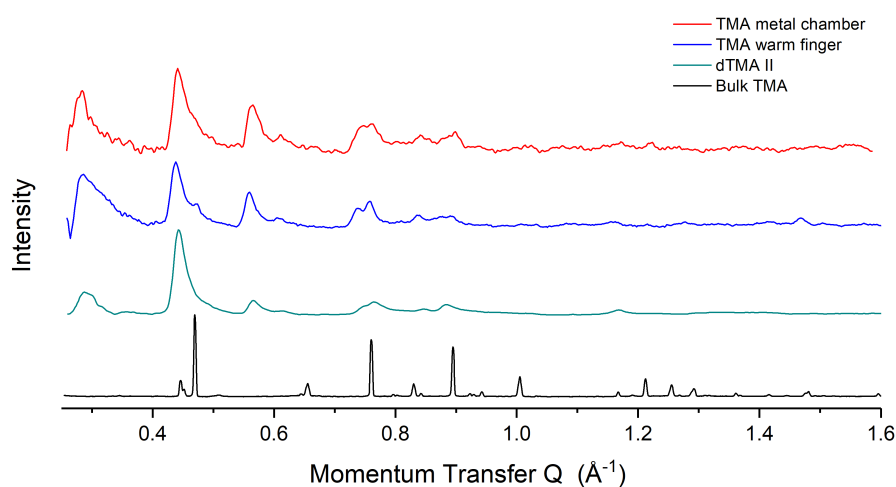


Fig. 7.16 Comparison of successful diffractograms of TMA deposited on graphite. Although there are some differences in peak intensity between the three samples, all three monolayer samples show asymmetric lineshapes, absence of some bulk TMA peaks, and presence of novel peaks. Hence, they can be considered as evidence of generation of a novel phase upon deposition of TMA onto the graphite.

Diffractogram analysis

Using the metal vessel slow anneal method described previously, it was possible to obtain reasonably consistent diffraction data for Trimesic acid monolayers on papyex. Figure 7.17 presents a typical diffractogram collected after graphite subtraction. Multiple diffraction peaks are visible. Importantly, it was not possible to index all of the observed peaks to a single unit cell. This can be an indication that several different phases may be present in the sample.

As discussed in chapter 1, a range of 2D phases have been observed or hypothesised to exist for trimesic acid monolayers in the literature. Ibenskas et al. utilised a triangular lattice to relate various observed structures together.¹⁰² At a simple level the "chickenwire" phase exists where each TMA molecule is bound solely through COOH dimers. At the other end of the spectrum, a hypothesised "superflower" phase would exhibit each trimesic acid molecule

having three bifurcated hydrogen bonds. In between these phases it is possible to imagine an infinite number of n th generation flower phases with varying degrees of bifurcation of hydrogen bonds.

Taking sensible estimates of the lattice parameter that would exist for each phase, it was possible to examine if any of the experimentally observed peaks match what may be expected for each of these phases. As seen from figure 7.17 it can be seen that all of the major observed diffraction peaks in this diffractogram match those of peaks from a combination of the chickenwire and flower TMA phases.

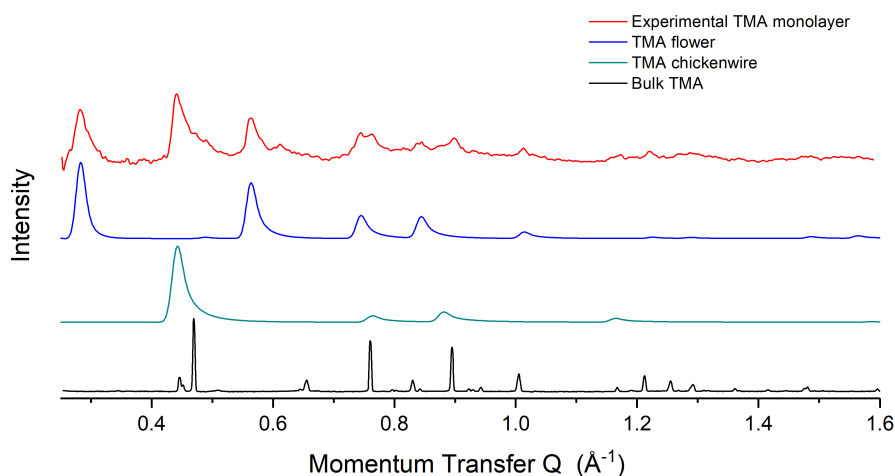


Fig. 7.17 Chart comparing the experimental diffractogram for TMA deposited on graphite using a slow anneal in a metal chamber, with predicted patterns for the TMA chickenwire and flower monolayers. The bulk TMA diffractogram is also included for comparison. The TMA on graphite patterns contains peaks with a characteristic sawtooth pattern that match well with those expected from the flower and chickenwire phases. A large degree of overlap between the bulk and predicted monolayer diffraction peaks is noticeable, so it is not possible to completely eliminate the possible presence of bulk TMA, however the asymmetry of the observed peaks strongly supports the predominance of two-dimensional periodicity in the structure.

More precise values for the size of the unit mesh for the chickenwire and flower phases can be obtained by refining the fit of the predicted and experimental diffraction patterns, similar to the analysis performed for previous systems. Table 7.2 presents the optimised lattice parameters for the chickenwire and flower polymorphs found for the three deposition methods.

The data includes protonated and perdeuterated TMA (the background from protons in neutron scattering prohibits their use). Perhaps surprisingly, minimal difference is seen between the protonated and deuterated refined lattice parameters. Using a combination

of analysis of the periodicity of Moire patterns of STM images of TMA on graphite and DFT calculation, Spitzer et al.¹⁰³ estimated the periodicity of the chickenwire structure as being $16.52 \pm 0.002 \text{ \AA}$, a value that is slightly smaller than those obtained here (16.54, 16.58, and 16.56 \AA). No such high precision value is available for the flower motif, however measurement of the packing density of the flower motif on a gold surface¹⁰¹ found a value of $25.8 \pm 1 \text{ \AA}$, with the diffraction results falling well within these error bars at 25.89, 25.98, and 25.87 \AA .

It is also possible to estimate the ratio of the amounts of the two phases present through optimising the fit and considering a simple addition of the two patterns to the experimental diffraction pattern. This is possible as the patternNx software used for structure prediction reports the calculated peak intensities for a grid of 4x4 unit meshes. These can be compared to the intensity of the diffraction peak of a 4x4 grid of an alternate phase. By accounting for the areas of the unit meshes of the two phases, and the number of TMA molecules per unit mesh, it is possible to estimate the number of TMA molecules that are in each phase.

Figure 7.18 presents an example of the fit for the deuterated TMA sample. The predicted pattern for a chickenwire:flower ratio of 0.82:0.18 is in black, while the experimental pattern is in grey. There is generally a good fit between the experimental and predicted data. However, some additional features at $Q = 0.33$ and 0.61 \AA are unexplained and not attributable to either of these two polymorphs. It wasn't possible to index these features to any previously observed TMA structure, monolayer or bulk.

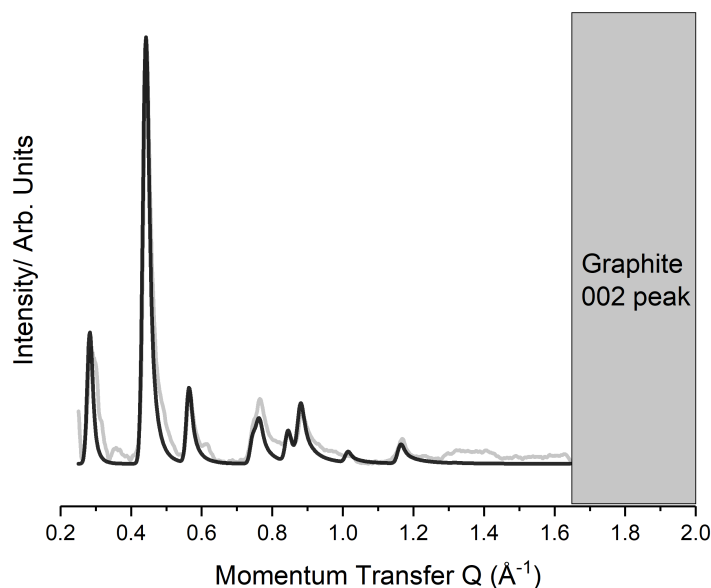


Fig. 7.18 Example plot comparing the experimental and predicted diffraction patterns for the deuterated TMA monolayer. The experimental pattern (grey) matches well with the pattern predicted for a 0.82:0.18 ratio addition of chickenwire (16.56 Å) and flower (25.87Å) polymorphs. As discussed in the text, not all experimentally observed peaks can be accounted for with this simple combination of 2D polymorphs.

This analysis has been performed for each of the successfully dosed TMA patterns and the ratio of flower:chickenwire extracted is given in table 7.2. From this it can be seen that for the different samples the estimated ratios of flower:chickenwire phases are different. This is perhaps unsurprising, as the uncontrolled nature of the dosing of these samples means that the total amount of TMA deposited on the surface (and hence the surface pressure of TMA) will be different for each system. However, for each system the chickenwire polymorph is predominant.

Table 7.2 Table comparing the lattice constants and molar ratios of the chickenwire and flower TMA polymorphs found from the diffraction results of three different samples. Sample dTMAII was deuterated and hence may be expected to exhibit larger differences than between the two protonated samples.

Sample	Chickenwire /Å	Flower /Å	Molar ratio Chickenwire	Molar ratio Flower
TMA metal chamber	16.54	25.89	0.53	0.47
TMA warm finger	16.58	25.98	0.60	0.40
dTMA II	16.56	25.87	0.82	0.18

It should be noted that all of the above analysis is based upon provisional results obtained from experiments that were chiefly designed to screen dosing methods, rather than to investigate minute changes in TMA lattice constant. A set of experiments designed to cover the variables of deuterated/non-deuterated and low temperature/room temperature were designed and attempted on several occasions, however in each case the deposition method was unsuccessful. This type of difficulty in obtaining reliable samples was never a problem for any of the previous systems studied, and shows the unique difficulty in equilibrating samples of TMA deposited on graphite.

However, there are some interesting conclusions that can be made. It is particularly significant that the diffraction results confirm the STM data indicating that the chickenwire and flower phases coexist. As discussed in section 1.3.4, based on the Gibbs Phase rule, a monocomponent system containing 2 phases can only exist at thermodynamic equilibrium where only one of temperature and pressure are allowed to vary. As coexistence is observed in this work for samples over a range of temperatures and coverages (surface pressures) a conclusion could be that the samples are **not** at thermodynamic equilibrium. However, given the long annealing step in the deposition, it would be thought a high degree of equilibration would exist. Previous work⁹⁸ has found the co-existence of two phases of trimesic acid even in solution phase STM, where dissolution and recrystallisation would be thought to ensure equilibrium is reached. An alternate explanation would be that the system is not truly monophasic. The above phase rule argument ignores the graphite as a component, treating it simply as an inert "infinite plane" with which to constrain the monolayer. If instead the graphite interacts strongly enough to be treated as an additional component, such as if it is a featured topography strongly interacting with the growth of the layer, then a thermodynamic account of trimesic acid assembly must also consider this surface. Using the phase rule, a system containing two components (TMA and graphite) can exhibit two phases ("chickenwire on graphite", and "flower on graphite") across a range of temperatures and pressures. Defects in the graphite plane may mean that at some points on the sheet the chickenwire phase is lowest in energy, and in others the flower phase.

7.2.5 Conclusion

Here I have successfully presented the first 2D monolayer diffraction patterns of TMA on graphite, overcoming very significant experimental challenges of dosing the graphite and the propensity of 3D crystallite formation. It was possible to identify peak positions and asymmetric lineshapes that can be considered indicative of monolayer dosing. Through analysis of these patterns it has been possible to deduce the coexistence of at least two polymorphs and obtain preliminary values for the lattice constants of these two phases of the

TMA monolayer. The coexistence, the monolayer structures and lattice values are broadly consistent with those estimated in previously published work using STM and DFT.

The confirmation of the previously reported STM result that the two phases of TMA monolayer (chickenwire and flower) coexist in the samples studied is an interesting result that appears to challenge the phase rule. Further investigation to better understand this effect would be desirable, however unfortunately experimental difficulties in repeatable dosing limited the number of samples that could be analysed.

Chapter 8

Conclusion

8.1 Summary

In this work the self assembly of a range of systems into ordered two-dimensional monolayer systems has been investigated. The initial aim of this work was to combine both STM and diffraction experimental work performed by myself, with the DFT simulations of co-workers.

Some initial significant advances with STM data collection were made, with some very high spatial resolution images of PTCDI obtained (chapter 3). However ongoing experimental difficulties with the STM limited what could be achieved using this technique. The limited STM images that could be collected provide a tantalising glimpse into the potential of this technique, explaining why it and related scanning probe techniques have become the analytical method of choice for investigation of two-dimensional systems. The origin of the unexpectedly high resolution of the obtained images of PTCDI remains unexplained, and demonstrate how much is still to be understood in terms of the exact nature of the STM tip - sample interaction.

A body of X-ray and neutron monolayer diffraction experiments were performed. These diffraction experiments have progressed previous work on halogen bonded monolayer systems, extending the work to utilise non-aromatic halogen bond donors, and tritopic building blocks in an attempt to form porous networks. I was able to gain access to one of the most intense lab based X-ray sources for my work, and developed a novel diffraction geometry to maximise the utility of modern area detectors for this study. This enabled the use of convenient lab based X-ray sources to study even weakly scattering systems such as monolayers of s-triazine, with 10 minutes of exposure, rather than multiple hours. We are most grateful to Fabrice Gorrec and the LMB for allowing myself access to these facilities.

Comparison of the results of the diffraction studies presented here generally agree well with literature work using STM and/or DFT where applicable. We have demonstrated how some systems such as TITFB that are difficult or impossible to image using scanning probe techniques can be investigated using less invasive diffraction methods.

In contrast the TMA monolayer system, which has provided such a rich vein of scanning probe research, proved to be extremely challenging to reliably dose onto diffraction substrate samples, and showed some evidence of degradation under ambient storage conditions. These examples serve as lessons against relying on a single technique for scientific investigation, particularly when considering the assembly of delicate structures such as physisorbed monolayers.

8.2 Further Work

Due to the aforementioned experimental difficulties, the aim of combining scanning probe and diffraction techniques to study the same system remains unfulfilled. If the vapour dosing of TMA onto graphite could be made more reliable then this system would provide a fascinating system to probe using different techniques. The effects of temperature and deuteration in modifying the lattice size of the monolayers is something which my collaborator (Markus Lackinger) had struggled to reliably determine using scanning probe techniques. The limited data collected in this diffraction work was unfortunately not sufficient to provide unambiguous results, however the potential of a repeatable dosing method to generate high quality data is a clear extension of the presented work.

The investigation into diffraction of TMA started as an interesting side project, but the difficulties in reliably dosing monolayer TMA onto graphite meant that the work became a recipient of substantial research effort. The factors behind unsuccessful and successful dosing regimes remain unknown, and could have substantial implication for the thermodynamic stability of the previously reported TMA systems. Use of alternative high surface area graphites would allow a comparison of the facile dosing performance onto HOPG crystals (as used in the literature) with the difficult dosing onto papyex. As well as this, a more complete vacuum system including a residual gas analyser (RGA) mass spec would allow determination of the effect residual quantities of water may have in influencing TMA crystallisation.

The high quality of the PTCDI STM images was a pleasing if surprising result considering the relatively high (77K) temperature of imaging. As discussed in chapter 3, similar atomic resolution had been observed with AFM only at significantly lower <10K temperatures with tips functionalised using a small probe molecule. An initial hypothesis would be that the electronic conductivity of the PTCDI molecule means that it can also act as a probe molecule,

with its larger size relative to CO or Xe allowing a larger effect on observed resolution. However, MD modelling the effect of this system on the tip and comparing the results with those observed in an analogous way to Temirov et al. would provide a way to test this.

Formation of a porous halogen bonded system has proven to be substantially more difficult than anticipated. Although halogen bonds are conventionally considered highly directional, the non-linear halogen bond angles observed in the $\alpha - \omega$ -terminally iodinated perfluoroalkanes in chapter 6 demonstrate that comparatively large deviations in halogen bond angle can be accommodated in exchange for improved close-packing interactions. Design of molecular systems where each vertex is joined by two or three halogen bonds, similar to TMA or PTCDI:melamine systems would be a logical next step, to strengthen the directional interaction and mimic the porous hydrogen bonded systems. However, design and synthesis of such building blocks would be a substantial challenge.

8.3 Concluding Remarks

Monolayer systems represent an intriguing field within nanoscience and surface science. The potential of 2D supramolecular chemistry to allow tunable interfaces could have a myriad of industrial uses. Despite that, the self assembly of monolayers is still in relative infancy. While bulk supramolecular systems benefit from a toolbox of applications for prediction and measurement of structure, those studying surface self assembly have comparatively few guidelines and analytical methods available. This work presents three different but complementary techniques (STM, XRD, and DFT) that, while useful alone, achieve greater utility when used in tandem. These techniques have been used to further investigate well known surface supramolecular systems (PTCDI, TMA), and to investigate novel halogen bonded systems.

References

- ¹ Y. He, T. Ye, M. Su, C. Zhang, A. E. Ribbe, W. Jiang, and C. Mao, "Hierarchical self-assembly of DNA into symmetric supramolecular polyhedra," *Nature*, vol. 452, pp. 198–201, mar 2008.
- ² S. Kassem, T. van Leeuwen, A. S. Lubbe, M. R. Wilson, B. L. Feringa, and D. A. Leigh, "Artificial molecular motors," *Chemical Society Reviews*, vol. 46, no. 9, pp. 2592–2621, 2017.
- ³ R. Otero, J. M. Gallego, A. L. V. de Parga, N. Martín, and R. Miranda, "Molecular Self-Assembly at Solid Surfaces," *Advanced Materials*, vol. 23, pp. 5148–5176, nov 2011.
- ⁴ J. N. Israelachvili, "Front Matter," in *Intermolecular and Surface Forces*, p. iii, Elsevier, 2011.
- ⁵ L. J. Prins, D. N. Reinhoudt, and P. Timmerman, "Noncovalent synthesis using hydrogen bonding," *Angewandte Chemie - International Edition*, vol. 40, pp. 2382–2426, jul 2001.
- ⁶ T. Steiner, "The hydrogen bond in the solid state," *Angewandte Chemie - International Edition*, vol. 41, pp. 48–76, jan 2002.
- ⁷ F. Biedermann, W. M. Nau, and H. J. Schneider, "The Hydrophobic Effect Revisited - Studies with Supramolecular Complexes Imply High-Energy Water as a Noncovalent Driving Force," 2014.
- ⁸ D. M. Watkins, Y. Sayed-sweet, J. W. Klimash, N. J. Turro, and D. A. Tomalia, "Dendrimers with Hydrophobic Cores and the Formation of Supramolecular Dendrimer-Surfactant Assemblies," *Langmuir*, vol. 13, no. 10, pp. 3136–3141, 1997.
- ⁹ C. A. Hunter and J. K. M. Sanders, "The nature of π - π interactions," *Journal of the American Chemical Society*, vol. 112, no. 14, pp. 5525–5534, 1990.
- ¹⁰ D. Quiñonero, A. Frontera, C. Garau, P. Ballester, A. Costa, and P. M. Deyà, "Interplay between cation- π , anion- π and π - π interactions.," *Chemphyschem : a European journal of chemical physics and physical chemistry*, vol. 7, no. 12, pp. 2487–91, 2006.
- ¹¹ P. Politzer, P. Lane, M. C. Concha, Y. Ma, and J. S. Murray, "An overview of halogen bonding," *Journal of Molecular Modeling*, vol. 13, pp. 305–311, jan 2007.

- ¹² G. R. Desiraju, P. S. Ho, L. Kloo, A. C. Legon, R. Marquardt, P. Metrangolo, P. Politzer, G. Resnati, and K. Rissanen, "Definition of the halogen bond (IUPAC Recommendations 2013)," *Pure and Applied Chemistry*, vol. 85, p. 1, jan 2013.
- ¹³ B. R. Mullaney, A. L. Thompson, and P. D. Beer, "An All-Halogen Bonding Rotaxane for Selective Sensing of Halides in Aqueous Media," *Angewandte Chemie International Edition*, vol. 53, pp. 11458–11462, oct 2014.
- ¹⁴ H. Takezawa, T. Murase, G. Resnati, P. Metrangolo, and M. Fujita, "Halogen-Bond-Assisted Guest Inclusion in a Synthetic Cavity," *Angewandte Chemie*, vol. 127, pp. 8531–8534, jul 2015.
- ¹⁵ S. Shankar, O. Chovnik, L. J. Shimon, M. Lahav, and M. E. Van Der Boom, "Directed Molecular Structure Variations of Three-Dimensional Halogen-Bonded Organic Frameworks (XBOFs)," *Crystal Growth and Design*, vol. 18, no. 4, pp. 1967–1977, 2018.
- ¹⁶ R. Wilcken, M. O. Zimmermann, A. Lange, A. C. Joerger, and F. M. Boeckler, "Principles and applications of halogen bonding in medicinal chemistry and chemical biology," *Journal of Medicinal Chemistry*, vol. 56, no. 4, pp. 1363–1388, 2013.
- ¹⁷ A. G. Slater (née Phillips), P. H. Beton, N. R. Champness, A. G. Slater, P. H. Beton, and N. R. Champness, "Two-dimensional supramolecular chemistry on surfaces," *Chemical Science*, vol. 2, no. 8, p. 1440, 2011.
- ¹⁸ E. Pensa, E. Cortés, G. Corthey, P. Carro, C. Vericat, M. H. Fonticelli, G. Benítez, A. A. Rubert, and R. C. Salvarezza, "The chemistry of the sulfur-gold interface: In search of a unified model," *Accounts of Chemical Research*, vol. 45, no. 8, pp. 1183–1192, 2012.
- ¹⁹ R. Madueno, M. T. Räisänen, C. Silien, and M. Buck, "Functionalizing hydrogen-bonded surface networks with self-assembled monolayers," *Nature*, vol. 454, pp. 618–621, jul 2008.
- ²⁰ D. Bonifazi, S. Mohnani, and A. Llanes-Pallas, "Supramolecular Chemistry at Interfaces: Molecular Recognition on Nanopatterned Porous Surfaces," *Chemistry - A European Journal*, vol. 15, pp. 7004–7025, jul 2009.
- ²¹ S. C. C. van der Lubbe and C. Fonseca Guerra, "The Nature of Hydrogen Bonds: A Delineation of the Role of Different Energy Components on Hydrogen Bond Strengths and Lengths," *Chemistry – An Asian Journal*, vol. 14, p. asia.201900717, jul 2019.
- ²² J. Řezáč, "Non-Covalent Interactions Atlas Benchmark Data Sets: Hydrogen Bonding," *Journal of Chemical Theory and Computation*, vol. 16, pp. 2355–2368, apr 2020.
- ²³ A. Extance, "The forgotten female crystallographer who discovered C-H...O bonds," *Chemistry World*, jul 2019.
- ²⁴ C. A. Hunter, "Quantifying intermolecular interactions: Guidelines for the molecular recognition toolbox," *Angewandte Chemie - International Edition*, vol. 43, pp. 5310–5324, oct 2004.

- ²⁵ L. Brammer, E. A. Bruton, and P. Sherwood, "Understanding the Behavior of Halogens as Hydrogen Bond Acceptors," *Crystal Growth and Design*, vol. 1, no. 4, pp. 277–290, 2001.
- ²⁶ M. Colin, "Note Sur Quelques Combinaisons de L'iode," *Ann. Chim.*, vol. 91, pp. 252–272, 1814.
- ²⁷ F. Guthrie, "XXVIII.—On the iodide of iodammonium," *J. Chem. Soc.*, vol. 16, pp. 239–244, 1863.
- ²⁸ O. Hassel, "Structural Aspects of Interatomic Charge-Transfer Bonding," *Science*, vol. 170, pp. 497–502, oct 1970.
- ²⁹ C. R. Groom, I. J. Bruno, M. P. Lightfoot, and S. C. Ward, "The Cambridge Structural Database," *Acta Crystallographica Section B Structural Science, Crystal Engineering and Materials*, vol. 72, pp. 171–179, apr 2016.
- ³⁰ T. Brinck, J. S. Murray, and P. Politzer, "Surface electrostatic potentials of halogenated methanes as indicators of directional intermolecular interactions," *International Journal of Quantum Chemistry*, vol. 44, pp. 57–64, mar 1992.
- ³¹ G. Cavallo, P. Metrangolo, R. Milani, T. Pilati, A. Priimagi, G. Resnati, and G. Terraneo, "The Halogen Bond," *Chemical Reviews*, vol. 116, pp. 2478–2601, feb 2016.
- ³² T. Clark, M. Hennemann, J. S. Murray, and P. Politzer, "Halogen bonding: the σ -hole," *Journal of Molecular Modeling*, vol. 13, pp. 291–296, jan 2007.
- ³³ P. Politzer and J. S. Murray, "Halogen Bonding: An Interim Discussion," *ChemPhysChem*, vol. 14, pp. 278–294, feb 2013.
- ³⁴ W. Wang, B. Ji, and Y. Zhang, "Chalcogen bond: A sister noncovalent bond to halogen bond," *Journal of Physical Chemistry A*, vol. 113, no. 28, pp. 8132–8135, 2009.
- ³⁵ S. Scheiner, "The pnictogen bond: Its relation to hydrogen, halogen, and other noncovalent bonds," *Accounts of Chemical Research*, vol. 46, no. 2, pp. 280–288, 2013.
- ³⁶ A. Bauzá, T. J. Mooibroek, and A. Frontera, "Tetrel-bonding interaction: Rediscovered supramolecular force?," *Angewandte Chemie - International Edition*, vol. 52, no. 47, pp. 12317–12321, 2013.
- ³⁷ R. Cabot and C. A. Hunter, "Non-covalent interactions between iodo-perfluorocarbons and hydrogen bond acceptors," *Chemical Communications*, no. 15, p. 2005, 2009.
- ³⁸ K. Shou, J. K. Hong, E. S. Wood, J. M. Hook, A. Nelson, Y. Yin, G. G. Andersson, A. Abate, U. Steiner, and C. Neto, "Ultralow surface energy self-assembled monolayers of iodo-perfluorinated alkanes on silica driven by halogen bonding," *Nanoscale*, vol. 11, no. 5, pp. 2401–2411, 2019.
- ³⁹ C. C. Robertson, R. N. Perutz, L. Brammer, and C. A. Hunter, "A solvent-resistant halogen bond," *Chemical Science*, vol. 5, no. 11, pp. 4179–4183, 2014.

- ⁴⁰ R. B. Walsh, C. W. Padgett, P. Metrangolo, G. Resnati, T. W. Hanks, and W. T. Pennington, "Crystal Engineering through Halogen Bonding: Complexes of Nitrogen Heterocycles with Organic Iodides," *Crystal Growth and Design*, vol. 1, no. 2, pp. 165–175, 2001.
- ⁴¹ M. Boterashvili, T. Shirman, S. R. Cohen, G. Evmenenko, P. Dutta, P. Milko, G. Leituss, M. Lahav, and M. E. van der Boom, "Interfacial halogen bonding probed using force spectroscopy," *Chemical Communications*, vol. 49, no. 34, p. 3531, 2013.
- ⁴² G. R. Desiraju and R. Parthasarathy, "The nature of halogen-halogen interactions: Are short halogen contacts due to specific attractive forces or due to close packing of nonspherical atoms?," *Journal of the American Chemical Society*, vol. 111, no. 23, pp. 8725–8726, 1989.
- ⁴³ F. Bertolotti, A. V. Shishkina, A. Forni, G. Gervasio, A. I. Stash, and V. G. Tsirelson, "Intermolecular bonding features in solid iodine," *Crystal Growth and Design*, vol. 14, no. 7, pp. 3587–3595, 2014.
- ⁴⁴ S. J. Ang, A. M. Mak, M. B. Sullivan, and M. W. Wong, "Site specificity of halogen bonding involving aromatic acceptors," *Physical Chemistry Chemical Physics*, vol. 20, no. 13, pp. 8685–8694, 2018.
- ⁴⁵ C. B. Aakeröy, T. K. Wijethunga, and J. Desper, "Practical crystal engineering using halogen bonding: A hierarchy based on calculated molecular electrostatic potential surfaces," *Journal of Molecular Structure*, vol. 1072, pp. 20–27, aug 2014.
- ⁴⁶ C. B. Aakeröy, T. K. Wijethunga, J. Desper, M. Daković, and M. Dakovic, "Electrostatic potential differences and halogen-bond selectivity," *Crystal Growth and Design*, vol. 16, pp. 2662–2670, may 2016.
- ⁴⁷ A. Mukherjee, S. Tothadi, and G. R. Desiraju, "Halogen Bonds in Crystal Engineering: Like Hydrogen Bonds yet Different," *Accounts of Chemical Research*, vol. 47, pp. 2514–2524, aug 2014.
- ⁴⁸ J. M. Lehn, "Cryptates: the chemistry of macropolycyclic inclusion complexes," *Accounts of Chemical Research*, vol. 11, pp. 49–57, feb 1978.
- ⁴⁹ D. S. Reddy, Y. E. Ovchinnikov, O. V. Shishkin, Y. T. Struchkov, and G. R. Desiraju, "Supramolecular Synthons in Crystal Engineering. 3. Solid State Architecture and Synthon Robustness in Some 2,3-Dicyano-5,6-dichloro-1,4-dialkoxybenzenes 1," *Journal of the American Chemical Society*, vol. 118, pp. 4085–4089, jan 1996.
- ⁵⁰ D. Su, X. Wang, M. Simard, and J. D. Wuest, "Molecular tectonics," *Supramolecular Chemistry*, vol. 6, pp. 171–178, oct 1995.
- ⁵¹ J. Teyssandier, S. D. Feyter, and K. S. Mali, "Host–guest chemistry in two-dimensional supramolecular networks," *Chemical Communications*, vol. 52, no. 77, pp. 11465–11487, 2016.
- ⁵² G. R. Desiraju, "Supramolecular Synthons in Crystal Engineering—A New Organic Synthesis," *Angewandte Chemie International Edition in English*, vol. 34, pp. 2311–2327, nov 1995.

- ⁵³ J. W. Gibbs and J. Tyndall, *On the equilibrium of heterogeneous substances : first [-second] part*, vol. 16. [New Haven: Published by the Academy, nov 1874.
- ⁵⁴ B. Franklin, W. Brownrigg, and M. Farish, "Of the Stilling of Waves by means of Oil. Extracted from Sundry Letters between Benjamin Franklin, LL. D. F. R. S. William Brownrigg, M. D. F. R. S. and the Reverend Mr. Farish," *Philosophical Transactions of the Royal Society of London*, vol. 64, pp. 445–460, jan 1774.
- ⁵⁵ : Dbroesch at English Wikipedia, "A cartoon of a LB film being compressed," 2008.
- ⁵⁶ I. Langmuir, "THE CONSTITUTION AND FUNDAMENTAL PROPERTIES OF SOLIDS AND LIQUIDS. II. LIQUIDS.," *Journal of the American Chemical Society*, vol. 39, no. 9, pp. 1848–1906, 1917.
- ⁵⁷ K. B. Blodgett, "Films Built by Depositing Successive Monomolecular Layers on a Solid Surface," *Journal of the American Chemical Society*, vol. 57, no. 6, pp. 1007–1022, 1935.
- ⁵⁸ W. Bigelow, D. Pickett, and W. Zisman, "Oleophobic monolayers. Films Adsorbed From Solution In Non-Polar Liquids," *Journal of Colloid Science*, vol. 1, no. 6, pp. 513–538, 1946.
- ⁵⁹ L. M. Blinov, "Physical Properties and Applications of Langmuir Monomolecular and Multimolecular Structures," *Russian Chemical Reviews*, vol. 52, no. 8, pp. 713–735, 1983.
- ⁶⁰ J. Sagiv, "Organized monolayers by adsorption. 1. Formation and structure of oleophobic mixed monolayers on solid surfaces," *Journal of the American Chemical Society*, vol. 399, no. 1976, pp. 92–98, 1980.
- ⁶¹ a. Ulman, "Formation and Structure of Self-Assembled Monolayers," *Chemical Reviews*, vol. 96, no. 4, pp. 1533–1554, 1996.
- ⁶² C. D. Bain, E. B. Troughton, Y. T. Tao, J. Evall, G. M. Whitesides, and R. G. Nuzzo, "Formation of monolayer films by the spontaneous assembly of organic thiols from solution onto gold," *Journal of the American Chemical Society*, vol. 111, no. 1, pp. 321–335, 1989.
- ⁶³ H. Häkkinen, "The gold–sulfur interface at the nanoscale," *Nature Chemistry*, vol. 4, no. 6, pp. 443–455, 2012.
- ⁶⁴ J. C. Love, L. A. Estroff, J. K. Kriebel, R. G. Nuzzo, and G. M. Whitesides, "Self-Assembled Monolayers of Thiolates on Metals as a Form of Nanotechnology," *Chemical Reviews*, vol. 105, pp. 1103–1170, apr 2005.
- ⁶⁵ R. P. Andres, J. D. Bielefeld, J. I. Henderson, D. B. Janes, V. R. Kolagunta, C. P. Kubiak, W. J. Mahoney, and R. G. Osifchin, "Self-Assembly of a Two-Dimensional Superlattice of Molecularly Linked Metal Clusters," *Science*, vol. 273, no. 5282, pp. 1690–1693, 1996.
- ⁶⁶ D. Amabalino, *Supramolecular Chemistry at Surfaces*. Monographs in Supramolecular Chemistry, Cambridge: Royal Society of Chemistry, 2016.

- ⁶⁷ J. Lander and J. Morrison, "A LEED investigation of physisorption," *Surface Science*, vol. 6, pp. 1–32, jan 1967.
- ⁶⁸ T. Arnold and S. M. Clarke, "Diffraction from physisorbed layers," *Current Opinion in Colloid and Interface Science*, vol. 17, no. 1, pp. 23–32, 2012.
- ⁶⁹ R. D. Diehl, M. F. Toney, and S. C. Fain, "Orientational Ordering of Nitrogen Molecular Axes for a Commensurate Monolayer Physisorbed on Graphite," *Physical Review Letters*, vol. 48, pp. 177–180, jan 1982.
- ⁷⁰ J. Cui and S. C. Fain, "Low-energy electron diffraction study of incommensurate H₂, HD, and D₂ monolayers physisorbed on graphite," *Physical Review B*, vol. 39, pp. 8628–8642, apr 1989.
- ⁷¹ M. Sakurai and C. Yamada, "Dynamics of physisorbed monolayer of methane on Ag(111)," *Surface Science*, vol. 593, pp. 195–201, nov 2005.
- ⁷² A. G. Cabello-Cartagena, J. Vogt, and H. Weiss, "Structure and infrared absorption of the first layer C₂H₂ on the NaCl(100) single-crystal surface," *The Journal of Chemical Physics*, vol. 132, p. 074706, feb 2010.
- ⁷³ S. Driver and D. King, "Methanethiolate structural phases on Cu{111} observed using a novel fibre-optic low-energy electron diffraction instrument," *Surface Science*, vol. 601, pp. 510–517, jan 2007.
- ⁷⁴ P. W. Stephens, P. Heiney, R. J. Birgeneau, and P. M. Horn, "X-Ray Scattering Study of the Commensurate-Incommensurate Transition of Monolayer Krypton on Graphite," *Physical Review Letters*, vol. 43, pp. 47–51, jul 1979.
- ⁷⁵ C. W. Mowforth, T. Rayment, and R. K. Thomas, "Long-period commensurate structures near the incommensurate–commensurate phase transition in xenon layers adsorbed on graphite observed by X-ray diffraction," *J. Chem. Soc., Faraday Trans. 2*, vol. 82, no. 10, pp. 1621–1634, 1986.
- ⁷⁶ K. Morishige, C. Mowforth, and R. Thomas, "Orientational order in CO and N₂ monolayers on graphite studied by x-ray diffraction," *Surface Science Letters*, vol. 151, p. A80, mar 1985.
- ⁷⁷ J. Coulomb, J. Suzanne, M. Bienfait, M. Matecki, A. Thomy, B. Croset, and C. Marti, "Two-dimensional polymorphism and melting in a monolayer of nitric oxide adsorbed on graphite," *Journal de Physique*, vol. 41, no. 10, pp. 1155–1164, 1980.
- ⁷⁸ T. Arnold, R. K. Thomas, M. A. Castro, S. M. Clarke, L. Messe, and A. Inaba, "The crystalline structures of the even alkanes hexane, octane, decane, dodecane and tetradecane monolayers adsorbed on graphite at submonolayer coverages and from the liquid-Electronic Supplementary Information available. See <http://www.rsc.org/suppdata/cp>," *Physical Chemistry Chemical Physics*, vol. 4, no. 2, pp. 345–351, 2002.
- ⁷⁹ T. Arnold, C. C. Dong, R. K. Thomas, M. A. Castro, A. Perdigon, S. M. Clarke, and A. Inaba, "The crystalline structures of the odd alkanes pentane, heptane, nonane, undecane,

- tridecane and pentadecane monolayers adsorbed on graphite at submonolayer coverages and from the liquidElectronic supplementary information (ESI) available: Fractional coord,” *Physical Chemistry Chemical Physics*, vol. 4, no. 14, pp. 3430–3435, 2002.
- ⁸⁰ J. E. Parker, S. M. Clarke, A. C. Perdigon, and A. Inaba, “The Crystalline Structures of Fluoroalkane Monolayers Adsorbed on Graphite at Submonolayer Coverages,” *The Journal of Physical Chemistry C*, vol. 113, pp. 21396–21405, dec 2009.
- ⁸¹ K. Morishige, Y. Tajima, S. Kittaka, S. M. Clarke, and R. K. Thomas, “The structure of chloromethane monolayers adsorbed on graphite,” *Molecular Physics*, vol. 72, pp. 395–411, feb 1991.
- ⁸² S. M. Clarke and R. K. Thomas, “The structure of a bromomethane monolayer adsorbed on graphite,” *Molecular Physics*, vol. 72, no. 2, pp. 413–423, 1991.
- ⁸³ R. Bucknall, S. Clarke, R. Shapton, and R. Thomas, “The structure of a methyl iodide monolayer adsorbed on graphite,” *Molecular Physics*, vol. 67, pp. 439–446, jun 1989.
- ⁸⁴ A. K. Bickerstaffe, N. P. Cheah, S. M. Clarke, J. E. Parker, A. Perdigon, L. Messe, and A. Inaba, “The crystalline structures of carboxylic acid monolayers adsorbed on graphite,” *Journal of Physical Chemistry B*, vol. 110, no. 11, pp. 5570–5575, 2006.
- ⁸⁵ T. Bhide, S. M. Clarke, T. K. Phillips, T. Arnold, and J. E. Parker, “Crystalline structures of alkylamide monolayers adsorbed on the surface of graphite,” *Langmuir*, vol. 26, no. 11, pp. 8201–8206, 2010.
- ⁸⁶ C. Sun, S. Clarke, A. Brewer, B. Li, J. Parker, and F. Demmel, “The structures of 1-bromoheptane and 1-bromononane monolayers adsorbed on the surface of graphite,” *Molecular Physics*, vol. 110, pp. 217–225, feb 2012.
- ⁸⁷ T. Arnold, M. Forster, A. Athanasiou Fragkoulis, and J. E. Parker, “Structure of Normal-Alkanes Adsorbed on Hexagonal-Boron Nitride,” *The Journal of Physical Chemistry C*, vol. 118, pp. 2418–2428, feb 2014.
- ⁸⁸ T. Arnold, S. Chanaa, S. M. Clarke, R. E. Cook, and J. Z. Larese, “Structure of an n-butane monolayer adsorbed on magnesium oxide (100),” *Physical Review B*, vol. 74, p. 085421, aug 2006.
- ⁸⁹ J. P. RABE and S. BUCHHOLZ, “Commensurability and Mobility in Two-Dimensional Molecular Patterns on Graphite,” *Science*, vol. 253, pp. 424–427, jul 1991.
- ⁹⁰ S. De Feyter and F. C. De Schryver, “Two-dimensional supramolecular self-assembly probed by scanning tunneling microscopy,” *Chemical Society Reviews*, vol. 32, no. 3, pp. 139–150, 2003.
- ⁹¹ K. Tahara, S. Lei, J. Adisoejoso, and D. Feyter, “Supramolecular surface-confined architectures created by self-assembly of triangular phenylene – ethynylene macrocycles via van der Waals interaction,” *Chem. Commun.*, vol. 46, pp. 8507–8525, 2010.

- ⁹² T. Kudernac, S. Lei, J. a. a. W. Elemans, and S. De Feyter, “Two-dimensional supramolecular self-assembly: nanoporous networks on surfaces,” *Chem. Soc. Rev.*, vol. 38, no. 2, pp. 402–421, 2009.
- ⁹³ S. Griessl, M. Lackinger, M. Edelwirth, M. Hietschold, and W. M. Heckl, “Self-Assembled Two-Dimensional Molecular Host-Guest Architectures From Trimesic Acid,” *Single Molecules*, vol. 3, pp. 25–31, apr 2002.
- ⁹⁴ D. J. Duchamp and R. E. Marsh, “The crystal structure of trimesic acid (benzene-1,3,5-tricarboxylic acid),” *Acta Crystallographica Section B Structural Crystallography and Crystal Chemistry*, vol. 25, pp. 5–19, jan 1969.
- ⁹⁵ F. H. Herbstein, M. Kapon, and G. M. Reisner, “Trimesic acid, its hydrates, complexes and polymorphism. VIII. Interstitial complexes of α - and (the hypothetical) γ -trimesic acid,” *Acta Crystallographica Section B Structural Science*, vol. 41, pp. 348–354, oct 1985.
- ⁹⁶ F. H. Herbstein, M. Kapon, and G. M. Reisner, “Catenated and non-catenated inclusion complexes of trimesic acid,” *Journal of Inclusion Phenomena*, vol. 5, pp. 211–214, apr 1987.
- ⁹⁷ O. Ochs, O. Ochs, M. Hocke, M. Hocke, S. Spitzer, S. Spitzer, W. M. Heckl, W. M. Heckl, N. Martsinovich, M. Lackinger, and M. Lackinger, “Origin of Solvent-Induced Polymorphism in Self-Assembly of Trimesic Acid Monolayers at Solid-Liquid Interfaces,” *Chemistry of Materials*, vol. 32, no. 12, pp. 5057–5065, 2020.
- ⁹⁸ M. Lackinger, S. Griessl, W. M. Heckl, M. Hietschold, and G. W. Flynn, “Self-assembly of trimesic acid at the liquid-solid interface - A study of solvent-induced polymorphism,” *Langmuir*, vol. 21, no. 11, pp. 4984–4988, 2005.
- ⁹⁹ N. Thi Ngoc Ha, T. G. Gopakumar, and M. Hietschold, “Polymorphism driven by concentration at the solid-liquid interface,” *Journal of Physical Chemistry C*, vol. 115, no. 44, pp. 21743–21749, 2011.
- ¹⁰⁰ N. Thi, N. Ha, T. G. Gopakumar, and M. Hietschold, “Surface Science Polymorphs of trimesic acid controlled by solvent polarity and concentration of solute at solid – liquid interface,” *Surface Science*, vol. 607, pp. 68–73, 2013.
- ¹⁰¹ Y. Ye, W. Sun, Y. Wang, X. Shao, X. Xu, F. Cheng, J. Li, and K. Wu, “A unified model: Self-assembly of trimesic acid on gold,” *Journal of Physical Chemistry C*, vol. 111, no. 28, pp. 10138–10141, 2007.
- ¹⁰² A. Ibenskas and E. E. Tornau, “Statistical model for self-assembly of trimesic acid molecules into homologous series of flower phases,” *Physical Review E*, vol. 86, p. 051118, nov 2012.
- ¹⁰³ S. Spitzer, O. Helmle, O. Ochs, J. Horsley, N. Martsinovich, W. M. Heckl, and M. Lackinger, “What can be inferred from moiré patterns? A case study of trimesic acid monolayers on graphite,” *Faraday Discussions*, vol. 204, pp. 331–348, 2017.

- ¹⁰⁴ S. J. H. Griessl, M. Lackinger, F. Jamitzky, T. Markert, M. Hietschold, and W. M. Heckl, "Incorporation and Manipulation of Coronene in an Organic Template Structure," *Langmuir*, vol. 20, pp. 9403–9407, oct 2004.
- ¹⁰⁵ Z. P. L. Laker, A. J. Marsden, O. De Luca, A. D. Pia, L. M. A. Perdigão, G. Costantini, and N. R. Wilson, "Monolayer-to-thin-film transition in supramolecular assemblies: the role of topological protection," *Nanoscale*, vol. 9, no. 33, pp. 11959–11968, 2017.
- ¹⁰⁶ F. H. Allen, W. D. Samuel Motherwell, P. R. Raithby, G. P. Shields, and R. Taylor, "Systematic analysis of the probabilities of formation of bimolecular hydrogen-bonded ring motifs in organic crystal structures," *New Journal of Chemistry*, vol. 23, no. 1, pp. 25–34, 1999.
- ¹⁰⁷ J. a. Theobald, N. S. Oxtoby, M. a. Phillips, N. R. Champness, and P. H. Beton, "Controlling molecular deposition and layer structure with supramolecular surface assemblies," *Nature*, vol. 424, no. 6952, pp. 1029–1031, 2003.
- ¹⁰⁸ M. Mura, F. Silly, G. A. D. Briggs, M. R. Castell, and L. N. Kantorovich, "H-bonding supramolecular assemblies of PTCDI molecules on the Au(111) surface," *Journal of Physical Chemistry C*, vol. 113, no. 52, pp. 21840–21848, 2009.
- ¹⁰⁹ J. M. Topple, S. A. Burke, W. Ji, S. Fostner, A. Tekiel, and P. Grütter, "Tailoring the morphology and dewetting of an organic thin film," *Journal of Physical Chemistry C*, vol. 115, no. 1, pp. 217–224, 2011.
- ¹¹⁰ E. Stevens, "Experimental electron density distribution of molecular chlorine," *Molecular Physics*, vol. 37, no. 1, pp. 27–45, 1979.
- ¹¹¹ X. Yang, F. Wang, Q. Chen, L. Wang, and Z. Wang, "Halogen bonded two-dimensional supramolecular assemblies studied by high resolution scanning tunneling microscopy," *Chinese Science Bulletin*, vol. 52, no. 13, pp. 1856–1859, 2007.
- ¹¹² S. M. Clarke, T. Frišćić, W. Jones, A. Mandal, C. Sun, and J. E. Parker, "Observation of a two-dimensional halogen-bonded cocrystal at sub-monolayer coverage using synchrotron X-ray diffraction," *Chem. Commun.*, vol. 47, no. 9, pp. 2526–2528, 2011.
- ¹¹³ M. Sacchi, A. Y. Brewer, S. J. Jenkins, J. E. Parker, T. Frišćić, and S. M. Clarke, "Combined Diffraction and Density Functional Theory Calculations of Halogen-Bonded Cocrystal Monolayers," *Langmuir*, vol. 29, pp. 14903–14911, dec 2013.
- ¹¹⁴ A. Y. Brewer, M. Sacchi, J. E. Parker, C. L. Truscott, S. J. Jenkins, and S. M. Clarke, "Supramolecular self-assembled network formation containing N...Br halogen bonds in physisorbed overlays," *Phys. Chem. Chem. Phys.*, vol. 16, no. 36, pp. 19608–19617, 2014.
- ¹¹⁵ G. Binnig, H. Rohrer, C. Gerber, and E. Weibel, "Surface Studies by Scanning Tunneling Microscopy," *Physical Review Letters*, vol. 49, pp. 57–61, jul 1982.
- ¹¹⁶ L. C. Giancarlo and G. W. Flynn, "Scanning tunneling and atomic force microscopy probes of self-assembled, physisorbed monolayers: peeking at the peaks," *Annual review of physical chemistry*, vol. 49, pp. 297–336, 1998.

- ¹¹⁷ J. Tersoff and D. Hamann, “Theory and application for the scanning tunneling microscope,” *Physical review letters*, vol. 50, no. 25, p. 1998, 1983.
- ¹¹⁸ D. Necas and P. Klapetek, “Gwyddion: an open-source software for SPM data analysis,” *Open Physics*, vol. 10, jan 2012.
- ¹¹⁹ S. Ernst, *Optimisation of the preparation process for tips used in scanning tunneling microscopy*. PhD thesis, Max Planck Institute For Chemical Physics of Solids, 2006.
- ¹²⁰ K. G. Huang, D. Gibbs, D. M. Zehner, A. R. Sandy, and S. G. J. Mochrie, “Phase behavior of the Au(111) surface: Discommensurations and kinks,” *Physical Review Letters*, vol. 65, no. 26, pp. 3313–3316, 1990.
- ¹²¹ D. C. Madden, I. Temprano, M. Sacchi, M. Blanco-Rey, S. J. Jenkins, and S. M. Driver, “Self-Organized Overlayers Formed by Alanine on Cu{311} Surfaces,” *The Journal of Physical Chemistry C*, vol. 118, pp. 18589–18603, aug 2014.
- ¹²² C. I. Carlisle, D. A. King, M. L. Bocquet, J. Cerdá, and P. Sautet, “Imaging the surface and the interface atoms of an oxide film on Ag(111) by scanning tunneling microscopy: Experiment and theory,” *Physical Review Letters*, vol. 84, no. 17, pp. 3899–3902, 2000.
- ¹²³ W. H. Bragg and W. L. Bragg, “The Reflection of X-rays by Crystals,” *Proceedings of the Royal Society A: Mathematical, Physical and Engineering Sciences*, vol. 88, pp. 428–438, jul 1913.
- ¹²⁴ E. P. Gilbert, P. A. Reynolds, and J. W. White, “Characterisation of a basal-plane-oriented graphite,” *Journal of the Chemical Society, Faraday Transactions*, vol. 94, no. 13, pp. 1861–1868, 1998.
- ¹²⁵ A. Y. Brewer, *Halogen Bonding in Physisorbed Layers*. PhD thesis, University of Cambridge, 2014.
- ¹²⁶ “<http://pd.chem.ucl.ac.uk/pdnn/inst1/xtube.htm>.”
- ¹²⁷ A. Bergamaschi, A. Cervellino, R. Dinapoli, F. Gozzo, B. Henrich, I. Johnson, P. Kraft, A. Mozzanica, B. Schmitt, and X. Shi, “The MYTHEN detector for X-ray powder diffraction experiments at the Swiss Light Source,” *Journal of Synchrotron Radiation*, vol. 17, pp. 653–668, sep 2010.
- ¹²⁸ M. M. Woolfson, *An Introduction to X-ray Crystallography*. Cambridge University Press, jan 1997.
- ¹²⁹ C. J. Gilmore, J. A. Kaduk, and H. Schenk, eds., *International Tables for Crystallography*, vol. H. Chester, England: International Union of Crystallography, jul 2019.
- ¹³⁰ C. Buchsbaum and M. U. Schmidt, “Rietveld refinement of a wrong crystal structure,” *Acta Crystallographica Section B Structural Science*, vol. 63, pp. 926–932, dec 2007.
- ¹³¹ H. H.P. Schildberg, “Lineshape calculations powder samples,” *Surface Science*, vol. 208, pp. 507–532, 1989.

- ¹³² A. Guinier, G. Fournet, C. B. Walker, and G. H. Vineyard, "Small-Angle Scattering of X-Rays," *Physics Today*, vol. 9, pp. 38–39, aug 1956.
- ¹³³ K. D. M. Harris, M. Tremayne, and B. M. Kariuki, "Contemporary Advances in the Use of Powder X-Ray Diffraction for Structure Determination," *Angewandte Chemie International Edition*, vol. 40, no. 9, pp. 1626–1651, 2001.
- ¹³⁴ H. M. Rietveld, "A profile refinement method for nuclear and magnetic structures," *Journal of Applied Crystallography*, vol. 2, pp. 65–71, jun 1969.
- ¹³⁵ K. D. M. Harris and M. Tremayne, "Crystal Structure Determination from Powder Diffraction Data," *Chemistry of Materials*, vol. 8, pp. 2554–2570, jan 1996.
- ¹³⁶ N. P. Cheah, L. Messé, and S. M. Clarke, "The Formation of Solid Monolayers of Linear Amines Adsorbed on Graphite from the Liquid," *The Journal of Physical Chemistry B*, vol. 108, pp. 4466–4469, apr 2004.
- ¹³⁷ S. Clarke, T. Friščić, A. Mandal, C. Sun, and J. Parker, "Monolayer structures of 4,4 bipyridine on graphite at sub-monolayer coverage," *Molecular Physics*, vol. 109, no. 3, pp. 477–481, 2011.
- ¹³⁸ C. Sun, A. Brewer, S. M. Clarke, T. Bhide, and J. E. Parker, "Adsorption of iodoalkanes on graphite," *Molecular Physics*, vol. 111, pp. 1005–1014, apr 2013.
- ¹³⁹ J. A. Davidson, S. J. Jenkins, F. Gorrec, and S. M. Clarke, "C–H...N hydrogen bonding in an overlayer of s-triazine physisorbed on a graphite surface," *Molecular Physics*, vol. 8976, pp. 1–5, dec 2019.
- ¹⁴⁰ J. A. Davidson, M. Sacchi, F. Gorrec, S. M. Clarke, and S. J. Jenkins, "Halogen Bonding in Bicomponent Monolayers: Self-Assembly of a Homologous Series of Iodinated Perfluoroalkanes with Bipyridine," *Langmuir*, p. acs.langmuir.0c02126, jan 2021.
- ¹⁴¹ J. A. Davidson, S. J. Jenkins, F. Gorrec, and S. M. Clarke, "2D constraint modifies packing behaviour: a halobenzene monolayer with X 3 halogen-bonding motif," *Molecular Physics*, vol. 119, aug 2021.
- ¹⁴² S. A. C. Carabineiro and B. E. Nieuwenhuys, "Adsorption of small molecules on gold single crystal surfaces," *Gold Bulletin*, vol. 42, pp. 288–301, dec 2009.
- ¹⁴³ F. Hanke and J. Björk, "Structure and local reactivity of the Au(111) surface reconstruction," *Physical Review B*, vol. 87, p. 235422, jun 2013.
- ¹⁴⁴ L. Gross, "Recent advances in submolecular resolution with scanning probe microscopy," *Nature Chemistry*, vol. 3, no. 4, pp. 273–278, 2011.
- ¹⁴⁵ L. Gross, F. Mohn, N. Moll, G. Meyer, R. Ebel, W. M. Abdel-Mageed, and M. Jaspars, "Organic structure determination using atomic-resolution scanning probe microscopy," *Nature Chemistry*, vol. 2, no. 10, pp. 821–825, 2010.

- ¹⁴⁶ R. Temirov, S. Soubatch, O. Neucheva, A. C. Lassise, and F. S. Tautz, "A novel method achieving ultra-high geometrical resolution in scanning tunnelling microscopy," *New Journal of Physics*, vol. 10, no. 111, 2008.
- ¹⁴⁷ P. Hapala, G. Kichin, C. Wagner, F. S. Tautz, R. Temirov, and P. Jelinek, "Mechanism of high-resolution STM/AFM imaging with functionalized tips," *Physical Review B*, vol. 90, no. 8, p. 085421, 2014.
- ¹⁴⁸ C. Weiss, C. Wagner, C. Kleimann, M. Rohlfing, F. S. Tautz, and R. Temirov, "Imaging Pauli repulsion in scanning tunneling microscopy," *Physical Review Letters*, vol. 105, no. 8, pp. 2–5, 2010.
- ¹⁴⁹ D. Mayer, T. Dretschkow, K. Ataka, and T. Wandlowski, "Structural transitions in 4,4'-bipyridine adlayers on Au(111) - An electrochemical and in-situ STM-study," *Journal of Electroanalytical Chemistry*, vol. 524-525, pp. 20–35, 2002.
- ¹⁵⁰ F. Cunha, N. J. Tao, X. W. Wang, Q. Jin, B. Duong, and J. D'Agnesse, "Potential-induced phase transitions in 2,2'-bipyridine and 4,4'-bipyridine monolayers on Au(111) studied by in situ scanning tunneling microscopy and atomic force microscopy," *Langmuir*, vol. 12, no. 26, pp. 6410–6418, 1996.
- ¹⁵¹ M. Lackinger, "Surface-assisted Ullmann coupling," *Chem. Commun.*, vol. 53, no. 56, pp. 7872–7885, 2017.
- ¹⁵² Y. Baskin and L. Meyer, "Lattice constants of graphite at low temperatures," *Physical Review*, vol. 100, no. 2, p. 544, 1955.
- ¹⁵³ P. Sinha, A. Datar, C. Jeong, X. Deng, Y. G. Chung, and L.-C. Lin, "Surface Area Determination of Porous Materials Using the Brunauer–Emmett–Teller (BET) Method: Limitations and Improvements," *The Journal of Physical Chemistry C*, vol. 123, pp. 20195–20209, aug 2019.
- ¹⁵⁴ C. Marti, B. Croset, P. Thorel, and J. Coulomb, "A neutron investigation of krypton adsorbed on a graphite," *Surface Science*, vol. 65, pp. 532–538, jul 1977.
- ¹⁵⁵ R. Birgeneau, P. Heiney, and J. Pelz, "High resolution X-ray studies of monolayer krypton on varied forms of graphite," *Physica B+C*, vol. 109-110, pp. 1785–1795, jul 1982.
- ¹⁵⁶ J. H. Hubbell and S. M. Seltzer, "X-Ray Attenuation and Absorption for materials of Dosimetric Interest," in *Physical Reference Data*, 2014.
- ¹⁵⁷ Q. N. Zheng, X. H. Liu, T. Chen, H. J. Yan, T. Cook, D. Wang, P. J. Stang, and L. J. Wan, "Formation of halogen bond-based 2D supramolecular assemblies by electric manipulation," *Journal of the American Chemical Society*, vol. 137, pp. 6128–6131, may 2015.
- ¹⁵⁸ E. Bosch and C. L. Barnes, "Triangular Halogen-Halogen-Halogen Interactions as a Cohesive Force in the Structures of Trihalomesitylenes," *Crystal Growth and Design*, vol. 2, no. 4, pp. 299–302, 2002.

- ¹⁵⁹ D. Peyrot, M. G. Silly, and F. Silly, "X3 synthon geometries in two-dimensional halogen-bonded 1,3,5-tris(3,5-dibromophenyl)benzene self-assembled nanoarchitectures on Au(111)," *Physical Chemistry Chemical Physics*, vol. 20, no. 6, pp. 3918–3924, 2018.
- ¹⁶⁰ L. C. Gilday, S. W. Robinson, T. A. Barendt, M. J. Langton, B. R. Mullaney, and P. D. Beer, "Halogen Bonding in Supramolecular Chemistry," *Chemical Reviews*, vol. 115, no. 15, pp. 7118–7195, 2015.
- ¹⁶¹ J. Teyssandier, K. S. Mali, and S. De Feyter, "Halogen Bonding in Two-Dimensional Crystal Engineering," *ChemistryOpen*, vol. 9, no. 2, pp. 225–241, 2020.
- ¹⁶² C. M. Reddy, M. T. Kirchner, R. C. Gundakaram, K. A. Padmanabhan, and G. R. Desiraju, "Isostructurality, polymorphism and mechanical properties of some hexahalogenated benzenes: The nature of halogen...halogen interactions," *Chemistry - A European Journal*, vol. 12, no. 8, pp. 2222–2234, 2006.
- ¹⁶³ J. He, A. Li, Y. Tao, N. Chu, Z. Wang, S. Xu, J. Wang, H. Zhang, J. Yu, and W. Xu, "The remarkable structural comparison between two-dimensional and three-dimensional of 4, 4'-trimethylenedipyridine/1, 3, 5-trifluoro-2, 4, 6-triiodobenzene co-crystal," *Thin Solid Films*, vol. 685, pp. 263–268, sep 2019.
- ¹⁶⁴ H. Huang, Z. Tan, Y. He, J. Liu, J. Sun, K. Zhao, Z. Zhou, G. Tian, S. L. Wong, and A. T. S. Wee, "Competition between Hexagonal and Tetragonal Hexabromobenzene Packing on Au(111)," *ACS Nano*, vol. 10, no. 3, pp. 3198–3205, 2016.
- ¹⁶⁵ Z. Han, G. Czap, C.-I. Chiang, C. Xu, P. J. Wagner, X. Wei, Y. Zhang, R. Wu, and W. Ho, "Imaging the halogen bond in self-assembled halogenbenzenes on silver," *Science*, vol. 358, pp. 206–210, oct 2017.
- ¹⁶⁶ A. C. B. Lucassen, A. Karton, G. Leitus, L. J. W. Shimon, J. M. L. Martin, and M. E. van der Boom, "Co-Crystallization of Sym-Triiodo-Trifluorobenzene with Bipyridyl Donors: Consistent Formation of Two Instead of Anticipated Three N...I Halogen Bonds," *Crystal Growth & Design*, vol. 7, pp. 386–392, feb 2007.
- ¹⁶⁷ A. Mukherjee, J. Teyssandier, G. Hennrich, S. De Feyter, and K. S. Mali, "Two-dimensional crystal engineering using halogen and hydrogen bonds: towards structural landscapes," *Chemical Science*, vol. 8, no. 5, pp. 3759–3769, 2017.
- ¹⁶⁸ P. Metrangolo, H. Neukirch, T. Pilati, and G. Resnati, "Halogen bonding based recognition processes: A world parallel to hydrogen bonding," *Accounts of Chemical Research*, vol. 38, no. 5, pp. 386–395, 2005.
- ¹⁶⁹ P. Metrangolo, F. Meyer, T. Pilati, D. M. Proserpio, and G. Resnati, "Highly Interpenetrated Supramolecular Networks Supported by N...I Halogen Bonding," *Chemistry - A European Journal*, vol. 13, pp. 5765–5772, jul 2007.
- ¹⁷⁰ L. Catalano, P. Metrangolo, T. Pilati, G. Resnati, G. Terraneo, and M. Ursini, "Metric engineering in hybrid per fl uorocarbon-hydrocarbon cocrystals," *Journal of Fluorine Chemistry*, vol. 196, pp. 32–36, 2017.

- ¹⁷¹ S. S. Jang, M. Blanco, W. A. Goddard, G. Caldwell, and R. B. Ross, "The source of helicity in perfluorinated N-alkanes," *Macromolecules*, vol. 36, no. 14, pp. 5331–5341, 2003.
- ¹⁷² D. F. Eaton and B. E. Smart, "Are fluorocarbon chains stiffer than hydrocarbon chains? Dynamics of end-to-end cyclization in a C8F16 segment monitored by fluorescence," *Journal of the American Chemical Society*, vol. 112, pp. 2821–2823, mar 1990.
- ¹⁷³ R. Pollice and P. Chen, "Origin of the Immiscibility of Alkanes and Perfluoroalkanes," *Journal of the American Chemical Society*, vol. 141, pp. 3489–3506, feb 2019.
- ¹⁷⁴ J. E. Parker and S. M. Clarke, "Solid monolayers of fluorocarbons adsorbed on graphite from liquids," *Colloids and Surfaces A: Physicochemical and Engineering Aspects*, vol. 298, no. 1-2, pp. 145–147, 2007.
- ¹⁷⁵ J. E. Parker, S. M. Clarke, and A. C. Perdigón, "Preferential adsorption of solid monolayers of hydrocarbons over fluorocarbons at the solid/liquid interface," *Surface Science*, vol. 601, no. 18, pp. 4149–4153, 2007.
- ¹⁷⁶ C. V. Tortelli, "Telomerization of tetrafluoroethylene and hexafluoropropene: synthesis of diiodoperfluoroalkanes," *F. Chemistry*, vol. 47, pp. 199–211, 1990.
- ¹⁷⁷ S. M. Clarke, L. Messe, J. Adams, A. Inaba, T. Arnold, and R. K. Thomas, "A quantitative parameter for predicting mixing behaviour in adsorbed layers: The 2D isomorphism coefficient," *Chemical Physics Letters*, vol. 373, no. 5-6, pp. 480–485, 2003.
- ¹⁷⁸ J. A. Gladysz and M. Jurisch, "Structural, Physical, and Chemical Properties of Fluorous Compounds," in *Structural, Physical, and Chemical Properties of Fluorous Compounds* (I. T. Horváth, ed.), vol. 308 of *Topics in Current Chemistry*, pp. 1–23, Berlin, Heidelberg: Springer Berlin Heidelberg, 2011.
- ¹⁷⁹ P. Metrangolo, Y. Carcenac, M. Lahtinen, T. Pilati, K. Rissanen, A. Vij, and G. Resnati, "Nonporous organic solids capable of dynamically resolving mixtures of diiodoperfluoroalkanes," *Science*, vol. 323, no. 5920, pp. 1461–1464, 2009.
- ¹⁸⁰ S. J. Clark, M. D. Segall, C. J. Pickard, P. J. Hasnip, M. I. J. Probert, K. Refson, and M. C. Payne, "First principles methods using CASTEP," *Zeitschrift für Kristallographie - Crystalline Materials*, vol. 220, pp. 567–570, jan 2005.
- ¹⁸¹ A. Y. Brewer, M. Sacchi, J. E. Parker, C. L. Truscott, S. J. Jenkins, and S. M. Clarke, "The crystalline structure of the phenazine overlayer physisorbed on a graphite surface," *Molecular Physics*, vol. 111, pp. 3823–3830, dec 2013.
- ¹⁸² A. Tkatchenko and M. Scheffler, "Accurate Molecular Van Der Waals Interactions from Ground-State Electron Density and Free-Atom Reference Data," *Physical Review Letters*, vol. 073005, no. February, pp. 6–9, 2009.
- ¹⁸³ S. Grimme, "Semiempirical GGA-type density functional constructed with a long-range dispersion correction," *Journal of Computational Chemistry*, vol. 27, pp. 1787–1799, nov 2006.

- ¹⁸⁴ J. A. Howard, V. J. Hoy, D. O'Hagan, and G. T. Smith, "How good is fluorine as a hydrogen bond acceptor?," *Tetrahedron*, vol. 52, no. 38, pp. 12613–12622, 1996.
- ¹⁸⁵ R. Taylor, "The hydrogen bond between N—H or O—H and organic fluorine: favourable yes, competitive no," *Acta Crystallographica Section B Structural Science, Crystal Engineering and Materials*, vol. 73, pp. 474–488, jun 2017.
- ¹⁸⁶ A. Martín-Recio, A. J. Martínez-Galera, and J. M. Gómez-Rodríguez, "Surface Diffusion of Azabenzene s-Triazine Molecules on a Strong Interacting Graphene–Metal System," *The Journal of Physical Chemistry C*, vol. 119, pp. 401–406, jan 2015.
- ¹⁸⁷ L. Rodrigo, P. Pou, R. Martínez-Casado, A. J. Martínez-Galera, J. M. Gómez-Rodríguez, and R. Pérez, "Characterizing self-assembled molecular layers on weakly interacting substrates: the role of van der Waals and the chemical interactions," *Nano Futures*, vol. 2, p. 045002, sep 2018.
- ¹⁸⁸ P. Coppens, "Comparative X-Ray and Neutron Diffraction Study of Bonding Effects in s-Triazine," *Science*, vol. 158, pp. 1577–1579, dec 1967.
- ¹⁸⁹ E. S. P. B. V, W. Pyckhout, I. Callaerts, C. V. A. N. Alsenoy, H. J. Geise, R. Seip, C. Van Alsenoy, H. J. Geise, A. Almenningen, R. Seip, E. S. P. B. V, W. Pyckhout, I. Callaerts, C. V. A. N. Alsenoy, H. J. Geise, R. Seip, C. Van Alsenoy, H. J. Geise, A. Almenningen, and R. Seip, "The molecular structure of s-triazine in the gas phase determined from electron diffraction, infrared/raman data and ab initio force field calculations," *Journal of Molecular Structure*, vol. 147, pp. 321–329, 1986.
- ¹⁹⁰ I. C. Walker, M. H. Palmer, and C. C. Ballard, "The electronic states of the azines. VI. 1,3,5-triazine, studied by VUV absorption, near-threshold electron energy-loss spectroscopy and ab initio multi-reference configuration interaction calculations," *Chemical Physics*, vol. 167, pp. 61–75, nov 1992.
- ¹⁹¹ V. V. Korolkov, S. Allen, C. J. Roberts, and S. J. B. Tendler, "Green Chemistry Approach to Surface Decoration: Trimesic Acid Self-Assembly on HOPG," *The Journal of Physical Chemistry C*, vol. 116, pp. 11519–11525, may 2012.

